University of Southampton

Faculty of Environmental and Life Sciences

School of Biological Sciences

A platform to investigate the neuronal determinants of *APOE* genotype on neuron function

by

Mercedes Erika Alexandra Beyna

ORCID ID 0000-0003-0603-3981

Thesis for the degree of PhD Biological Sciences

October 13, 2023

University of Southampton

Abstract

Faculty of Environmental and Life Sciences

School of Biological Sciences

Thesis for the degree of Doctor of Philosophy Biological Sciences

A platform to investigate the neuronal determinants of *APOE* genotype on neuron function

by

Mercedes Erika Alexandra Beyna

Alzheimer's disease (AD), the most prevalent form of dementia worldwide, affects a growing proportion of the elderly and poses a significant societal burden. Pathological hallmarks include the appearance of misfolded proteins in the brain. This is evidenced by the deposition of amyloid-β (Aβ) plaques and tau-containing neurofibrillary tangles leading to neuron loss.

Advanced age is the single most important factor that leads to the dementia associated with AD. Additionally, genetic factors underlie the severity and/or age of onset. *APOE* ε4 is the strongest genetic risk factor for sporadic AD. Subtle changes in the gene lead to three common variants: *APOE* ε4, *APOE* ε3, and *APOE* ε2. In terms of AD, ε4 is associated with increased while ε2 is associated with decreased incidence compared with ε3. The protein from this gene, apolipoprotein E (ApoE), is involved in numerous functions in the brain including cholesterol homeostasis and clearance of Aβ. Functional complexity is increased as ApoE is primarily synthesized and secreted from astrocytes while neuronal expression has also been identified in the context of injury, damage, or stress. ApoE is a secreted molecule, which raises questions regarding which cell source and what fundamental functions of ApoE modulate AD susceptibility. Is there a neuron-intrinsic disease trigger and/or disproportionately high neuron-autonomous contribution to AD?

I compared isogenic cell lines in which the genome is engineered to carry homozygosity for each of the three *APOE* alleles listed above. I interrogated the impact of genotype on neuronal differentiation, morphology, and potential variation in vulnerability to stress. This latter aspect was modeled by exposing mature cultures to kainate-induced excitotoxic insult. These approaches revealed that *APOE* had little impact on neuron differentiation, except for subtly affecting connectivity-related gene expression in the ε4/ε4 versus neurons of the other two genotypes. Upon kainic acid exposure, ε4/ε4 neurons again showed a small difference; compared to ε3/ε3 and ε2/ε2 neurons, there was a delay in mounting an *ATF4* response, a stress-protective

mechanism. No other differential response to excitotoxicity emerged. Although these neurons did show a detectable low level of *APOE* transcript, there was no upregulation of *APOE* upon kainate exposure. My established neuronal platform of APOE variants is now available for further studies to more deeply probe genotype-specific mechanistic differences based on my initial observations.

These subtle but clear changes in ε4-related altered neurodevelopment and delayed stress response suggest that the ε4 allele may have limited effect early in life. However, over multiple stress events that may occur over a lifetime, these changes could provoke neurodegeneration. Another implication is that because ε2/ε2 neurons did not simply show the opposite phenotype of ε4 neurons, the neuroprotective mechanism of ε2 does not overlap with the pathways responsible for ε4's detrimental effects.

Table of Contents

Table of Tables

Table of Tables

Table of Figures

Table of Figures

Table of Figures

Table of Figures

Research Thesis: Declaration of Authorship

Print name: Mercedes Erika Alexandra Beyna

Title of thesis: A platform to investigate the neuronal determinants of *APOE* genotype on neuron function

I declare that this thesis and the work presented in it are my own and has been generated by me as the result of my own original research.

I confirm that:

1. This work was done wholly or mainly while in candidature for a research degree at this University;
2. Where any part of this thesis has previously been submitted for a degree or any other qualification at this University or any other institution, this has been clearly stated;
3. Where I have consulted the published work of others, this is always clearly attributed;
4. Where I have quoted from the work of others, the source is always given. With the exception of such quotations, this thesis is entirely my own work;
5. I have acknowledged all main sources of help;
6. Where the thesis is based on work done by myself jointly with others, I have made clear exactly what was done by others and what I have contributed myself;
7. None of this work has been published before submission
8. Signature: Mercedes Beyna Date: July 24, 2023

For

My sisters, wind beneath my wings.

And,

My mother, a reason I fly.

Acknowledgements

Thank you to my Ph.D. supervisors, Katrin Deinhardt and Vincent O'Connor, for your unwavering belief in me during this quest for my doctorate. You are both incredibly patient, generous, genuine, open-minded, and kind. I am going to miss our weekly sessions. I'm already fondly looking back at time spent puzzling over my data, answering your thought-provoking questions, discussing next steps, and streamlining this thesis. Overall, you help me continually hone clarity. Aside from all that, I love learning about each other and seeing your worldviews unfurl.

I sincerely thank Erik Hett, Heike Hering, Michael Ehlers, and Anabella Villalobos. Without your advocacy, I would not have been able to embark on this Biogen-sponsored PhD path in the first place. Special thank you to Heike for helping me choose my Ph.D. project and being a most excellent, empowering, empathetic mentor and role model, enabling me to do this!

Thank you to Sandi Engle, Naomi Okugawa, Zhonghua Zhu, Joe Wang, and the Harvard Stem Cell Institute for advice and/or training on CRISPR and iPSC methods and/or reagents. Thank you, Laura Blaha, for training me on lentiviral transductions and differentiation workflows; as I write this, I can hear your cheerful voice "No problem! Ladies helping ladies!". Thank you, Liron Noiman, for the handholding on my first NanoString experiment; as I write this, I can taste the luscious Lemon Lavender birthday cake you baked for one of my first in-person events post-pandemic. Thank you to the people who donated your tissue for iPSC generation and for research in general, and to the ADAPTED consortium researchers for generating isogenic sets of iPSCs used in this work. I thank Biogen co-workers who have been supportive cheerleaders. Many of you have become dear friends, especially Claude Ambroise, Ceren Tezer, Bekim Bajrami, Sue Swalley, Abby Mariga, Olga Golonzhka, Laura Ingano, Christilyn Graff, Aram Parsegian, and Aftabul Haque. Thank you, Chia-Chen Liu, for comments on this thesis and Richelle Sopko for kindly proofreading.

Many others have helped me grow, apart from scientifically, throughout these last few years. Thank you for the fortitude you have poured into me: Maria B., Kevin and Debra L., TEAL, Synphen W., Van T., Stacey S-R., Sarita Y., Herbert K., Nicole and Mariëtte M-T., Diane S., Larry J, Benjamin B., Mary C., Tina M, Audine I, Christine P, and Daniel L.

So many not named here have contributed to my getting here — this Ph.D. is a lifelong dream. For example, without my foundation at my beloved high school with inspirational teachers like Grace Baston, the little girl from a small island nation would not be this grownup earning her Ph.D. from a big island nation; via a most scenic, meandering, and exciting route. I am eternally grateful for the connections and experiences along the way enriching my life.

Acknowledgements

Most cartoons have been created with BioRender.com.

Abbreviations

AAVS1	Adeno-Associated Virus Integration Site 1
ABCA1	Adenosine triphosphate (ATP)-binding cassette A1
ABCA7	Adenosine triphosphate (ATP)-binding cassette A7
AD	Alzheimer's disease
APOE	Apolipoprotein E
APP	Amyloid-beta precursor protein
ATF4	Activating transcription factor 4
ATP	adenosine triphosphate
Aβ	Amyloid-beta
BDNF	Brain derived neurotrophic factor
bHLH	Basic helix-loop-helix
Cas	CRISPR-associated endonuclease
Cas9	CRISPR-associated endonuclease 9
CLU	Clusterin (Apolipoprotein J)
CNS	Central nervous system
CRISPR	Clustered, regularly interspaced short palindromic repeats
crRNA	CRISPR RNA
CSF	Cerebrospinal fluid
dbcAMP	Dibutyryl cyclic AMP
DEG	Differentially expressed gene
DLK	Dual-leucine zipper kinase
Dll1	Delta-like1
DMT	Disease modifying therapy
DSB	Double strand DNA break
EBiSC	European Bank for induced pluripotent Stem Cells
EGFP	Enhanced green fluorescent protein
EOAD	Early-onset AD
ER	Endoplasmic reticulum

ERK1/2	Extracellular signal-regulated kinase (ERK)1/2
ESC	Embryonic stem cell
fAD	Familial AD
FOS	Fos proto-oncogene
FTD	Frontotemporal dementia
GABA	γ-aminobutyric acid
GAP43	Growth associated protein 43
GAPDH	Glyceraldehyde-3-Phosphate Dehydrogenase
GFAP	Glial Fibrillary Acidic Protein
GRIA3	Glutamate ionotropic receptor AMPA type subunit 3
GRIK1	Glutamate ionotropic receptor kainate type subunit 1 (GLUR5)
GRIK2	Glutamate ionotropic receptor kainate type subunit 2 (GLUR6)
GRIN2D	Glutamate ionotropic receptor NMDA type subunit 2D
GRM1	Glutamate metabotropic receptor 1 (MGLUR1)
gRNA	Guide RNA
GSK3B	Glycogen synthase kinase 3 beta
HDL	High density lipoprotein
HDR	Homology-directed repair
HEK293	Human embryonic kidney 293 cells
Hes1	Hes Family bHLH Transcription Factor 1
HMGR	3-hydroxy-3-methyglutaryl-coenzyme A reductase
iPSC	Induced pluripotent stem cell
iN	Induced neuron
KA	Kainic acid or kainate
KO	Gene knockout
LDLR	Low-density lipoprotein receptor
LOAD	Late-onset AD
LRP1	LDLR-related protein 1
MAP	Mitogen-activated protein
MAPK	Mitogen-activated protein kinase
MAP2	Microtubule Associated Protein 2

MAPT	Microtubule Associated Protein Tau
MCI	Mild cognitive impairment
MRI	Magnetic resonance imaging
MT	Microtubule
MYC	V-myc avian myelocytomatosis viral oncogene homolog (c-Myc)
NFT	Neurofibrillary tangles
NGFR	Nerve Growth Factor Receptor
NGN2	Neurogenin2
NHEJ	Non-homologous end joining
NICD	Notch intracellular domain
NMDA	N-methyl-D-aspartate
NPC	Neuronal progenitor cell
NPC1	Niemann-Pick C1 intracellular cholesterol transporter 1
NSC	Neural stem cell
NSE	Neuron specific enolase
PAM	Protospacer adjacent motif
PBS	phosphate-buffered saline
PET	Positron emission tomography
PGK1	Phosphoglycerate kinase 1
PPP1R12C	Protein phosphatase 1 regulatory subunit 12C gene
PSD95	Postsynaptic density-95
PSEN1	Presenilin 1
PSEN2	Presenilin 2
p-tau	Phosphorylated tau
PTM	Posttranslational modification
ROCKi	Rho-associated protein kinase inhibitor
RNP	Ribonucleoprotein
rtTA	Tetracycline transactivator
sAD	Sporadic AD
sgRNA	Single gRNA
SLC17A6	Solute carrier family 17 member 6 (*VGLUT2*)

SLC17A7	Solute carrier family 17 member 7 (*VGLUT1*)
SNP	Single nucleotide polymorphisms
SRE-1	Sterol-regulated element-1
SREBP	Sterol-regulated element binding protein
SV2	Synaptic vesicle protein 2
SV2B	Synaptic vesicle glycoprotein 2B
SYN1	Synapsin1
SYP	Synaptophysin
TetR	Tetracycline-responsive repressor protein
TF	Transcription factor
TH	Tyrosine hydroxylase
tracrRNA	Trans-activating crRNA
UbC	Ubiquitin C
UPR	Unfolded protein response
VGLUT1	Vesicular glutamate transporter type 1
VGLUT2	Vesicular glutamate transporter type 2
VLDLR	Very-low-density lipoprotein receptor

Chapter 1 Introduction

Alois Alzheimer first brought this now eponymous disease to light at a conference in Tübingen, Germany, in 1906 in a lecture entitled “On the peculiar disease process of the cerebral cortex” (*Über eine eigenartige Erkrankung der Hirnrinde;* Alzheimer 1906) (1). He described progressive symptoms and psychological deterioration in a 51-year-old woman (Auguste Deter). He highlighted stark cognitive deficits, disorientation, aphasia, hallucinations, and erratic behavior. He also described postmortem evaluation of her brain revealed general atrophy and cortical manifestations, later to become known as amyloid beta plaques and tau neurofibrillary tangles. In a follow-up publication, he asserted that his discoveries “*demonstrate to us, in an impressive way, how difficult it is to define diseases solely with respect to their clinical features, especially in the case of those mental disorders which are caused by an organic disease process*” (1).

Since then, knowledge concerning the organic processes of Alzheimer’s disease (AD) has grown tremendously. Progressively, new appreciation of causal and protective genetic factors, identification of new biomarkers, and new access for patients to disease-modifying treatments (DMTs) are building. Yet, AD is without a cure and increasingly one of the most costly, devastating, and deadly illnesses of our time (2, 3). This Introduction Chapter serves to, first, offer a current and broad overview of AD, second, provide insight into my gene of interest, *APOE*, and lastly, set the stage for my exploration into whether a neuronal source of this gene product, in three critical variants, alters response to stress in an *in vitro* setting. The knowledge I can add to our understanding of the disease processes will help in our collective quest to make medicines that will keep vulnerable neurons alive and healthy.

1.1 Alzheimer’s Disease

Dementia broadly refers to the severe decline in cognition that seriously compromises daily life activities. AD is the most common form of dementia which exists on a continuum preceded by mild cognitive impairment (MCI) in which affected individuals show more memory loss than expected for their age group (4). Transition, or phenoconversion, from MCI to more severe cognitive impairment, i.e., a person losing their abilities for independence, happens within five years in one-third of MCI cases (5). A typical early symptom is episodic memory loss, such as trouble recalling recent conversations and events (4). Progressively, additional symptoms such as impaired communication, confusion, poor judgment, behavior changes, sleep disturbances and difficulty speaking, swallowing, and walking take hold (4). Affected individuals eventually become bedbound, incontinent, and require continuous care. Invariably, AD is ultimately fatal (4).

Advanced age is the strongest risk factor in developing the disease. As the global population ages, AD prevalence grows (6). Over 55 million people worldwide currently have AD; the number is projected to reach 131.5 million by 2050 (2, 7). An even more sobering statistic is that the global number of people on the AD continuum is currently estimated at 416 million, i.e., about one-fifth of all people over 50 years old (8). In terms of the economic burden, in the USA alone, total annual costs for people with AD or other dementias are expected to increase from $321 billion in 2022 to just under $1 trillion in 2050 (9).

Treatments highly effective in slowing or stopping this disease are an urgent, unmet medical and societal need (2, 3, 9). Traditional treatment options for AD improve cognitive symptoms in the short term but do not delay, stop, or cure the disease. New DMTs promise to slow the disease, and the magnitude of their effectiveness will become more apparent in time (Section 1.2.1.3).

1.2 Neuropathology

The core histopathological features of AD are brain atrophy or wasting away of brain tissue (Figure 1.1, A), accumulation of intracellular neurofibrillary tangles (NFTs) (Figure 1.1, B), and extracellular neuritic (senile) plaques (Figure 1.1, C).

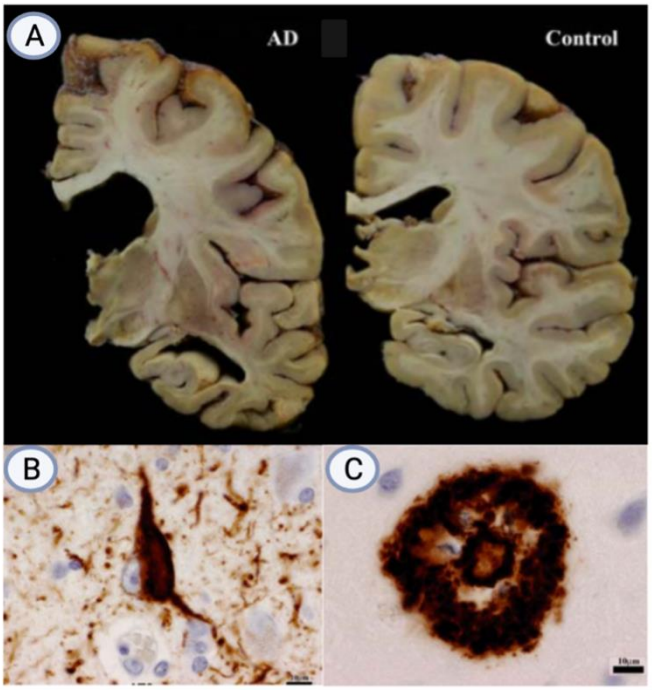

Figure 1.1 Neuropathological hallmarks of Alzheimer's disease.

Neuropathological hallmarks of Alzheimer's disease (AD) are shown. Macroscopically, atrophy is observed in the brain of a patient with AD (A, left) compared to one from an age- and sex-matched control (A, right). Histological staining in AD brain sections reveals intracellular NFT (AT8 immunohistochemistry) (B) and a neuritic plaque (C). Scale bars = 10 µm. Adapted from (10).

1.2.1 Amyloid beta plaques

Plaques (Figure 1.1, C) consist primarily of the amyloid beta (Aβ) peptide (detailed in Section 1.2.1.1) and appear extracellularly in the neuropil at least a decade before clinical symptoms surface (11). For neuropathologic staging, plaques are categorized in various ways. For example, their distribution across brain regions can be noted on a scale ranging from phase 1, which indicates occurrence in the frontal, parietal, temporal, or occipital cortex, and progressing to phase 5, which places them in the brainstem and cerebellum (11). Neuropathologic and quantitative neuroimaging evaluations reveal the spatiotemporal deposition of Aβ. Deposits start in the neocortex, expand to the allocortex, then to the brainstem, and finally to the cerebellum, as depicted in Figure 1.2 (12).

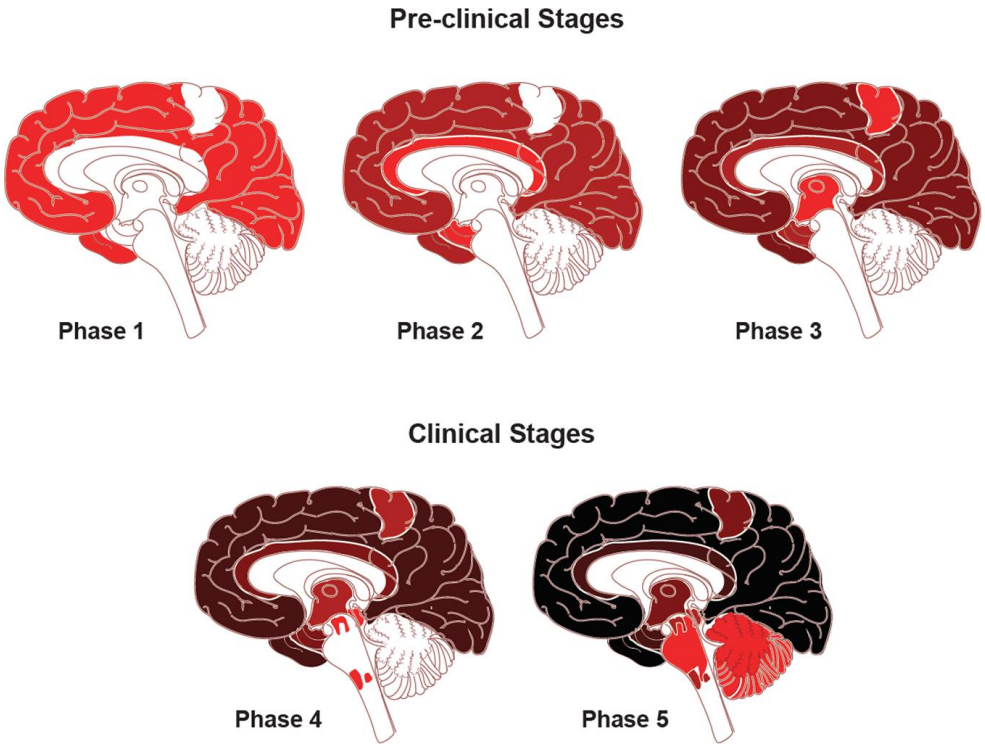

Figure 1.2 Spatiotemporal tracking of brain amyloid β.

Shaded regions in Phase 1 represent neocortical areas where amyloid-β (Aβ) first accumulates in early pre-symptomatic stages. Accumulation in the matching regions is shown in darker shading in the following phases, with fresher deposits showing Aβ in a lighter hue in each phase; the gradual switch to darker shading signals the constant buildup of Aβ. Progressive regions with early accumulation of Aβ are association cortices (Phase 1), allocortex (Phase 2), midbrain (Phase 3), brain stem (Phase 4), then cerebellum (Phase 5). Phases 4 and 5 represent late clinical stages (12).

1.2.1.1 Amyloid beta (Aβ)

Aβ is a 37 to 49 amino acid peptide (~4 kDa) generated from cleavage of the single transmembrane protein, amyloid precursor protein (APP) (13). Physiological roles of APP and Aβ

are implicated in synaptic homeostatic regulation, dendritic spine remodeling, neurotransmission, immunity, and lipid processing (14-16). The two enzymes that proteolytically convert intact APP to Aβ are β -secretase and γ-secretase (17). Presenilins are components of the γ-secretase complex (and mutations in encoding genes are risk factors for AD; Section 1.3.1) (17). Cleavage by γ-secretase can occur at multiple sites to yield several C-terminal truncated isoforms, including: Aβ40 and Aβ42 (17, 18). The degree of toxicity of the different Aβ species is disputed (19). Soluble, oligomeric Aβ can disrupt synaptic plasticity and calcium homeostasis, presumably precipitating memory dysfunction and neuron death (19, 20).

1.2.1.2 Amyloid β cascade hypothesis

The 'Amyloid Cascade Hypothesis' for AD posits that it is the abnormal buildup of Aβ as described above, that initiates pathogenesis and that subsequent changes in the brains of people that will be diagnosed with AD (i.e., tau pathology [Section 1.2.2] and neuron loss [Section 1.2.3]) are a result of the accumulation of Aβ pathology (16, 21-23). Aβ exists in the CNS of both healthy and AD-diagnosed individuals at very low nanomolar concentrations (24, 25). Brain Aβ accumulation occurs upon imbalance between its rate of production and removal (13, 26). This disequilibrium may result from Aβ's tendency to fold into oligomers and fibrils (13).

Genetic observations (Section 1.3.1) also support the notion that Aβ pathology is the primary trigger of AD.

1.2.1.3 Amyloid β targeting therapies

Most therapies tested in randomized clinical trials in recent years target the Aβ cascade mapped out above. Inhibitors of β - and γ-secretase designed to reduce the Aβ load by preventing its proteolytic generation have not slowed cognitive decline (27). Antibody drugs designed to bind Aβ and help clear plaques are the first to break the barrier of slowing cognitive decline (28, 29). FDA-approved antibodies against Aβ are currently the only disease modifying options for patients with AD; at this point treatment is initiated in individuals diagnosed with early AD (MCI due to AD or mild AD dementia) that have confirmed brain Aβ pathology (30). However, cognitive decline is not reversed or halted in the face of lowered Aβ via immunotherapy, thus calling for persistence in chasing other targets. Also, these drugs may not be helpful for patients with AD who carry the *APOE* ε4 gene variant (introduced in Section 1.3.2) because they are at greatest risk for developing a particular side effect, i.e., amyloid-related imaging abnormalities (ARIA) (30). Because Aβ antibody treatment may not be an appropriate option for these individuals, other

drugs with differentiated mechanisms of action are desired, especially for patients carrying *APOE* ε4.

1.2.2 Neurofibrillary tangles

AD brains accumulate NFTs (Figure 1.1, B), neuropil threads, and dystrophic neurites composed mainly of the hyperphosphorylated form of the microtubule-associated protein, tau (detailed in Section 1.2.2.2) (31). The presence of tau pathology places AD in the group of neurodegenerative disorders classified as 'tauopathies'. NFTs appear inside neurons, and this histopathological hallmark, which lags behind Aβ plaque manifestation (up to many years), correlates more closely than Aβ plaques with cognitive decline (32). According to the Braak and Braak staging system of AD, NFTs accumulate in a gradual way starting in the deep structures of the brain then spread with time in a stereotypical manner (31). NFTs initially appear in the entorhinal region (Braak's stages I and II), progress to the hippocampal area (stages III and IV) and then cover neocortical regions (stages V and VI) as depicted in Figure 1.3. Generally, NFT appearance in the hippocampus correlates with memory impairment and coverage of the neocortex correlates with additional cognitive decline (33).

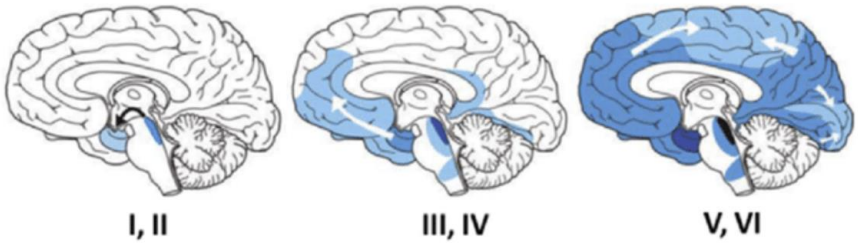

Figure 1.3 Spatiotemporal tracking of neurofibrillary tangles according to Braak and Braak.

NFTs first appear in the entorhinal region (Braak's stages I and II), progress to the hippocampus (stages III and IV) and eventually cover the neocortex (stages V and VI). The cerebellum is typically spared from tau pathology in AD. Adapted from Jouanne *et al*. (34).

1.2.2.1 Tau

The gene encoding tau, MAPT (microtubule-associated protein tau), comprises 16 exons, alternative splicing of which gives rise to 6 main tau isoforms in the human brain (35). Tau is a 'natively unfolded' or 'intrinsically disordered' protein because of the nature of its hydrophilic peptide sequence, which confers flexibility and very little secondary structure. However, tau can adopt disrupted conformations that aggregate and tauopathies are aggregation diseases featuring hyperphosphorylated tau (36).

Tau is highly expressed in axons where its microtubule (MT) binding domain interacts with MTs to modulate neurite outgrowth, among other functions (35, 36). The most well-described role of tau involves direct binding to the "stable" domain of MTs to promote their stabilization and assembly (36, 37). Newer models of tau function suggest tau is instead enriched on "labile" domains of MTs to regulate MT assembly *not by stabilizing* them but rather to enable them to have long labile domains (37). Tau is also involved in axonal transport by interacting with dynein and kinesin motor proteins that traffic intracellular cargo, modulating retro- and antero-grade transport (35). Tau localizes to dendrites and dendritic spines and has been directly implicated in synaptic functions (38). A role for tau in synaptic plasticity was put forward upon observations of activity-dependent synaptic tau translocation (39). In addition, tau has been localized to the nuclei in neurons and non-neuronal cells. The accumulation of nuclear tau has been implicated in cellular response to stress with regard to preserving DNA and nuclear RNA integrity (40). Also, tau has been reported to modulate RNA translation upon interacting with ribosomes (41, 42).

1.2.2.2 Tau-mediated pathophysiology

One hypothesis for tau-mediated neurodegeneration is that tau pathology starts with hyperphosphorylation and other post-translational modifications (PTMs) that cause tau to detach from MTs and slowly build up into insoluble NFTs. Dysfunctional dissociation of tau from MTs leads to tau missorting and inappropriate accumulation in pre- and post-synaptic compartments causing synaptic dysfunction (35). The disruption in tau binding is presumed to also lead to axonal MT instability, which can contribute to several negative outcomes (36). Further, aggregated tau species may hinder ribosomal function, decreasing RNA translation and impairing new protein synthesis (42). Tau is required for AB-induced toxicity as an enabler of this upstream toxic insult (43). Tau toxicity is mainly considered due to gain-of-toxic function, but the field does not know precisely how tau is toxic, as discussed by Chang *et al.* (43).

On the basis of the Braak and Braak staging of the appearance of tau pathology (Figure 1.3), the propagation of pathology occurs in a pattern that overlays with synaptically connected pathways rather than anatomical proximity (44). Evidence supports the hypothesis that pathological tau spreads through distinct neural networks, initially throughout close and later long-range circuits, via transsynaptic connections (45-47). Tau aggregates that are discharged into the extracellular space are thought to be taken up by other neurons, wherein they induce further aggregation in a templated conformational pattern, hence spreading the tau pathology (48).

1.2.2.3 Tau targeting therapies

A rationale for tau-directed therapies for AD is that tau pathology, more closely than AB lesions, correlates with the decline of neurocognition (32). Nearly a dozen anti-tau antibody therapies have been in development for AD or other tauopathies. Recently four have failed to show benefit in major clinical trials (semorinemab, gosuranemab, tilavonemab, and zagotenemab) and were discontinued (49). These were designed to work extracellularly by interfering with cell-to-cell propagation of pathogenic tau (27). Tau is mostly localized intracellularly and other tau-targeting DMTs currently undergoing clinical trials include modalities that interact with tau inside cells such as tau-lowering antisense oligonucleotides (ASO) and enzyme inhibitors (for e.g., O-GlcNAc transferase (OGT) inhibitors) (50-53).

Early phase clinical data showed that the investigational MAPT ASO therapy, BIIB080, reduced both soluble tau protein in the cerebrospinal fluid (CSF) and aggregated tau pathology in the brain of patients with early-stage AD (54). Patient recruitment is underway for a clinical trial essentially testing whether BIIB080 can slow the worsening of AD compared to placebo (clinical trials.gov identifier NCT05399888).

1.2.3 Brain atrophy, neurodegeneration, and synaptic degeneration

Brain atrophy can be readily revealed upon autopsy or magnetic resonance imaging (MRI) and is associated with loss of neurons and white matter volume and enlargement of ventricles (10). Of the three neuropathological hallmarks shown in Figure 1.1, loss of neurons (and by extension, synapses and brain connectivity) most strongly correlates with decline in cognitive function (55). In the beginning stages, people afflicted with AD have mainly memory symptoms and almost no other clinical signs of brain impairment, which may imply an issue with synaptic function that is preventing the ability to retain new information and make new memories, i.e., “AD represents, at least initially, an attack on synapses” (56). Synaptic changes represent the first in a sequence of steps that connect molecular activity at the synapse and subsequent intracellular biochemical cascades and cellular changes with the cognitive aspects of memory. For example, postsynaptic receptors link synapse structural and functional plasticity and are critical for generating short-term memories (11). Thus, synaptic plasticity is hypothesized to be partially responsible for memory formation (55, 57). In fact, a therapy for memory loss in AD, memantine, blocks the postsynaptic receptor, NMDAR, but this is only effective in the short-term (55, 57).

Synaptic degeneration in AD is hypothesized to stem from complex interactions involving toxic soluble forms of Aβ and tau that initiate synapse loss (synaptotoxicity) and spread it through connected neural circuits, putative mechanisms of which are highlighted in Figure 1.4 (55, 57). In

early phases of AD, in both mouse models and human patients, soluble forms of Aβ trigger synaptotoxicity in cortical and hippocampal neurons before insoluble Aβ plaques are present (58). One of the putative biological roles of Aβ is homeostatic fine-tuning of synapses. APP and its cleaving enzymes, β-secretase and γ-secretase, that yield the formation of AB are found at both pre- and post-synaptic membranes and studies suggest when this pathway malfunctions, it may contribute to synapse loss early in the disease process (11). Loss of synapses and dendritic spines is linked to Aβ-mediated removal of postsynaptic receptors (11). Tau has been shown to bind several synaptic vesicle proteins, such as synaptophysin (SYP) (59). Injecting human tau oligomers into the brains of mice induced memory impairment associated with reduced levels of synaptic vesicle proteins, including SYP, and mitochondrial dysfunction (59). Treating human neuronal cultures with tau oligomers triggered aggregation and hyperphosphorylation of tau and altered intracellular calcium ion (Ca^{2+}) levels that correlated with loss of synapses and imbalanced neurotransmitter release (60).

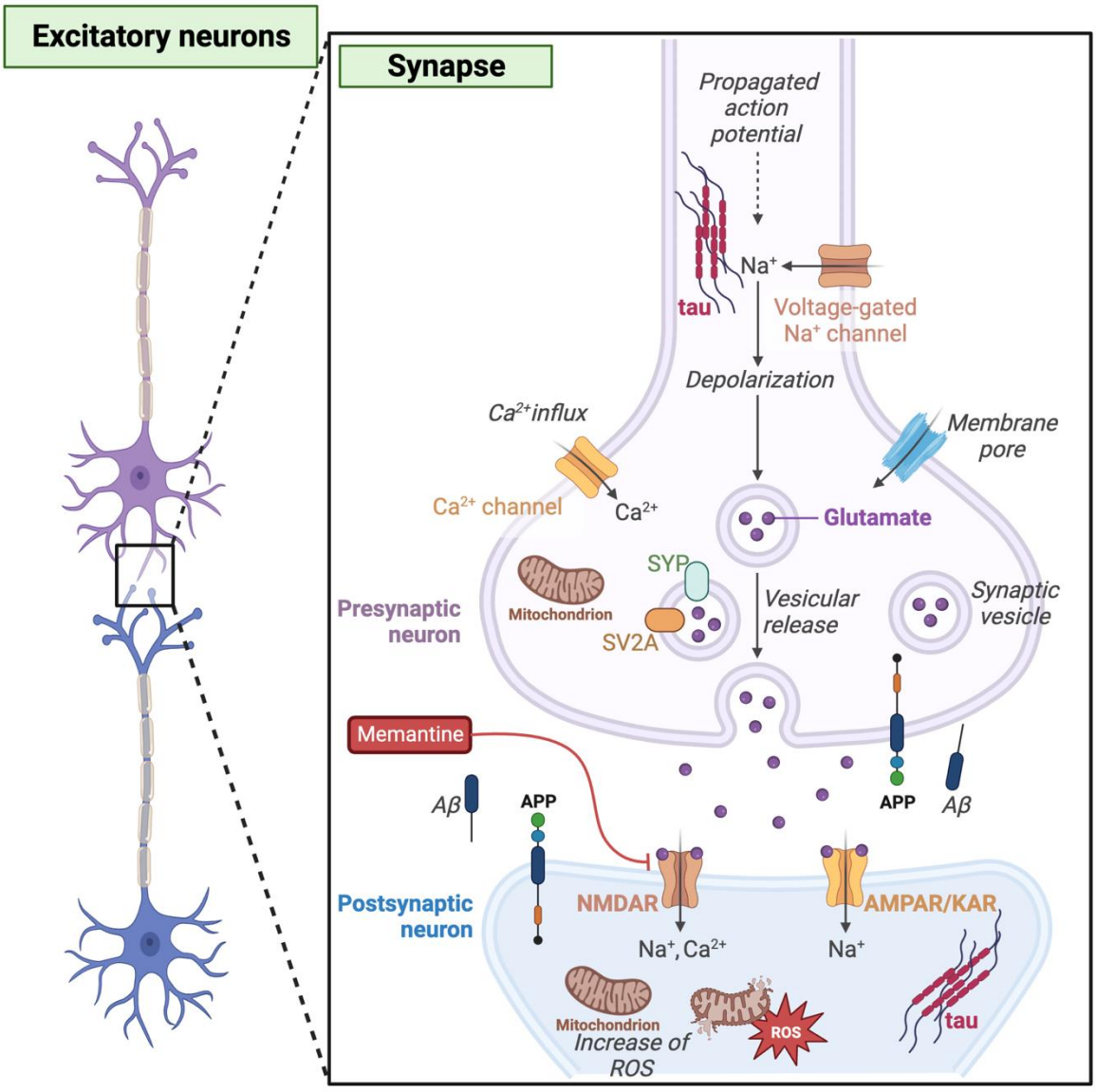

Figure 1.4 Some putative mechanisms of synaptic degeneration in Alzheimer's disease.

Putative (not exhaustive) mechanisms of synapse degeneration in AD are highlighted on a cartoon of a synapse. For illustration purposes, this example uses glutamate as its signaling molecule or neurotransmitter (i.e., from excitatory glutamatergic neurons) so glutamate is released from the synaptic vesicles upon depolarization when the neuron fires an electrical impulse (action potential). Upon activation, glutamate receptors on the postsynaptic side (NMDAR, AMPAR and KAR) allow influx of positive ions (Na^+ and Ca^{2+}) into neurons. APP is found on the membrane at the synapse. APP is cleaved to generate Aβ. Aβ can form toxic Aβ oligomers that can induce ecotoxicity by causing excessive Ca^{2+} influx which includes generation of membrane pores that allow dysregulation of Ca^{2+} entry. Pathogenic conformations of tau have been linked to reduction of synaptic vesicle proteins, such as SYP, leading to exhaustion of the synaptic vesicle pool. Reduction of the synaptic vesicle protein, SV2A, is observed in patients with AD. Buildup of toxic reactive oxygen species (ROS) caused by mitochondrial dysfunction has been reported in both the pre- and post-synaptic compartments in models of AD. The NMDAR antagonist, memantine, shows some efficacy as a cognition-enhancing drug in patients with AD (55, 57). Aβ = amyloid- β; AMPAR = α-amino-3-hydroxy-5-methyl-4-isoxazolepropionic acid receptor; APP = Amyloid-β precursor protein; KAR = Kainic acid receptor or Kainate receptor; NMDAR = N-Methyl-d-aspartate receptor; SYP = Synaptophysin; SV2A = Synaptic vesicle protein 2A.

Neurodegeneration in AD could partially stem from compromised brain lipid metabolism and distribution as aberrant cholesterol metabolism has been implicated in AD pathogenesis. Meta-analysis of serum cholesterol revealed hypercholesterolemia as a significant risk factor for AD and cognitive decline (61). Cholesterol interacts with both APP and Aβ and elevated membrane cholesterol stimulates β -secretase activity, leading to an accumulation of Aβ40 and Aβ42 (Section 1.2.1.1), and subsequently, increased extracellular amyloid deposits (62). Tau filament formation has been reported to increase intraneuronal, unesterified cholesterol and a feedback loop has been proposed whereby perturbed cholesterol metabolism promotes tau pathology and tau filament formation perturbs cellular trafficking, thus altering cholesterol homeostasis (63).

While synaptic degradation and neurodegeneration are also largely influenced by neuroinflammation, involving glial cells (astrocytes and microglia) that have been altered in AD, this topic is beyond the scope of my thesis.

1.3 Genetic risk factors

After increased age, the next leading risk factor for AD is having a family history of this disease which is usually divided into early-onset (prior to 60 years of age) and late-onset (about 65 years of age or older) (64). Genetic determinants represent ~5% of all cases and are primarily associated with early-onset AD (EOAD). This means that 95% of the root causes are thought to be sporadic and are likely multifactorial (65). Environmental and biological factors likely contribute in unique ways for each affected person, in an extension of the nature-nurture question. Genome-wide association studies (GWAS) compare millions of single nucleotide polymorphisms (SNPs) in the genomes between groups of people with and without disease and have revealed risk loci for late-onset AD (LOAD) also referred to as sporadic AD or sAD.

1.3.1 Early-onset Alzheimer's disease

As described above, AB derives from proteolytic processing of APP (Section 1.2.1.1). Disruptive mutations in three genes whose functions converge on APP metabolism are causative genetic factors for AD: amyloid precursor protein (*APP*), presenilin 1 (*PSEN1*), and presenilin 2 (*PSEN2*). These mutations promote APP processing and presenilin interactions that favor the formation of aggregation prone Aβ species. These are mostly autosomal dominant mutations, inherited in a Mendelian fashion, giving rise to 'true familial' EOAD or familial AD (fAD). Though, not all cases of fAD are linked to these genes (46, 66, 67).

In people with Down syndrome (which features three copies of chromosome 21 which harbors *APP*), the increased genetic load of trisomy 21 is concomitant with an increase in AB protein load

and increased aberrant processing and an age-related, accelerated AD-like plaque burden which runs in parallel with cognitive dysfunction (9, 68). In contrast, a neuroprotective mutation in the *APP* gene, A673T, is associated with decreased Aβ levels and lowered AD susceptibility (69). Together, these observations underpin the amyloid β hypothesis (Section 1.2.1.2) (16).

1.3.2 Late-onset Alzheimer's disease

LOAD, unlike EOAD, is associated with susceptibility, rather than deterministic, genes that increase one's likelihood of, without guaranteeing, disease development. Studies have indicated that concordance of LOAD heritability in twins is about 60-80% (67, 70). Genetic risk factors include genes associated with cholesterol/lipid metabolism (e.g., *APOE*, *CLU*, and *ABCA7*), immune (e.g., *TREM2* and *CR1*), endocytosis, cytoskeletal, and epigenetic functions (Figure 1.5). Of the LOAD susceptibility genes, the only one consistently and robustly replicated in numerous GWAS reports is the polymorphic *APOE* gene, specifically the *APOE* ε4 variant, which was first reported as a risk factor in 1993 (46, 71).

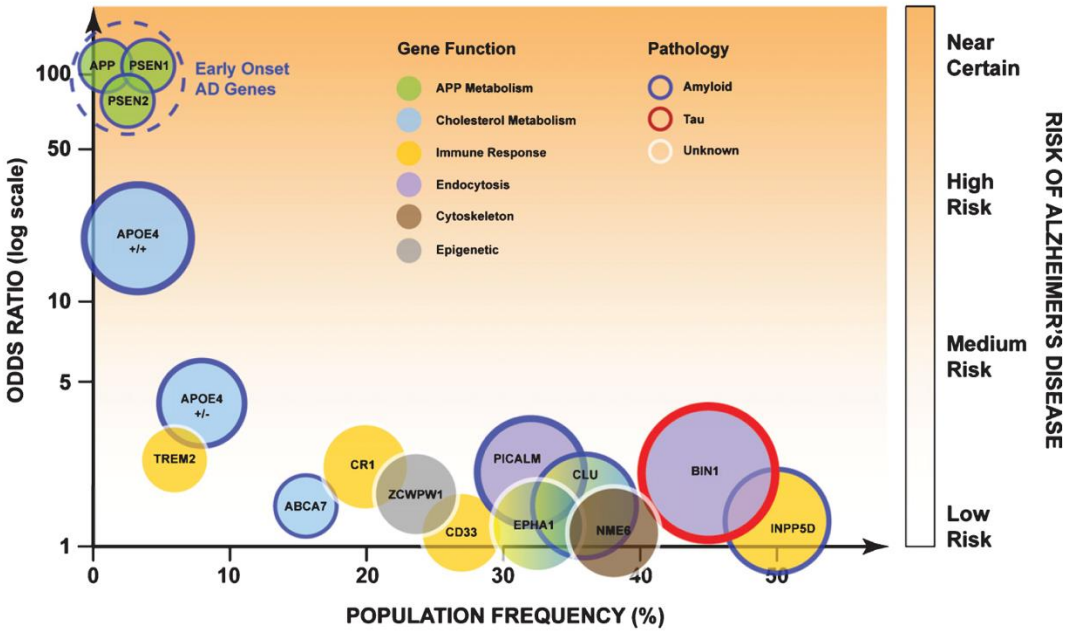

Figure 1.5 Genetic underpinnings of Alzheimer's disease.

Genetic risk factors of AD annotated with each gene's physiological role are shown. High-risk genes (labeled on the right y-axis) link to severe disease phenotypes and earlier age of onset while low-risk genes are associated with later disease onset and lower severity. The size of the circles depicts relative attributable fraction, such that 'bigger' genes represent those that have a more considerable impact on AD risk. Figure from Robinson *et al*. (72)

1.4 *APOE* variants differentially affect genetic risk for LOAD

APOE contains two nonsynonymous SNPs, identified as rs429358 (C >T) and rs7412 (C >T), that alter the gene's coding sequence to generate its three most frequent allelic variants: ε2, ε3, and ε4 (57). The consequences of the SNPs on amino acid sequence, protein structure, and function are covered in Section 1.5. The distribution of the *APOE* alleles across populations of different ancestries is variable. Although ε3 is the most common in all populations, it can range from 54% (Pygmies of Africa) to 91% (Native American Mayans) in frequency (73). The ε4 allele frequency ranges from 5% (Sardinians of Europe) to 41% (Pygmies) across the globe (73). *APOE* ε2 is absent in Aboriginal Australians and several Indigenous American groups (including Mayans) and shows up at the highest frequency in Papuans at 15% (73).

1.4.1 *APOE* ε4 is a major risk allele for AD

Genetic evidence shows *APOE* polymorphisms bestow allele-specific susceptibility to AD. *APOE* ε4 carriers show an earlier age of onset and a shorter time to phenoconversion (Section 1.1) from MCI to AD dementia compared with the general population (74). *APOE* ε4 impacts risk to variable degrees for different racial/ethnic groups. A meta-analysis reported a stronger association between the *APOE* ε4 genotype and AD in Japanese people versus people of European ancestry; this association was much weaker —though still a critical high-risk allele— amongst African Americans and Hispanics (Table 1.1) (64). Interestingly, although the ε4 allele is less related to cognitive decline in Blacks than Whites, it does occur at a higher frequency in Blacks (74). Which factors, and the degree to which, support cognitive reserve or promote cognitive decline amongst *APOE* ε4 carriers in various populations remains unclear (75). One report has identified a novel ancestry-specific genetic locus in Africans that decreases the AD risk effect in *APOE* ε4 homozygotes by about 75% (76). The mechanism of how this locus mitigates AD is not yet known but its existence (along with other profoundly protective variants like those mentioned Section 1.4.3) opens the possibility of discovering new targets for therapeutic intervention in AD or in ε4 carriers specifically.

The ε3 allele occurs in 78% of people of European ancestry and is designated the neutral allele concerning AD modulation (Table 1.1) (64). *APOE* ε4, which has a 14% incidence in people with European ancestry, is enriched in patients with AD; 65–80% of patients harbor at least one copy (64). Individuals bearing *APOE* ε3/ε4 or *APOE* ε4/ε4 genotypes are 3.2 or 14.9 times, respectively, more likely to develop AD than those with an ε3/ε3 genotype (64). *APOE* ε2, occurring in only 8% of the general population of European ancestry, is rare in people with AD and thus is a neuroprotective variant (64, 71, 77).

Table 1.1 ***APOE*** **allele distribution and odds ratios for developing Alzheimer's disease (AD)(64).**

Ethnic Group		No.	*APOE* genotype frequency, % / AD odds ratio, CI						*APOE* allele frequency, %		
			ε2/ε2	ε2/ε3	ε2/ε4	ε3/ε3	ε3/ε4	ε4/ε4	ε2	ε3	ε4
European Ancestry	A	5107	0.2/ 0.6, 0.2-2.0	4.8/ 0.6, 0.5-0.8	2.6/ 2.6, 1.6-4.0	36.4/ 1.0, ref	41.1/ 3.2, 2.8-3.8	14.8/ 14.9, 10.8-20.6	3.9	59.4	36.7
	C	6262	0.8	12.7	2.6	90.9	21.3	1.8	8.4	77.9	13.7
African American	A	235	1.7/ 2.4, 0.3-22.7	9.8/ 0.6, 0.4-1.7	2.1/ 1.8, 0.4-8.1	36.2/ 1.0, ref	37.9/ 1.1, 0.7-1.8	12.3/ 5.7, 2.3-14.1	7.7	59.1	32.2
	C	240	0.8	12.9	2.1	50.4	31.8	2.1	8.3	72.7	19.0
Hispanic	A	261	0.4/ 2.6, 0.2-33.3	9.6/ 0.6, 0.3-1.3	2.3/ 3.2, 0.9-11.6	54.4/ 1.0, ref	30.7/ 2.2, 1.3-3.4	2.7/ 2.2, 0.7-6.7	6.3	74.5	19.2
	C	267	0.4	12.0	0.8	67.4	17.6	1.9	6.7	82.3	11.0
Japanese	A	336	0.3/ 1.1, 0.1-17.2	3.9/ 0.9, 0.4-2.5	0.9/ 2.4, 0.4-15.4	49.1/ 1.0, ref	36.9/ 5.6, 3.9-8.0	8.9/ 33.1, 13.6-80.5	2.7	69.5	27.8
	C	1977	0.4	6.9	0.8	75.7	15.5	0.8	4.2	86.9	8.9

A = patient with AD; C = controls; No. = number of cases, ref = referent genotype

1.4.2 *APOE* ε2 has a strong protective role in AD yet is relatively understudied; why?

Until recently, by exactly how much does ε2 lower AD risk had not been clearly quantified because ε2 allele has low frequency and ε2 homozygosity has been largely absent in study populations. In 2020, an epidemiological study that analyzed an extraordinarily high number of neuropathologically confirmed AD cases and cognitively unimpaired controls was able to determine that ε2 homozygosity lowered risk by 87% compared with ε3/ε3, and by 99.6% compared with ε4/ε4, genotypes (77). Basically, Reiman *et al.* analyzed 4,018 autopsy-confirmed AD cases and 989 pathologically and cognitively unaffected donors (77). Such a large cohort gathered enough numbers of ε2 homozygotes, 24 people, to power conclusive results. The graph in

Figure 1.6 shows the percentage of people for each *APOE* genotype (all neuropathologically confirmed as either AD cases or cognitively unimpaired non-AD controls) that remained free from dementia as a function of age. Essentially, most people with ε4/ε4 genotype developed AD while very few with ε2/ε2 did. Of note, when the ε2 and ε4 alleles were both present, i.e., ε2/ε4 genotype, the protective effect of ε2 could not override the AD risk imposed by ε4; suggesting the dominant nature of ε4 (77).

Importantly, Reiman *et al.* showed people with ε2/ε2 genotype have less Aβand tau pathology (77). After correcting for AB plaque burden, the protective effect on tau pathology was upheld.

This was reminiscent of results in a tau mouse model study, discussed in Section 1.6.2, showing an allele-specific effect whereby ε4 exacerbated tau pathology compared to ε2 (77, 78).

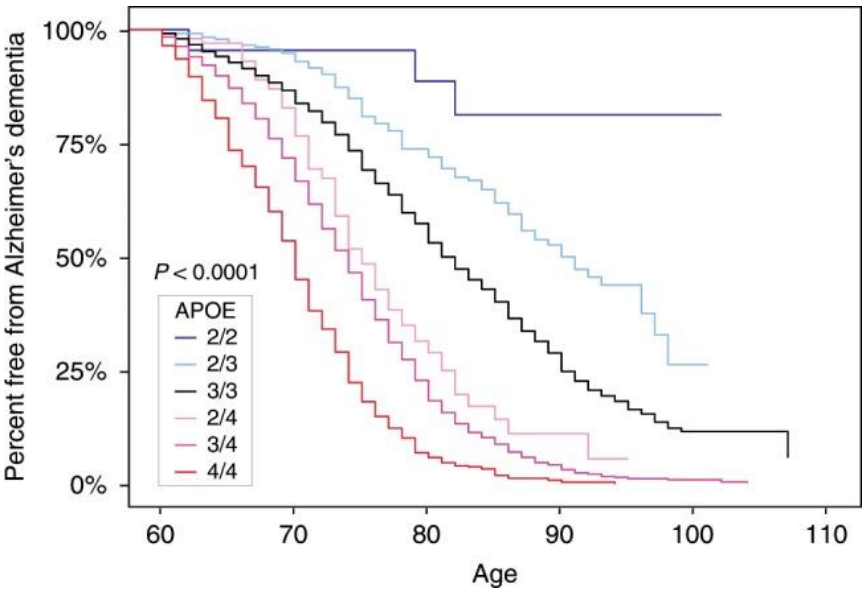

Figure 1.6 Kaplan–Meier graph showing percent free from Alzheimer's dementia.

The Kaplan–Meier plot shows the percentage of people from 4,018 neuropathologically (autopsied) confirmed cases and 989 matched controls with each *APOE* genotype versus age. The 24 people with the rare *APOE* 2/2 genotype remained dementia-free. X-axis designates age at death for controls and age at onset of cases of dementia. If age at onset was unavailable, then it was substituted with age at death. Graph from Reiman *et al*. (77).

Even with a constraining number of ε2 homozygotes, the degree of this allele's neuroprotective influence was beyond that previously described. Considering it has such strong protective effects, it is relatively understudied, compared to ε4. As a rough estimate example, my PubMed (12 May 2023) search (for the terms "*APOE* e2" and "*APOE* e4") pulled up 444 articles relating to ε2 and 2637 to ε4 for the 2017–2023 period. The true protective nature of the ε2 allele is still emerging highlighting the importance in incorporating into comparison studies. Use of technologies to genetically edit cells allows for further study of this rare allele versus ε3 and ε4 variants.

1.4.3 Other *APOE* variants protect against LOAD

Other impactful but ultrarare *APOE* SNPs exist. In a woman homozygous for the so-called *APOE*3-Christchurch variant who also harbored a pathogenic PSEN1 mutation, dementia that would be near certain due to the PSEN1 mutation was delayed by 30 years, even though postmortem examination showed extensive Aβ plaques and an unusual distribution of NFTs (79). The SNP responsible for the *APOE*3-Christchurch mutation maps to the receptor and heparan sulfate

proteoglycan (HSPG) binding region of ApoE (ApoE structure and receptors are discussed in Section 1.5) (80). Another rare neuroprotective variant named *APOE*3-Jacksonville, bearing mutation in the ApoE lipid-binding region, was found to lower Aβ plaques and neurodegeneration via a mechanism that interfered with ApoE self-aggregation and altered lipid metabolism (ApoE in lipid metabolism is covered in Section 1.6.1) (80, 81). These findings further highlight the impact of *APOE* variants on AD disease processes (80).

1.5 ApoE molecular function

The *APOE* gene is located on the long arm of chromosome 19 and consists of 4 exons (Figure 1.7; a) (65). The three protein isoforms resulting from the rs429358 and rs7412 SNPs (Section 1.4) show amino acid sequence substitutions at two residues located at positions 112 and 158 of this 299-amino-acid (34-kDA) glycoprotein: ApoE2 (Cys112, Cys158), ApoE3 (Cys112, Arg158), and ApoE4 (Arg112, Arg158) ((Figure 1.7 and Table 1.2). Mice have one form of apoE which possesses an arginine at both relevant amino acid locations, thus, matching human ApoE4 in this respect (82). Likewise, the single apoE variant found in rats, orangutans, chimpanzees and gorillas most resembles that of human ApoE4 (73).

ApoE's N-terminal domain houses its receptor-binding region, which connects, via a flexible hinge region, to its C-terminal domain, which contains a lipid-binding region (Figure 1.7; b). The ApoE4 isoform displays a unique structural interaction between its C- and N-terminal domains. This biophysical interaction results from a salt bridge between Arg61 and Glu255, modulated by the presence of Arg112 (Figure 1.7; b). ApoE3, with only a single amino acid difference from E4, fails to engage such a salt bridge because Cys112 does not present a similarly conducive side chain (38). Domain interaction renders ApoE4 vulnerable to proteolytic processing in neurons creating fragments that have been suggested to be neurotoxic (83, 84). Interestingly, mouse apoE and that of all other non-human mammals does not exhibit domain interaction because it lacks Arg61 (they all have a threonine at position 61 and thus no salt bridge) and therefore, structurally, resembles human ApoE3 (82). The structural change conferred by the distinct alleles results in a reduced ability of ApoE2 to bind one of the major ApoE receptors, low-density lipoprotein receptor (LDLR). ApoE2 exhibits <2% binding activity compared to that of ApoE3 and ApoE4 (38, 85). Table 1.2 summarizes the main differences amongst the three isoforms.

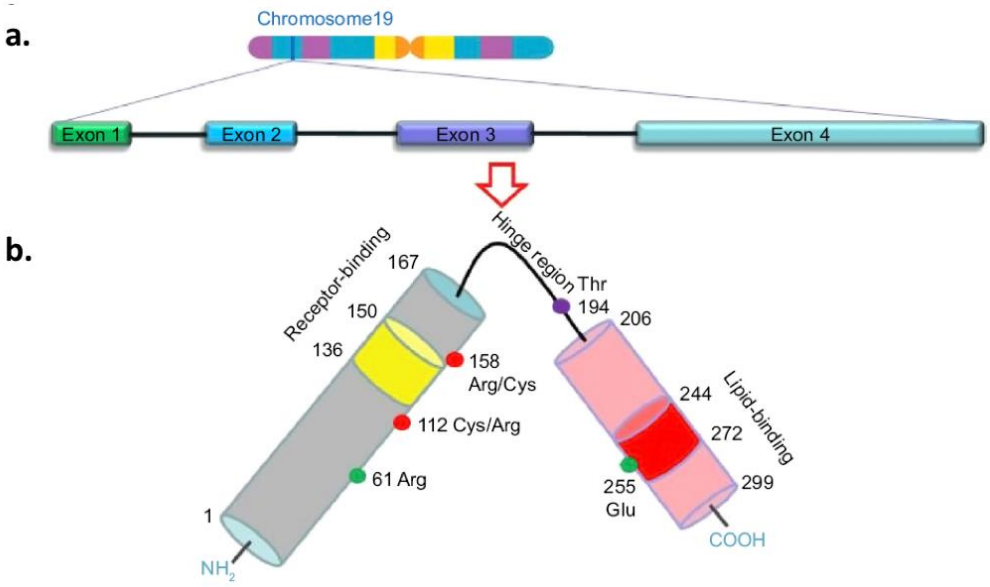

Figure 1.7 The Molecular and structural variation of distinct ApoE isoforms.

(a.) *APOE* is on chromosome 19 and has 4 exons. (b.) The ApoE protein encompasses a receptor-binding domain (residues 136–150) in the N-terminal region (residues 1–167) and a lipid-binding domain (residues 244–272) in its C-terminal (residues 206–299). Isoform polymorphisms occur at residues 112 and 158 (red circles), where ApoE2 has Cys residues at both sites, ApoE3 has a Cys at 112 and an Arg at 158, and ApoE4 has Arg residues at both sites. Domain interaction between Arg61 and Glu255 (green dots) is facilitated by Arg112 specific to ApoE4. Figure adapted from Giau *et al.*(86).

Table 1.2 Principal ApoE isoform differences

Property	ApoE2	ApoE3	ApoE4
AD susceptibility factor	Protective	Neutral	Risk
Amino acid polymorphism	Cys-112 Cys-158	Cys-112 Arg-158	Arg-112 Arg-158
LDLR binding (%)	2	100	100
Domain interaction	no	no	yes
Preferential lipoprotein binding	HDL (smaller lipoproteins)	HDL (smaller lipoproteins)	VLDL (larger lipoproteins)

1.6 ApoE in health and Alzheimer's disease

Lipoproteins are the structure by which lipids (which being insoluble in aqueous environments must be carried packaged with a protein partner) are transported around the body and essentially consist of a water-soluble protein scaffold, i.e., an apolipoprotein, and its fat-soluble cargo (87). Biochemically, lipoproteins consist of a hydrophobic center, mainly of cholesterol esters and triglycerides, wrapped inside a hydrophilic exterior made up of phospholipids, free cholesterol,

and apolipoproteins (Figure 1.8a). Apolipoproteins are mostly known for their following roles: structural protein in lipoprotein particle, ligand for lipoprotein receptor, and modulator of enzyme activities associated with lipoprotein metabolism (87). Multiple classes of apolipoproteins exist. The brain is the second highest ApoE-expressing organ after the liver (88).

The gene product of *APOE*, apolipoprotein E (ApoE), plays an important role in lipid transport. It mediates cholesterol delivery to neurons as well as lipid, including fatty acid, removal and recycling, particularly after injury (89). The brain accounts for ~2% of the total body mass yet contains ~25% of the total unesterified ('free' or 'active' conformation) cholesterol in the body, making it the most cholesterol-rich organ (90, 91). The cholesterol in the brain is mainly (>95%) unesterified and found mostly within myelin (90-92). Unesterified brain cholesterol is important in the development and maintenance of neuronal function. Cholesterol unevenly distributes across distinct cellular compartments and is a vital constituent of membranes; helping define their fluidity. It contributes to cellular structure and repair including membrane integrity and permeability, electrical conductance, synaptogenesis, and maintenance of synapses; thus, highlighting the significance of lipid biology in neuron repair and degeneration (92).

Because of ApoE2's reduced affinity for LDLR, compared to ApoE3, ApoE2-containing lipoproteins show reduced clearance. As a result, people who are homozygous for *APOE ε2* have higher plasma ApoE levels, are susceptible to hyperlipidemia owing to impaired clearance of certain lipoproteins in the periphery and are at increased risk for atherosclerotic disease (38, 85). ApoE4, compared to ApoE3, mediates more rapid clearance of ApoE-containing remnant lipoproteins. As such, individuals with *APOE*4 alleles have lower plasma ApoE levels, but increased LDL cholesterol levels and increased cardiovascular risk (93).

In the CNS, ApoE is expressed in a constitutive manner by several distinct cell types including astrocytes, vascular cells, and choroid plexus cells. Injury and other stress conditions induce neuronal and microglial expression of ApoE. ApoE is predominantly secreted by astrocytes in discoidal high-density lipoprotein (HDL)-like particles associated with phospholipids and cholesterol. ApoE in CSF appears in spherical particles like the HDL-like entities secreted by glia, but additionally contain a cholesteryl ester core (Figure 1.8a). ApoE in the CSF occurs at a concentration of approximately 6 to 10 µg/mL (94, 95).

1.6.1 ApoE and CNS cholesterol homeostasis

ApoE does not easily cross the blood-brain barrier so peripheral- and brain-derived ApoE exist in discrete pools, a phenomenon conserved in mice (96). This is illustrated by patients who received liver transplants having their plasma ApoE isoform switch to that of the organ donor while ApoE in

their CSF ApoE persisted in its original phenotype (97). Consequently, cholesterol (which depends on apolipoproteins for transport) is hardly shared between the periphery and the CNS. Cholesterol is synthesized *de novo* in the CNS and resourcefully recycled, where its half-life ranges from 1 to 5 years, contrasting with only several days in the rest of the body (90, 98-100).

Figure 1.8b illustrates salient points regarding ApoE's role in brain cholesterol metabolism. Astrocytes are the primary source of the cholesterol that neurons use (92). Astrocytes produce cholesterol in the endoplasmic reticulum (ER) via 3-hydroxy-3-methyglutaryl-coenzyme A reductase (HMGR) activity, under control of sterol-regulated element binding protein (SREBP) that interacts with sterol-regulated element-1 (SRE-1) in the HMGR gene. Astrocytes secrete cholesterol bound to ApoE, and lipid associated ApoE is called lipidated ApoE. The loading of cholesterol onto nascent ApoE involves adenosine triphosphate (ATP) binding cassette (ABC) transporter protein family member A1 (ABCA1). Internalization of the ApoE-cholesterol complex is mediated by the low-density lipoprotein (LDL) family of receptors or LDLRs (See last paragraph in this Section). Intracellular cholesterol trafficking is dependent on Niemann-Pick type C (NPC) proteins type 1 (NPC1) and 2 (NPC2). The cytochrome P450 enzyme, CYP46, converts cholesterol to blood-brain-barrier-penetrant hydroxylated cholesterol (24-OHC) that can traverse through plasma and CSF.

Cholesterol efflux via ABCA1 is considered critical in AD. ABCA1 gene mutations are linked with AD and decreased Aβ. ABCA1 protein transporter functions have been reported to be diminished in patients with MCI or AD (101). In mice, ablating ABCA1 lowers ApoE levels, suggesting poorly-lipidated ApoE is more quickly catabolized, and heightens AB plaque deposition (102). ApoE lipidation status differs for the various isoforms and gives rise to the hypothesis that the level of lipidation influences ApoE interactions with AB (103).

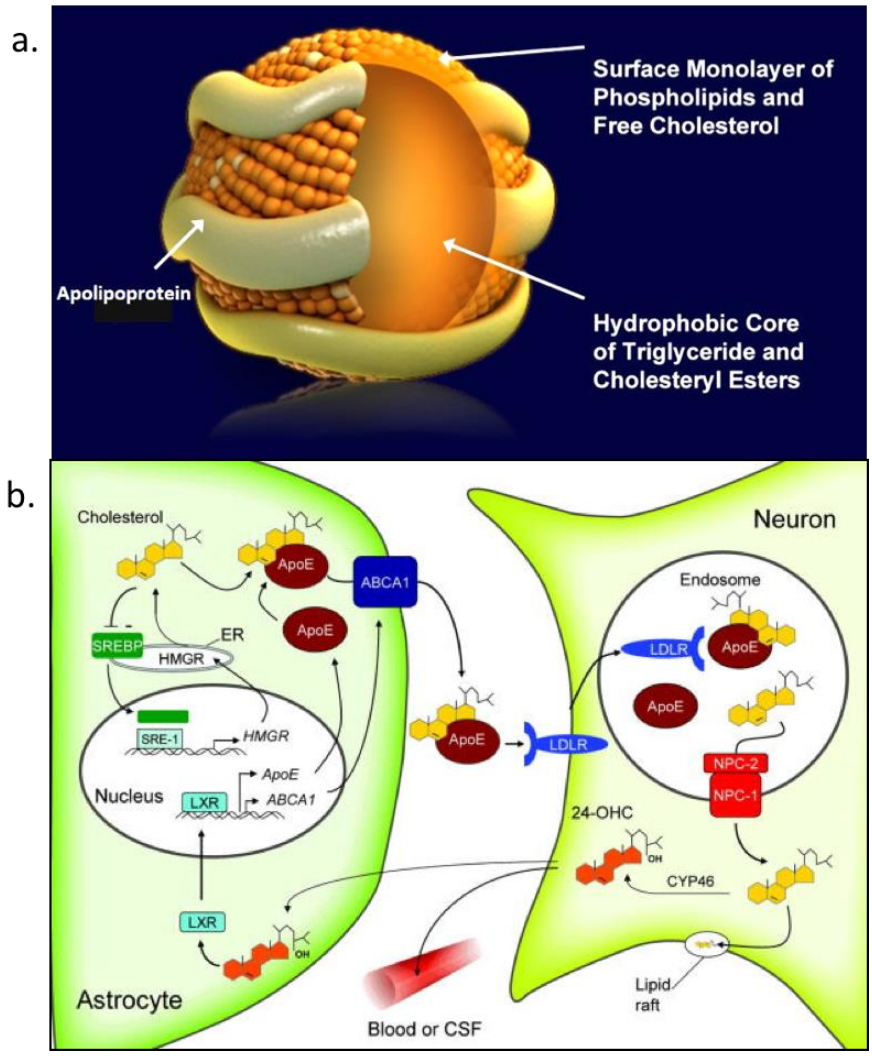

Figure 1.8 CNS cholesterol metabolism

a) Depiction of a lipoprotein particle b) Astrocytes make cholesterol by 3-hydroxy-3-methyglutaryl-coenzyme A reductase (HMGR) activity, which is regulated by sterol-regulated element binding protein (SREBP) downstream of sterol-regulated element-1 (SRE-1) regulation of HMGR expression. Adenosine triphosphate (ATP) binding cassette (ABC) transporter protein family member A1 (ABCA1) loads cholesterol onto ApoE. The ApoE-cholesterol complex is internalized with the help of the low-density lipoprotein receptors (LDLR). Niemann-Pick type C (NPC) proteins type 1 (NPC1) and 2 (NPC2) promote intracellular trafficking. The cytochrome P450 enzyme, CYP46, converts cholesterol to hydroxylated cholesterol (24-OHC) that can traverse through plasma and/or CSF. Figure from Benarroch (92).

ApoE-containing lipoprotein particles secreted into the interstitial fluid by astrocytes become internalized by neurons through receptor-mediated endocytosis. The ApoE portion of the lipoprotein particle provides the ligand for cell-surface ApoE receptors. Most ApoE receptors belong to the LDLRs (as mentioned above) which primarily functions in the transport of plasma lipoproteins. This receptor family includes the following members: LDLR (mentioned in Table 1.2), LDLR-related protein 1 (LRP1), very-low-density lipoprotein receptor (VLDLR), and apolipoprotein E receptor 2 (Apoer2, also known as LRP8) (38). LDLR and LRP1 are both associated with

controlling ApoE brain levels and the main ApoE receptor on neurons is LRP1 (38). On top of binding to the LDL receptor family, ApoE also binds to cell surface heparan sulfate proteoglycans (HSPG). In addition, LRP1 can form a complex with HSPG facilitating an HSPG/LRP1 uptake pathway of lipoprotein particles into cells. Of note, many ApoE receptors bind other ligands, for example, interestingly, LRP1 has at least 30 binding partners, including AB and APP (104).

1.6.2 Intersection of ApoE with Aβ and tau

The significance of *APOE* genotype in the etiology of AD is supported by the observation that *APOE*4 initiates brain changes early in life, especially in AD-related areas, leading to the hypothesis that these alterations prime some brain regions to Aβ toxicity (105). Brain imaging shows lifelong diminished gray matter volume in *APOE* ε4, compared to *APOE* ε3, carriers that is already evident in childhood (Figure 1.9). *APOE* ε4 individuals also show diminished brain glucose homeostasis before the onset of cognitive decline. As they age, *APOE* ε4 carriers show earlier Aβ plaque deposition, followed by development of tau tangles and atrophy (Figure 1.9) (105). The differential baseline brain activity and accelerated Aβ accumulation, and then tau tangles, jointly accelerate *APOE* ε4 carriers towards earlier age of disease onset and faster decline in cognition. Studies suggest that ApoE intersects with Aβ metabolism and connects with tau at multiple points (106, 107). Several neuropathologic studies demonstrate a correlation between *APOE* genotype and Aβ deposition in senile plaques as well as NFT burden (106). Tiraboschi *et al.* found that ε4 homozygosity was associated with neuritic plaques in AD (107). *APOE* genotype robustly affects Aβ accumulation; people with ε4 have more Aβ accumulation compared with those carrying the ε3 allele, and less Aβ accumulation is seen with ε2 carriers (38).

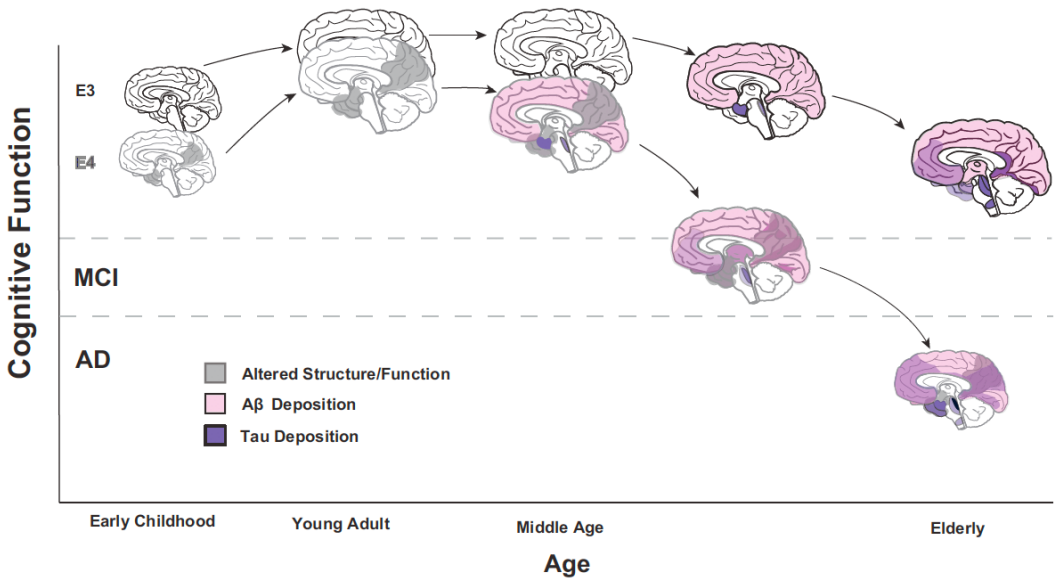

Figure 1.9 *APOE*4 and AD development.

APOE ε4, compared to *APOE* ε3, carriers show changes in brain structure and function early in life. MRI shows diminished gray matter volume in posterior/middle cingulate, lateral temporal, and medial occipitotemporal regions in *APOE* ε4 carriers, a trend that persists for life. With age, ε4 carriers show earlier Aβ plaque deposition followed by tau deposition and atrophy. Figure from Lane-Donovan *et al*. (105).

Aβ binds ApoE via its N-terminal 28 amino acid residues and ApoE was found in senile plaques and NFTs in brain tissue from patients with AD (108-110). ApoE co-deposited with Aβ in senile plaques was more abundant in ε4 versus ε3 carriers (106). ApoE binding of Aβ contributes to Aβ internalization by neurons, but there is no consensus on the consequence of this interaction (108, 109). This ability of ApoE to shuttle Aβ from the extracellular space into neurons implicates ApoE in enhancing neuronal Aβ uptake. Some researchers hypothesize that intraneuronal accumulation of Aβ is a source of Aβ toxicity. An *in vivo* study using *APOE* gene knockout (KO) in APP transgenic mice implicated apoE as having crucial roles in both Aβ plaque formation and disrupted Aβ clearance (111). These kinds of data fuel the concept of ApoE4 as a 'pathological chaperone' catalyzing Aβ neurotoxicity (112). On the other hand, it has been posited that ApoE clears Aβ from the brain and that the ApoE4 isoform is failing in this role.

ApoE interacts with several MT associated proteins, including tau and, depending on the ApoE isoform, can lead to NFT formation (113). ApoE4 inhibits neurite outgrowth and the mechanism suggested was that ApoE4 can destabilize MTs (114). Since this neurite outgrowth inhibition occurred in a mouse neuroblastoma cell line, it would be important to understand how this finding extrapolates to humans.

Since Aβ deposition has been implicated in promoting tau pathology, it has been hard to understand whether ApoE4, which drives Aβ deposition, may also independently contribute to

tau pathology and disease progression in AD. This question of whether the ε4 allele can cause tau pathology independently of Aβ pathology was addressed in a landmark *in vivo* study. In a mouse model of tauopathy (PS19 mice which do not show Aβ pathology), the presence of ε2, ε3, and ε4, all increased pathological tau accumulation and enhanced neuronal susceptibly to degeneration compared to situations where apoE was knocked out, which proved neuroprotective (78). *APOE* genotype worsened tau accumulation and tau-mediated neurodegeneration in an allele-specific manner, with *APOE* ε4 having the strongest effect (E4 > E3 > E2) and the lack of *APOE* almost fully rescuing the neurodegeneration.

1.6.3 Intersection of ApoE with brain atrophy, connectivity, and synaptic plasticity

Evidence suggests that *APOE* genotype impacts brain structure, memory, and synaptic function. Structural MRI studies have shown that healthy *APOE* ε4 carriers, compared with non-carriers, have a loss in cortical thickness and hippocampal volume that tightly correlates with cognitive performance (115, 116). Meanwhile, functional MRI studies show that healthy *APOE* ε4, versus *APOE* ε3, carriers have increased hippocampal activation during memory tasks (117, 118). Such observations lead to the hypothesis that in people bearing the ε4 allele, increased network activity plays a compensatory role as increased cognitive resources are needed to reach a level of memory performance comparable that of non-ε4 carriers (118).

ApoE has been connected to the regulation of synaptic plasticity and repair in transgenic mice expressing human ApoE isoforms. For example, ApoE4 selectively impaired the activity of the synaptic glutamate receptor, NMDAR (119). Also, in a mouse model of Aβ pathology coupled with human ApoE isoforms, ApoE4, as opposed ApoE3, did not prevent the age-dependent synaptic decline that was seen in murine apoE-deficient mice. This finding implied that ApoE4 either lacked the neuroprotective functions of ApoE3, or, had a gain of an adverse activity that impeded beneficial effects (120). Elucidating why ApoE4 fails to provide neuroprotective effects at the synapse in the backdrop of Aβ pathology, and the extrapolation of this observation to AD remains an outstanding and important question.

1.6.4 ApoE hypotheses for AD pathogenesis

For thirty years now, the definitive mechanism of ApoE4 in AD susceptibility has remained elusive. Because ApoE intersects with so many physiological processes, its mechanism in AD risk suggests a “butterfly effect”. That is, small multifaceted contributions from *APOE* genotype create a differential foundational cellular milieu that over a lifespan either increase (*APOE* ε4) or decrease (*APOE* ε2) propensity for neurodegeneration when compared with *APOE* ε3. The kinds of

hypotheses being articulated are exemplified below. Essentially, the single amino acid change from the E3 isoform has multiple, subtle cellular consequences, impacting multiple tissues and, because ApoE has an integrative role within various systems, these subtle but fundamental alterations eventually impact the biology of the whole organism over a lifespan.

1.6.4.1 ApoE cascade hypothesis

The ‘‘ApoE Cascade Hypothesis’’ in AD posits that “the biochemical and biophysical properties of ApoE impact a cascade of events at the cellular and systems levels, ultimately impacting aging-related pathogenic conditions including AD. As such, ApoE-targeted therapeutic interventions are predicted to be more effective by addressing the biochemical phase of the cascade” (85). Figure 1.10 outlines key aspects. The biochemical and biophysical properties of ApoE in play include isoform, structure, lipidation, protein levels, receptor binding, and oligomerization. Variations in these set up the “Biochemical Phase” of the hypothesis. The biochemistry then sets the stage for the “Cellular Phase” in which cellular homeostasis shifts, for example, to stress and dysregulated intracellular trafficking and lipid metabolism. Cellular disturbances cause the “Phenotypic Phase” marked by alterations at the whole organism, or systems, level (manifested as neuroinflammation, vascular dysfunction, and neuropathology, leading to synaptic dysfunction and neurodegeneration) which then ushers in the “Clinical Phase” marked by age-related cognitive decline and AD.

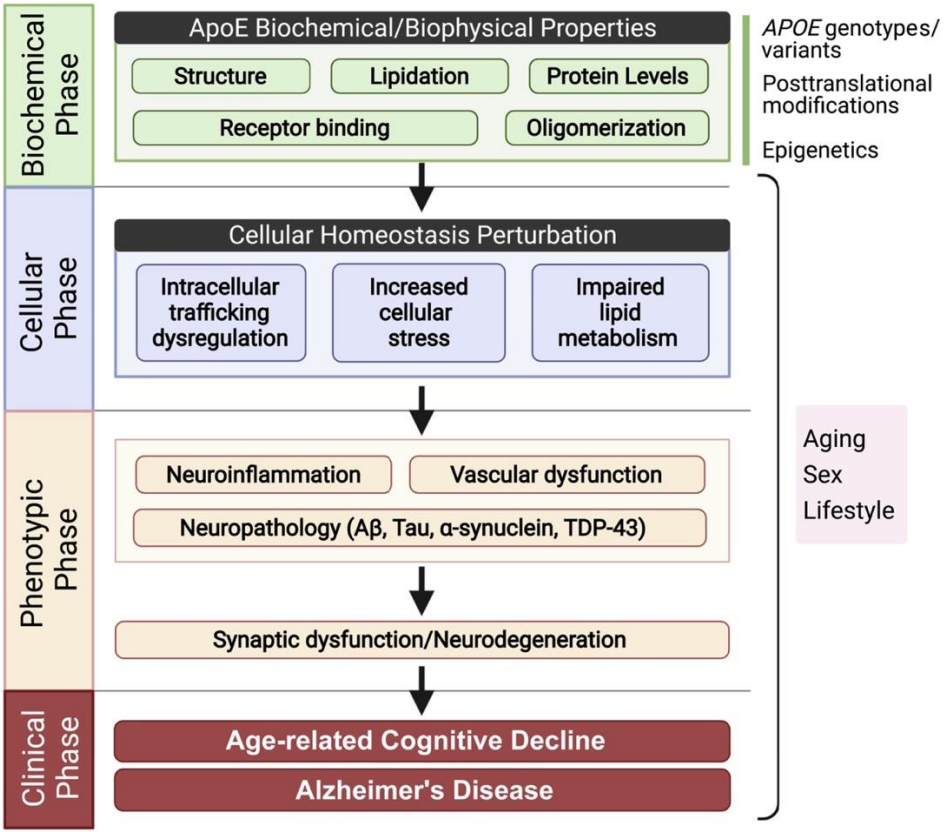

Figure 1.10 Apolipoprotein E cascade hypothesis.

Varying biochemical and biophysical properties such as ApoE structure, lipidation, protein levels, receptor binding, and oligomerization inform the Biochemical Phase of the apolipoprotein E (ApoE) cascade hypothesis. These variables then transmit to a Cellular Phase in which cellular homeostasis is perturbed causing, for example, stress and dysregulated intra-cellular trafficking and lipid metabolism. These cellular disturbances give rise to the Phenotypic Phase characterized by changes at the systems level in neuroinflammation, vascular dysfunction, and neuropathology, leading to synaptic dysfunction, neurodegeneration, and ushering in the Clinical Phase marked by age-related cognitive decline and AD. Graphic from Martens *et al.* (85).

1.6.4.2 ApoE4 multi-hit hypothesis

In short, the "ApoE4 Multihit Hypothesis" posits that ApoE4 promotes a "basal cellular susceptibility state *"with initially low-level dysfunction that accumulates with age*" (121). Figure 1.11 shows the multiple interconnected ApoE4-mediated hits which are: neurodegeneration, neurovascular dysfunction, neuroinflammation, oxidative stress, endosomal trafficking disturbances, lipid and cellular metabolism impairments, calcium dyshomeostasis, and altered transcriptional regulation. Aging or some type of stress compounds the primed system to manifest an overt phenotype which shows up, in part, as synaptic dysfunction and cognitive impairment. The authors expect that future studies would mostly address how and to what extent ApoE contributes to generate the vulnerable pathophysiological state (121).

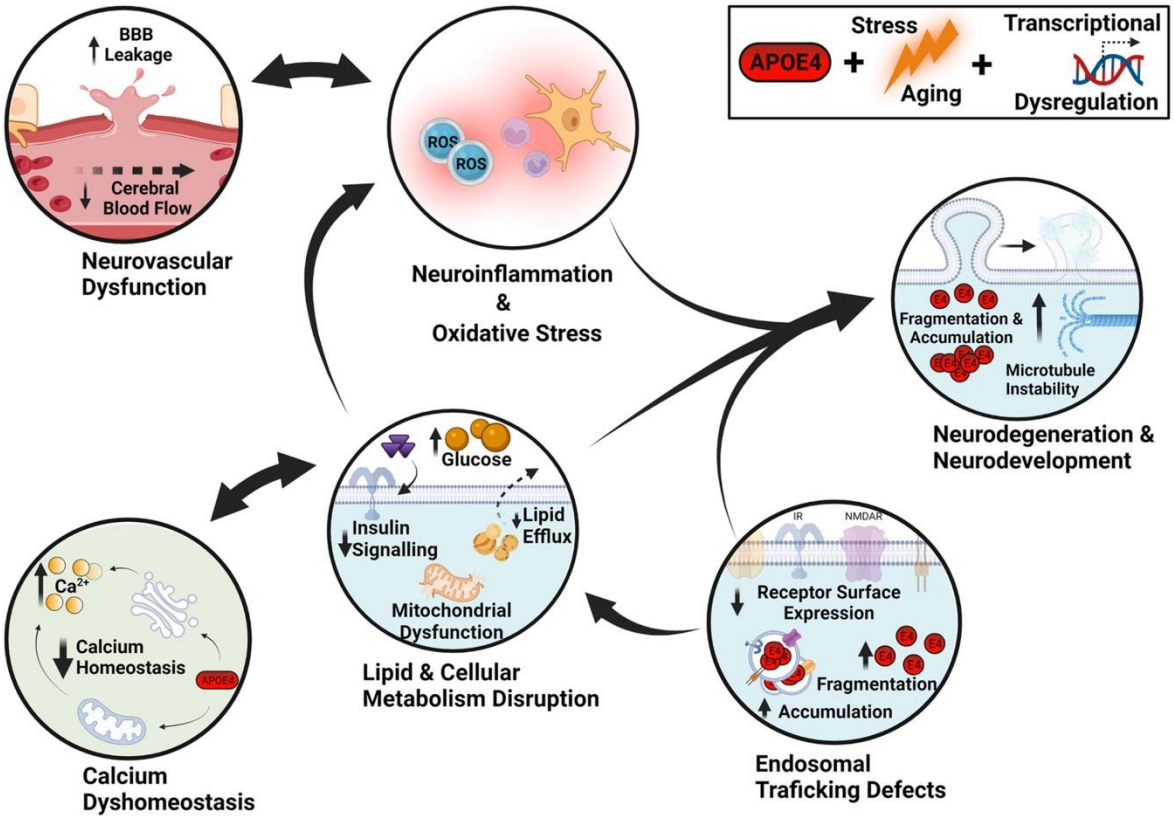

Figure 1.11 Apolipoprotein E4 multihit hypothesis.

APOE ε4 genotype fosters a pathophysiological state of susceptibility to damage through multiple "hits". Cellular stress, ageing and an altered transcriptional landscape (box; top right) modulate the various hits. The ApoE4-mediated hits include interactions with processes such as: lipid and metabolic homeostasis and neuronal maintenance; calcium homeostasis and transcriptional regulation; neuroinflammation, oxidative stress and neurovascular dysfunction; and disrupted endosomal trafficking and lipid homeostasis and neurodegeneration. Adapted from Steele *et al.* (121).

1.10 Implication of neuron expressed Apolipoprotein E

While the bulk of ApoE in the CNS comes from astrocytes, it is also produced to a lesser extent by other cell types, including microglia and neurons (Section 1.6). The cellular source of ApoE could make a functional difference.

1.10.1 Human evidence

ApoE in neurons has been documented in both physiological and pathophysiological states. However, as to whether neurons produce their own ApoE (and if so, why?) had been an open question in the field for a long time. As early as 1999, *APOE* mRNA transcription (via *in situ* hybridization techniques) was observed in select neurons in autopsied brains from people with AD as well as individuals without dementia (122). Aoki and colleagues autopsied stroke victims and observed that neurons at the periphery of ischemic foci had ApoE-positive immunoreactivity while neighboring astrocytes were ApoE-negative, suggesting that the neurons expressed their own ApoE and did not endocytose it from the pool of ApoE in the neuropil secreted by astrocytes (123). The above-mentioned studies did not, however, fully address the question concerning whether neurons generate their own ApoE. For example, a limitation of immunostaining is that it could not distinguish between ApoE expressed by the neurons (endogenous ApoE) themselves versus ApoE that had been secreted from surrounding cells (like astrocytes, exogenous ApoE) and then internalized by neurons (via ApoE receptors). Nonetheless, the implication was that neuronal regenerative mechanisms in the face of injury may be linked to this increase in ApoE of neuronal origin (123).

Only in recent years, with the use of more powerful, highly quantifiable, sensitive techniques like single-nucleus RNA sequencing (snRNA-seq) studies, has it been clear that neurons have endogenous ApoE expression (at least at the mRNA level). This clarity and accompanying new datasets help develop richer hypotheses about what role it plays. For example, in 2021, Zalocusky *et al.* analyzed, in an unbiased way, the transcriptomic profile of thousands of single cells from the brains of people with and without AD (124). They found that *APOE* expression robustly contributed to neuronal heterogeneity and that up to 20% of neurons had significantly high levels

of *APOE* mRNA. Low neuronal *APOE* expression correlated to people without cognition deficits while higher neuronal *APOE* levels linked to people with MCI and the neuron type associated with this cluster of neurons was selectively depleted in patients with AD. The authors reported that some of the molecular pathways associated with high *APOE* levels included cellular stress, neurodegeneration, and immune signaling. Therefore, they interpreted increased neuronal *APOE* expression as being a harbinger of neuronal death (124). The cause of *APOE* upregulation and neuronal death is an outstanding area of scientific exploration.

1.10.2 Animal evidence

In physiological conditions, wildtype mice show only glial apoE immunoreactivity. However, when transgenic mice in which murine apoE was ablated and replaced with genomic sequences for each of the human *APOE* alleles - ε2, ε3, and ε4 - neuronal immunoreactivity of ApoE was observed; a pattern in keeping with physiological conditions in human brains (125).

1.10.2.1 Rodent apoE is upregulated upon injury, for example, Kainic Acid insult

Murine apoE, in both neurons and astrocytes, is induced upon excitotoxic insult in mice (126). Using an enhanced green fluorescent protein (EGFP) apoE-reporter system where EGFP replaced one allele of the apoE gene allowing for real-time tracking of apoE expression (the other apoE allele was kept intact to maintain physiological apoE functions) researchers saw strong EGFP expression in astrocytes in uninjured mice. Excitotoxic injury from kainic acid (KA) administration then induced apoE production, ie, EGFP fluorescence increased dramatically, in damaged neurons and astrocytes (Figure 1.12) (126). Since EGFP is not a secreted protein trafficked between cells, this was strong evidence that it, and therefore apoE, was generated within neurons. In rats also, neuronal localization of apoE in the soma and dendrites was seen upon acute brain injury (ischemic insult) (127). Such data implicate endogenous apoE as part of an adaptive response of neurons to injury.

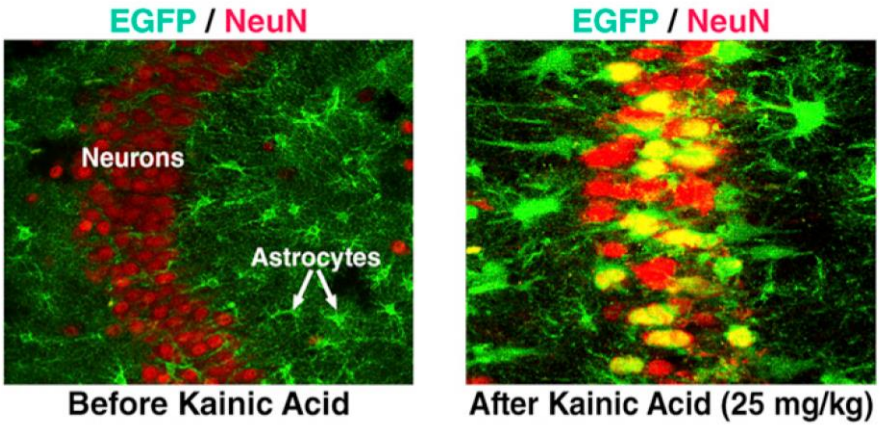

Figure 1.12 Neuronal apoE expression in EGFP-tagged apoE reporter mouse.

Photomicrograph of hippocampus of EGFP-apoE-reporter knock-in mice. Uninjured condition shows expression in astrocytes (green cells, arrows). NeuN labels neuronal nuclei (red). Injured condition (after kainic acid treatment) shows colocalized expression of neuronal marker with EGFP (yellow). Figure from Xu *et al*. (126).

1.10.2.2 Based on cellular source, ApoE differently impacts tau-induced pathology

Global manipulation of ApoE in a mouse tauopathy model brought to light its robust regulation of tau-induced neurodegenerative phenotypes (Section 1.6.2). *APOE* ε4 genotype increased tau pathology relative to *APOE* ε2 and *APOE* ε3 and the pathology was rescued by complete genetic apoE ablation (78). According to this result, a potential therapeutic approach for AD is to lower ApoE (regardless of isoform) to protect against tau-mediated pathology.

In the above experiment, *APOE* could have been acting through a glial-mediated or a more direct interaction on tau pathogenesis. Therefore, continuing with that same mouse model, a series of studies set out to investigate the effect of ApoE from distinct cell types explicitly. Shi *et al.* researched the role of microglia in mediating the tau-induced phenotypes (128). In mice homozygous for human *APOE* ε4 or with ablation of apoE, the authors pharmacologically depleted microglia during the critical age range when neurodegeneration occurs in this tauopathy model. While microglial ablation increased ApoE4 levels in in *APOE* ε4 mice (neurons and astrocytes), neurodegeneration was rescued, implying microglia act downstream of ApoE4 and its effect on neurodegeneration is mediated mainly by microglia (128). According to this result, preserving microglial function would rank higher than lowering ApoE as a potential therapeutic approach for AD.

In a similar tauopathy-combined-with-human-*APOE* paradigm, Wang *et al.* explored the role of astrocyte-derived ApoE on tau-induced pathology (129). With savvy genetic tools, the authors conditionally and selectively genetically ablated apoE from astrocytes. Selective removal of astrocytic apoE reduced apoE protein in the brain more than 90%; convincing confirmation that this cell type produces most of the apoE in the CNS. When compared with ε4-expressing counterparts, mice that do not express astrocytic apoE showed reduced pathological tau, tau-mediated neurodegeneration, and rescue of synapse loss. The study suggested that astrocytes are key mediators of tau-induced pathology and the strong protective effect of removal of astrocytic *APOE* implies ApoE lowering treatments would be beneficial against tauopathies.

Koutsodendris *et al.* examined the effects of neuronal *APOE* in the same mouse model of tauopathy (PS19 mice which are transgenics expressing mutant human tau driven by the mouse prion protein promoter) (130). Selective removal of neuronal ApoE reduced total ApoE protein in

the brain by about 20%; not surprising, as neurons produce a small proportion of the total ApoE (130). Surprisingly, however, removal of neuronal APOE ε4 produced strikingly increased pathological tau (phosphorylation and aggregation), increased tau spreading, increased loss of neurons and hippocampal volume, increased loss of oligodendrocytes, their precursors, and myelin, increased loss of neuronal network hyperexcitability and increased unhealthy cellular genetic signatures (130). Surprisingly, the loss of neuronal, as opposed to astrocytic, ApoE4 had a disproportionately outsized effect on driving tau pathology.

1.10.3 Neuronal culture evidence

Dekroon and Armati, in 2001, were the first to show that cultured primary human neurons express *APOE* mRNA transcript (via *in situ* hybridization) in addition to ApoE protein (colocalization of ApoE and neuron-specific class III β-tubulin via immunostaining) (131).

Recently, studies are emerging in human neuronal cultures derived from embryonic and induced pluripotent stem cells (ESCs and iPSCs, respectively) that enable probing physiological and pathological ApoE-associated cellular transduction pathways. These systems can be interrogated by adding exogenous ApoE. As such, it was shown that ApoE activated a non-canonical mitogen-activated protein (MAP) kinase signaling pathway that caused Aβ levels to increase. Specifically, ApoE bound its neuronal receptor, LRP1, to initiate a molecular cascade whereby dual leucine zipper kinase (DLK) activated ERK1/2 MAP kinase which, in turn, phosphorylated cFos and induced the transcription factor, AP-1, to drive APP expression and subsequently Aβ concentrations were enhanced (Figure 1.13). The isoform efficacy for activating the pathway mirrored those of the gene dosage susceptibility risk for AD: ApoE4 was more potent than ApoE3 which activated downstream signaling more robustly than ApoE2 (132). Such a mechanism potentially explains how ε4 confers risk for AD - by increasing AB production, the root cause of AD according to the AB hypothesis (Section 1.2.1.2), people with the ε4 allele have progressive accumulation during their lifetime.

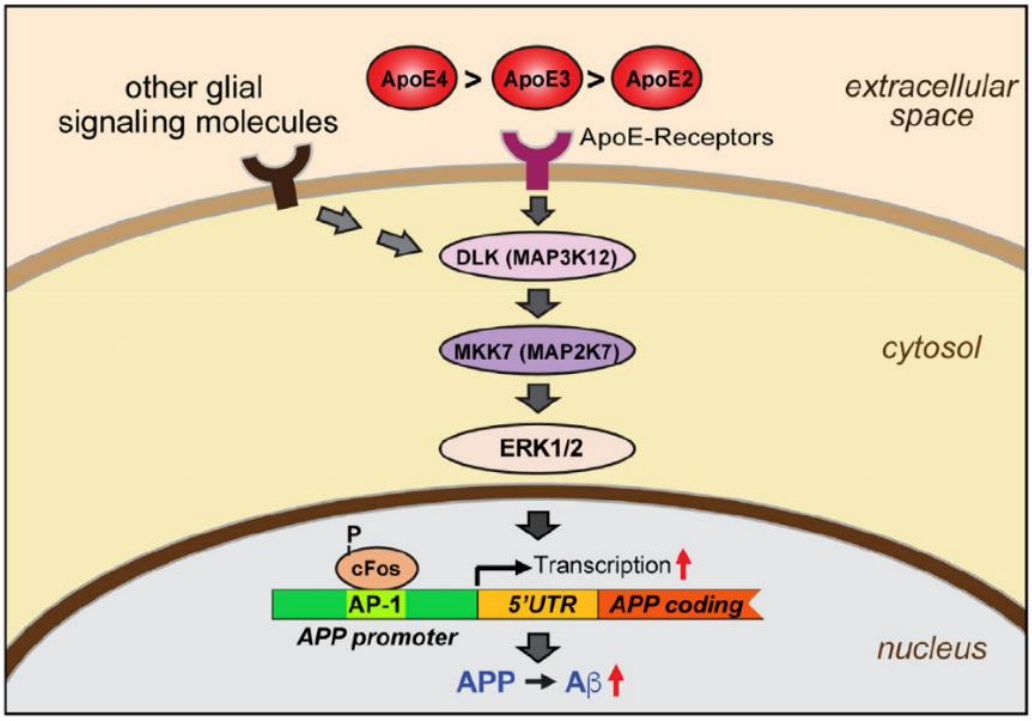

Figure 1.13 Implicated ApoE signaling pathway regulating APP and AB production.

Model of the ApoE signaling pathway modulating *APP* transcription and AB production by activating the Dual-Leucine zipper Kinase (DLK) mitogen-activated protein (MAP) kinase cascade. ApoE isoforms activated this signaling cascade with a potency rank order that reflects their comparative risk for AD: ApoE4>ApoE3>ApoE2. Figure from Huang *et al.* (132)

Wang *et al.* has demonstrated differential phenotypes associated with ApoE4 and ApoE3 in human neuronal cultures generated from iPSCs reprogrammed from donors with $\varepsilon4/\varepsilon4$ and $\varepsilon3/\varepsilon3$ genotypes (133). ApoE4 neurons secreted less ApoE into the culture medium, retaining more of their ApoE pool inside the cell. Intracellular ApoE, however, existed in a truncated form inside ApoE4 neurons, compared with less truncated forms in ApoE3 neurons. This suggests increased ApoE proteolysis in the ApoE4 context and is consistent with the notion of ApoE4 isoform vulnerability to fragmentation (Sections 1.5). Other ApoE4 neuronal phenotypes that contrasted with those carrying $\varepsilon3/\varepsilon3$ included: increased tau phosphorylation levels, increased AB40 and AB42 secretion into the media, and reduction neurons that produce γ-aminobutyric acid (GABA). Even though AB production was increased, the authors did not detect increased *APP* mRNA expression levels, implying that ApoE4 did not influence *APP* transcriptional regulation (unlike the model proposed in Figure 1.13). Transforming the $\varepsilon4/\varepsilon4$ line into one with $\varepsilon3/\varepsilon3$ genotype alleviated the $\varepsilon4/\varepsilon4$-related phenotypes; implying that *neuron-derived* ApoE4 may also play key roles in tau and AB pathogenesis (133).

Lin *et al.* showed iPSC-derived neural cells have *APOE* genotype-dependent phenotypes relevant to AD pathophysiology (134). *APOE* $\varepsilon4$ isogenic astrocytes exhibited impaired Aβ clearance and

increased cholesterol content when compared to *APOE* ε3 counterparts. And, when comparing *APOE* ε3 and *APOE* ε4 isogenic microglia, reduced Aβ uptake and reduced morphological complexity of ε4 microglia emerged (134). With respect to *APOE* ε3 versus *APOE* ε4 isogenic glutamatergic neurons, the presence of ε4 changed synaptic structure and function such that ε4 neurons displayed more synapses and increased spontaneous neurotransmission activity compared to ε3 controls (134).

A study covering the first characterization of *APOE ε2* human iPSC-derived neurons was published in 2021 (135). Upon conversion to ε2 homozygosity of iPSC lineages carrying fAD mutations, the authors saw lessening of the disease-related phenotypes typically observed in the parental lines (135). For example, mixed neuronal-astrocytic cultures from isogenic pairs of iPSCs with conversion of ε3 to ε2 showed dramatically reduced secreted Aβ levels in ε2 cultures; mimicking the clinical observation that patients with AD and an ε2 allele have reduced amyloid deposition (135). Interestingly, disease-relevant phenotypes in induced neurons from iPSCs generated from donors with sAD have been variable or absent (135). As such, the authors suggested that more studies that employ *APOE* isogenic sAD iPSCs are needed to increase the translation of their findings to LOAD (135).

1.11 Cellular models for studying neuronal ApoE

The work referenced in Section 1.10.3 indicates that human stem cell-derived systems are favorable platforms for studying ApoE form and molecular function and that they are useful for understanding neuron-specific mechanisms, especially those that have an underlying genetic factor. These studies form a precedence for employing iPSC derived neurons in generating a deeper understanding of how ApoE normally functions in neurons and how these functions may influence ApoE4 predisposition to, and ApoE2 protection against, AD.

Defining discrete contributions of ApoE from neurons to AD and neurodegeneration will involve the use of reduced systems that allow for manipulation. Cultured cells have been a workhorse for describing the function and molecular mechanisms that inform disease pathology (136). Furthermore, developing cellular platforms enable drug discovery (136). I took advantage of reduced systems, in the form of neuronal cellular models, that lend themselves to the dissection of ApoE function and AD disease mechanisms. Owing to the complexity of the pathophysiology of AD and the species differences of *APOE* variants in humans versus rodents, human cellular models for studying neurodegeneration, including the role of ApoE, are critical for deepening our understanding and generating more effective treatments (136, 137). The advent of iPSC

technology expands human cell-based disease modeling as a complementary platform to investigate ApoE biology in human contexts.

1.11.1 Induced pluripotent stem cells (iPSCs)

When exposed to permissive environments, pluripotent stem cells have the capacity to form all the cell types that give rise to all of the body's specialized tissues and organs during development (138). If differentiated into neuronal cells, they offer an exceptional way to study aspects of the human brain. Historically, pluripotent stem cells were harvested from embryos in their blastocyst stage, resulting in the demise of the embryo which makes it an ethically sensitive and limited source. Adult stem cells can be obtained from bone marrow, liver, or pancreas but they are not pluripotent thus form fewer cell types (only those associated with the organs from which they were harvested) and their source also is limiting.

Induction of pluripotency in terminally differentiated mouse and human cells was first demonstrated in 2006 and 2007, respectively (139, 140). These groundbreaking studies showed that somatic cells could be reprogrammed into an embryonic-like pluripotent state by over-expressing a combination of transcription factors. These transcription factors, known as Yamanaka factors, are: Oct3/4, Sox2, Klf4, and c-myc. The iPSCs showed a differentiation potential largely indistinguishable from that of ESCs. The iPSC technology has rapidly advanced and is widely utilized to create amenable sources of almost all human cell types (136). Progress in human iPSC technology has initiated a growing number of innovative platforms for disease modeling in neuroscience (136, 141). Moreover, since iPSCs can be made from relatively easily accessible samples (such as skin fibroblasts or blood draw), they are generally available from both patients with neurological diseases and unaffected people, alike (138). Techniques for generating iPSC lines include overexpression of reprogramming transcription factors via: non-integrating viruses, single cassette reprogramming vectors, and mRNA transfection (138). Many iPSC cell lines are becoming increasingly available commercially or through various consortia. Repositories acting as a source of iPSCs include: Coriell Institute (https://www.coriell.org), European Bank for induced pluripotent Stem Cells (EBiSC; https://ebisc.org), Riken Bioresource Center (https://cell.brc.riken.jp/en/hps), and WiCell (https://www.wicell.org) (136).

1.11.1.1 Neurons from iPSCs

Once generated, iPSCs are proliferative in culture and can be differentiated into various neuronal cell types; essentially generating large numbers of these difficult-to-source human post-mitotic cells. Non-affected subject- and patient-derived iPSCs, along with their derived neurons, potentially recapitulate more relevant models and disease phenotypes than other cellular systems

(136). Mechanisms of neurodegenerative and neuropsychiatric disease initiation and progression, both sporadic and familial forms, can more faithfully be modelled in the laboratory culture dish with iPSC-derived neurons compared to neuroblastoma cell lines (141).

1.11.1.2 Limitations of iPSC-derived neurons

Reprogramming resets the epigenome and reverts many aged phenotypes (e.g., telomere length) to a 'juvenile-like' state (142). This raises a criticism regarding the use of iPSC-derived neurons in AD. Specifically, the lack of clarity regarding how well they recapitulate aged phenotypes and, thus, their appropriateness for neurodegenerative disease modeling. Another discussion point in the field is the degree of heterogeneity or homogeneity, depending on differentiation methods; for some neuronal cultures, particularly those of purely one cell type, there exists skepticism whether the cells mature fully without the presence of other cell types where cell-cell interactions are predicted to drive developmental maturation. For these reasons, it is necessary to characterize iPSC-derived models for neuronal identity, maturity, functionality, and applicableness for the intended scientific question (142).

Another consideration when using iPSC-based models is whether phenotypes exhibited by cells carrying physiological, endogenous protein levels, such as ApoE3 versus ApoE4 from different donors, would be too subtle for detection compared to situations of overexpression of mutant proteins. One way to address this could be comparison of isogenic lines in which only the specific allele of interest is altered. Lessening the genetic variability between lines can permit dependable evaluation of modest phenotypes.

1.11.1.3 Modeling neuronal ApoE function in iPSC-derived neurons

Several reports show that iPSCs are a viable cellular model for studying AD-related phenotypes. Aβ peptides and intraneuronal buildup of phosphorylated tau, in aged cultures, can be recapitulated. Aβ peptides, e.g., the relative amount of Aβ40 to Aβ42, in either culture medium or cell lysates, can be measured. Different versions of phosphorylated tau (such as phospho-Thr 231 tau which is associated with NFTs) can be measured and reported as normalized values against total tau levels (143).

Several laboratories have now published on ApoE studies that were conducted using iPSC-derived neurons. One such study, already discussed in Section 1.10.3, utilized iPSCs from two donors with AD bearing $\varepsilon 4$ homozygosity. The lines were also genetically converted (via CRISPR; Section 1.14.1) to the $\varepsilon 3/\varepsilon 3$ genotype (thus avoiding confounding factors from the varying genetic backgrounds of different donors). After converting the stem cell cultures to that of homogenous forebrain excitatory neurons with no glial cell types (avoiding potential confounding factors from

astrocyte-secreted ApoE), unedited ε3/ε4 neurons proved more vulnerable to ionomycin-induced neurotoxicity than the edited ε3/ε3 counterparts. In addition, ε4/ε4 neurons showed markedly higher tau phosphorylation and ERK1/2 activation, secreted higher levels of phosphorylated tau into the culture medium and showed decreased neurite branching morphology compared to isogenic ε3/ε3 counterparts. These types of results strengthen the notion that iPSC-derived neurons recapitulate relevant aspects of AD pathophysiology and they can be used to model the role of neuronal-expressed *APOE* in AD pathology (144).

1.12 Generating neurons from iPSCs

Conversion of iPSCs into self-renewable, neural stem cells (NSCs), neuronal progenitor cells (NPCs), and neurons in sizable quantity with reliable reproducibility has been achieved (136, 145, 146). The method of generating neurons from iPSCs that I used is based upon the forced expression of a proneuronal transcription factor (136).

Certain proteins are required (determined by loss-of-function studies) and sufficient (determined by gain-of-function studies) to induce development of neuronal cell fate and initiate progenitor cells to differentiate into specific neuronal subtypes and thus are said to be encoded by 'proneural' genes (147, 148). Pang *et al.* showed that overexpression of a set of four proneuronal transcription factors (Brn2/Pou3f2, Ascl1, Myt1l and NeuroD1) could yield functional neurons from human iPSCs in as quickly as 6 days after starting overexpression; signifying a practical alternative to other more cumbersome, time consuming differentiation protocols (149).

Later, conversion of iPSC to neurons was achieved by overexpression of just two transcription factors, Neurogenin-1 and Neurogenin-2 (149, 150). The resultant induced neurons (also referred to as iNs) expressed glutamatergic synaptic proteins (such as vesicular glutamate transporter 1 (VGLUT1), postsynaptic density-95 (PSD95) and synapsin1 (SYN1) and showed excitatory synaptic function *in vivo* upon transplantation into mouse brains (150). Thus, it was demonstrated that this approach rapidly and efficiently yielded homogenous populations of functional excitatory neurons (150). Subsequently, Neurogenin-2-mediated neuronal induction protocols have utilized overexpression of either mouse Neurogenin 2 (mNgn2; Ngn2) or human NEUROGENIN 2 (hNGN2; NGN2) in human iPSCs (150, 151). Ngn-mediated neurogenesis in iPSC cultures occurred though various progenitor states involving critical transcription factors and miRNAs (150). Consequently, the potent neural induction ability of Ngns has been harnessed to convert iPSCs into neurons and, eventually, forced over-expression of only Ngn2 is shown to be sufficient to induce functional excitatory neurons in both human and mouse iPSCs (150-153).

1.13 The neurogenin (Ngn) family of transcription factors (TFs)

Neurogenins are categorized as a 'pioneer' TF by virtue of their ability to single-handedly kickstart a genetic differentiation program. Ngns can interact with closed chromatin regions to activate genes that are crucial for stimulating neuronal differentiation. Simultaneously, they can bind astrogliogenic genes to repress their transcription (154). NGN protein has a helix-loop-helix motif, that mediates protein–protein interactions, and a basic DNA binding domain, as shown in Figure 1.14 (155). NGNs activate neuronal differentiation by forming heterodimers that bind CANNTG consensus sequences, termed E-boxes, in the promoter region of neuron-specific genes (155). Several Ngn genes have been discovered (155). Alignment with respect to their conserved bHLH domain shows that different homologs occur in different species. Mouse and human show three paralogs (Ngn1, Ngn2 and Ngn3) (155, 156). The homologs exhibit some overlapping but also divergent activities regarding neuronal versus glial cell fate specification, specification of subtype cell identities, and directing axonal versus dendritic development (155).

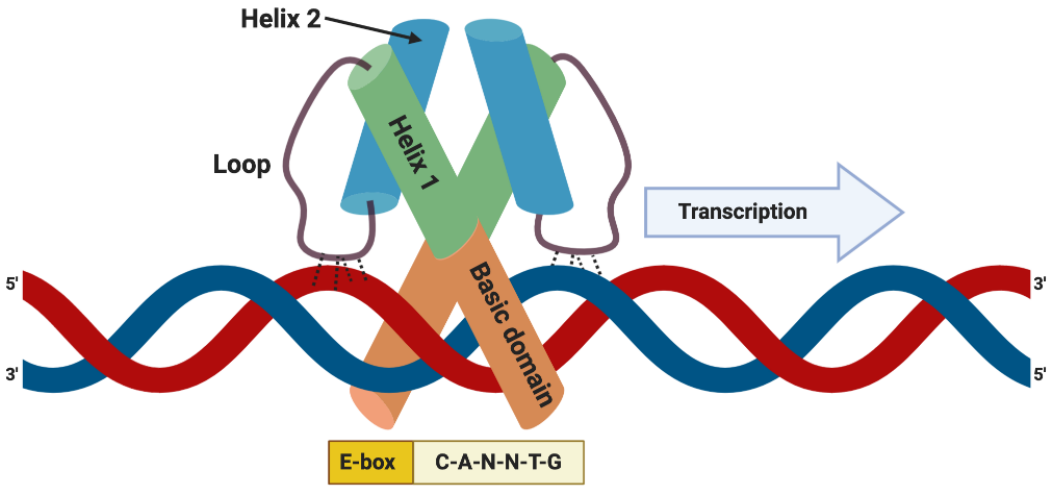

Figure 1.14 Structure of the basic helix-loop-helix (bHLH) transcription factor family.

The bHLH TFs have 2 alpha helices, which facilitate dimerization, and a basic domain, that interacts with CANNTG DNA consensus sequences (E- boxes) in the promoter region of neuronal specific genes.

Proneural mechanisms of Ngns are, in part, mediated by the Notch signaling cascade. During CNS development, the Notch molecular signaling cascade supports continual self-renewal of NSCs and NPCs. Ngn2 affects Notch signaling by indirectly modulating a well-characterized downstream effector and transcriptional repressor, Hes Family bHLH Transcription Factor 1 (Hes1) (155). Ngn2

upregulates the Notch ligand, Delta-like1 (Dll1), which subsequently activates Notch receptors on neighboring cells; in a process known as Notch lateral inhibition which permits only the progenitors with persistently high levels of Ngn2 expression to progress through neuronal differentiation (155).

Through a negative feedback loop, Hes1 oscillations culminate in driving oscillatory expression of both Ngn2 and Dll1. As diagrammed in Figure 1.15, the oscillatory protein expression pattern of Ngn2 and Hes1 is inversely correlated and cycles about every 2 hours (157). It is this dynamic pattern of Hes1 and Ngn2 expression that permits stem cell identity and proliferation. However, when the Ngn2 expression pattern switches to a persistent one, neuronal differentiation ensues. Post-mitotic neurons show persistent Ngn2 and Dll1, and no Hes1, expression. Therefore, depending on the mode of expression, persistently vs rhythmically, Ngn2 is involved in either the upkeep of the progenitor pool (by inducing a Dll1 oscillatory expression pattern which mirrors its own), or driving neuronal differentiation.

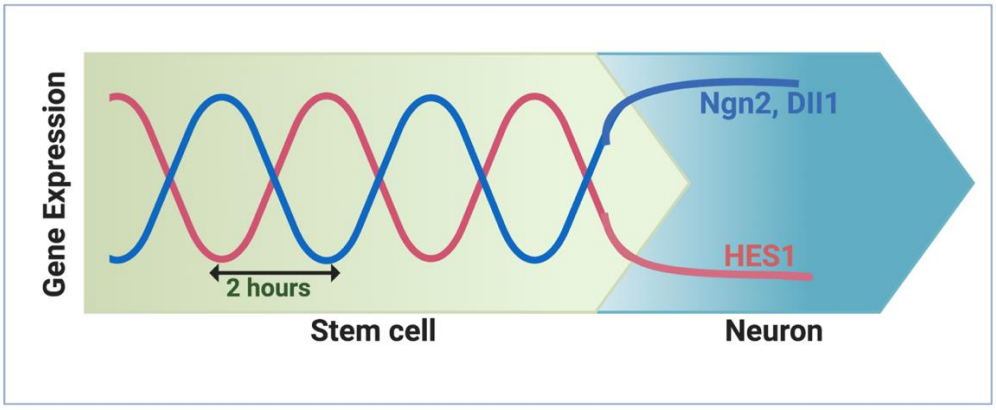

Figure 1.15 Sustained, versus periodic, expression levels of Ngn2 in stem cells triggers neuronal differentiation.

Ngn2 indirectly modulates Hes1 by upregulating Dll1 which subsequently activates Notch receptors in neighboring cells to promote transactivation of the Hes1 promoter. Only stem cells experiencing persistently high levels of Ngn2 differentiate into neurons, while oscillating expression, over 2-hour intervals, maintains stem-cell identity.

Ngns also function in complex spatial and temporal paradigms (147, 155). During mouse early cerebral cortex development, both Ngn1 and Ngn2 transcripts are expressed not only in the ventricular zone where neuronal precursors are found, but also only during the limited time period when neurogenesis is occurring; a time period which precedes gliogenesis throughout mammalian CNS development (155). Meanwhile, Ngn1 suppresses astrocyte differentiation, in part, by inhibiting the signal transducer and activator of transcription (STAT) signaling pathway (148, 155). Culmination of neurogenesis is accompanied by Ngn1 downregulation, freeing

progenitor cells to then respond to glial-promoting mechanisms (148). Figure 1.16 summarizes the notion that once Ngn2 expression is stabilized in neural progenitor cells, it triggers the differentiation of neurons while inhibiting or delaying the differentiation of glia such as astrocytes.

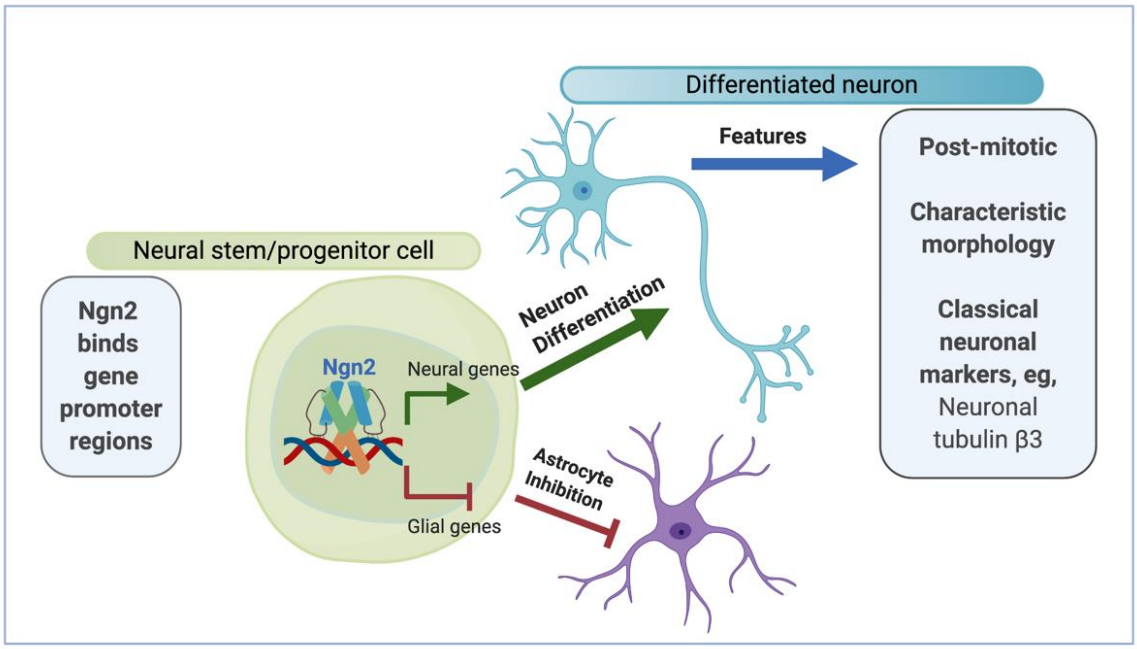

Figure 1.16 Ngn2 drives neuronal identity while inhibiting glial gene expression in NSCs.

In NSCs, Ngn2 binds gene promoter regions to increase neuronal, and simultaneously decrease glial, gene expression. As a result, stem cells differentiate into neurons. Neurons are recognizable by characteristic morphology, molecular markers, and post-mitotic nature.

Crucial functions in initiating the differentiation of specific neuronal subtypes from progenitor cells have been described. For example, Ngn2 is shown to initiate differentiation of glutamatergic neurons while simultaneously inhibiting GABAergic identity via induction of genes like NeuroD1 and NeuroD2 which antagonize GABAergic differentiation regulated by Mash1 (156).

Aside from cell fate determinant actions, Ngns also contribute to axonal and dendritic growth, thus promoting neuronal network formation. Ngn2 is necessary for regulating dendritic morphology and axonal guidance in pyramidal neurons (156). Acute conditional knockout of Ngn2 in cortical progenitors generated deficiencies in both cellular migration and dendritic morphology (158).

1.14 Select gene editing techniques

Gene-editing of iPSCs permits further refinement of CNS disease modeling in the culture dish. For instance, disease relevant mutations may be incorporated into healthy iPSCs, or conversely,

genetic correction of mutations may be performed in diseased iPSC. Disease-relevant genes could be knocked out or tagged to study their function in neurons when expressed at physiological levels. Gene editing has been utilized in the context of neuronal *APOE*. Separate groups have now published on genetic conversion of *APOE* ε3/ε3 and ε4/ε4 genotypes in AD-derived iPSCs to investigate consequence of ApoE4 expression in neurons. These groups had utilized the precision of **c**lustered, **r**egularly **i**nterspaced **s**hort **p**alindromic **r**epeats (CRISPR) gene-editing technology to specifically switch the nucleotides required for conversion to the different *APOE* genotypes. Alternatively, many groups have shown the use of lentiviral-mediated, stable introduction of whole genes into the genomes of iPSCs.

1.14.1 CRISPR genome editing technology

Genome editing via CRISPR technology couples efficiency with precision that is distinct from previously developed gene editing methods. Precision genetic editing is based on targeting specific regions of the genome using CRISPR DNA sequences and a CRISPR-associated, or Cas, endonuclease. Gene modulation relies on delivering the Cas endonuclease into cells along with a targeting guide RNA (gRNA) which ushers the enzyme to the genetic locus of interest. When the endonuclease snips the DNA at the targeted nucleotide sequence, a double strand DNA break (DSB) is made. Endogenous cellular DNA repair mechanisms then patch the DSB. The repair may occur via a highly efficient, but error-prone mechanism, called non-homologous end joining (NHEJ), or, via a complex, but precise process, called homology-directed repair (HDR). The repair pathways selected by cells to repair the DSB is not influenced by the CRISPR system.

NHEJ generally creates inaccuracies, such as nucleotide insertions or deletions (indels), which typically result in ablation, or knockout (KO), of the targeted gene (159). Inserting genes, knockin (KI), is more difficult than deleting them because this relies on the repair of the DSB being performed precisely and with incorporation of specific sequences. Genetic KI necessitates exploiting HDR as this process can copy the desired sequence modification from a donor DNA repair template that is co-delivered with the CRISPR machinery. Because HDR occurs with far less frequency than NHEJ, it presents a bottleneck in the targeted incorporation of modified DNA sequences (159).

Cas9 is the most widely used restriction endonuclease in CRISPR approaches, although a wide variety of them exist, including Fanzor, the first programmable RNA-guided endonuclease to be discovered in eukaryotes (160). The gRNA that targets Cas9 to the cut site, is comprised of 2 RNA molecules: (1) the CRISPR RNA (crRNA) that carries a target-specific region of about 20 nucleotides long and (2) the trans-activating crRNA (tracrRNA) which has a universal sequence

that associates with crRNA and assists with recruiting the Cas enzyme. The active crRNA:tracrRNA:Cas9 complex is guided to the target DNA sequence complementary to the crRNA and which must be located upstream of a protospacer adjacent motif (PAM) site. Figure 1.17 emphasizes that the endogenous machinery that cells harness to repair the cut (created by Cas9) is not influenced by the CRISPR technology and can yield a variety of outcomes (159).

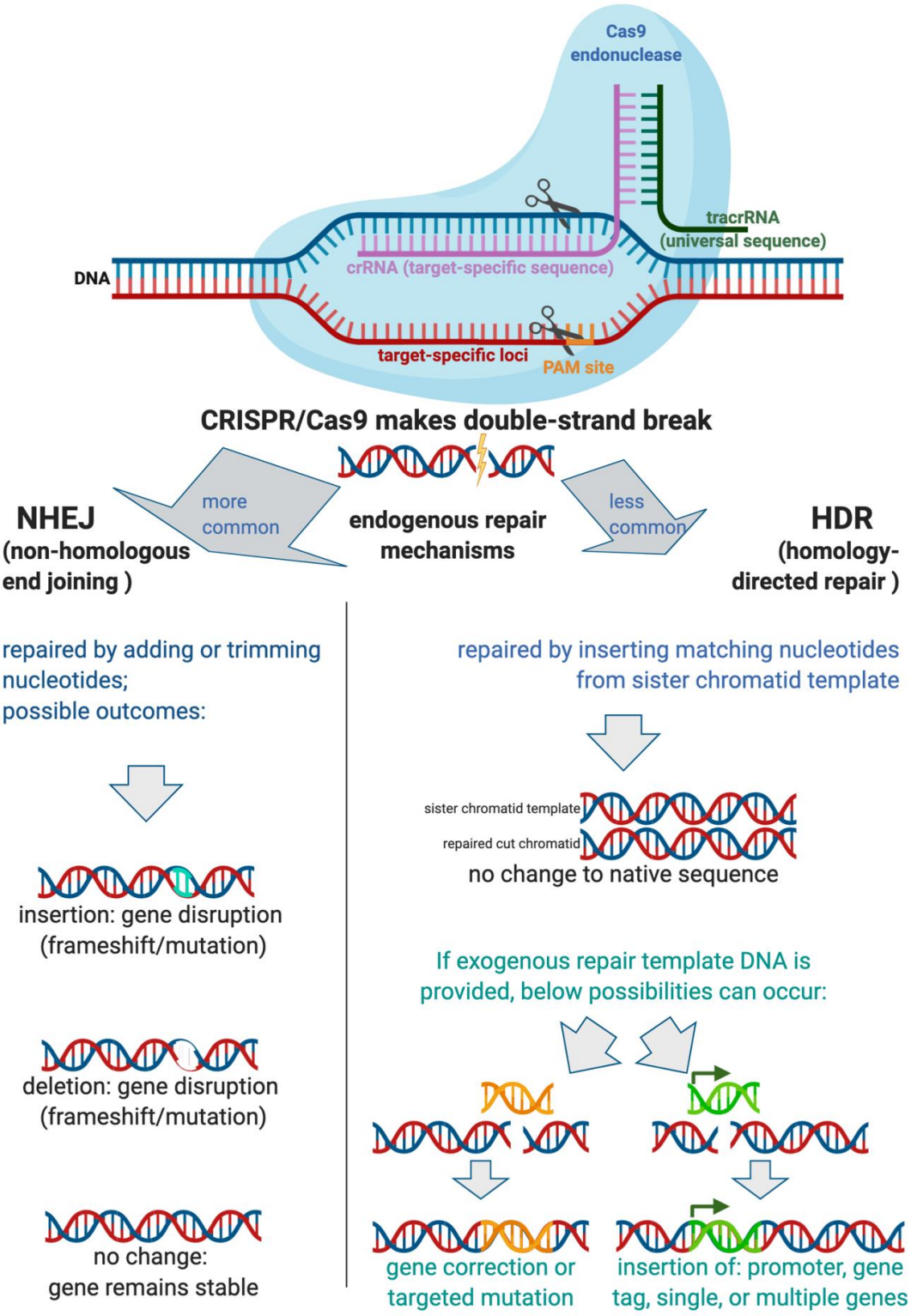

Figure 1.17 CRISPR-mediated genome editing overview.

Cas9 is directed to the cut site by a gRNA, whose **target site specificity** is governed by the RNA sequence within its **crRNA region** while its **trRNA region** carries a universal sequence containing the secondary structure required for Cas9 binding to the gRNA. The only prerequisite for Cas9 targeting is the presence of a **PAM sequence** directly 3' of the crRNA sequence. Cas9 creates a DSB at the targeted genomic DNA site which is exploited for gene knockout, targeted gene modulation, or gene knock in. Endogenous machinery that cells harness to repair the break is not controlled by CRISPR technology and yields several possibilities. For knock in experiments, a repair DNA template sequence is delivered to the cells in conjunction with the Cas9 and gRNA.

1.14.1.1 Practical considerations for CRISPR experiments

To implement CRISPR-Cas9 genomic editing, at the very least, Cas9 and the gRNA must be delivered inside the nucleus. These can be achieved by transfection or viral transduction of expression cassettes encoding both. Although this method has demonstrated to be reliable, possible limitations are:

- Extensive optimization of promoters for both Cas9 and gRNA to achieve appropriate expression levels
- Plasmid DNA could randomly integrate into the host genome
- Off-target effects can accumulate upon persistent Cas9 expression
- The kinetics of cellular transcription and translation of Cas9 can confound editing.

Instead of relying on the cellular machinery to express Cas9 and the gRNA, an active complex could be introduced directly to the cells. Recombinant Cas9 protein in tandem with chemically synthesized gRNAs could be delivered as an active ribonucleoprotein (RNP) complex. A benefit to synthesized gRNA is that it can be chemically modified to enhance its efficiency. The 2-part gRNA (crRNA plus tracrRNA) would need to be allowed to anneal together by incubating them *in vitro* or they could be synthesized as a single molecule that is fused together with a linker loop, to form what is termed a single gRNA, or sgRNA. The RNP is allowed to form *in vitro* by incubating together immediately prior to use. Delivering RNPs minimizes potential complications of Cas9 protein expression from unoptimized promoters. The RNP delivery method does not involve Cas9 DNA so the RNP, along with all cutting functions, gets degraded over time yielding transient exposure thus limiting the potential for off-target effects (161).

Different methods exist for efficient and direct delivery of the RNP complex into cells. These include lipofection and electroporation and protocols are typically developed empirically according to the cell lines. For KI or mutagenesis experiments, where the HDR pathway is critical for integration of an exogenous sequence, the DNA sequence is co-delivered to the cells, as the so called ‘donor DNA’; providing a repair template DNA for incorporation of the desired mutation or genes at the desired genomic site (Figure 1.17; right side).

CRISPR-mediated gene editing in iPSC does pose some challenges. Delivery of the editing reagents could be cytotoxic. Persistent expression of Cas9 in the cells could increase off-target effects. In knock-in experiments in which a repair template is co-delivered, there is a risk of random incorporation of this donor template in non-specific sites in the genome. During a KI experiment, a heterogenous outcome emerges; consisting of unedited (naïve or wildtype), incorrectly edited, or correctly edited cells. As such, typically single-cell isolation of potentially edited cells is a

requisite, then single-cells are expanded into a population that comprises a clonal cell line. With respect to iPSCs which are maintained as colonies and passaged clumped together, opposed to dissociated single cells, making clonal-cell lines is challenging. One thing to account for is that single-cell dissociation results in a high death rate and when the cell population subsequently expands, there is a chance that clonal lines lose their pluripotency and hence their capacity to differentiate downstream. The frequency of HDR is low in iPSCs requiring a laborious screening method by which to identify successfully edited KI clones.

1.14.1.2 Insertion site considerations

When inserting a gene, or set of genes, into the human genome, a benign insertion location is the preferred approach. The Adeno-Associated Virus Integration Site 1 (AAVS1) is considered such a location or locus. At first, researchers discovered it as a hotspot where the adeno-associated virus (AAV) integrates into the human genome. The locus is in intron 1 of the protein phosphatase 1 regulatory subunit 12C (PPP1R12C gene) on chromosome 19 (162). Later, the AAVS1 locus was described as permissive for stable, long-lived transgene expression in multiple types of cells, including ESCs (163). It was also shown to shelter neighboring genes from transcriptional perturbations; qualities resulting from its naturally occurring chromatin insulator borders. Genetic insulators are DNA-protein structures that delimit gene expression levels by obstructing enhancers from influencing promoters and by providing borders to nearby heterochromatin that silence the bounded gene (163-165).

An example of the potential success towards overcoming variability amongst genetically engineered cell lines related to insertion site has been demonstrated by Wang *et al.* (145). A doxycycline-regulatable Ngn2 expression cassette was inserted into the AAVS1 locus (using what is known as Transcription activator-like effector nuclease or “TALEN” based editing technology) of human iPSCs that were subsequently differentiated into functional excitatory neurons (145). Similarly, colleagues in Biogen considered it crucial to have an inducible NGN2 gene inserted into a safe harbor locus in iPSCs slated for use as iPSC-derived cortical neurons in our company’s drug discovery pipeline. My colleagues likewise targeted the AAVS1 locus in engineering an iPSC line to stably express a doxycycline-inducible human NGN2 transgene. Their strategy for targeting transgenes to specific genomic locations was CRISPR-assisted gene editing.

1.14.2 Lentiviral vector mediated transgene insertion

In general, viral transduction yields higher editing efficiency than nonviral methods. In human iPSC, lentiviral vectors achieve high stable transduction efficiency and have been proven a robust tool for gene delivery. For example, high titer self-inactivating lentiviruses have shown about 70%

transduction efficiency in human ES cells (166). Lentiviral vectors permanently integrate into the host genome and offer stable, inheritable expression of their cargo transgene which can be as large as 10 kb in size. A concern regarding lentiviral vectors, however, is that where they insert into the genome is uncontrolled. If they randomly integrate into actively transcribed genes, this results in insertional mutagenesis. A broader drawback regarding viral vectors is that viral transgenes may be inactivated (e.g., via silencing) by the host cells (166).

1.14.3 An inducible gene expression system demonstrated to work in iPSCs

When converting iPSC to neurons via overexpression of Ngn2, it is necessary to be able to turn on the expression of the gene only in the desired differentiation timeframe. A commonly used way to temporally regulate activation of Ngn2 expression in iPSC cultures is by employing the well characterized Tetracycline (Tet) Inducible Expression system. The technology allows for turning on or off gene expression in response to an effector molecule (167, 168).

Tetracycline (and its derivative, doxycycline) is an antibiotic that prevents bacterial protein synthesis by inhibiting the 30S ribosomal subunit and bacteria have created ways, such as tetracycline efflux, to counteract its activity (167). Tetracycline efflux is mediated by a membrane protein, TetA, whose expression is regulated by the tetracycline-responsive repressor protein, TetR. Protein levels are controlled by regulation of their gene expression via the transposon Tn10 tetracycline resistance operon (167). Tet-inducible systems are based on the tetracycline resistance operon of *Escherichia coli* (*E. coli*) transposon Tn10 which also functions in mammalian cells (169). Two versions of the expression system are commercially available, Tet-On and Tet-Off®, and rely on an inducible recombinant transcriptional activator. The transcriptional activator can be controlled reversibly as well as quantitatively upon exposure to doxycycline.

An advanced system, called Tet-One™, incorporates a more sensitive and efficient doxycycline-responsive transactivator protein and a convenient single expression cassette includes all the components of this technology (168). Tet-One™ is depicted in Figure 1.18. According to the user manual for the commercially available Tet-One™ Inducible Expression System, the transactivator protein, termed Tet-On 3G, is positioned in the forward direction from the human phosphoglycerate kinase 1 (PGK1) promoter while the inducible promoter, PTRE3GS, drives expression of the gene of interest from the reverse orientation. The PTRE3GS inducible promoter comprises 7 repeats of a 19-bp tet operon sequence located upstream of a minimal promoter and is devoid of binding sites for mammalian transcription factors making it silent in the absence of induction. The Tet-On 3G transactivator is expressed constitutively but is not able to bind to the promoter. When doxycycline binds Tet-On 3G, it undergoes a conformational change that then

permits it to bind to the tet operon sequences on PTRE3GS (170). Tet-inducible expression systems have been introduced into, and shown to function in, iPSCs (132).

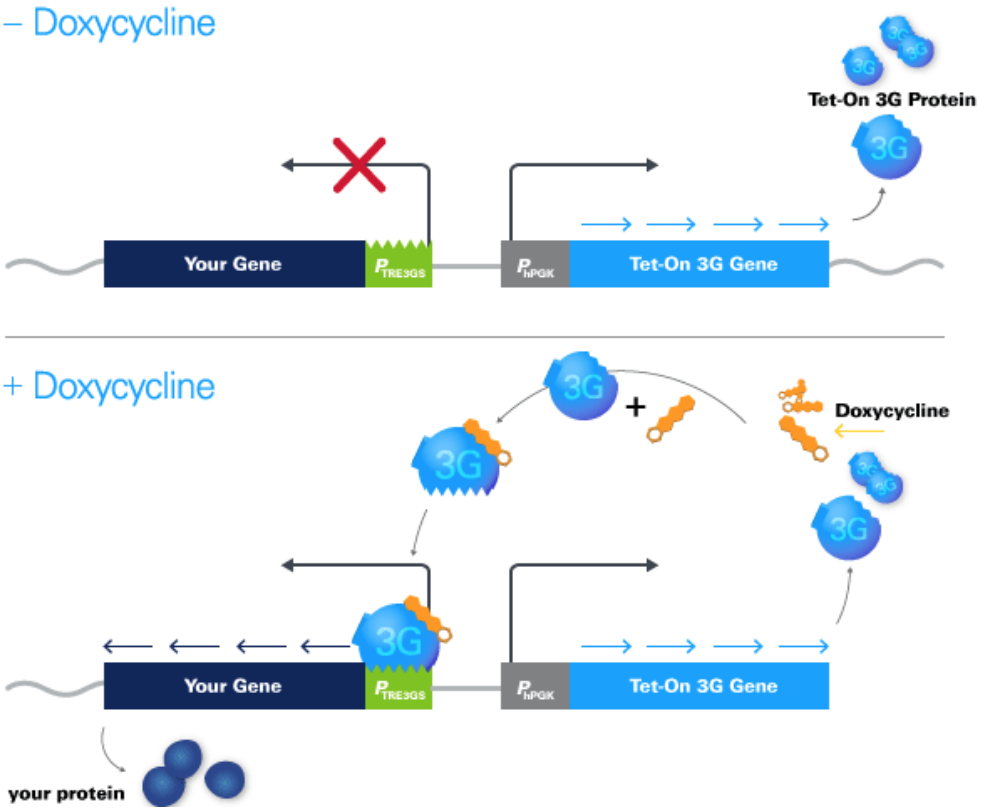

Figure 1.18 Schematic of the inducible gene expression cassette, Tet-One.

The Tet-On 3G transactivator protein is expressed in a constitutive manner but is inactive in the absence of doxycycline (Top panel). When bound by doxycycline, Tet-On 3G then takes on a confirmational change that allows it to interact with the PTRE3GS promoter; initiating transcription of any transgene cloned downstream (figure from manufacturer's user manual).

1.15 Hypothesis, aim, and objectives

1.15.1 Hypothesis

APOE genotype has an important consequence for LOAD susceptibility and age of onset. How and to what extent neuronal ApoE plays a role is unclear. I hypothesize the endogenously expressed *APOE* ε4 reduces neuronal resilience to stress and ageing, while neuronally expressed *APOE* ε*2* is protective compared to *APOE* ε3. The neuronal ApoE-dependent component of neuronal repair and resilience will manifest in a rank order from strongest to weakest neurons being: $\varepsilon2/\varepsilon2$ > $\varepsilon3/\varepsilon3$ > $\varepsilon4\varepsilon4$.

1.15.2 Aim

Studies illustrate that ApoE has some common functions amongst species (eg, human ApoE corrected cholesterol disturbances caused by murine apoE knockout and both rodent and human systems upregulate neuronal expression in injured conditions [Section 1.10]). At the same time, studies suggest ApoE also has uniquely human roles that call for its expression in unstressed neurons. Besides intrinsic species differences, a question that is starting to receive more attention is whether different roles of ApoE exist depending on its cellular source. Further investigations are needed to refine the conditions for neuronal transcription and expression of this gene in human neurons and to examine possible differences in how *APOE* allelic variation impacts neuronal lipid metabolism, aging, and response to injury.

My aim was to provide a better explanation for how *APOE* genotype impacts the complex neuronal interactions underlying disease mechanism and progression by characterizing whether neuronal ApoE modulates response to stress in an isoform-specific manner. To do so, my objective was to produce a human cellular platform that allowed me to focus on cell autonomous modulation in neurons to probe neuronal ApoE mediated function and dysfunction.

1.15.3 Objectives

My main objectives were to:

1. Assess technologies best suited to providing an in vitro system amenable to investigating *APOE* variant-dependent differences in neurons.
2. Understand whether neuronal differentiation and phenotype occurred in a comparable manner amongst iPSCs of the same genetic background but differing in only their *APOE* genotype.

3. Examine whether *APOE* expression and neuronal resilience differentially responded to pharmacological stress in isogenic neurons homozygous for the *APOE* genetic variants: ε2, ε3, and ε4.

Chapter 2 Materials and Methods

2.1 Materials

Chemicals and culture materials were obtained from ThermoFisher Scientific and StemCell Technologies (unless otherwise stated). Details of materials are given in the pertinent sections.

2.2 Cells, culture maintenance, differentiation, and treatments

IPSC lines were used in this work. All cultures were always manipulated in Biosafety Level 2 (BSL2) conditions (171).

2.2.1 Isogenic iPSC lines carrying *APOE* genetic variants (Ɛ2/Ɛ3/Ɛ4) and knock-out

APOE gene-targeted iPSC isogenic cell lines engineered to knock out or selectively express 3 ApoE variants are listed in Table 2.1 (blue colored rows). These cells were generated by the ADAPTED consortium (https://www.imi-adapted.eu/) and were obtained from the European bank of induced pluripotent stem cells (EBiSC). They comprise two sets of lines: each set originating from a separate male donor. The set of iPSCs derived from a non-AD affected subject (19-year-old at the time of biopsy) is named BIONi010-C (*APOE* 3/4) and its gene-edited derivatives are: 2/2 (BIONi010-C-6), 3/3 (BIONi010-C-2), 4/4 (BIONi010-C-4), and KO (BIONi010-C-3) (172). Later, after I already started working with the 3/3 (BIONi010-C-2) line, I found out that the E33, E44, and E22 lines have only one functional ε3, ε4, ε2 allele (Section 4.4), respectively, owing to unintended incorporation of on-target insertions during CRISPR editing (173). The other set of iPSCs is derived from a patient with AD (80-year-old at the time of biopsy), based on the line designated UKBi011-A (4/4), and similarly covers the desired range of *APOE* genotypes and do not show any CRISPR editing issues (174).

2.2.1.1 Ethical framework covering iPSC lines from EBiSC

EBiSC ensured that donor consent was obtained in accordance with Research Ethics Committees in the UK and the USA for production of and research on iPSCs from primary donated tissue and anonymization of donor data according to their website: https://ebisc.org/customer-information/consent-primary-tissue-procurement/.

2.2.2 Control iPSC line (*APOE* Ɛ3/Ɛ3) carrying inducible-NGN2

The iPSC line (APOE 3/3) originating from a 40-year-old male donor without AD was established at Biogen (Table 2.1; iNGN2-iPSC control, grey colored row). Chapter 3 Section 3.1.5 describes engineering of the line to express human NGN2 under the control of a doxycycline inducible promoter in the AAVS1 locus. I used this iPSC line as a comparator line to benchmark my CRISPR-mediated gene editing workflow and the lentiviral-mediated differentiation of the of the isogenic iPSCs.

Table 2.1 iPSC lines for generating a neuronal *APOE* study platform

Original line from which *APOE* isogenic lines were derived (*APOE* genotype)	*APOE* Modification	Derivative *APOE* isogenic line name (EBiSC repository)	Current *APOE* status	Working name of *APOE* isogenic line name
BIONi010-C (*APOE* 3/4)	*APOE* gene knock-out via insertion of a frame shift mutation in exon 1	BIONi010-C-3	KO	CKO
	nucleotides at both SNPs rs7412 and rs429358 were changed to a T	BIONi010-C-6	E2/KO	C22
	base position described by rs429358 changed from T/C to T/T	BIONi010-C-2	E3/KO	C33
	base position described by rs429358 changed from T/C to C/C	BIONi010-C-4	E4/KO	C44
UKBi011-A (*APOE* 4/4)	*APOE* gene knock-out via insertion of a frame shift mutation in exon 1	UKBi011-A-1	KO	AKO
	nucleotides at both SNPs rs7412 and rs429358 were changed to T/T	UKBi011-A-2	**E2/E2**	**A22 or 22**
	base positions for rs429358 changed from C/C to T/T	UKBi011-A-3	**E3/E3**	**A33 or 33**
	none (original rs7412 is C/C, and rs429358 is C/C)	UKBi011-A	**E4/E4**	**A44 or 44**
Unpublished (*APOE* 3/3)	none	Not applicable	**E3/E3**	**iNGN2-iPSC control**

2.2.3 Human iPSC cell lines maintenance

My maintenance methods for iPSC cultures were adapted from the Stem Cell Technologies manual, as described below.

2.2.4 Maintenance and passaging of iPSCs

All iPSC cultures were kept in incubators at 37°C, 5% CO2, with >95% humidity. Their maintenance/growth media was complete mTeSR™1 (Stem Cell Technologies) (Table 2.2) and they were grown in a 6-well format on Matrigel or laminin-521 matrix. Passaging occurred about every 4-6 days when most of the colonies became compact with dense centers where cells grew on top of each other rather than in monolayer. Too frequent passaging or too small colony sizes result in passaged cell clumps either failing to reattach upon re-plating or differentiating in an uncontrolled manner. If iPSC cultures become overconfluent before passaging, they are prone to spontaneous differentiation. Unwanted differentiation was scored by noting cells or colonies with abnormal iPSC morphology and such cultures were discarded.

Table 2.2 iPSC Growth/Maintenance medium

mTeSR™1 (Stem Cell Technologies)	Component	Volume (500 mL)
500 mL (Catalog #85850)	mTeSR™1 Basal Medium (#85851)	400 mL
	mTeSR™1 5X Supplement (#85852)	100 mL

In preparation for passaging, mTeSR™ medium was equilibrated to room temperature for >1hr in the dark (not warmed in 37°C water bath) and 6-well destination plates were coated with Matrigel (Section 2.2.6). For maintenance passaging, iPSC cultures were manipulated as clumps rather than single cells using the enzyme-free dissociation reagent called ReLeSR™. After washing the cells with Ca^{2+} and Mg^{2+}-free Dulbecco's phosphate-buffered saline (D-PBS), 1 mL of ReLeSR™ was added to each well, then subsequently almost all ReLeSR™ was removed to leave only a thin film of liquid on the cells. The cells were placed in the tissue culture incubator for about 6-8 minutes. Next, 1mL of mTeSR™ was added and the plate was firmly tapped until cells sloughed off, in clumps. Cell clumps were gently mixed by pipetting then a portion, a 1:6 or 1:10 split ratio depending on the iPSC line, was re-plated in new Matrigel pre-coated wells containing mTeSR™. The new plate was gently rocked by hand to spread out the cell clusters then placed in the 37°C incubator. Culture medium was fully replaced every day with fresh mTeSR™ and the cells were checked for the need to be passaged using criteria mapped out above.

2.2.5 Coating of plates with CellAdhere™ Laminin-521 growth substrate

CellAdhere™ Laminin-521 (normally stored at -20°C) was thawed at 4°C, then diluted in Dulbecco's phosphate-buffered saline containing Ca^{2+} and Mg^{2+} (ThermoFisher Scientific catalog # 14040141) to a final concentration of 10 µg/mL. After gentle hand mixing, 1 mL of the diluted

laminin was immediately added to each well of 6-well plates. The plates were rocked back and forth to spread the laminin solution across the entire culture surface then placed in the tissue culture incubator, at 37°C, for at least 2 hours before use. Just prior to plating with cells, the bathing laminin solution was removed and the plates used without further washing.

2.2.6 Coating of plates with Matrigel growth substrate

Stock Matrigel (hESC-Qualified Matrix; Corning catalog # 354227) was thawed at 4°C and kept on ice to avoid gelling. After the initial thaw, undiluted stock Matrigel was aliquoted into 600 µL volumes and immediately stored at -20°C to lessen freeze-thaw cycles. When required, an aliquot was thawed and diluted with cold DMEM/F12, according to the "dilution factor" per batch as instructed by the manufacturer. Immediately after diluting, Matrigel was applied at 1 mL per well of a 6-well dish, or 50 µL per well of 96-well plates, and swirled, or tapped, to uniformly coat the wells. Matrigel-coated plates were placed in the tissue culture incubator for at least an hour before use (but not more than 2 days and they were never allowed to dry out). When ready to plate iPSC cells, the Matrigel solution was aspirated and replaced with 2mL, or 50 µL, of fresh mTeSR™ per well of 6-well or 96-well plates, respectively.

2.2.7 Freezing of iPSCs

Human iPSC cultures grown in mTeSR1 in 6-well plate format were cryopreserved when the cultures were ready for the next passage, as defined in Section 2.2.4. The cultures were dissociated into clusters per ReLeSR method described in Section 2.2.4. To remove existing mTeSR™ medium from the freshly harvested cell clumps, cells were spun at 300 x g for 5 minutes at room temperature (15 - 25°C) and the medium was gently aspirated off the cell pellet. The pellet was resuspended in 1 mL per well cold freezing medium (mFreSR) using a 5 mL serological pipette to facilitate retention of the clusters and 1 mL cell suspension was placed per cryovial (Corning, catalog # 432008) such that one well of cells was preserved into a single cryovial. Cryovials were placed in a rate-controlled cooling container (Corning® CoolCell™ LX Cell Freezing Container, catalog # CLS432002) that slowly dropped temperature by 1°C/min from 4°C to -80°C before transferring the cryovials to long-term storage in liquid nitrogen.

2.2.8 Thawing of iPSCs

Pre-warmed mTeSR™1 (15 - 25°C) and pre-coated Matrigel plates were made ready before starting the rapid thawing steps for the iPSCs. Cryovials were quickly thawed in a 37°C water bath by lightly moving the vials around constantly until only a small ice pellet was visible

(approximately 2 minutes). At that point the cryovial was sprayed with 70% ethanol. With a 5mL serological pipette, the contents of a cryovial were moved to a 50 mL conical tube and 10 mL of warm mTeSR™1 was added dropwise with a gently rocking motion as the medium was added. Cells were then spun at 300 x g for 5 minutes at room temperature (15 - 25°C) and the medium aspirated off. The cell pellet was gently resuspended in 1 mL of mTeSR™1 (supplemented with 10 µM of a rho-associated protein kinase inhibitor (ROCKi) to enhance survival during recovery from freeze-thawing) using a 5 mL serological pipette. Following resuspension 3 wells of a 6-well plate were seeded from 1 frozen vial. The plates were gently rocked by hand to spread out the cell clusters before being placed in a 37°C incubator. Culture medium was fully changed daily, and the cells checked for when they need to be passaged next based on size and morphology of the colonies (Section 2.2.4). This was usually between 4 and 6 days post initial dispensing into mTeSR™1 medium.

2.2.9 Generation of single cell suspensions using Accutase™

Single cell suspensions of iPSCs were generated using Accutase, a proteolytic and collagenolytic enzyme-based cell detachment solution. Accutase stock solution was diluted 1:3 in PBS before use. Growth medium was aspirated from cells which were washed with PBS. After washing, Accutase was added at 10 mL per 75 cm^2 surface area and plates were incubated at 37°C degrees for about 8 minutes. During this incubation, iPSCs were periodically monitored under the microscope to discern when they were just beginning to dissociate out of the colonies. Cells were then detached to completion by adding 3 volumes of mTeSR™ and mixing into the Accutase by gently pipetting up and down. Cells were transferred to a 50 mL tube to be counted (Section 2.2.10) as appropriate for the distinct procedures described below.

2.2.10 Cell counting

I counted single-cell suspensions of iPSCs using one of two different methods depending on equipment availability in the moment.

2.2.10.1 Acridine orange (AO) and propidium iodide (PI) (AO/PI) staining

For cell counting and viability assessment with AO/PI staining, 20 µl of dissociated single cell suspension (Section 2.2.9) and 20 µl of AO/PI Staining Solution (Nexcelom Bioscience LLC.) were mixed then 20µl of this mixture was immediately added to a Cellometer counting slide and placed into the Cellometer Auto2000 (Nexcelom Bioscience LLC.) for analysis. The instrument reported live and dead cell numbers as well as cell density and viability values based on the premise that

these DNA dyes cause live nucleated cells to emit green and dead nucleated cells to emit red fluorescence, respectively.

2.2.10.2 Trypan blue exclusion staining

For cell counting and viability assessment with trypan blue exclusion staining, 20 µl of the dissociated cell suspension and 20 µl of 0.4% trypan blue dye (Bio-Rad Laboratories, Inc.) were mixed and 10µl of this mixture was immediately added to the appropriate counting slide for the TC20 cell counter (Bio-Rad Laboratories, Inc.). Based on the principle that dead cells specifically take up trypan blue while live cells do not, the instrument reported live and dead cell numbers, cell density/mL as well as the percent viability of the sample.

2.2.11 Generation of induced neurons (iNs) from iNGN2-iPSC control line

Neuronal induction from stable inducible-NGN2 iPSCs in their undifferentiated state (Section 2.2.2) was performed according to the plan shown in Figure 2.1 and cells were daily observed under the microscope. The iPSCs maintained in growth media (mTESR) were designated Day 0. Upon defrosting them, I did so in the presence of a ROCKi (Section 2.2.8). Twenty-four hours later, the culture was switched to N2B27 medium (Table 2.3 and Table 2.4), supplemented with ascorbic acid and dibutyryl cyclic AMP, and contained doxycycline (to induce NGN2 expression) and puromycin (for selection) at concentrations shown in Table 2.4. The day of first exposure to doxycycline was designated iN Day 1. After 5 or 6 days, at iN Day 5 or iN Day 6, cells were dissociated into single cells suspensions (using Accutase; Section 2.2.2.8) before being transferred to a 50 mL tube and counted using the Nexcelom AOPI staining protocol (2.2.10.1). The desired number of viable cells were aliquoted into a 50 mL conical tube and centrifuged at 90 x g for 5 minutes at room temperature. The supernatant was carefully removed from the cell pellets. Cell pellets were subsequently resuspended in N2B27 medium and plated on PDL-coated plates (providing a growth substrate more amenable to neuronal conditions compared to Matrigel) at a density of 1.5 x 10^6 in a 6-well format.

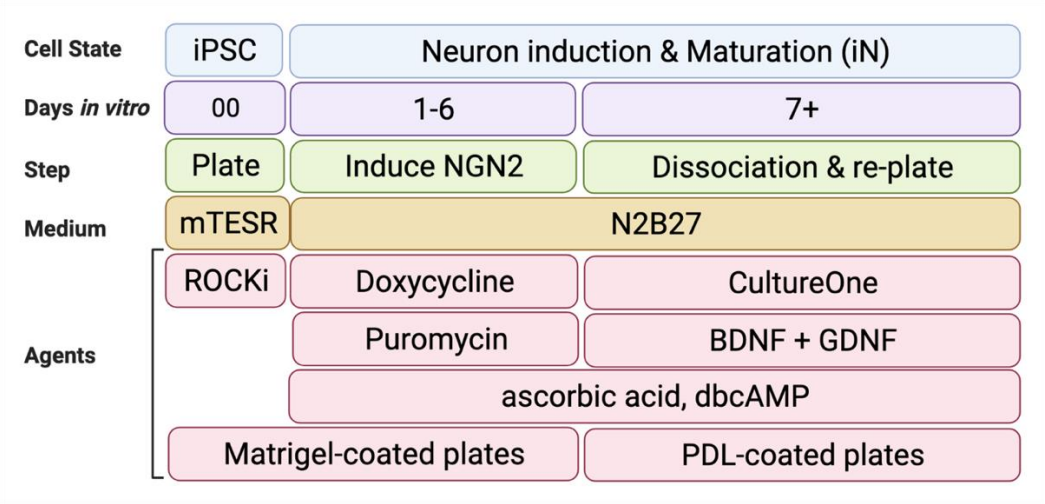

Figure 2.1 Schematic delineating neuronal induction timeline and key reagent changes and additions used to support the indicated cell type conversion.

Day 00 cells represent undifferentiated NGN2-stable iPSCs. During days 1 to 6 cells are maintained in neuronal media and exposed to doxycycline and puromycin. On Day 6 cells are dissociated and can either be re-plated immediately or frozen down for future experiments.

Doxycycline treatment was withdrawn at this point as well (Day 6). Additives to the neuronal media at Day 7 onwards, such as brain-derived neurotrophic factor (BDNF), glial cell-derived neurotrophic factor (GDNF) were added to assist in further neuronal maturation. CultureOne, also added to the cultures Day 6, is a proprietary supplement that limits the number of possibly remaining dividing progenitors which can potentially overgrow post-mitotic neurons.

Doxycycline solution was prepared by dissolving 100 mg doxycycline hyclate in 10 mL water (10 mg/mL was considered a 1000x stock) and sterile filtered through a 0.22 µm pore filter. Doxycycline stock solution was stored in 30 µL aliquots at -20°C, protected from light.

Table 2.3 Base media recipe and agents for neuronal differentiation of iNGN2-iPSC control

N2B27 Media		
Component	**Final Concentration**	**Amount for 1000 mL**
DMEM:F12; ThermoFisher Scientific (10565-018)	n/a	500 mL
Neurobasal™ Medium; Life Technologies (21103-049)	n/a	500 mL
Gibco® GlutaMAX™ (100x stock)	2 mM	5 mL
Pen/Strep 100x	1x	10 mL
N2 (100x); Life Technologies (17502-048)	0.5x	5 mL
B27 without Vitamin A (50x); Life Technologies (12587010)	0.5x	10 mL
*** dibutyryl cyclic AMP (db-cAMP) (1M stock; 1000x)**		
dbcAMP; Sigma (D0260)	1 mM	2.46 mg
Water	n/a	5 mL
*** ascorbic Acid (200 mM Stock; 1000x)**		
Ascorbic Acid; Sigma (A4403)	200 mM	100 mg
Water	n/a	2.8 mL
*** Rock Inhibitor Y-27632 (10mM stock; 1000x)**		
Rock Inhibitor Y-27632; Sigma (Y0503-1MG)	10 mM	1 mg
Water	n/a	295.6 µL

*N2B27 is freshly supplemented with 200 µM ascorbic acid, 1 µM dbcAMP, 1 ug/ml Doxycycline, and Culture 1 at 1x, as required, just before use.

Table 2.4 Media and substrate conditions for neuronal differentiation of iNGN2-iPSC control

Day	Growth substrate	Medium Components	Final Concentration
Day 0 (iPSC)	Matrigel	Complete mTESR Medium	n/a
		Rock Inhibitor (10mM stock)	10 µM
iN Day 1-6 (induced neurons)		N2B27 Media (recipe in Table 2.6)	n/a
		Doxycycline Hyclate; (Catalog #D9891; Sigma; 100mg/mL in water)	1 µg/mL
		Puromycin (Catalog # A1113803; Gibco; 1 mg/mL)	200 ng/mL
		Ascorbic Acid (200 mM Stock; 1000x)	200 µM
		Dibutyryl cyclic AMP (db-cAMP) (1M stock; 1000x)	1 µM
iN Day 7-14 (induced neurons)	PDL	N2B27 Media (recipe in Table 2.6)	n/a
		CultureOne™ Supplement (Catalog # A3320201; ThermoFisher Scientific; 100x stock)	1X
		BDNF (human) (Catalog # 2837; R&D Systems; 0.1mg/mL)	10 ng/mL
		GDNF (human) (Catalog # 212-GD; R&D Systems; 0.1mg/mL)	10 ng/mL
		Ascorbic Acid (200 mM Stock; 1000x)	200 µM
		Dibutyryl cyclic AMP (db-cAMP) (1M stock; 1000x)	1 µM
iN Day 15+ (induced neurons)		N2B27 Media (recipe in Table 2.6)	n/a
		Ascorbic Acid (200 mM Stock; 1000x)	200 µM
		Dibutyryl cyclic AMP (db-cAMP) (1M stock; 1000x)	1 µM

2.3 CRISPR methods for generating stable inducible-NGN2 iPSC clones

2.3.1 Overview of CRISPR-assisted genetic editing workflow

My overall CRISPR gene-editing workflow, designed to generate iPSCs engineered to express NGN2 in a doxycycline inducible manner, is outlined in Figure 2.2. To introduce the editing

components into the cells, I used the form of delivery most optimal for iPSC which was transfection via electroporation (according to my colleagues as well as a 2018 Harvard Stem Cell Institute's CRISPR genome editing 4-day hands-on course that I attended). I co-electroporated the inducible-NGN2 donor DNA cassette (described in Section 2.3.3) along with the editing agents (in the form of a pre-assembled RNP complex) individually, in parallel, into each of 4 *APOE* lines originating from an individual without dementia (Figure 2.2, step 1).

My next step (Figure 2.2, step 2) was to subject the cultured electroporated cells to puromycin treatment to kill non-transfectants and thus enrich for cells that incorporated the transgene cassette. The puromycin resistant cultures for all 4 lines were then cryopreserved (Figure 2.2, step 3). Although all lines of the puromycin resistant pools of cells were intended to be analyzed for positive results of the editing experiment, for practical reasons, only 2 lines, the ε3/ε3 and KO, were thawed and taken forward at first (Figure 2.2, step 4). At the point of initial thaw, genomic DNA was purified from a portion of the cells and assessed, via PCR, for evidence of successful transgene integration (Figure 2.2, step 5). The expanded electroporated cultures were next sorted into single cells via flow cytometry into 96-well formats to give rise to isolated clones from individual cells (Figure 2.2, step 6). Individual clones were grown up and split into duplicate cultures in identical 96-well plate formats (Figure 2.2, step 7). One plate of each matching 96-well plates was then screened for candidate clones, or hits, showing successful editing at the 5'-integration site (Section 2.3.8.1) while the other plate was frozen down (Section 2.3.8.3) creating an archive of cultures from which to revive and further screen hits identified from the primary PCR screen (Figure 2.2, step 8).

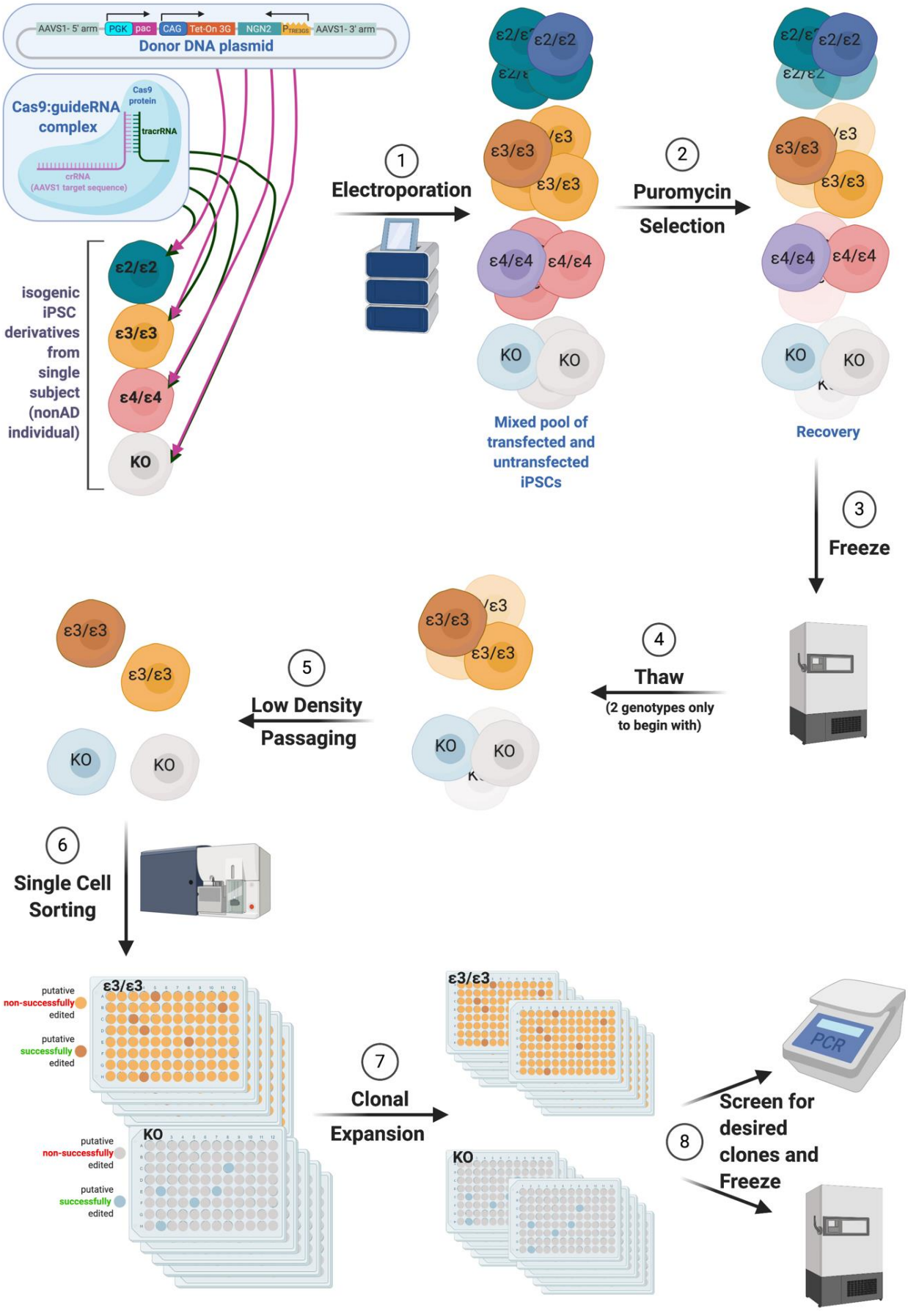
AAVS1- 5' arm
PGK
pac
CAG
Tet-On 3G
NGN2
AAVS1- 3' arm
Donor DNA plasmid
Cas9:guideRNA complex
Cas9 protein
tracrRNA
crRNA (AAVS1 target sequence)
isogenic iPSC derivatives from single subject (nonAD individual)
ε2/ε2
ε3/ε3
ε4/ε4
KO
1 Electroporation
Mixed pool of transfected and untransfected iPSCs
2 Puromycin Selection
Recovery
3 Freeze
4 Thaw
(2 genotypes only to begin with)
5 Low Density Passaging
6 Single Cell Sorting
putative non-successfully edited
putative successfully edited
7 Clonal Expansion
8 Screen for desired clones and Freeze
PCR

Figure 2.2 Workflow for CRISPR-assisted integration of inducible-NGN2 donor DNA.

Dissociated iPSC lines (4 *APOE* genotypes) were individually electroporated with CRISPR gene-editing reagents (Cas9-sgRNA RNP) plus the donor DNA template (1). I treated with puromycin (2) then cryopreserved the cultures (3). Two iPSC lines (3/3 and KO) were thawed (4) and taken forward from this point by: passaging as single cells at low density under puromycin selection to further enrich for cells that incorporated puromycin resistance (5), single cell sorted via flow cytometry into 96-well formats to generate isolated clones from individual cells (6), expanded to generate identical sister plates (7) then, matching 96-well plates were either screened via PCR for successfully edited candidates or archived for subsequent recovery of the putative positive clones identified from screening (8).

2.3.2 Guide RNA solution: TrueGuide™ synthetic gRNA

The guide RNA with the sequence ACCCCACAGUGGGGCCACUA was designed to selectively target the AAVS1 safe harbor and was purchased from Invitrogen as a synthetic, modified, guide RNA in the TrueGuide™ Synthetic gRNA brand. It was synthesized as a single gRNA (sgRNA) molecule in which the crRNA and the tracrRNA (defined in Section **1.14.1**) are already fused via a molecular linker. This sgRNA was received in lyophilized form in a 1.5 mL microcentrifuge tube. I added TE buffer solution (Sigma-Aldrich, Inc.; Catalog # 93302) to the tube then vortexed and lightly centrifuged to collect the contents at the bottom of the tube, then incubated on the bench top for 30 minutes to allow the sgRNA oligos to dissolve. This generated the stock sgRNA solution at a concentration of 100 pmol/µL which was always handled in standard RNAse-free conditions. Dissolved sgRNA was either used immediately or stored in 10 µL aliquots at -20°C.

2.3.3 Homology-directed repair donor DNA template plasmid

The donor DNA template plasmid encoding inducible NGN2 was a gift from Biogen colleagues. The full transgene to be inserted into the AAVS1 locus consisted of the NGN2 cDNA cloned into the Tet-ON system. Figure 2.3 shows Tet-On 3G is driven by the CAG promoter and NGN2 is driven by the PTRE3GS promoter which becomes activated by doxycycline-bound Tet-On 3G. The DNA insertion cassette also includes a puromycin resistance gene (pac). The transgene is flanked by upstream and downstream sequences that overlap those of the AAVS1 locus offering the chance

that cells would use the exogenous sequence in the donor plasmid during HDR allowing its integration into the selected site.

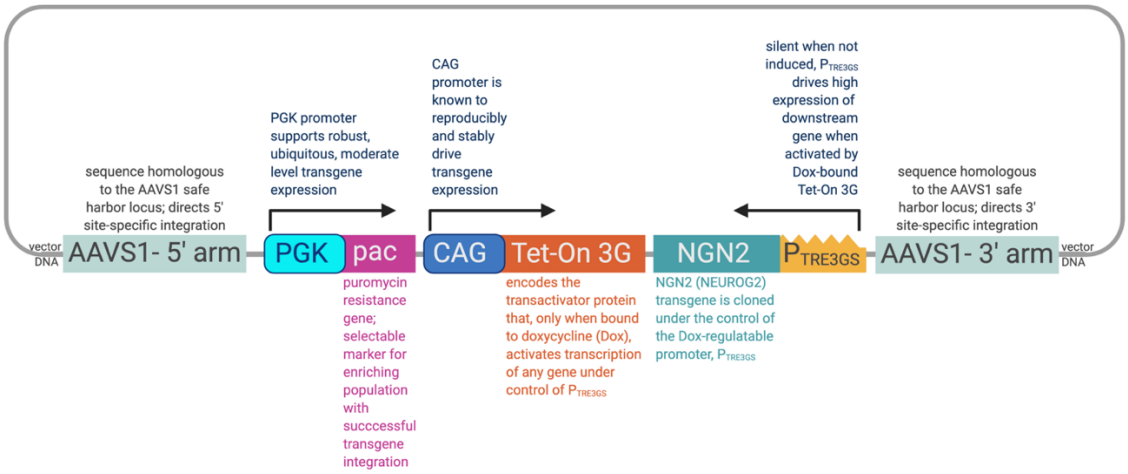

Figure 2.3 Schematic of the AAVS1 targeting vector which served as the donor DNA template for HDR after the genome is selectively cut by CRISPR/Cas9.

Rendering of the circular plasmid indicating the DNA cassette flanked by upstream (AAVS1-5' arm) and downstream (AAVS1-3' arm) sequences homologous to the AAVS1 safe harbor locus.

Further details which are important for design of the PCR screening strategy covered in Section 2.3.8 are shown in Figure 2.4. The sizes of various elements of the 6,722 base pair transgene cassette including the AAVS1 homology arms (HA) is depicted: 5' (659 bp) and 3' (837 bp) AAVS1 Has, a PGK promoter (487 bp) driving the puromycin resistance gene (600 bp), the CAG promoter (1786 bp), the Tet-On 3G transactivator (914 bp), and human NGN2 cDNA (819 bp) and the TRE3Gs promoter (365 bp). Figure 2.4 also shows that the transgene cassette was housed in a plasmid totaling 9,394 base pair in size.

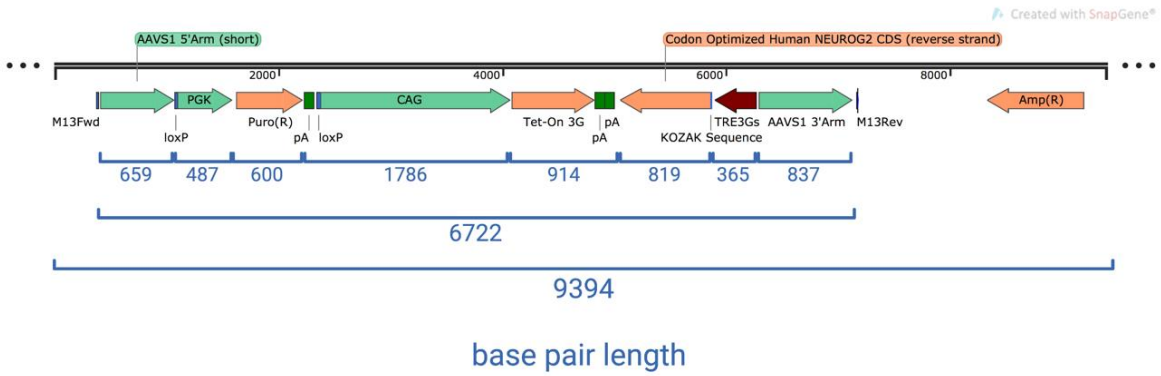

Figure 2.4 The sizes, in base pairs, of the elements of the HDR donor DNA plasmid.

This linear rendering of the 9.4 kb HDR plasmid indicates the sizes of various elements: 5' (659 bp) and 3' (837 bp) AAVS1 homology arms flanking a PGK promoter (487 bp) that drives a puromycin resistance gene (600 bp), a CAG promoter (1786 bp) that controls the Tet-On 3G transactivator (914 pb), and a human NGN2 cDNA sequence (819 bp) driven by the TRE3Gs promoter (365 bp).

2.3.4 Delivery of CRISPR editing reagents into iPSCs

2.3.4.1 Electroporation with the 4D-Nucleofector™ system

Destination plates for receiving the cells after electroporation were prepared by adding 1 mL per well of growth media (mTeSR™1) supplemented with 10 µM ROCKi to laminin-coated (Section 2.2.5) 6-well culture plates. Destination plates were kept in a 37°C incubator. The various transfection conditions that were utilized are tabulated in Table 2.5.

Table 2.5 Transfection conditions

Transfection condition	Transfection substrate	Purpose
Mock control 1	Cells transfected without Cas9 but with sgRNA	Monitor when to stop puromycin selection.
Mock control 2	Cells transfected without Cas9, without sgRNA, with the plasmid	Monitor when to stop puromycin selection.
GFP Negative control	pMAX GFP (Lonza) but no electroporation pulse	Assess transfection efficiency (without the use of RNPs).
GFP Positive control	pMAX GFP (Lonza)	Assess transfection efficiency (without the use of RNPs).
Experimental transfection	Cas9 complexed with targeting sgRNA AAV locus	Generate iN lines.

Nucleofector™ Supplement was added to the Nucleofector™ Solution (according to kit manufacturer's protocol) before use. RNP complexes (5:1 sgRNA to Cas9 ratio) were assembled according to the reaction volumes in Table 2.6 and were added to the reaction tube in the order,

top to bottom, listed. Importantly, the tube of reaction components was allowed to incubate for 10 minutes at room temperature before addition of plasmid DNA.

Table 2.6 Nucleofection reaction components

Component	Stock Concentration	Volume (1 reaction)
P3 Primary Cell Nucleofector™ Solution	-	22 µL
sgRNA	100 µM (pmol/µL)	1 µL (100 pmols)
Cas9 (Aldevron)	62 µM (62 pmol/µL)	0.33 µL (20 pmols)
DNA (such as HDR Template plasmid)	1ug/µL	2 µL (2 ug)
Total volume	-	25.33 µL

APOE variant iPSC cultures representing a common donor (non-AD individual) were dissociated into single cell suspensions using Accutase (Section 2.2.9), counted using the Nexcelom AOPI staining protocol (Section 2.2.10.1) and 5 x 10^5 viable cells/electroporation condition were aliquoted into a 50 mL conical tube and centrifuged at 90 x g for 5 minutes at room temperature. Supernatant was carefully removed from the cell pellets which were subsequently resuspended in the appropriate Nucleofector™ Solution + Substrate mix as indicated in Table 2.6.

Each electroporation reaction mix was put into a well of the Nucleocuvette™ 16-well strip. The Nucleocuvette™ strip was tapped on the benchtop to ensure that each sample covered the bottom of each well and that there were no bubbles in the wells. After pulsing (using the manufacturers preset program called “CA137”) the cells in the electroporator, the mixture was gently resuspended in pre-warmed mTeSR™ that included 10 µM ROCKi, mixed gently by pipetting up and down then transferred to the pre-warmed destination culture plates. Twenty-four hours post-electroporation, a full media change to mTESR1 was performed.

2.3.4.2 Electroporation with the Neon™ Transfection system

In a second approach, the Neon™ system was used. I thawed a fresh batch of *APOE* variant iPSCs derived from a common donor (non-AD individual). Representative photomicrographs from the thawed lines in culture are shown in Figure 2.5 at 2 days after thawing. I transfected the cultures

in proliferative phase when they had just reached 80% to 90% confluency (Figure 2.6).

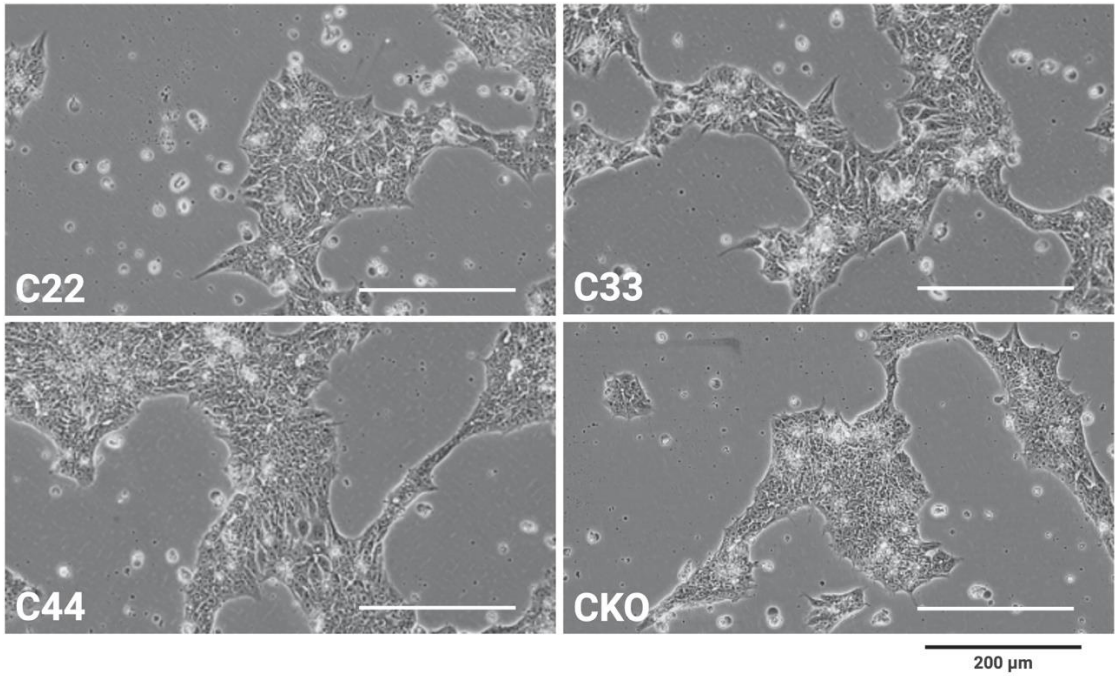

Figure 2.5 Representative images of iPSCs freshly thawed for Neon™ Transfection

Visualization of the freshly thawed batches of isogenic iPSCs (originating from an unaffected individual) at 2 days post-thaw: C22, C33, C44, and CKO (*APOE* null).

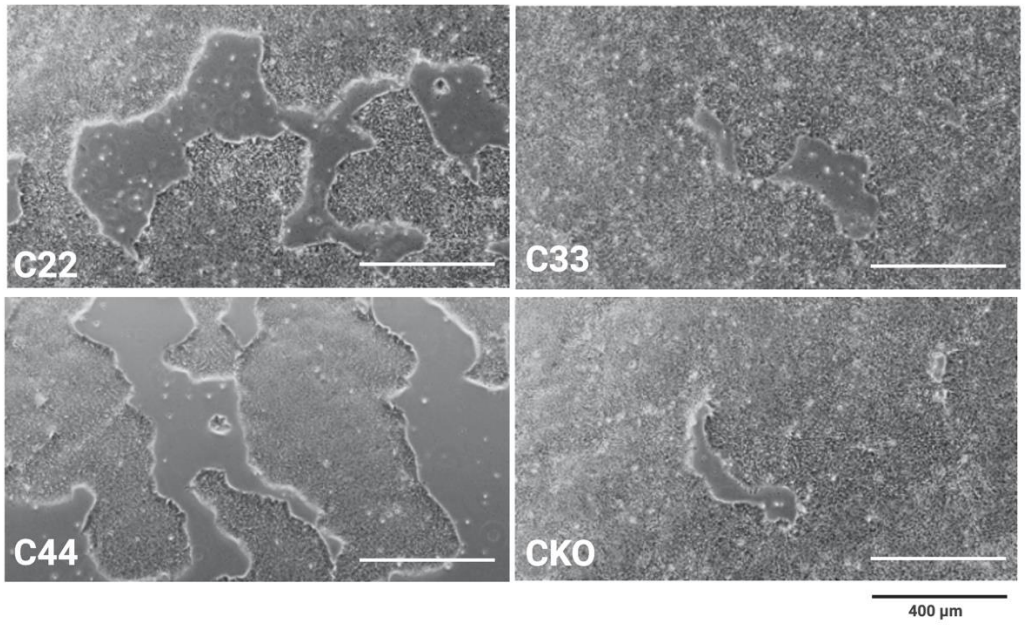

Figure 2.6 Representative images of iPSCs just prior to Neon™ Transfection

Visualization of the cultures from Figure 2.7 at the point when they were just about to be dissociated for electroporation: C22, C33, C44, and CKO (*APOE* null).

Destination plates for receiving cells immediately after electroporation were prepared by adding 1 mL mTeSR™1 (with 10 µM ROCKi) per well of a Matrigel-coated, 6-well cell culture plate per reaction and were put in a 37 °C tissue culture incubator until needed. The iPSCs to be electroporated were given fresh mTeSR™1 (containing 10 µM ROCKi) for 2 hours before transfection. The Cas9/sgRNA RNP mixture for Neon electroporation (in the manufacturer's 100 µL format system) was prepared according to the volumes shown in Table 2.7 and incubated on the bench top at room temperature for 10 minutes before use.

Table 2.7 Neon™ Transfection System reaction setup

Component	Stock Concentration	Volume (1 reaction)
R Buffer	-	62 µL
sgRNA	60 µM	2 µL
Cas9 (ThermoFisher)	5 µg/µL	3 µL
HDR Template plasmid	1ug/uL	3 µL
Total volume	-	70 µL

Cultures were dissociated into single cell suspensions using Accutase (Section 2.2.9), counted (Section 2.2.10.1), then 1.0 x 10^6 cells were transferred to a 15 mL conical tube and centrifuged at 800 rpm (120 g) for 5 minutes at room temperature. Cell pellets were then resuspended with gentle pipetting to obtain single cell suspensions in Resuspension Buffer R (from the Neon™ Transfection System kit) to a final cell density of 2.0 × 10^7 cells/ mL. The cell suspensions were then mixed with the RNP complex prepared above (Table 2.7) and 100 µL was loaded in a 100-µL Neon Tip and electroporated via the Neon™ Transfection System according to the manufacturer's instructions using Neon Program 7 (1200 V/30 ms/1 pulse). Electroporated cells were then dispensed into two wells of pre-warmed Matrigel-coated 6-well plates containing 4 mL of mTeSR™1 (supplemented with 10 µM ROCKi) and the plates were gently rocked back and forth to evenly distribute the cells in the wells. Plates were incubated at 37°C in a humidified 5% CO2 incubator and cells were allowed to recover for 48 hours without medium change.

2.3.5 Antibiotics selection

Three days post-electroporation puromycin selection was started by supplementing media with 100 ng/mL puromycin. On day 4 after electroporation, I performed a full media change and increased the puromycin concentration to 200 ng/mL.

2.3.6 Single cell cloning into 96-well plates via flow cytometry

Fresh mTeSR™ medium (10 µM ROCKi) was added to cells about 2 hours before cell sorting. Cloning medium and sorting medium were prepared according to Table 2.8. Electroporated cultures after plating and recovering were dissociated into a single cell suspension using Accutase (Section 2.2.9), counted (Section 2.2.10.1), then 1 x 10^6 cells were transferred to a 15 mL conical tube and centrifuged at 800 rpm (120 g) for 5 minutes at room temperature. Supernatant was aspirated and cell pellets were resuspended in 1mL of Sorting Medium (Table 2.8) using gentle pipetting to obtain a single cell suspension. Cells were sorted within 2 hours in a SONY SH800 cell sorter (Biogen cell sorting facility). Cells were dispensed into Matrigel-coated 96 well plates at 1 cell per well in 200ul of cloning medium (Table 2.8). A total of 5 plates were prepared per iPSC line, to yield about 480 single-cell clones per transfected line. Cells were left to recover in the cell culture incubator for 72 hours without medium change and after that, I refreshed the medium every 2 days (I replaced only half of the media at a time, i.e., 100 µL of fresh mTeSR™1 medium). Small iPSC colonies became visible under the microscope around 9 to 12 days after sorting.

Table 2.8 Single cell cloning via flow cytometry media recipes

Cloning Medium (100 mL)	
Component	**Volume**
mTeSR™1 medium	89 mL
CloneR™	10 mL
Penicillin-Streptomycin (10,000 units/mL)	1 mL
Sorting medium (10 mL)	
Component	**Volume**
mTeSR™1 medium	8 mL
KnockOut™ Serum Replacement	1 mL
CloneR™	1 mL
Penicillin-Streptomycin (10,000 units/mL)	100 µL
Rock Inhibitor (10mM stock)	10 µL

2.3.6.1 Sorting parameters

In collaboration with colleagues in Biogen's FACS facility, a Sony SH800S microfluidic flow sorting machine was used with sterile PBS as sheath fluid. Multiple gates were created (forwards scatter and side scatter gates) to eliminate debris. Further gating on forward versus side scatter (FSC vs SSC) singlets sorted single cells into 96 well plates containing 200 µL of cloning medium per well.

2.3.7 Splitting, freezing, and thawing of clones (96-well plate format)

Four weeks after single cell sorting, the clones in the 96-well plates were passaged with a split ratio of 1:2 to generate matching sister plates each containing a subculture of each clone. Eventually, 1 plate was used to make cell lysates for the initial PCR used to screen for putative positive clones (Section 2.3.8.1), while the other plate was frozen down to allow for recovery of candidate clones resulting from the primary screen. Revived clones from the frozen plate were subsequently investigated further in follow-up PCR assays (Section 2.3.8.3).

2.3.7.1 Splitting of cultures in a 96-well plate format

Destination 96-well plates pre-coated with Matrigel (Section 2.2.6) were prepared by adding 150 µL mTeSR1 with ROCKi (10 µM) per well and kept in a 37°C incubator. Culture media for the clones was removed from the wells via aspiration then the cells were washed with 100 µL PBS. After washing with at 30 µL per well of ReLeSR (Section 2.2.4), plates were incubated at 37°C for up to 10 minutes. During this time, cells were monitored periodically under a microscope for evidence of detachment. Once detached, 30 µL of mTESR1 was added per well and cells were resuspended by mixing through a P200 pipette tip. Half of the resultant cell suspensions each were then plated into sister wells of a pair of destination plates.

2.3.7.2 Freezing of cultures in a 96-well plate format

FBS containing 12.5% DMSO was used as freezing solution. Destination freezing plates were prepared by adding 120 µL of freezing solution to each well of a 96-well plate. Clones (resultant sister plates from Section 2.3.7.1), allowed to proliferate over several days to reach 50 to 80% confluency, were washed with PBS and 30 µL of Accutase (Section 2.2.9) was added per well, and plates were incubated at 37°C for up to 15 min while being checked for detachment under a microscope. Once detached, 30 µL of mTESR1 was added per well and cells were resuspended by mixing with a pipette and 30 µL of the cell suspension was transferred into the freezing plates containing the freezing solution. The plates were wrapped in Parafilm and put inside a Styrofoam box which was then placed in a -80°C freezer.

2.3.7.3 Thawing of cultures in a 96-well plate format

After the initial PCR screening (Section 2.3.8.1), plates containing candidate cell clones were removed from the -80°C freezer and placed in a 37°C incubator. When contents of the plates were thawed, plates were spun at 1200 rpm for 5 minutes. Freezing solution was removed using a 200 µL pipette. In only the wells containing the clones to be recovered, 100 µL of mTeSR1 with ROCKi was added and mixed with the pipette to resuspend the cells which then were transferred to a

new destination culture plate (96-well format). The destination plates utilized had been precoated with Matrigel™ (Section 2.2.6) and contained 80 µL mTeSR1 with ROCKi in each well and kept warm in a 37°C incubator.

2.3.8 PCR screening to identify successful CRISPR-edited NGN2 clones

I deployed several PCR assays in a stepwise fashion to investigate whether co-delivery of CRISPR/Cas9 gene editing agents alongside the HDR template DNA yielded the desired genomic modulation. The native AAVS1 allele was detected with the Locus PCR assay that utilized primer pair L-F and L-R (depicted on top in Figure 2.7) to yield an amplification product of 782 bp in size. In edited cells the Locus PCR assay would not yield any amplification product because the reaction extension time was weighted to prevent the amplification of the expected longer 1,600 bp product. The 5' INT PCR assay (with primer pair 5' F and 5' R) detected successful insertion of the transgene where its 5'-end joined with host genomic DNA (Figure 2.7; bottom left). Properly edited cells would be expected to generate a PCR amplicon of 898 bp in size, while native cells would yield no PCR product. The 3' INT PCR assay (with primers 3' F and 3' R) was designed to detect successful insertion of the transgene at the 3'-end where it connects with host genomic DNA to yield a PCR product of 1051 bp in size in edited cells and no product from native cells (Figure 2.7; bottom right).

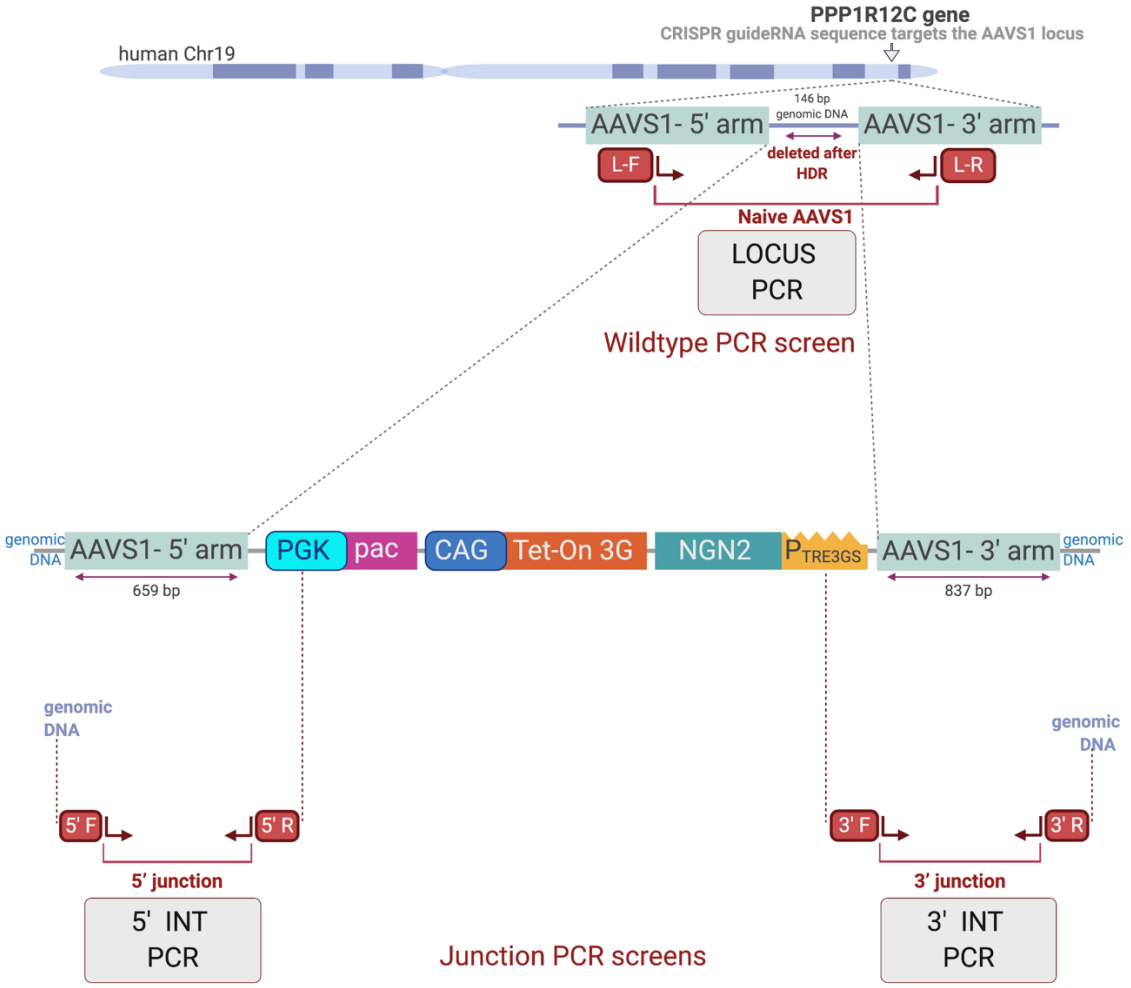

Figure 2.7 PCR assays for confirming successful targeted transgene integration.

Diagrammatic representation of the PCR-based approaches to screen for HDR of the NGN2 cassette into the AAVS1 one locus. Three PCR assays were used: the Locus PCR (top), the 5' INT PCR (bottom left) and the 3' INT PCR (bottom right).

2.3.8.1 Primary PCR screen to identify putative CRISPR-edited NGN2 clones

All clones isolated in the 96 well formats were initially screened with the 5' INT PCR assay (Figure 2.7). Clones were washed with PBS and lysed in 35 µL lysis buffer (25 mM NaOH, 0.2 mM EDTA, pH of 12). The lysis reaction was incubated at room temperature for 30 minutes, followed by a further 30-minute incubation at 95°C. At this point 35µL Neutralization buffer (40 mM Tris-HCL, pH of 5.0) was added per well. The contents and thermal cycling parameters of this PCR reaction are shown in Table 2.9.

Table 2.9 PCR reaction for initial 5' junction screening from cell lysates from 96-well format

PCR assay for clones using lysates from 96-well format and Taq PCR Core kit (Qiagen Cat # 201225)		
Component	**1 PCR reaction**	**Thermal cycling parameters**
10 x PCR buffer	2 µL	67°C for 10 cycles; 72°C for 24 cycles with extension for 45 seconds
Q buffer	4 µL	
DNTP (2.5 mM)	1 µL	
Taq (5 units/µL)	0.1 µL	
5' F (10 pM/µL)	1 µL	
5' R (10 pM/µL)	1 µL	
Cell lysate	1 µL	
Water	10 µL	
Total reaction volume	**20 µL**	

2.3.8.2 Positive control DNA template for the PCR screen

Genomic DNA purified from iNGN2-iPSC control line described in Section 3.1.5 was used as the positive control signal in the PCR screen. Ten nanograms of this gDNA was spiked into the lysate in well A1 of each 96-well plate (thus converting the lysate from 1 clone per plate from being a candidate to serve as an in-plate positive control in the screen).

2.3.8.3 Secondary PCR screen to validate hits from the primary screen

Putative candidate clones identified in the primary PCR screen (Section 2.3.8.1) from the sister plates that had been frozen (Section 2.3.7.2) were revived to reinitiate cultures (Section 2.3.7.3). I expanded them until there were enough cells to plate 3 wells of a 6-well plate. From one of these wells, genomic DNA (gDNA) was isolated using a DNeasy kit (Qiagen cat # 69504) according to the manufacturer's instructions. The quantity and purity of the extracted gDNA was assessed using a NanoDrop 2000 spectrophotometer (Thermo Fisher Scientific). Purified gDNA served as the PCR template for validation of correctly targeted insertions via the 3 PCR-based approaches shown in Figure 2.7. The PCR conditions using purified gDNA as template are shown in Table 2.10. The positive control signal for these PCR screens was generated using the gDNA described in Section 2.3.8.2.

Table 2.10 PCR reaction for validation of putative positive clones from purified gDNA template

PCR assay for verification using purified genomic DNA from putative positive clones and Q5 high fidelity Master Mix (New England Biolabs; M0492)	
Component	**1 PCR reaction**
Q5 2x Master Mix	25 µL
Forward primer (100µM) [0.5 µM final]	0.25 µL
Reverse primer(100µM) [0.5 µM final]	0.25 µL
gDNA template (100 ng/mL)	1 µL
Water	23.6 µL
Total reaction volume	**50**

Table 2.11 PCR primers list and sequences

PCR assays for genomic validation of CRISPR-mediated insertion of transgene cassette			
Application	**Primer name**	**Sequence (5' → 3')**	**Thermal cycling parameters**
Amplifying the 5' junction at both colony screening and verification stages (5' INT PCR)	5' F	GGAACTCTGCCCTCTAACGCT	30 sec at 98°C; 35 x [98°C for 10 sec, **71°C** for 30 sec, 72°C for 25 sec]; 2 min at 72°C
	5' R	TGGATGTGGAATGTGTGCGA	
Amplifying the 3' junction at the colony verification stage (3' INT PCR)	3' F	GATAGGGAGACCCGCCACCTAA	30 sec at 98°C; 35 x [98°C for 10 sec, **67°C** for 30 sec, 72°C for 25 sec]; 2 min at 72°C
	3' R	GAGTGAGTTTGCCAAGCAGTCA	
Amplifying the wildtype, non-integrated AAVS1 site at the colony verification stage (Locus PCR)	L-F	CACGTGATGTCCTCTGAGCGG	
	L-R	CTCTGGCTCCATCGTAAGCAAAC	

Sequences of the screening PCR primers and the thermal cycling parameters used in the confirmation screen are listed in Table 2.11. Primers were synthesized by the Integrated DNA Technologies Corporation (Coralville, Iowa, USA) and I received 100 µM solutions. Following amplification, PCR products were electrophoresed on a 2% agarose gel (E-Gel Precast Agarose Electrophoresis System, Invitrogen) to visualize amplification of a single band of the correct size.

2.4 Lentiviral-Mediated NGN2 induction

2.4.1 Lentiviral Vectors

Lentiviral vectors were a gift from Biogen colleagues. These vectors were engineered to resemble those described and previously used by others (151). The vector, LV-rtTA, drives constitutive expression of reverse tetracycline transactivator (rtTA), under the UbC promoter (Figure 2.8, A). The LV-iNgn2/pac vector drives doxycycline-inducible expression of Ngn2 under the control of a TetO promoter. Its design incorporates a T2A linker in-between 2 distinct cDNA sequences to allow translation of 2 discreet proteins from a single mRNA. The inducible puromycin resistance gene co-expressed from the same promoter that drove expression Ngn2 allowed for selection of cells expressing only the inducible Ngn2 (Figure 2.8 B) (151). To give the approach further flexibility, inducible EGFP expressed from a separate viral construct, LV-iEGFP (Figure 2.8, C) provided a monitoring control condition in triple transduced cells. Ultra-high titer (>1x10^9 IFU/mL) viral stock preparations were packaged and concentrated by ALSTEM, LLC (Richmond, CA, USA). Transduction efficiency was not measured directly however was visually estimated based on the percentage of cells that initially express EGFP upon induction.

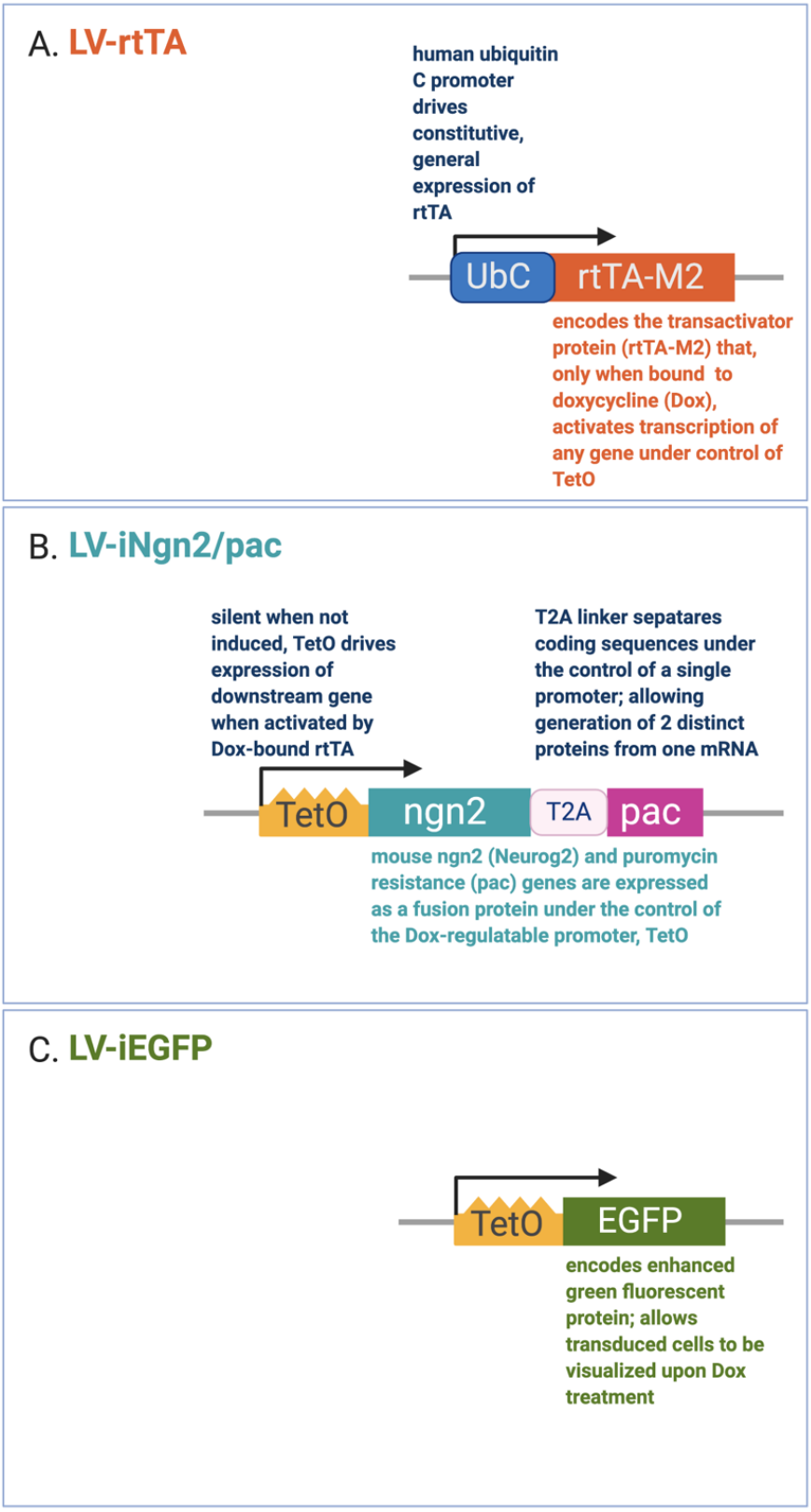

Figure 2.8 Lentiviral constructs for stable inducible Ngn2 transgene integration.

Schematic of the functional elements of the lentiviral vectors used to transduce iPSCs. (A) The LV-rtTA construct expresses the rtTA transactivator under the control of a constitutively active promoter, UbC. (B) The LV-iNgn2/pac construct expresses Ngn2 and pac genes under the control of the doxycycline-inducible TetO promotor. (C) LV-iEGFP expresses EGFP in an inducible manner under the control of a TetO promotor.

2.4.2 Lentiviral transduction and banking of transduced isogenic iPSC lines

The 8 iPSC lines introduced in the blue rows of Table 2.1 were thawed (Section 2.2.8) and each plated into 3 wells of a Matrigel™-coated 6-well plate (Section 2.2.6). Once cells were ~75% confluent, they were passaged at a 1:6 splitting density into 6 wells of a Matrigel™-coated 12 well-plate. The media was replaced after 48 hours with 1 mL of media containing lentivirus. This was prepared at 3.3 µL/well of each viral stock in fresh mTeSR™1 medium containing polybrene (5 µg/µL, Sigma) as shown in Table 2.12. Because cells were transduced as colonies of tightly packed cells which had been passaged as clumps, I do not have an estimation of the multiplicity of infection (MOI) of the virus at this point (this can be estimated in the future by dissociating a representative well of cells at the time of a transduction experiment and counting single cells).

Plates were incubated at 37°C for 24 hours, after which, media containing viruses was removed by performing a full media change with fresh complete mTeSR™1. The 8 lines were co-transduced in 2 formats: with only 2 vectors, LV-rtTA and LV-iNgn2/pac, or, with all 3 vectors to yield a total of 16 transduction samples. Once cells were about 80% confluent, they were passaged into full 6-well plates, using ReLeSR to lift cells (Section 2.2.4). When cultures in the 6-well plates were ~75% confluent, they were frozen down in mFreSR at a density of 2 wells/vial to serve as an iPSC bank conducive to neuronal differentiation for future work. The cryovials were labelled “Day 0 Ngn2”.

Table 2.12 Lentivirus transduction mixtures

Component	Volume (for a single 12 well plate; 6 mL)	Volume (for a single 12 well plate; 6 mL)	Titer
Complete mTeSR medium	6 mL	6 mL	Ultra-high titer (>1x10^9) IFU/mL packaged and concentrated by ALSTEM, LLC (Richmond CA, USA)
LV-iNgn2/pac	20 µL	20 µL	
LV-rtTA	20 µL	20 µL	
LV-iEGFP	none	20 µL	
Polybrene (sigma; 10 mg/mL)	3 µL [5 µg/mL final]	3 µL [5 µg/mL final]	

2.4.3 Generation of induced neurons (iNs) from NGN2-lentiviral transduced isogenic iPSCs

2.4.3.1 Initial testing (Chapter 4)

One cryovial of transduced iPSCs labelled “Day 0 Ngn2” (Section 2.4.2) was thawed and the iPSCs evenly distributed into 3 wells of a Matrigel™-coated 6-well plate in 2 mL per well complete mTeSR™1 medium. The various media recipes used for the next steps are shown in Table 2.13 and Table 2.14. When cultures became ~60% confluent, the medium was switched to KSR-containing doxycycline. The addition of doxycycline timestamped the cultures as Day 1 of neuronal induction (iN Day 1) medium (Table 2.14). After 24 hours, the medium was switched to Day 2 medium

(Table 2.14). After another 24 hours, the medium was replaced with Day 3 medium (Table 2.14). After another 24 hours, the medium was replaced with Day 4 medium to facilitate neuronal maintenance (Table 2.14). After another 24 hours, the medium was replaced with Day 5+ medium, at which point doxycycline administration and puromycin selection were stopped (Table 2.14). After day 5, half of the medium is to be exchanged every other day with Day 5+ medium in order to keep the iN cultures going, however, I harvested cells at Day 6 for preliminary investigation of neuronal identity (transcriptional profiling of select neuronal markers via RT-PCR; Section 2.5.2).

Table 2.13 Precursor media recipes for differentiation of neurons from lentiviral transduced iPSCs

Base media for doxycycline induction and differentiation in the lentivirus-mediated editing workflow			
KSR Medium			
Component	**Final Concentration**	**Source (catalog #)**	**Example Volume**
DMEM/F-12 (Dulbecco's Modified Eagle Medium/Nutrient Mixture F-12)	n/a	ThermoFisher Scientific (10565-018)	415 mL
Knockout™ Serum Replacement (KOSR) (100% stock)	15%	ThermoFisher Scientific (10828028)	75 mL
MEM Non-Essential Amino Acids Solution (MEM NEAA) (100x stock)	1x	ThermoFisher Scientific (11140050)	5 mL
β-mercaptoethanol (50 mM)	0.05 mM	ThermoFisher Scientific (31350010)	0.5 mL
Gibco® GlutaMAX™ (100x stock)	1x	ThermoFisher Scientific (35050-061)	5 mL
N2 Medium			
Component	**Final Concentration**	**Source (catalog #)**	**Example Volume**
DMEM/F-12 (Dulbecco's Modified Eagle Medium/Nutrient Mixture F-12)	n/a	ThermoFisher Scientific (10565-018)	500 mL
Gibco® GlutaMAX™ (100x stock)	1x	ThermoFisher Scientific (35050-061)	5 mL
Dextrose (45% in water)	0.3%	Sigma (G8769)	3.3 mL
N2 supplement (100x)	1x	ThermoFisher Scientific (17502-048)	5 mL
B27 without Vitamin A (50x)	1x	ThermoFisher Scientific (12587010)	10 mL
Neurobasal Medium (NBM)			
Component	**Final Concentration**	**Source (catalog #)**	**Example Volume**
Neurobasal™ Medium	n/a	ThermoFisher Scientific (21103-049)	485 mL
Gibco® GlutaMAX™ (100x stock)	1x	ThermoFisher Scientific (35050-061)	5 mL
Dextrose (45% in water)	0.3%	Sigma (G8769)	3.3 mL
MEM Non-Essential Amino Acids Solution (MEM NEAA) (100x stock)	1x	ThermoFisher Scientific (11140050)	2.5 mL

Table 2.14 Media recipes for differentiation of neurons from Ngn2-lentiviral transduced iPSCs

Day	Component	Final Concentration	Example Volume
Day 1 medium	KSR Medium (DMEM/F-12 , 15% v/v KOSR, 1x glutaMAX, 100 µM MEM NEAA , 0.05 mM β-mercaptoethanol)	n/a	50 mL
	LDN193189 (Catalog # 72149; STEMCELL Technologies Inc.; 10mM stock in DMSO)	1 µM	5 µL
	XAV939 (Catalog # 72674; STEMCELL Technologies Inc.; 20mM stock in DMSO)	4 µM	10 µL
	SB431542 (Catalog # 72234; STEMCELL Technologies Inc.; 20mM stock in DMSO)	10 µM	25 µL
	Doxycycline Hyclate; (Catalog #D9891; Sigma; 100mg/mL in water)	2 µg/mL	1 µL
Day 2 medium	Day 1 Medium (above)	50%	25 mL
	N2 Medium (recipe in table above)	50%	25 mL
	Doxycycline Hyclate; (Catalog #D9891; Sigma; 100mg/mL in water)	2 µg/mL	1 µL
	Puromycin (Catalog # A1113803; Gibco 1 mg/mL)	200 ng/mL	
Day 3 medium	N2 Medium (recipe in table above)	n/a	50 ml
	B27 without Vitamin A (Catalog # 12587010; ThermoFisher Scientific; 50x stock)	0.5X	500 µL
	BDNF (human) (Catalog # 2837; R&D Systems; 0.1mg/mL)	10 ng/mL	5 µL
	CNTF (human) (Catalog # 257-NT; R&D Systems; 0.1mg/mL)	10 ng/mL	5 µL
	GDNF (human) (Catalog # 212-GD; R&D Systems; 0.1mg/mL)	10 ng/mL	5 µL
	Doxycycline Hyclate; (Catalog #D9891; Sigma; 100mg/mL in water)	2 µg/mL	1 µL
	CultureOne™ Supplement (Catalog # A3320201; ThermoFisher Scientific; 100x stock)	1X	500 µL
	Puromycin (Catalog # A1113803; Gibco 1 mg/mL)	200 ng/mL	100 µL
Day 4 medium	NBM (table above)	n/a	50mL
	Penicillin Streptomycin (Catalog # 15140122; Thermo Fisher ; 10,000Unit/mL)	100 U/mL	500µL
	B27 without Vitamin A (Catalog # 12587010; ThermoFisher Scientific; 50x stock)	0.5X	500µL
	BDNF (human) (Catalog # 2837; R&D Systems; 0.1mg/mL)	10 ng/mL	5µL
	CNTF (human) (Catalog # 257-NT; R&D Systems; 0.1mg/mL)	10 ng/mL	5µL
	GDNF (human) (Catalog # 212-GD; R&D Systems; 0.1mg/mL)	10 ng/mL	5µL
	Doxycycline Hyclate; (Catalog #D9891; Sigma; 100mg/mL in water)	2 µg/mL	1µL
	CultureOne™ Supplement (Catalog # A3320201; ThermoFisher Scientific; 100x stock)	1X	500µL
	Puromycin (Catalog # A1113803; Gibco 1 mg/mL)	200 ng/mL	
Day 5+ medium	NBM (recipe in table above)	n/a	50mL
	Penicillin Streptomycin (Catalog # 15140122; Thermo Fisher ; 10,000Unit/mL)	100 U/mL	500µL
	B27 without Vitamin A (Catalog # 12587010; ThermoFisher Scientific; 50x stock)	0.5X	500µL
	BDNF (human) (Catalog # 2837; R&D Systems; 0.1mg/mL)	10 ng/mL	5µL
	CNTF (human) (Catalog # 257-NT; R&D Systems; 0.1mg/mL)	10 ng/mL	5µL
	GDNF (human) (Catalog # 212-GD; R&D Systems; 0.1mg/mL)	10 ng/mL	5µL
	CultureOne™ Supplement (Catalog # A3320201; ThermoFisher Scientific; 100x stock)	1X	500µL

2.4.3.2 Four-week time course characterization (Chapter 5)

The procedure to drive neuronal induction based on the lentiviral-mediated NGN2-induction platform was further optimized for the experiments in Chapter 5. In these experiments, I simultaneously characterized iN differentiation and maturation in the isogenic AD-associated cell lines of distinct *APOE* genotypes listed in Table 2.15. When comparing iPSC lines simultaneously, the "Day 0 Ngn2" (Section 2.4.2) transduced lines were thawed, in parallel, into Matrigel™-coated 6-well plates and expanded until 70-90% confluency. They were then dissociated into single cells and replated at 1 x 10^6 cells/well 6-well-plate (again, on Matrigel) in the presence of the anti-apoptotic, ROCKi, and this time point was designated Day -1. In parallel, 0.035 x 10^6 iPSCs were seeded per well for 3 wells of a 96-well plate and collected 24 hours later to serve as the iPSC (iN0) counterparts in the transcriptional profiling experiments. For the iPSCs in the 6-well plates, doxycycline treatment was started 24 hours after seeding, marking the culture as Day 0 or "iN0". Twenty-four hours following the start of doxycycline treatment, puromycin selection was started. Three days following the start of doxycycline treatment, the cultures were dissociated into single cells then plated at 0.035 x 10^6 cells/well in a 96-well plate format, on PDL. These iN3 cells were

distributed amongst multiple plates such that one plate per time-point could be harvested without disturbing any cultures designated for a subsequent collection timepoint. The next day, iN4 cells were harvested. To mitigate against occasional undifferentiated, proliferating cells remaining in the cultures after puromycin selection potentially dividing and overtaking the long-term cultures, I pulsed the cultures with an antimitotic agent, β-D-arabinofuranoside (AraC), for 24 hours, from iN6 to iN7. At iN7, I changed the culture media in full to remove araC and maintained the cultures until iN28 by changing half the growth media every 7 days. The stars in Figure 5.1 represent progression points along the process at which I collected samples. I assayed ATP levels with the intention of using this assessment as a quantitative value validating whether the cultures had been evenly plated across *APOE* genotypes (iN4 determination) and were progressing the same way metabolically as the cultures matured. The results in Chapter 5 were generated from 3 independent differentiation and maturation (through iN28) experiments. I used 3 culture wells (technical replicates) per experiment for evaluation of transcription (high throughput protocol in Section 2.5.4) and ATP levels (Cell Titer Glo assay; Section 2.5.5). Representative morphological changes across culture period were documented using the EVOS FL imaging system (ThermoFisher Scientific) from a different set of wells. Figure 2.9 shows my plate layout for generating samples the time course assessments.

Table 2.15 Cell lines simultaneously characterized for evaluating *APOE* status on iN culture differentiation and maturation

iPSC line name	APOE status	Original donor line	Donor age at biopsy	Sex	NGN2-editing strategy
A22-NGN2-G	ε2/ε2	UKBi011-A (APOE ε4/ε4) derived from an individual with AD	80	Male	Lentiviral-mediated
A33-NGN2-G	ε3/ε3				
A44-NGN2-G	ε4/ε4				

Table 2.16 Series of media changes, highlighting key steps, during the conversion of iPSCs to neurons and 4-week maturation time course

Optimized Media Schedule I used for Chapter 5 experiments	
Reagents	**Final concentration**
Day -1 media (Thaw vial of transduced iPSCs into 6-well plates)	
mTeSR Plus+ supplement	
10 mM ROCKi	10 µM
Day 0 media (Add doxycycline)	
N2/B27 media without Culture 1 (Recipe in Table 2.3)	
200 mM Ascorbic acid	200 µM
1 mM cAMP	1 µM
10 mg/mL Dox	1 ug/mL
Day 1 and 2 media	
N2/B27 media	
200 mM Ascorbic acid	200 µM
1 mM cAMP	1 µM
10 mg/mL Dox	1 ug/mL
10 mg/mL Puromycin	2000 then 2500ng/mL
iN3 dissociation and re-plating media (35,000 cells/96-well plate)	
N2/B27 media	
200 mM Ascorbic acid	200 µM
1 mM cAMP	1 µM
10 mg/mL Dox	1 ug/mL
10 mg/mL Puromycin	2500 ng/mL
BDNF	10ng/mL
GDNF	10ng/mL
iN4 full media change (100µL/96-well plate)	
N2/B27 media	
200 mM Ascorbic acid	200 µM
1 mM cAMP	1 µM
10 mg/mL Dox	1 ug/mL
BDNF	10ng/mL
GDNF	10ng/mL
iN6 Add AraC 2x (100µL/96-well plate)	
N2/B27 media	
200 mM Ascorbic acid	200 µM
1 mM cAMP	1 µM
10 mg/mL Dox	1 ug/mL
BDNF	10ng/mL
GDNF	10ng/mL
AraC stock 20mM	5 µM
iN7 After 24HR AraC-- full media change (100µL/96-well plate)	
N2/B27 media	
200 mM Ascorbic acid	200 µM
1 mM cAMP	1 µM
10 mg/mL Dox	1 ug/mL
BDNF	10ng/mL
GDNF	10ng/mL
iN14 half-media change and every week thereafter (50µL/96-well plate)	
N2/B27 media	
200 mM Ascorbic acid	200 µM
1 mM cAMP	1 µM
BDNF	10ng/mL
GDNF	10ng/mL

Plate layout for maturity time course (photomicrography, RT-PCR, and ATP measurements)												
	no cells	APOE**22** (35K cells/well)			APOE**33** (35K cells/well)			APOE**44** (35K cells/well)			no cells	
	1	2	3	4	5	6	7	8	9	10	11	12
A												
B												
C												
D												
E												
F												
G												
H												

Figure 2.9 96-well culture plate layout for generating time course samples for photomicrography, and transcript and ATP measurements.

Schematic of the 96-well plate layout from which samples were generated for the characterization of iN morphology, select transcripts, and ATP levels over time (Results in Chapter 5). Each APOE-variant line was plated at 35,000 cells/well for a total of 9 wells; creating the source cells for 3 technical replicates per technique. Multiple plates were seeded at the same time. Afterwards, one plate per time point (to demonstrate the following days post neuronal induction: 0, 4, 7, 14, 21, and 28) was harvested. Row B was committed to imaging. Row C was used for ATP measurements. Row D was lysed and stored for transcriptional analysis of select genes which was performed at the end of collection of all plates per experimental round. The wells that did not receive cells contained PBS.

2.4.4 Kainic acid challenges (Chapter 6)

To initiate excitotoxic stress, cultures were challenged with Kainic acid (KA) (Tocris Bioscience cat # 0222). KA was prepared as a stock 25 mM solution in sterile water and 150µL aliquots were stored at -80 °C. KA treatment was done by adding varying concentrations of KA to the cultures for varying timepoints, as indicated. Prior to each experiment (at iN28 culture age), a fresh 25 mM aliquot solution of KA was thawed and diluted with culture media that was already equilibrated to 37 °C to create 2× working stocks. 100uL of the 2x KA solutions were added into the cultures which contained 100 µL volume of media; vehicle controls received an equal volume of sterile water diluted in the same manner as KA stock solution. Vehicle control was 1.2% water in the time course experiments looking at 30 and 300 µM KA. In the 6-hour experiment with only 30 µM concentration, the vehicle control was 0.12% water.

2.5 Molecular Methods

2.5.1 Quantity and quality of extracted DNA and RNA assessment

The quantity and purity of DNA or RNA extracted from cells was assessed using a NanoDrop 2000 spectrophotometer (Thermo Fisher Scientific). The type of nucleic acid (RNA or DNA) to be

analyzed was selected on the Nanodrop software and the instrument was blanked with 2 µL of the solvent in which the samples were eluted (e.g., TE buffer or water). Sample (2 µL each) spectra were measured, and the instrument software was used to calculate concentration and the ratios of absorbance at both 260 and 280 nm as well as at 260 and 230 nm. For the 260/280 ratio my cutoff for acceptable quality for use was 1.5 for DNA and 1.7 for RNA.

2.5.2 Reverse transcription-polymerase chain reaction (RT-PCR)

Cells in the 6-well plate formats (Chapter 4) were subjected to RNA extraction using the RNeasy Mini Kit (Qiagen) as described by the manufacturer. The quantity and purity of the extracted RNA was assessed using a NanoDrop 2000 spectrophotometer (Section 2.5.1) and 1 or 2 µg of total mRNA was converted to cDNA using the SuperScript™ VILO™ cDNA Synthesis Kit (Thermo Fisher Scientific) as indicated by the manufacturer's instructions. The composition of each 20 µL cDNA reaction mix is indicated in Table 2.17. Reverse transcription-polymerase chain reaction (RT-PCR) using these cDNA templates was executed using TaqMan Fast Advanced Master Mix from Thermo Fisher Scientific. The composition of each 5 µL RT-PCR reaction mix is shown in Table 2.18. Alternatively, when cells were cultured in the miniaturized 96-well setting, cDNA synthesis and RT-PCR were performed in a single reaction mix described in Section 2.5.4.

Table 2.17 cDNA synthesis reaction components

cDNA synthesis reaction; (1 hour at 42°C)	
Component	**1 reaction**
SuperScript® VILO™ Master Mix (ThermoFisher Scientific; 11755-500)	4uL
RNA (1 or 2 µg)	x uL
nuclease-free water	To 20uL

Table 2.18 RT-PCR reaction components

RT-PCR using synthesized cDNA and 20x TaqMan assay mix (5 µL reaction volume)	
Component	**1 reaction**
2x TaqMan fast advance Master Mix (ThermoFisher Scientific; 4444556)	2.5 µL
TaqMan gene expression assay (20x)	0.25 µL
TaqMan GAPDH endogenous control (20x)	0.25 µL
cDNA template from above SuperScript® VILO™ synthesis reaction	2 µL

Indicated target genes were amplified utilizing FAM dye-labelled TaqMan™ gene expression assays (Thermo Fisher Scientific), utilizing oligonucleotides designed by the manufacturer (Table 2.19). Each RT-PCR reaction was duplexed with a GAPDH TaqMan™ assay (labelled with VIC dye) which provided in-well endogenous control gene amplification. Quadruplicate RT-PCR reactions were carried out in a QuantStudio12 PCR machine (Thermo Fisher Scientific) and the thermal cycling parameters were: 95°C for 20 seconds, 40x (95°C for 1 second, 60°C for 20 seconds). The

Ct values of the genes of interest were normalized to those of the GAPDH housekeeping gene. Where indicated, relative mRNA levels were then further compared to a baseline or non-treated sample.

Table 2.19 TaqMan™ assays (ThermoFisher Scientific) for RT-PCR

Gene Symbol	Gene Name	Taqman™ Assay ID
ATF4	activating transcription factor 4 (CREB2)	Hs00909569_g1
APOE	Apolipoprotein E	Hs00171168_m1
APP	Amyloid beta precursor protein	Hs00169098_m1
BDNF	Brain Derived Neurotrophic Factor	Hs02718934_s1
CLU	Clusterin (Apolipoprotein J)	Hs00156548_m1
FOS	Fos proto-oncogene	Hs99999140_m1
GAP43	Growth associated protein 43	Hs00967138_m1
GFAP	Glial Fibrillary Acidic Protein	Hs00909233_m1
GRIA3	Glutamate ionotropic receptor AMPA type subunit 3	Hs01557466_m1
GRIK1	Glutamate ionotropic receptor kainate type subunit 1	Hs00543710_m1
GRIN2D	Glutamate ionotropic receptor NMDA type subunit 2D	Hs00181352_m1
GRM1	Glutamate metabotropic receptor 1	Hs00168250_m1
GSK3B	Glycogen synthase kinase 3 beta	Hs01047719_m1
LRP1	LDL receptor related protein 1	Hs00233856_m1
MAP2	Microtubule Associated Protein 2	Hs00258900_m1
MAPT	Microtubule Associated Protein Tau	Hs00902194_m1
MYC	v-myc avian myelocytomatosis viral oncogene homolog (c-Myc)	Hs00153408_m1
NEUROG2	Neurogenin 2 (NGN2)	Hs00935087_g1
NGFR	Nerve Growth Factor Receptor	Hs00609976_m1
SLC17A6 (VGLUT2)	Solute carrier family 17 member 6 (vesicular glutamate transporter type 1)	Hs00220439_m1
SLC17A7 (VGLUT1)	Solute carrier family 17 member 7 (vesicular glutamate transporter type 1)	Hs00220404_m1
SV2B	Synaptic vesicle glycoprotein 2B	Hs00208178_m1
SYP	Synaptophysin	Hs00300531_m1

2.5.3 *APOE* Variant Genotyping

Commercial SNP genotyping assays (ThermoFisher TaqMan™) were used to verify the *APOE* genotype of the iPSC lines. Each SNP assay contains two probes, each specific for one of the SNP alleles and labelled with a distinct fluorescent dye, either VIC or FAM. The presence of the allele (or both alleles for heterozygotes) is signaled by the probe's corresponding fluorescence as listed in Table 2.20.

Table 2.20 *APOE* SNP genotyping assays

Gene location (Ensembl coordinates)	19:45411941	19:45412079
SNP ID	rs429358	rs7412
Gene position (amino acid position)	3937 (112)	4075 (158)
TaqMan Assay ID	C___3084793_20	C____904973_10
APOE2 [VIC/FAM] codon context (amino acid)	**[C/T]**GC (Cys)	**[C/T]**GC (Cys)
APOE3 [VIC/FAM] context (amino acid)	**[C/T]**GC (Cys)	**[C/T]**GC (Arg)
APOE4 [VIC/FAM] context (amino acid)	**[C/T]**GC (Arg)	**[C/T]**GC (Arg)

Genomic DNA was extracted using the Dneasy Mini Kit (Qiagen) as described by the manufacturer. The quantity and purity of the extracted DNA was assessed using a NanoDrop 2000 spectrophotometer (Section 2.5.1) and 12 ng of gDNA was subjected to genotyping by PCR reaction. The composition of each 10 µL PCR reaction mix is shown in Table 2.21. Triplicate PCR reactions were carried out in a QuantStudio12 PCR machine (Thermo Fisher Scientific) and the thermal cycling parameters were: 50^{o}C for 2 minutes, 95^{o}C for 10 minutes, 40 x (95^{o}C for 15 second, 60^{o}C for 60 seconds). I viewed the allelic discrimination plots and chose the automatic method of SNP calling by the QuantStudio software.

Table 2.21 *APOE* SNP genotyping PCR reaction components

Component	µL
TaqMan Gene expression Master Mix (2×) Catalog number: 4369016	5.00
TaqMan genotyping assay mix (40×)	0.25
Dnase-free, Rnasefree water	0.00
Volume of DNA Sample in Water Per Reaction (2.4 ng/µL)	4.80
Total volume of reaction per 384-well	10.05

2.5.4 High throughput targeted transcript profiling (Chapter 5)

To achieve higher throughput of transcriptional profiling for the time course described in Chapter 5, I used a protocol designed to take cells from lysates directly to real-time analysis; eliminating the traditional RNA purifications (175). As such, I worked with three cell lines in parallel, each featuring six differentiation timepoints in three technical replicates (three wells of 96-well plate) and three biological replicates (three independent rounds of differentiation experiments).

I used the Cells-to-C$_T$ 1-Step TaqMan® Kit (Thermo Fisher Scientific Inc., Waltham MA, USA) workflow, with minor modifications to the manufacturer's instructions, depicted in Figure 2.10. Essentially, immediately after having washed the cells (from Section 2.4.3.2 which had been plated earlier in 96-well plates at 35,000 cells per well) with 100 µL of PBS, I added 50 µL of lysis buffer freshly supplemented with DNAse (supplied in the kit) per well to the cells. The plates containing lysis buffer were

then shaken for 12 minutes at room temperature (19 – 25 °C) after which 5 µL of stop solution was added and the plates were shaken for 2 - 5 min to inhibit the DNAse, then immediately stored at -80 °C. The complete 4-week time course was collected and stored at -80 °C prior to analysis. I assembled the TaqMan® 1-Step qRT-PCR Mix with TaqMan® Gene Expression Assay (selected from Table 2.19) according to the volumes in

Table 2.22. These incubations were vortexed for 5–10 seconds to mix before using the reactions utilizing PCR cycling conditions depicted in Table 2.23. Two-way ANOVA with Dunnett's posttest was performed on the relative mRNA expression to GAPDH from 3 independent rounds of differentiations (each with 3 biological replicates) using GraphPad Prism Software.

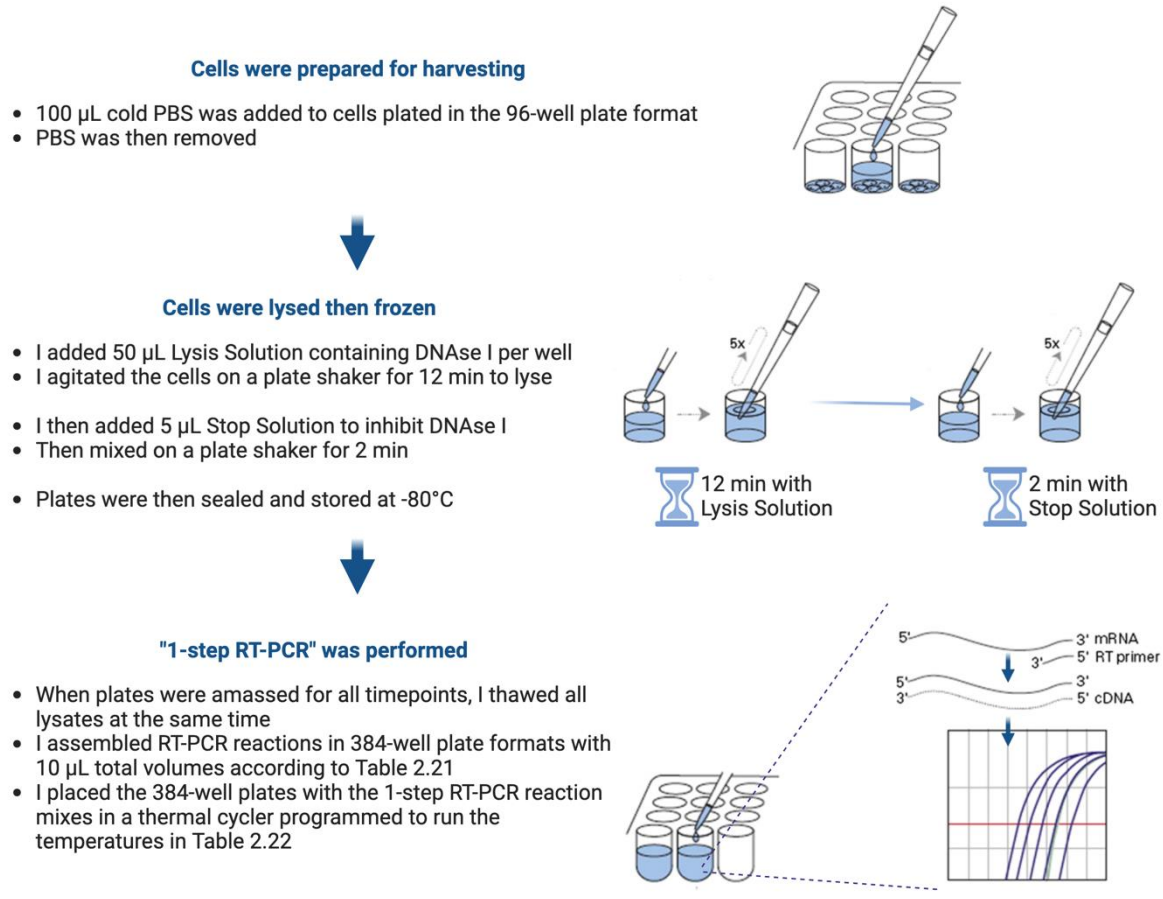

Figure 2.10 Depiction of the Cells-to-C_T workflow.

Schematic of the Cells-to-CT workflow that generates RT-PCR readouts directly from cell lysate without RNA purification and separate cDNA generation reactions; adapted from Abruzzese *et al*. (175).

Table 2.22 RT-PCR reaction components for Cells-to-CT 1-Step TaqMan® Kit

Component	µL
TaqMan® 1-Step qRT-PCR Mix	2.5
TaqMan® Gene Expression Assay (from Table 2.19) FAM dye formulation (20×)	0.5
Human GAPDH Endogenous Control (VIC™/TAMRA™ probe, primer limited) (20×)	0.5
Dnase-free, Rnasefree water	5.5
Volume of thawed cell lysate (30,000 cells in 50 µL lysis buffer)	1
Total volume of reaction	10.0

Table 2.23 Cycling Parameters for Cells-to-CT 1-Step TaqMan® Kit

Step	Number of cycles	Temperature ; °C	Time
Reverse transcription	1	50	5 min
RT inactivation/initial denaturation	1	95	20 sec
Amplification	40	95	3 sec
		60	30 sec

2.5.5 Adenosine triphosphate (ATP) assay protocol

The CellTiter-Glo® luminescent cell viability assay (Promega, catalog number: G7571) was performed with slight modification from the manufacturer's instructions. Briefly, cells were plated in triplicate at 35, 000 cells/well as described above. At the indicated developmental time point cells were rinsed with 100 µL PBS, lysed in 50 µL CellTiter-Glo reagent diluted 1:1 in PBS, and shaken on an orbital shaker for 12 minutes. 30 µL of the lysed cells were transferred to a new multiwell plate (Corning™ 4512) and then incubated at room temperature for 20 minutes to stabilize luminescent signal. Luminescence was recorded with a Synergy H1 plate reader (Agilent Technologies, Inc.) at the following settings: Integration Time of 1 second; Emission at Full light; Optics on Top, and Gain at 135.

2.5.6 Multiplexed transcript profiling via NanoString

The set of transcripts assembled in the "Human Neuropathology Panel" were probed simultaneously with NanoString's nCounter technology (http://www.nanostring.com/). To do this, total RNA samples were generated from 2 independent rounds of differentiation cultures that

were then treated with KA at iN28 developmental stage. Each *APOE* genotype line was plated in 18 wells in the same 96-well plate at 35,000 cells/well at iN03. Cells were seeded in the inner wells and the outer wells that did not receive cells were filled with 150 µL PBS. At iN28, 9 wells of each genotype were subject to KA at [30 µM] or vehicle treatment for 6 hours; according to the plate layout in Figure 2.11. Total RNA was extracted using the Rneasy Mini Kit (Qiagen). Lysates from 9 wells per condition were pooled to generate a single RNA sample. Extracted RNA was quantified via NanoDrop spectrophotometer (Section 2.5.1).

The mRNA molecules for each target in the panel were counted using 100 ng of RNA and following the manufacturer's nCounter protocol. Briefly, RNA samples were brought to 20 ng/µl, hybridized with the capture and reporter probes from the nCounter Neuropathology CodeSet for 18 hours at 65 °C. Samples were transferred to the Nanostring Prep station where unbound probes were washed away. Samples were then immobilized and aligned on the nCounter Cartridge followed by automated image capture and analysis by the Digital Analyzer.

2.5.6.1 Calculation of differentially expressed genes NanoString

The NanoString data was analyzed using the nSolver 4.0 software. Raw counts were normalized to the geometric mean of 6 housekeeping genes in the panel after data quality was validated against positive and negative control probes included in the manufacturer's kit. The geometric mean of negative controls was subtracted from gene transcript counts and gene expression data were adjusted to the geometric mean of the following housekeeping genes: AARS, CCDC127, CNOT10, LARS, MTO1, and TADA2B.

Background thresholding was set to 34 counts which was 2 standard deviations above the average (18 counts) of the negative controls. Fold changes were calculated using the average of each group. Fold changes were calculated comparing kainic acid treated and untreated cells within each genotype or comparing between untreated APOE3 and APOE4 genotypes and untreated APOE3 and APOE2 genotypes. False discovery rate adjusted p-value using the Benjamini–Yekutieli method were calculated after t-tests for pair-wise analyses were made. Note that the nSolver software performs t-tests if there are two or more replicates within each group even though three biological replicates per group is the recommended minimum sample size (176). As such, volcano plots from nSolver to represented comparisons of mRNA from genotype and KA treatment as co-variants in iN28 neurons, (n = 2 independent sets of iN differentiation and maturation samples per genotype in a single NanoString run). Differential expression of 50% lower or higher (i.e., 1.5-fold decrease or increase) with adjusted p-value <0.05 compared to that of the neutral genotype, 33, were extracted as differentially expressed genes (DEGs). Heatmaps and scatter plots were created in Prism.

Sample generation for NanoString: KA [30μM] 6 hr												
	no cells	APOE22 (35K/well)			APOE33 (35K/well)			APOE44 (35K/well)			no cells	
	1	2	3	4	5	6	7	8	9	10	11	12
A												
B		veh	veh	veh	veh	veh	veh	veh	veh	veh		
C		veh	veh	veh	veh	veh	veh	veh	veh	veh		
D		veh	veh	veh	veh	veh	veh	veh	veh	veh		
E		KA	KA	KA	KA	KA	KA	KA	KA	KA		
F		KA	KA	KA	KA	KA	KA	KA	KA	KA		
G		KA	KA	KA	KA	KA	KA	KA	KA	KA		
H												

Figure 2.11 Culture plate treatment layout for generating NanoString samples.

Schematic of the 96-well plate layout for NanoString experiments. Each APOE-variant line was plated at 35,000 cells/well for a total of 18 wells. The wells that did not receive cells contained PBS. At iN28, half of the wells of each *APOE* genotype was subject to KA or vehicle treatment for 6 hours.

2.6 Statistical analysis

Apart from DEG calling (Section 2.5.6.1), GraphPad Prism (version 8) was used for statistical analysis. For temporal profiling of mRNA expression over the 28-day differentiation time course, the statistical significance of the equality of the means of the groups of all three genotypes from 3 independent experiments (each with n=3 technical replicates) was analyzed by parametric, repeated measures two-way analysis of variance (ANOVA) followed by post hoc Dunnett's multiple comparison's testing for differences between 33 and 22 or 33 and 44 genotype groups. This same analysis was applied to question whether ATP showed significantly different levels over the 28-day differentiation time course amongst the cultures of different genotypes. For temporal profiling of *FOS*, *ATF4*, and *APOE* transcripts and ATP levels over the 18-hour KA treatment time course, the statistical significance of the means of the groups of all three genotypes from 3 independent experiments (each with n=3 technical replicates) was analyzed by parametric, repeated measures two-way ANOVA followed by post hoc Sidak's multiple comparison's testing for differences between 33 and 22 or 33 and 44 genotype groups. P-value < 0.05 was selected as significant to reject the null hypothesis that the differences observed between groups resulted from random variation. The mean, error of measurement (SEM), and number of biological replicates are reported.

Chapter 3 CRISPR-based genetic editing to develop a platform of human isogenic neurons

3.1 Introduction

3.1.1 Induced neuron (iN) approach for developing an *APOE* study platform

To investigate the mechanistic roles of neuronal ApoE in a reduced model, human derived neurons are more translational compared to murine ones because of the low degree of homology between mouse and human ApoE (Section 0) (174). Technological advancements have opened up innovative cellular platforms in the human context which could more reliably construct "AD-in-a-dish" models to uncover the molecular underpinnings of AD pathogenesis (177). Neurons differentiated from iPSCs have been increasingly shown to provide a route to facilitate the *in vitro* investigation of AD (133, 134, 178). These studies of wider AD application have been extended to include explicit investigation of APOE and its alleles.

Earlier *APOE* studies evaluating iPSC-neurons used lines from different donors thus introducing a confound from variability arising from genetic background. More recent studies eliminate the genetic background variability confounds by genetically altering *APOE* alleles in cells derived from a single donor. These newer studies mainly focus on the ε3 and ε4 alleles; leaving out the ε2 allele even though it has profound protective effects regarding AD (Section 1.4.2).

Table 3.1 lists some *APOE* findings in neurons differentiated from iPSCs and highlights, compared to the ε4 allele, that studies regarding the cellular and molecular functions associated with *APOE ε2* are meagre (134). Elucidating the mechanisms that drive the protective effects of ε2 in AD pathology using human iPSC model systems deserves further investigation. It is not known whether the activities of the ε2 allele are opposite to those of ε4 (though sometimes assumed to be the case) (73, 135).

Table 3.1 APOE studies specifically in neurons differentiated from human iPSCs

APOE Geno-type	APOE gene editing (method)	APOE isogenic lines?	Neuron Induction Method	Neuronal Culture Phenotypes	Conclusion	REF
2/3 and 3/3	n/a	No	Culture-driven; first forming neural rosettes containing NSCs	iPSC-neurons from 4 people with AD (2 fAD and 2 sAD) and 2 controls without dementia showed	Neurons from 2 of the 4 AD cases had increased Aβ40, p-tau and active GSK3β	(143)

				extremely variable phenotypes		
3/4	n/a	No	Culture-driven; first forming neurospheres containing NSCs	iPSC-neurons from people with AD were more vulnerable to ionomycin and glutamate toxicity and had more Aβ42/40 than controls without dementia	AD phenotype modeling and survival assay for screening	(179)
3/4 and ND	n/a	No	Culture-driven; first forming neurospheres containing NSCs	iPSC-neurons from 5 people with AD (2 fAD and 3 sAD) and 3 controls without dementia showed variable phenotypes	Increased $A\beta_{42/40}$ ratio seen only in a some sAD-derived neurons	(178)
ND	n/a	No	Lentiviral mediated overexpression of mouse Ngn2	Exogenously added apoE induced *APP* transcription and Aβ production; E4 was more and E2 was less potent than E23	ApoE acts through non-canonical MAPK pathway	(180)
3/3, 4/4 and KO	3/3→4/4 (ZFN)	Yes	Culture-driven; first forming neurospheres containing NSCs	4/4 had AD-related pathologies: increased ApoE fragmentation, p-tau, Aβ production, and neurodegeneration from 3/3	Switching E4 structure with a small molecule to E3 rescued 4/4-related toxicity	(133)
3/3 and 4/4	3/3→4/4 and 4/4→3/3 (CRISPR)	Yes	Lentiviral mediated overexpression of mouse Ngn2-GFP	4/4 had increased synapse number, $A\beta_{42}$, and distinct transcriptomic differences from 3/3	4/4→3/3 conversion in iPSCs from patient with AD ameliorated molecular and cellular phenotypes	(134)
3/3 and 4/4	4/4→3/3 (CRISPR)	Yes	Lentiviral mediated overexpression of mouse Ngn2-GFP	4/4 was predisposed to ionomycin-induced injury showing calcium dysregulation and neurodegeneration; 4/4 showed increased p-tau and pERK1/2 over 3/3	Neuronal ApoE can contribute to neurodegeneration and tau pathology in E4-harboring patients with AD	(144)
3/3 and 2/2	3/3→2/2 (CRISPR)	Yes	Culture-driven; first forming embryoid bodies containing NSCs	3 isogenic pairs of fAD and 1 pair on controls without dementia lines. Mixed neuronal-astrocytic cultures. 3/3→2/2 conversion with fAD-related mutations mitigated the disease-related phenotypes like Aβ production	Authors claim first isogenic hiPSC-derived culture system reporting on APOE2	(135)

4/4	n/a	No	dual SMAD inhibition	Decreased autophagy and mitophagy	neuroprotective role of mitophagy in the context of AD	(181)

Abbreviations: fAD, Familial AD; ERK1/2, extracellular signal-regulated protein kinase 1/2; GSK3β, glycogen synthase kinase-3β; HDAC3, Histone Deacetylase 3; DMT, disease modifying therapeutic; MAPK, mitogen-activated protein kinase; n/a, not applicable; ND, not disclosed or not known; NSC, Neural stem cells; p-tau, phosphorylated tau; sAD, Sporadic AD; ZFN, Zinc finger nucleases.

Therefore, a comprehensive *APOE* cellular platform that compares/contrasts all *APOE* alleles, based on isogenic neurons where only the *APOE* genotype is varied, remains a gap in the field. For these reasons, the platform I intended to build encompasses two independent sets of neuronal cells each from a common genetic background of iPSCs harboring homozygosity for all three major *APOE* alleles. Such isogenic platforms then allow for in depth interrogation of the impact of the full range of *APOE* homozygote genotypes on neuronal differentiation, neuronal structure and/or function, and neuronal vulnerability to AD-associated insults, and neurodegeneration; all devoid of the confound of genetic background variability. This sets up an improved ability to define the cellular and molecular interactions that underpin the modulation of disease induction or progression by the different neuron expressed *APOE* variants (143, 179).

3.1.2 Isogenic iPSC lines that form the foundation of the platform

To compare neuronal phenotypes associated with the various *APOE* genetic variants and investigate the cellular and molecular mechanisms underpinning the influence of neuronal expressed ApoE on neurodegeneration, I focused efforts on a foundational set of iPSCs that are homozygous for the three common *APOE* alleles, as well as a line in which the gene is ablated. The blue colored rows in Table 2.1 shows these 8 lines. They originated from 2 male individuals: a patient with AD (and homozygous for the *APOE* ε4 allele) and a person without AD at the time of biopsy (and bearing the genotype of *APOE* ε3/ε4) (172, 174). Both master originating iPSC lines are genetically engineered to carry the following APOE genotypes: *APOE* knockout (KO), *APOE* ε2 /ε2 (2/2), *APOE* ε3/ε3 (3/3), and *APOE* ε4/ε4 (4/4). My intent was to convert all of them into dependable sources of isogenic neurons.

3.1.3 The specific molecular switch enabling temporal control of NGN2 expression

One protocol used repeatedly in the scientific literature to generate iPSC-derived neurons is based on the forced expression of the neuronal cell fate determining TF, human NGN2 (or mouse Ngn2), known to drive neurogenesis during development (Section 1.13) (151, 156, 180, 182, 183).

Resultant iNs reproducibly recapitulate morphological, transcriptional, and operative homogeneity of glutamatergic cortical neurons; a relevant cell type in AD (151).

In my CRISPR approach, I used a version of the Tet-ON system introduced in Section 1.14.3, called "Tet-One", to facilitate the conversion of iPSCs into neurons after doxycycline induced NGN2 expression (constructed by Biogen collaborators and which I validated in Section 3.2). Figure 3.1 illustrates that this version diverged from that described in Section 1.14.3 in that the Tet-On 3G transactivator protein was under the control of a different promoter, CMV early enhancer/chicken β-actin (CAG) promoter. Other than that, the design remained similar and addition of doxycycline to the system turns on NGN2 expression (184). The potency of doxycycline had been shown to be orders of magnitude below the levels that induces cytotoxicity (167, 185).

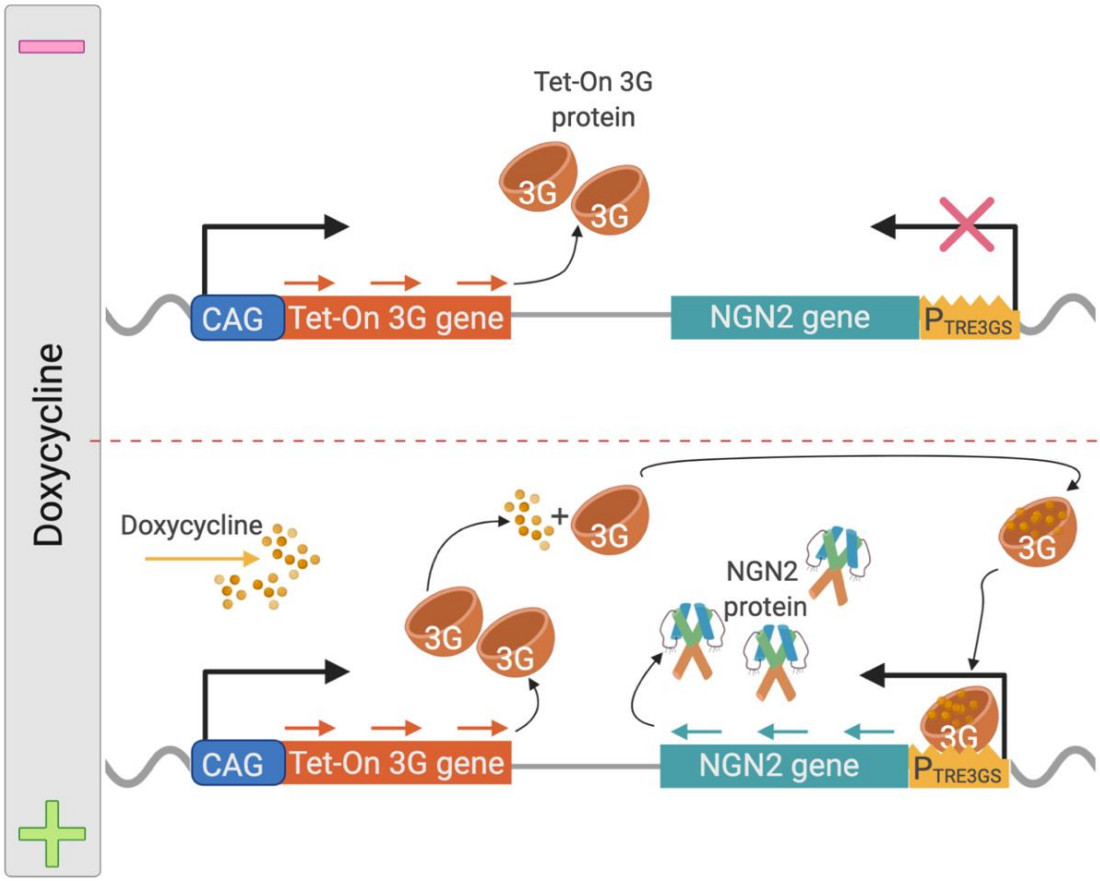

Figure 3.1 Schematic of molecular switch enabling temporal control of NGN2 expression.

The CAG promoter promotes constitutive expression of a transcriptional activator protein, Tet-On 3G. The PTRE3GS promoter that can drive expression of the downstream positioned gene, NGN2, is normally silent (Top panel). Binding of exogenously added doxycycline triggers a conformational change in the Tet-On 3G transactivator, which then interacts with the PTRE3GS, leading to doxycycline induced transcription of NGN2 (Bottom panel).

3.1.4 Rationale for CRISPR editing approach

Human stem cells are challenging to genetically alter, particularly in a regulatable manner (184). I reasoned that an important determinant to the success of my approach would be to avoid variegated transgene expression subsequent to random insertion into the genome or silencing and/or down-regulation of transgenes in a promoter-dependent manner (166, 186). Furthermore, if transgenes insert randomly into the genome, this potentially disrupts endogenous genes (184). These limitations can be mitigated by an approach in which transgenes are inserted into well-characterized "safe harbor" genomic loci such as the AAVS1 site described in Section 1.14.1.2. Such considerations prompted me to standardize gene editing across the distinct genotype comparisons, supporting the use of technology that allowed deliberately placing the inducible-NGN2 transgene at the preselected AAVS1 safe harbor genomic site in all APOE cell lines in the platform.

3.1.5 A benchmark iPSC line for my CRISPR editing work: iNGN2-iPSC control

Figure 3.2 outlines Biogen colleagues' development of an NGN2-stable iPSC line. Somatic cells (B-lymphocytes) from a donor without dementia and with the most common *APOE* genotype (*APOE* ε3/ε3) were reprogrammed into iPSCs. Doxycycline-inducible NGN2 (in a Tet-On expression DNA cassette [Section 1.14.3]) was then knocked in into genome at the AAVS1 safe harbor locus (Section 1.14.1.2). This dividing iNGN2-stable iPSC line can be maintained as ongoing, proliferating undifferentiated cultures and as required, can be converted into post-mitotic (non-dividing cells) human neurons whose differentiation is triggered by adding doxycycline to the culture medium. This authenticated AAVS-1 integrated inducible NGN2 line provided both the proof-of-concept to suggest a similar approach would be valuable in comparing neurons across APOE genotypes, as well as, served as a control or benchmark for my investigations described in this chapter.

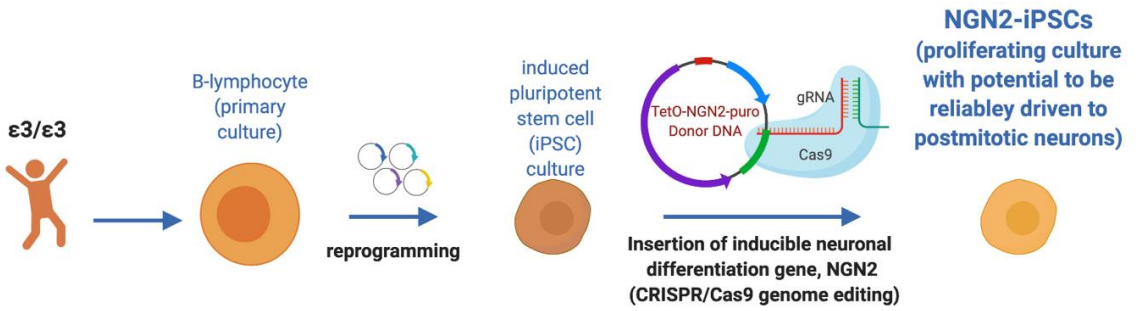

Figure 3.2 Development of the NGN2-stable iPSC line used as a control in my experiments.

Somatic cells from an *APOE* ε3/ε3 donor with no documented disease were reprogrammed into iPSCs which were next engineered to express NGN2, under control of an inducible promoter (using CRISPR-assisted gene editing). This iPSC cell line developed by colleagues now serves as a renewable source of human post-mitotic neurons at the bench and is called the iNGN2-iPSC control.

3.2 Characterization of the iNGN2-iPSC control line

Before embarking on inducible NGN2 gene-editing of the *APOE*-edited isogenic cohorts from Table 2.1, I observed how the inducible NGN2 neuronal conversion system works by taking the iNGN2-iPSC control line (Figure 3.2) through the neuronal differentiation process and characterizing the resultant iNs. I monitored induction of neuronal morphological features and transcriptional markers. My workflow is summarized in Figure 3.3. I treated the iNGN2-iPSC control line with doxycycline to turn on NGN2-transgene expression which subsequently initiates a neuronal differentiation genetic program. Live cells were monitored under phase contrast microscopy to verify neuronal morphology. Cells were then dissociated, re-plated, fixed and immunostained for a neuron-specific protein, β-III-Tubulin, as well as, harvested for transcriptional profiling of neuron-specific mRNA expression.

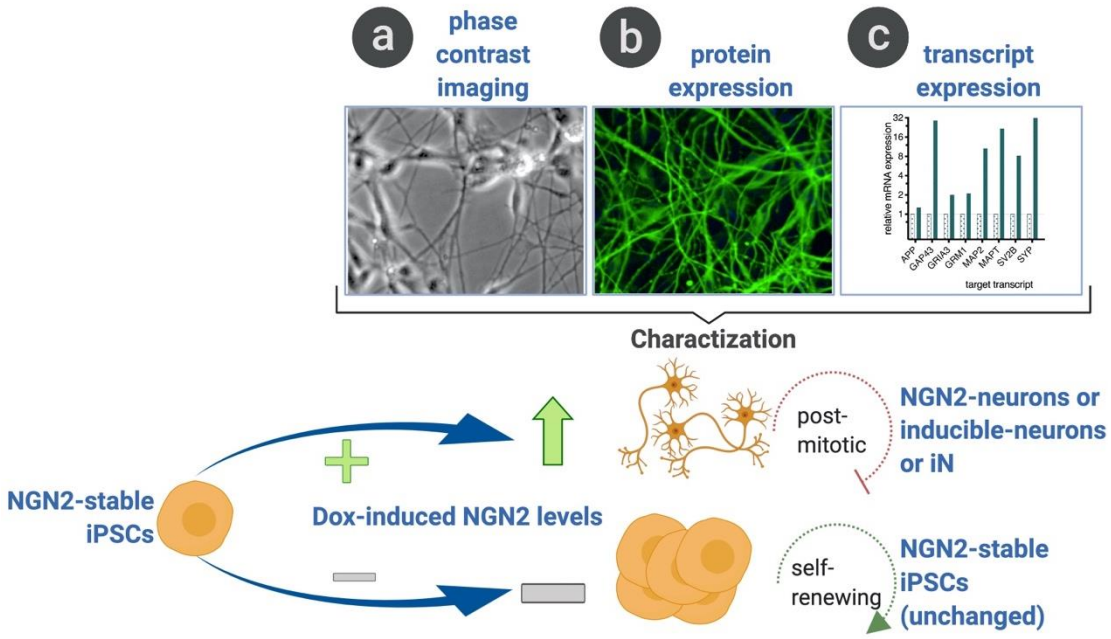

Figure 3.3 Neuronal differentiation and characterization workflow of the control NGN2-stable iPSC line.

The schematic on the bottom shows that iNGN2-iPSC control line was exposed to doxycycline. The top panel depicts the way the subsequent cellular population output was characterized. Neuronal morphology was confirmed using phase contrast microscopy (a). Neuron specific protein expression, as well as morphology, was confirmed using immunohistochemistry (b). Induction of neuron-specific mRNA transcription was confirmed using RT-PCR (c).

3.2.1 Undifferentiated phenotype of the iNGN2-iPSC control line

Upon initially working with the iPSCs, I sought to satisfactorily establish that my iPSC maintenance procedures (based on mTeSR™ growth medium, Matrigel™ growth substrate, and enzyme-free cell aggregate passaging as detailed in Section 2.2.4) reproducibly upheld high-quality, undifferentiated cultures (Figure 3.4 and Figure 3.5). I monitored undifferentiated iPSC colonies under phase contrast microscopy as colonies with distorted morphologies signal a disruption of their undifferentiated nature (187). Cultures of the iNGN2-iPSC control line showed the expected morphological standards of healthy undifferentiated iPSCs and representative images are shown in Figure 3.4. The features I observed were consistent with the descriptions of iPSCs in the undifferentiated state and include compact colonies with distinct borders and well-defined edges that are made up of cells showing a large nucleus (arrows in Figure 3.4) to cytoplasm ratio (188). As the cultures become fully confluent, the cells began to grow on top of each other resulting in a 3-dimensional pattern as opposed to the monolayer in which they started. It is at this point that they are passaged. Stress-free passaging and passaging before overcrowding, are critical for keeping the undifferentiated pluripotency iPSCs otherwise they are prone to spontaneous differentiation (189, 190). Figure 3.5 shows the results of my selected maintenance and passaging

protocol, where cells are passaged as clumps, or aggregates, after dissociation from the culture plate using an enzyme-free reagent; like published protocols (190).

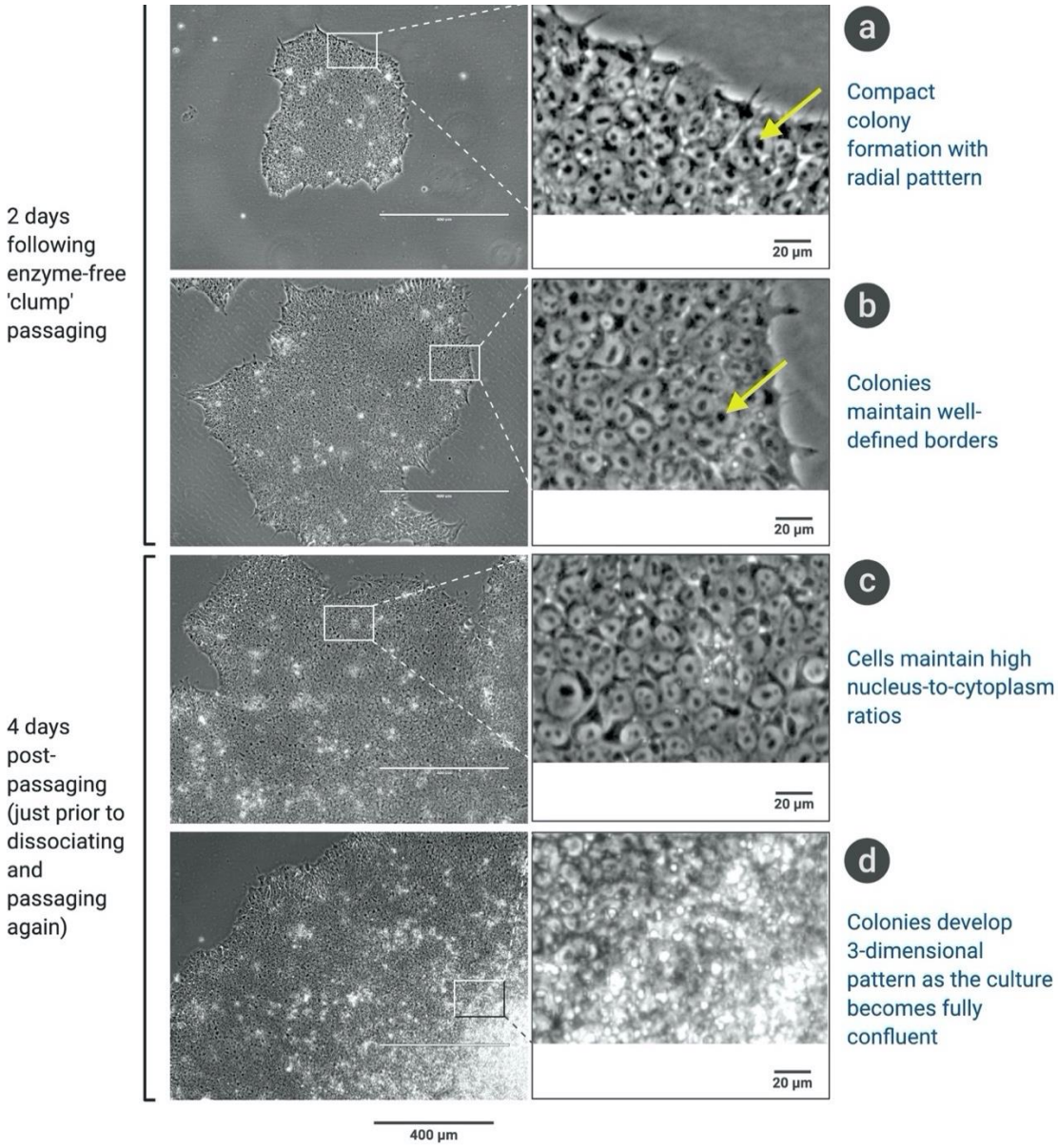

Figure 3.4 Behavior of the NGN2-stable iPSC cell line through passaging and propagating procedures.

Representative images of iPSCs maintained on Matrigel matrix verify these iPSCs have typical morphological characteristics which include compact rounded colonies (a, b) with well-defined borders (a, b) comprised of cells that show a prominent nucleus (arrow) and little cytoplasm (a, b). As the colonies proliferate the colonies become larger and achieve full confluency (c), then cells start to grow on top of each other and the monolayer takes on a 3-dimensional pattern (d).

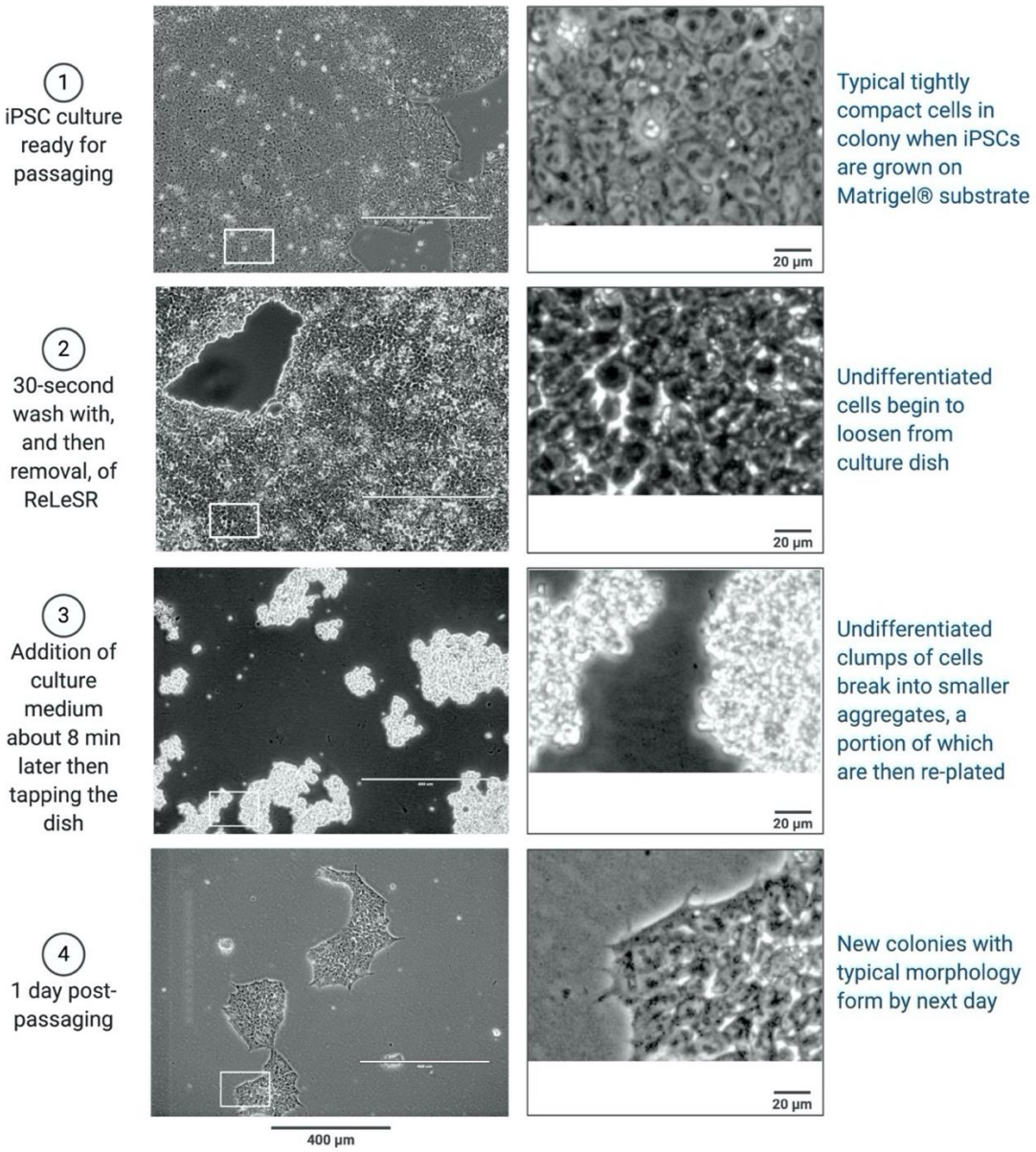

Figure 3.5 Representative phase contrast photomicrographs demonstrating enzyme-free 'clump' passaging of iPSC.

Results of my method of passaging shows generation of fresh colonies that continue to maintain healthy undifferentiated morphology.

3.2.2 Induction of neuronal morphology in iNGN2-iPSC control line

I next sought to validate doxycycline-induced differentiation of the control iNGN2-iPSCs into neuronal cultures. I investigated cells subjected to the treatments and passaging outlined in Section 2.2.11 to verify expected indicators of differentiation. I first monitored morphological transformation, depicted in Figure 3.6. By 6 days of doxycycline treatment, the iNGN2-iPSC control cells stopped dividing and took on clear multipolar neuronal morphology with distinct soma and a network of neurites. Stopped proliferation was noted (an expected result as this is a

well-known feature of terminally differentiated post-mitotic neurons). The transformation to this neuronal phenotype was gradual and intermediates are depicted in Figure 3.6 (panels a, b, c, d, e, right). At 2 days of exposure to doxycycline the iPSCs no longer show compact colonies of cells with high nucleus-to-cytoplasm ratio, but instead, cells are comparatively more diffuse and irregularly shaped as seen in Figure 3.6 (b, right). By day 3, cellular protrusions reminiscent of neurites had clearly emerged and the cells were no longer packed against each other in compact multicellular colonies (Figure 3.6, c, right). With time, the cell protrusions became clearly neuronal and longer such that by 6 days of doxycycline treatment the morphology was conspicuously neuronal (Figure 3.6, e, right). Importantly, cells cultured in parallel but not treated with doxycycline did not exhibit any of these morphological characteristics, showing the doxycycline dependence of these cellular changes (Figure 3.6 a, b, c, d, e, left).

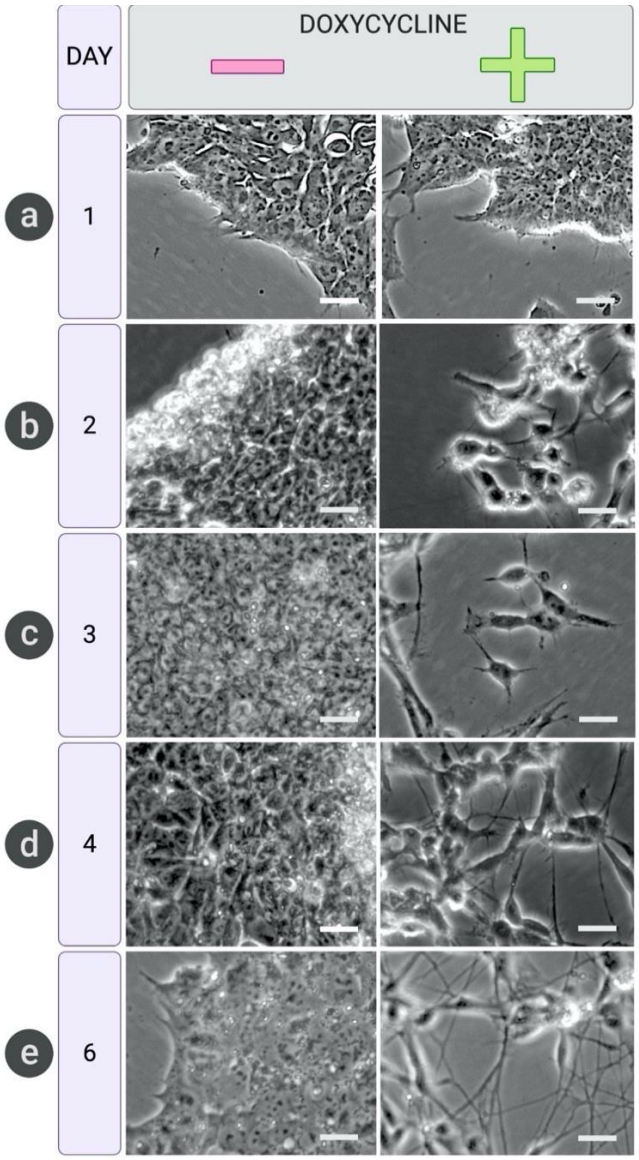

Figure 3.6 Changes in cell morphology of iNGN2-iPSC control line treated with doxycycline.

Microscopy of live cells showed the gradual development and expansion of a neurite network from days 0 to 6. (a, b, c, d, e, right). By 48 hours of doxycycline treatment, clear morphological changes became evident: cellular protrusions reminiscent of neurites appeared and the cells were no longer as tightly compact against each other (Day 2, b, right). Over time, the cell protrusions became longer and more elaborated such that cell morphology was distinctly neuronal by Day 4 (d, right) with more mature appearance by day 6 (e, right). Meanwhile, cells not exposed to doxycycline did not display any of these neuronal features (even though they were similarly exposed to neuronal growth media) (a, b, c, d, e, left). Scale bars = 17 to 20 µm.

3.2.3 Induction of molecular neuronal phenotype in the iNGN2-iPSC control line

I extended the morphological characterization to molecular characterization by investigating transcriptional and protein expression changes as measures associated with neuronal differentiation. Morphological tracking (Section 3.2.2) guided the selection of the point at which iNs could feasibly be investigated for molecular neuronal markers. After 6 days of doxycycline

treatment, the iN culture was dissociated and a portion was lysed and subjected to transcriptional analysis (Section 3.2.3.1). In parallel, a subset of cells was re-plated on PDL-coated plates and subsequently subjected to a protein expression study (Section 3.2.3.2).

3.2.3.1 Induction of neuronal transcriptional phenotype

I transcriptionally profiled iNs against a pre-specified set of classical pan-neuronal markers. My RT-PCR results comparing the iNGN2-iPSC control line in its undifferentiated state versus iNs at 6 days after initial exposure to doxycycline revealed clear differential gene expression of *GAP43* and *MAP2* which exhibited a 29- and 11-fold increase, respectively, over their stem cell counterpart (Figure 3.7, a). *GAP43* protein is linked to nerve growth and is critically localized to neurite branch points, neuronal growth cones, and axon terminals while they are extending and is also involved in the release of neurotransmitters and synaptic vesicle recycling (191) (192). The *MAP2* gene encodes a protein known to stabilize neuronal shape by interacting with other components of the cytoskeleton and is a characteristic mature neuron marker (193). The transcript for synaptic proteins, *SYP*, a ubiquitous component of synaptic vesicles (Figure 1.4), and *SV2B*, an isoform of SV2 which is a part of all synaptic vesicles, were both robustly induced in differentiating conditions. *SV2B* and *SYP* were induced by 8- and 32-fold, respectively (Figure 3.7, a).

I also performed evaluation as to whether there was evidence of glutamate receptor induction. Transcripts from both GRIA3 (encoding glutamate ionotropic receptor AMPA type subunit 3) and GRM1 (which encodes glutamate metabotropic receptor 1) showed 2-fold increases over the levels observed in the progenitor cells (Figure 3.7, b). Since, not only are *APP* and MAPT dysregulation associated with AD, but it has also been asserted that there is some interplay between ApoE4 and both Aβ and tau protein, I included them in the transcriptional profiling experiment. A clear induction of MAPT transcription was observed (22-fold increase over progenitor iPSCs) but no induction of *APP* transcript was apparent. (Figure 3.7, c). Meanwhile, APOE transcript was greatly reduced while LRP1 levels showed no clear changes in expression (although both were detectable) compared to undifferentiated iPSCs (Figure 3.7, d).

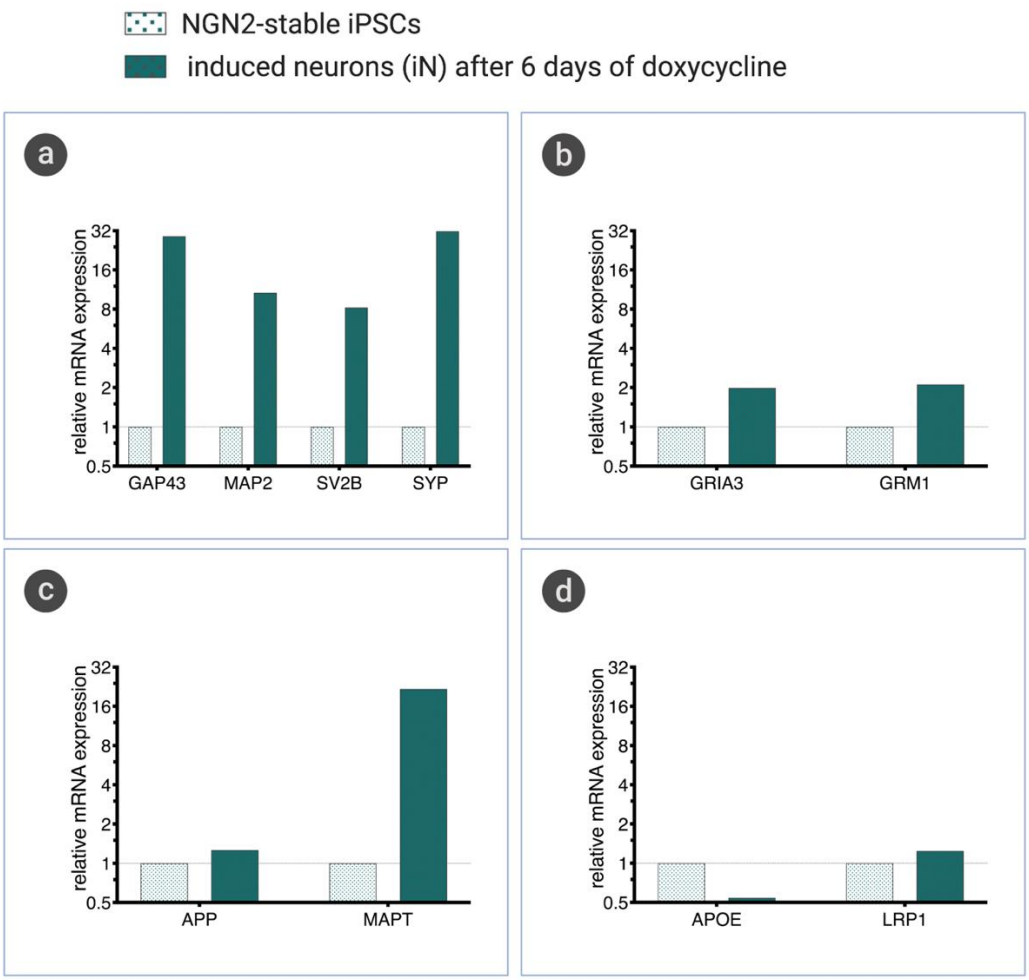

Figure 3.7 Transcriptional profiling of iNs.

RT-PCR confirmed induced expression of neuronal genes upon doxycycline-induced differentiation of iNGN2-iPSC control line. Transcript levels of the genes encoding pan-neuronal markers *GAP43* and *MAP2*, as well as, synapse associated transcripts, *SV2B* and *SYP*, prominently increased (a). Glutamate ionotropic and metabotropic receptor subunit markers, GRIA3 and GRM1, both increased 2-fold over levels detected in progenitors (b). MAPT levels increased while *APP* transcript showed very little change (c). APOE transcript was decreased in the neuronal context and there was no change in LRP1 transcription (d). These experiments were performed as a single dish therefore there are no replicates.

3.2.3.2 Induction of a classical neuronal protein marker

As a final approach to combining molecular and morphological assessments, I investigated neuronal protein expression. Immunofluorescence staining using an anti-Tuj1 antibody confirmed that neuronal tubulin β3, a protein typically evaluated during neuronal differentiation, was expressed in abundance in iNs, Figure 3.8 shows that this cytoskeletal protein appears in cell bodies and neurites, effectively highlighting the shape of the cells, which are visibly of neuronal morphology. The cells in this culture were immunostained at 7 days post the start of doxycycline exposure (and 24 hours after counterpart cultures had been harvested for the mRNA extraction that yielded results in Section 3.2.3.1).

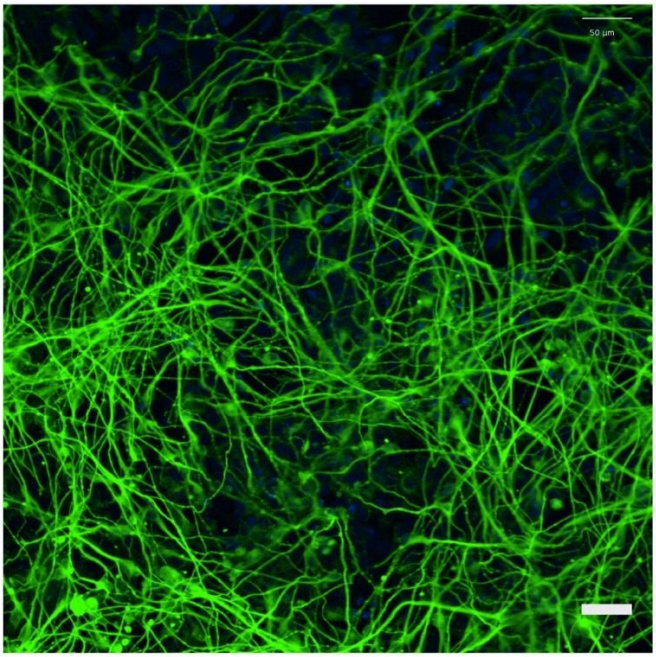

Figure 3.8 Neuronal cytoskeletal protein expression in iN cells.

Representative image of neuronal tubulin β3 immunostaining in the iNGN2-iPSC control line at 7 days after induction of neurons with doxycycline.

3.3 Establishment of analysis parameters to identify genetically modified iPSCs for my CRISPR editing experiments

The desired outcome of CRISPR-mediated insertion of the inducible-NGN2 transgene was investigated using PCR-based approaches for which a simplified depiction is shown in Figure 3.9 (while the PCR assays are detailed in Section 2.3.8).

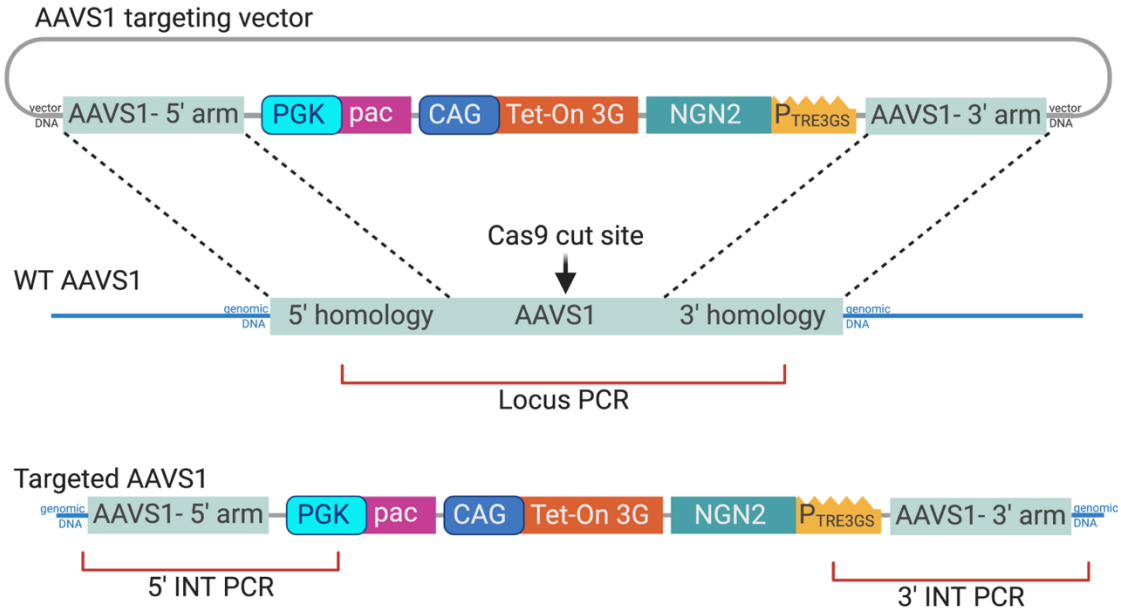

Figure 3.9 Schematic of the desired outcome of CRISPR/Cas9-mediated insertion of the inducible-NGN2 transgene.

Top Panel depicts the AAVS1 targeting vector carrying the transgene cassette and is the donor DNA template during the CRISPR-assisted gene editing. Middle Panel depicts that Cas9 is targeted to the AAVS1 locus. In the absence of the targeted insert, a "Locus" PCR can generate a PCR product from the unedited, wildtype allele. Bottom Panel shows the desired editing outcome. Successful integration would yield PCR products at the 5'- or 3'-end insertion junctions via two PCR assays: "5' INT" and "3' INT".

Optimization of the PCR protocols was critical for establishing a robust assay to screen for positive clones that successfully integrated the transgene at the target site. I took the approach of optimizing the 5'- integration PCR assay using purified genomic DNA (gDNA) from the iNGN2-iPSC control line that I validated in Section 3.2. At first, I tested the optimal annealing temperature (T_a) of the primers by assessing identical reaction mixes with fixed primer concentrations over a gradient of annealing temperatures ranging from 55°C to 69°C. Figure 3.10 (Panel A) indicated that the primer pair 5'F2 and 5'R1 robustly generated the expected PCR amplification product, a 900 bp band, at an annealing temperature of 68°C. However, when screening many clones, a higher throughput protocol would involve providing crude cell lysates, rather than purified gDNA, directly to the PCR reaction as the source of PCR template. Upon checking whether addition of cell lysis buffer affected the effectiveness of the 68°C annealing temperature, other non-specific bands were now being generated (Figure 3.10, Panel B). After further optimization, I determined that an annealing temperature of 71°C was optimal for the PCR conditions when conducting the PCR screen using crude lysates (Figure 3.10, Panel C, lane with the check mark).

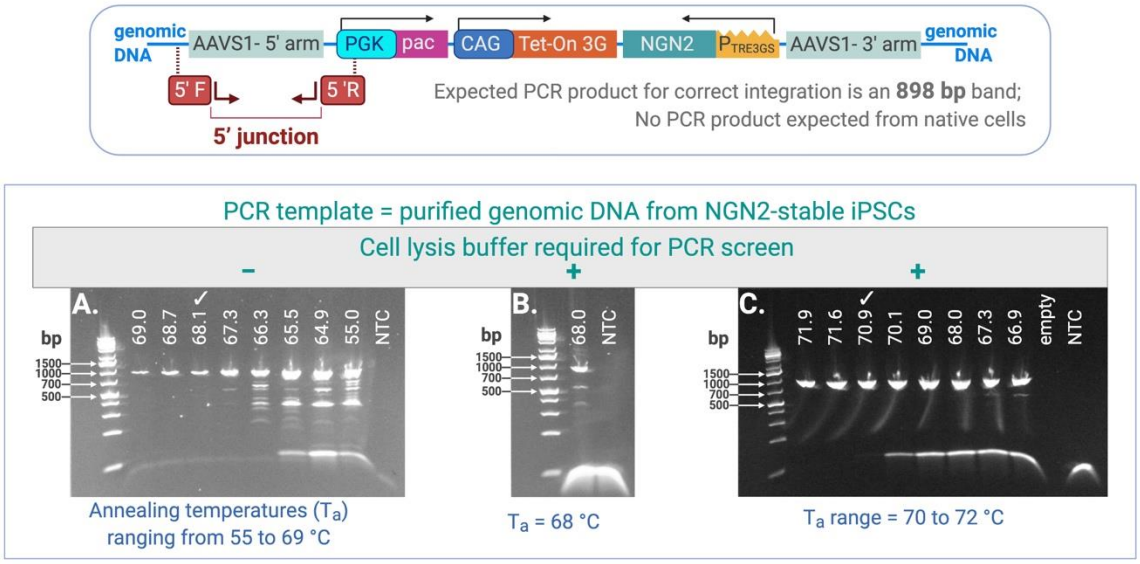

Figure 3.10 Optimization of PCR assay for initial screening for edited cells.

The 5'- integration PCR assay was tested using purified gDNA from the iNGN2-iPSC control line as the PCR template DNA. Panel A shows that the primer pair 5'F2 and 5'R1 robustly generated the expected PCR 900 bp amplification product at an annealing temperature of 68°C (lane with the check mark). Panel B shows that when the PCR reaction was spiked with cell lysis buffer, a component of scaled-up PCR for screening, the 68°C annealing temperature required further optimization because other non-specific bands were now generated. Panel C suggested that the optimal annealing temperature was 71°C when using crude lysate with unpurified gDNA (lane with the check mark).

3.4 Generating iNGN2-iPSCs from an isogenic set of iPSCs differing in only their APOE genotype

3.4.1 Gross morphology of iPSCs with different APOE genotypes

Though I intended to genetically engineer all 8 *APOE* lines (Table 2.1), I approached the project in a staged manner and initially worked with only 4 of the iPSC lines. These were the derivatives from the non-AD subject. Upon thawing and culturing these iPSC lines, I noted that their gross morphology appeared similar to each other (Figure 3.11), which was not overtly different than that of the iNGN2-iPSC control line (see Figure 3.4 panels a and b for comparable culture stages).

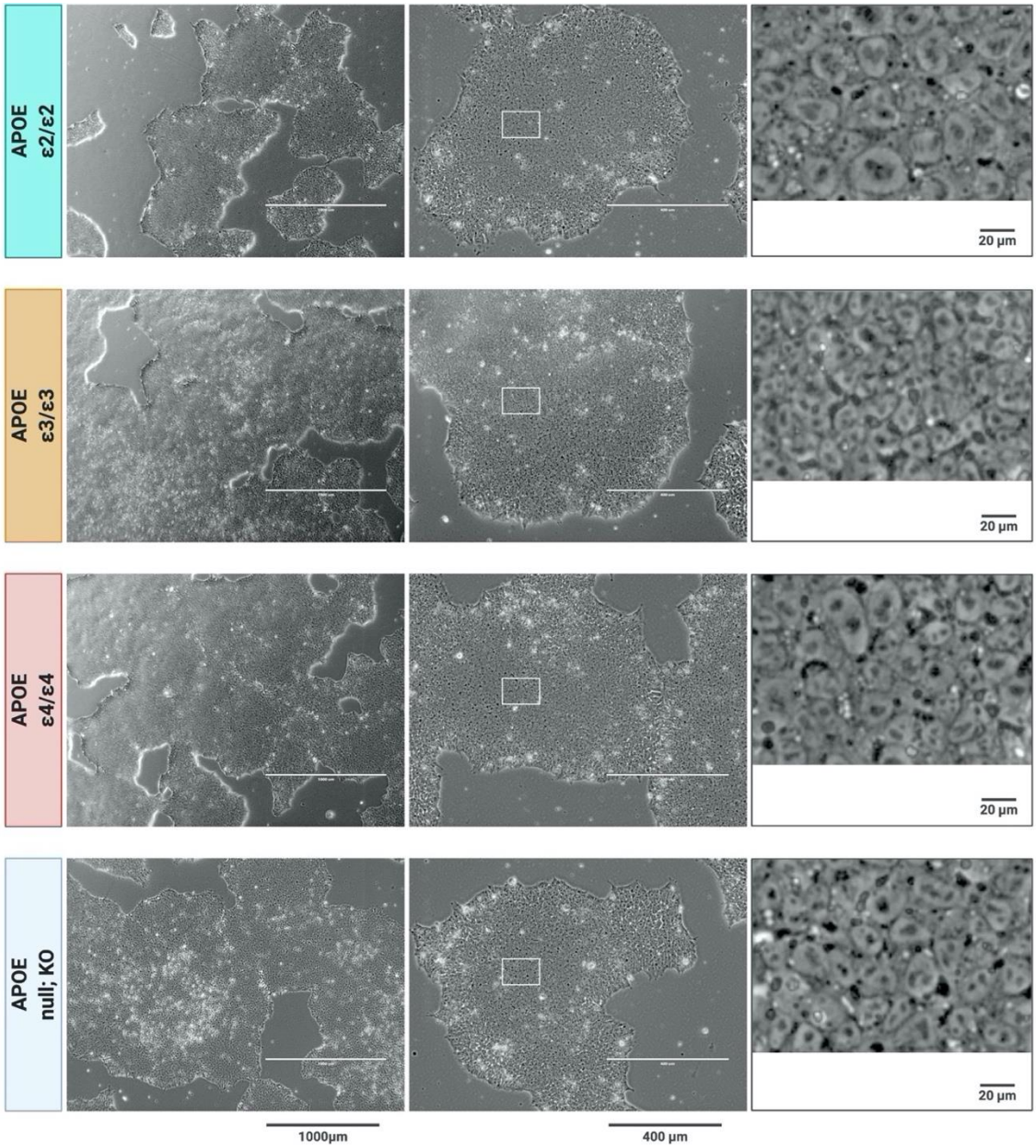

Figure 3.11 Gross morphology of an isogenic cohort of iPSCs bearing APOE variants.

The iPSC lines derived from a single non-AD individual but homozygous or null for various APOE alleles showed indistinguishable gross morphology. Images are of cultures just prior to dissociation for electroporation with CRISPR gene editing agents.

3.4.2 Detailed PCR evaluation of puromycin-resistant cultures after transfection with CRISPR editing reagents

I extracted gDNA from 2 iPSC cultures (representing APOE 3/3 and KO genotypes) after electroporating them with the editing agents as well as taking them through several rounds of passaging in puromycin (represented as Step 4 in Figure 2.2). This gDNA represented a population of cells carrying different possible CRISPR editing outcomes (Section 1.14.1). The gDNA was evaluated for evidence of transgene integration via the HDR pathway at the desired genomic

location using the 3 PCR assays that were clarified in previous sections (Section 3.3, and Figure 2.7 and 4.12). In all 3 PCR assessment cases, the gDNA from the parental 3/3 and KO lines (control electroporated cells that were not exposed to NGN2 transgene donor DNA plasmid nor CRISPR reagents) provided the negative control comparators whilst gDNA from the iNGN2-stable iPSC line (Section 3.1.5) served as the positive control.

As expected, the AAVS1 locus PCR (Figure 3.9) produced a robust PCR product of ~800 bp in size from the unedited, wildtype allele in both the parental lines (Figure 3.12, lanes 3 and 4), while the iNGN2-iPSC control line, as expected, did not generate a PCR product (Figure 3.12, lanes 5 and 9 with check marks). In the PCR using gDNA from cultures derived from the electroporations with CRISPR and the HDR donor DNA, wildtype allele bands were also observed (Figure 3.12, lanes 6 and 7). However, these wildtype bands were of a lesser intensity than those observed for the naïve parental cells. Because equal amounts of DNA were put in all PCR reactions and equal volumes of PCR reaction were loaded per lane, the weaker band suggested less wildtype alleles in the PCR template. This data could be indirect evidence of insertion of NGN2 sequence with the caveat being that this is not a quantitative PCR therefore additional data would need to be gathered.

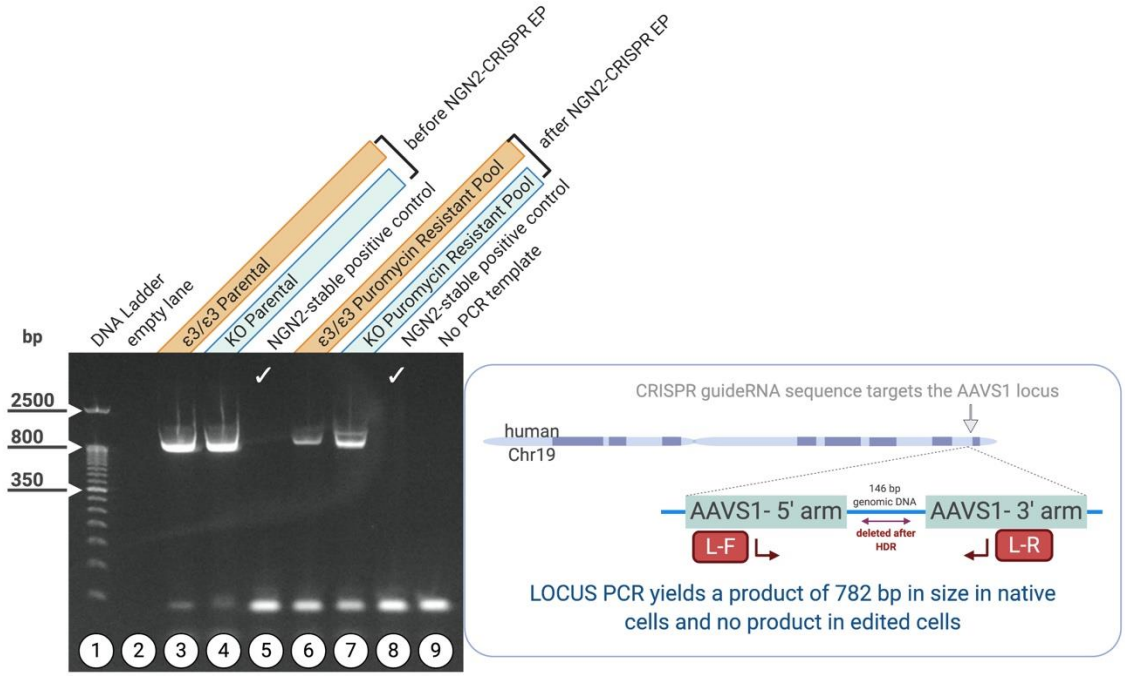

Figure 3.12 Native AAVS1 Locus evaluation via PCR from the 3/3 and KO iPSCs; before and after exposure to CRISPR editing agents.

The electrophoresis gel image of the puromycin resistant cultures subjected to the AAVS1 locus PCR is shown. The expected PCR product was observed for naïve parental lines (lanes 3 and 4.). The edited iNGN2-iPSC control line did not generate a PCR product (lanes 5 and 8 with check marks; 2 independent PCR reactions). Cell cultures that had been electroporated with the editing reagents also showed the wildtype allele band, but at a lesser intensity than that seen for the wildtype parental cultures (lanes 6 and 7). Equal amounts of DNA template were input in all PCR reactions and the equal volumes of the PCR reactions were loaded per lane. EP = electroporation.

I next evaluated integration of the transgene by performing the 5'-integration PCR assay (Figure 3.9) and results are shown in Figure 3.13. As expected, both naïve parental lines did not generate a PCR product. Also, as expected, the transgenic iNGN2-iPSC control line consistently exhibited a robust amplification product of approximately 900 bp in size (Figure 3.13, lanes 5 and 8 denoted with check marks). The APOE 3/3 iPSC culture exposed to the editing reagents similarly showed a ~900 bp amplification product, though at a lesser intensity than that seen for the positive control iNGN2-iPSCs. This was considered a promising result and that single cell sorting would achieve isolation of the clone/s responsible for this transgenic integration signal. The APOE KO iPSC culture exposed to the editing reagents yielded an inconclusive banding pattern. There was a band slightly of lower size than expected (Figure 3.13, lane 7). Also, a ~500 bp band was consistently observed for all PCR reactions (Figure 3.13; yellow arrow), including those of both the negative and positive controls. I considered it an unspecific band of the PCR reaction therefore not meaningful in terms of transgenic clone generation.

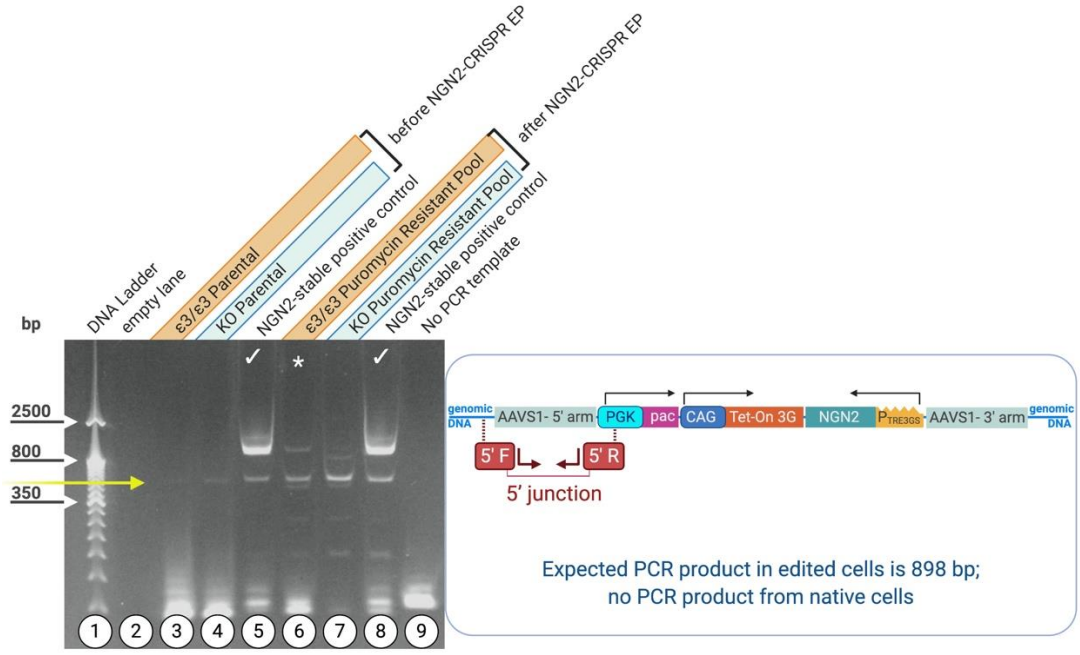

Figure 3.13 Evaluation of the 5'- end of the insertion junction via PCR from the 3/3 and KO iPSCs; before and after exposure to CRISPR editing agents.

The electrophoresis gel image of the puromycin resistant cultures subjected to the 5' INT PCR is shown. Parental naïve lines did not generate a PCR product (lanes 3 and 4). The positive control iNGN2-iPSCs generated a robust ~900 bp amplicon in 2 independent PCR reactions (lanes 5 and 8 with check marks). The APOE 3/3 iPSC culture exposed to the editing reagents similarly show the ~900 bp amplification product highlighted with an asterisk, but at a lesser intensity than that seen for the positive control cells (lane 6). The APOE KO iPSC culture exposed to the editing reagents showed an unexpected banding pattern (lane 7). An artifact background band was seen in all lanes (yellow arrow). EP = electroporation.

Next, the 3'-end of the insertion junction was evaluated via PCR in the cultures derived from the electroporated iPSCs carrying the 3/3 and KO genotypes. Results from the 3'-integration PCR assay (Figure 3.9) are shown in Figure 3.14. As expected, the positive control iNGN2-iPSCs generated a robust ~1000 bp amplification product (Figure 3.14; lanes 5 and 8 denoted with check marks). Both APOE 3/3 and KO iPSCs exposed to the editing reagents showed an amplification band similar to the desired one (Figure 3.14; lanes 6 and 7 denoted with asterisks), but the band of interest was at a lower signal intensity than that seen for the negative control parental line (despite having used the same amount of gDNA input for all PCR reactions and loading the same PCR reaction volumes on the gels). This was a promising result which aligned with my conclusion from the 5'-integration PCR assay that the cultures were composed of a mix of edited and unedited pools of clones. I next moved forward by expanding these cultures via low density passaging (as opposed to clump passaging) under puromycin selection (Step 5 in Figure 2.2) in the hopes of ensuring that non-resistant cells were faithfully eliminated from the cultures thus

increasing the likelihood that single cell sorting would isolate the clone/s responsible for this evidence of transgene integration.

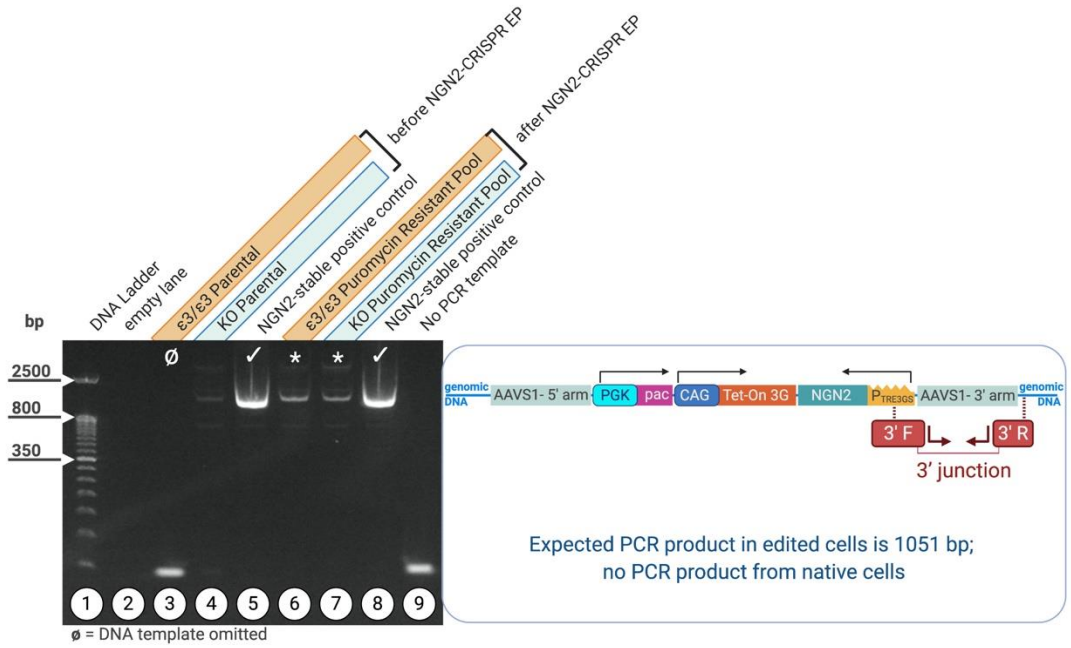

Figure 3.14 The 3'- end of the insertion junction was evaluated via PCR in the puromycin resistant cultures after electroporation with CRISPR editing agents (3/3 and KO iPSCs).

A naïve parental line generated a faint PCR product (lane 4). Positive control iNGN2-iPSCs robustly generated the expected ~1000 bp amplicon in 2 independent PCR reactions (lanes 5 and 8 with check marks). Both the electroporated APOE 3/3 and KO iPSCs showed amplification signals like the band of interest in the lanes marked with asterisks (lanes 6 and 7). EP = electroporation.

3.4.2.1 Further PCR evaluation of puromycin-resistant cultures after low density passaging

After expanding the electroporated cell cultures (both the APOE 3/3 and KO iPSCs) using low density passaging under puromycin selection for several passages, I once again extracted gDNA and performed the 5' INT PCR (Figure 3.9) in hopes of achieving a more robust signal regarding transgene integration. Figure 3.15 shows that the APOE 3/3 iPSCs showed a clear PCR amplification signal of the band of interest in the final low density passaging in puromycin condition (Figure 3.15, lane 9*) but not in the earlier passages. I took this as an indication that it would be possible to isolate positive clones from the electroporated APOE 3/3 iPSC culture. While the APOE KO iPSCs exposed to the editing reagents did not show a positive signal at any of the passages, I reasoned that isolating single cell clones could allow for finding putative clones that were possibly present (because of the earlier result in Figure 3.14) but the signal was probably too weak to be consistently detected from being mixed in within a pool of incorrectly edited cells. In the case of an isolated clone, the normalized amount of DNA template (10ng/mL) was able to

produce a far more robust signal than in mixed populations, as shown in Figure 3.15 (lane 3) from the undiluted signal coming from the control iNGN2-stable iPSC line.

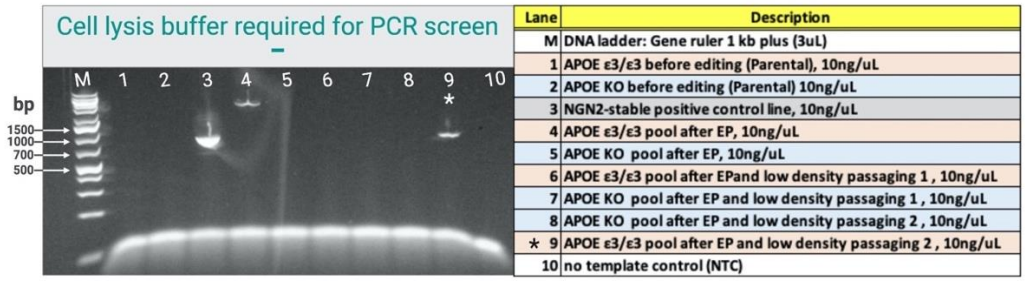

Lane	Description
M	DNA ladder: Gene ruler 1 kb plus (3uL)
1	APOE ε3/ε3 before editing (Parental), 10ng/uL
2	APOE KO before editing (Parental) 10ng/uL
3	NGN2-stable positive control line, 10ng/uL
4	APOE ε3/ε3 pool after EP, 10ng/uL
5	APOE KO pool after EP, 10ng/uL
6	APOE ε3/ε3 pool after EPand low density passaging 1 , 10ng/uL
7	APOE KO pool after EP and low density passaging 1 , 10ng/uL
8	APOE KO pool after EP and low density passaging 2 , 10ng/uL
* 9	APOE ε3/ε3 pool after EP and low density passaging 2 , 10ng/uL
10	no template control (NTC)

Figure 3.15 The 5'- end of the insertion junction was tracked for the pool of puromycin resistant mixed clones from the 3/3 and KO genotypes over several rounds of expansion and independent gDNA extraction.

As expected, the negative control wildtype parental lines yielded no PCR products (lanes 1, 2). As expected, the positive control iNGN2-iPSCs showed a robust ~1000 bp amplicon (lane 3). Pools of the APOE 3/3 iPSCs exposed to the editing reagents showed a clear PCR amplification signal like the band of interest only in subsequent puromycin passaging (lane 9*) but not in the earlier passages (lanes 4 and 6). The APOE KO iPSCs exposed to the editing reagents did not show a positive signal at any of the passages (lanes 5, 7, and 8).

Altogether, the initial results from the pool of cells were encouraging enough in the 3/3 line to prompt me to move forward with single cell sorting to try isolating potentially suitable genetically modulated clones from the mixed cell population. Although the APOE KO iPSC culture at this point did not appear to show clear potential for successful editing by PCR, I however, chose to proceed to single cell sorting with this line as well, in hopes of uncovering successfully integrated clones because there might still be a small chance of a clone whose signal was diluted out at this point by the overwhelming presence of non-successful integrated DNA. My decision to continue holding out hope regarding finding positive clones from this APOE KO iPSC culture was because the culture was puromycin resistant and the possibility that in this final experimental run of the pooled cells, the PCR signal was not robust enough for detection.

3.4.3 Results of the PCR screen of individual puromycin-resistant clones

My next step in order to identify individual clones harboring the desired genetic alterations was to dissociate both the 3/3 and KO cultures consisting of pooled transfectants and plating them, via a single cell sorting, as individual cells in 96-well plates according step 6 of my CRISPR workflow shown in Figure 2.2). The single-cell sorting process facilitated the production of isolated cultures; each derived from a potentially distinct gene-editing event. The individual clones were grown up then split into two sister plates of identical 96-well formats (Section 2.3.7). From each pair of

plates, one plate allowed for lysing the cells and screening for presence of the NGN2 transgene cassette by detecting the 5' junction with the PCR assay whose optimization for scaled up capacity was outlined in Section 3.3. Meanwhile, matching sister plates were archived for later retrieval of putative hits from the screen (2.3.7.2).

Single cell sorting had yielded a total of 5 full plates totaling 480 clones per 3/3 and KO genotype cells. Clones slated for the screen were lysed and crude lysate (without gDNA purification) was directly input into the PCR reactions to deliver the PCR templates. Results of the full screen of isolated puromycin resistant clones are shown in the table in Figure 3.16, which lists all putative hits. Both genotypes showed a 2% hit rate, meaning, about 2% of clones showed a PCR band that was like that of the iNGN2-iPSC positive control line. Figure 3.16 also shows a representative gel image from the screen with asterisks (*) indicating appearance of hits. I attempted to thaw all candidate clones on the hit list for validation of the genomic insertion. Rows colored grey in the table (Figure 3.16) indicate clones that did not successfully recover from the frozen archive.

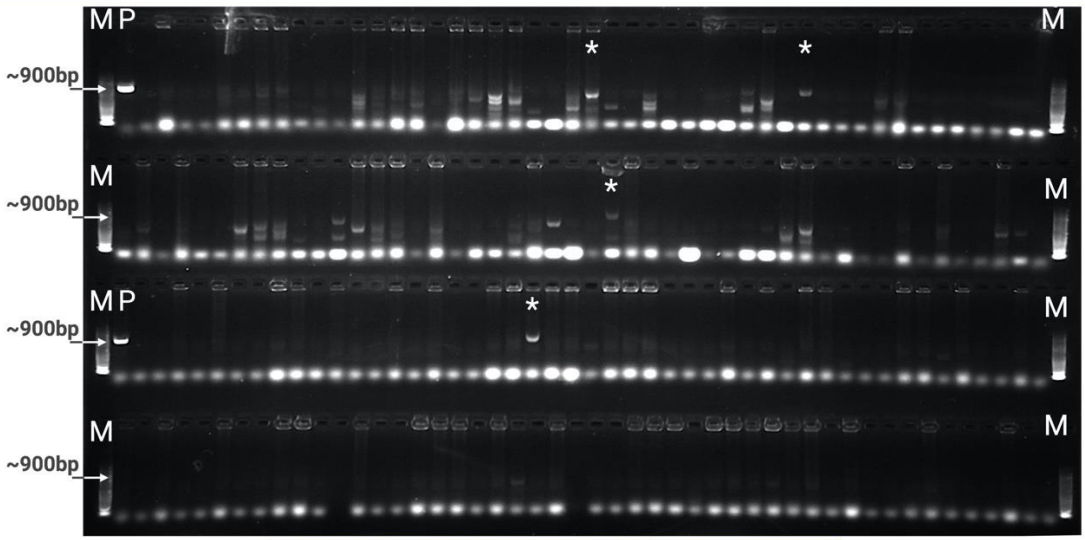

APOE genotype	Candidate positive clone to be validated (identifier)	Candidate clones from 475 wells (%)
ε3/ε3	plate 33A-well B10 (33AB10)	1.9
	plate 33B-well A11 (33BA11)	
	plate 33B-well B7 (33BB7)	
	plate 33B- well C10 (33BC10)	
	plate 33B-well H2 (33BH2)	
	plate 33B-well H9 (33BH9)	
	plate 33C-well E12 (33CE12)	
	plate 33C-well G10 (33CG10)	
	plate 33D-well H9 (33DH9)	
	plate 33E-well B7 (33EB7)	
	plate 33E-well D10 (33ED10)	
	plate 33E-well E8 (33EE8)	
	plate 33E-well E9 (33EE9)	
	plate 33E-well G12 (33EG12)	
KO	plate KOA-well A9 (KOAA9)	1.7
	plate KOA-well C1 (KOAC1)	
	plate KOA-well C12 (KOAC12)	
	plate KOA-well G2 (KOAG2)	
	plate KOA-well F11 (KOAF11)	
	plate KOB-well A7 (KOBA7)	
	plate KOB-well A10 (KOBA10)	
	plate KOB-well C6 (KOBC6)	
	plate KOB-well C11 (KOBC11)	
	plate KOB-well E6 (KOBE6)	
	plate KOB-well F7 (KOBF7)	
	plate KOB-well G3 (KOBG3)	
	plate KOE-well C9 (KOEC9)	

Figure 3.16 Results of PCR screening of isolated clones from the 3/3 and KO genotypes.

Top image is a representative agarose gel from the screening of single cell clones with the 5' INT PCR assay. "M" designates the molecular weight marker placed at either end of the 4 rows of PCR reactions loaded per gel. "P" indicates the positive control PCR reaction created by spiking in gDNA from the iNGN2-iPSC control line and shows the expected ~900 bp product. This positive control occurs in the 1st and 3rd rows. All other lanes contain PCR reactions from individual candidate clones. Asterisks (*) designate putative hits throughout the gel. The table lists all putative hits with the last column indicating the hit rate was 2% from 475 clones per genotype. Grey shaded rows indicate clones that subsequently failed to revive from frozen archived 96-well plates.

Candidate clones that successfully recovered from frozen archived plates were grown up then gDNA was extracted and subjected to validation via the same PCR assay used for screening. The PCR validation results are shown in Figure 3.17 with Table 1 confirming good quality DNA was input into these PCR reactions. The gDNA was of high purity as determined by their spectral ratios at both 260/280 and 260/230 UV absorbance, which, in pure nucleic acid samples should be close to 2.0. The PCR reaction results for 9 clones of the 3/3 genotype and 8 clones bearing the KO genotype are shown in gel images A and B. The 5'-junction PCR validation did not show evidence of AAVS1 site-specific integrants in any of the clones. The iNGN2-iPSC control line, as usual, confirmed that the PCR technique itself functioned properly.

Table 1

Purified Genomic DNA for PCR validation				
Sample ID		Conc. (ng/µl)	260/280	260/230
33	AB10	103.2	2.1	2.19
33	BB7	271.4	2.05	2.06
33	BC10	61.97	2.05	2.3
33	BH9	145	2.05	2.36
33	CE12	140.3	2.05	2.18
33	DH9	154.1	2.06	2.21
33	EB7	242.4	2.05	2.16
33	ED10	224.8	2.07	2.1
33	EE8	246.6	2.07	2.1
KO	AA9	115	2.09	2.38
KO	AC1	83.9	2.07	2.38
KO	BA7	58.56	2.14	2.46
KO	BC6	98.54	2.06	2.17
KO	BC11	154	2.07	2.18
KO	BE6	240	2.06	2.14
KO	BF7	180.3	2.06	2.12
KO	BG3	56.64	2.13	2.41
buffer		0.2494	-1.46	5.2

Table 2

Gel	Lane	Description
A	M	DNA ladder
	1	NGN2-stable positive control DNA
	2	EE8
	3	BC10
	4	BH9
	5	BB7
	6	ED10
	7	BA7
	8	BE6
	9	AC1
	10	EB7
B	M	DNA ladder
	1	BF7
	2	AA9
	3	DH9
	4	BG3
	5	BC6
	6	BC11
	7	CE12
	8	AB10
	9	no template control
	10	NGN2-stable positive control DNA

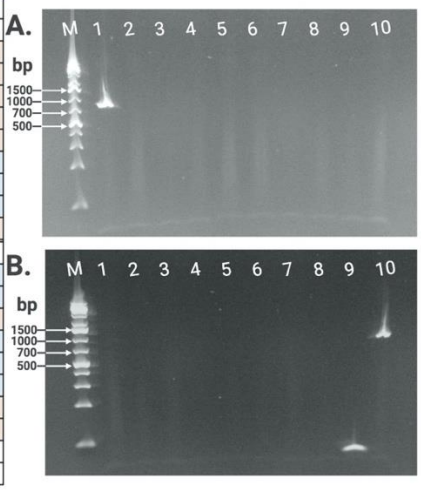

Figure 3.17 PCR validation of candidate hits from the 3/3 and KO genotypes.

Table1 confirms the DNA purified from the grown-up candidate clones was of high quality as evidenced by their spectral purity ratios at 260/280 and 260/230 respectively. Despite this, none of the clones showed evidence of transgene integration via the 5'-integration PCR assay. PCR results for 9 clones with the 3/3 genotype and 8 clones with the KO genotype are dispersed throughout gels A (lanes 2 -10) and B (lanes 1 – 8); the description of each lane being listed in Table 2. The NGN2-stable iPSC line positive control appears in gel A, lane 1 and gel B, lane 10.

Results of additional assessments of candidate clones are shown in Appendix G.

3.5 Discussion

3.5.1 Neuronal induction in the iNGN2-iPSC control line

Morphological observation and molecular characterization of iNs validated that the iNGN2-iPSC control line, wherein CRISPR technology was used to target the integration of inducible NGN2 into

the AAVS1 locus, successfully differentiated into neurons upon exposure to doxycycline. Induction of neuronal morphology, transcripts (*GAP43*, *MAP2*, *SV2B*, *SYP*, and MAPT) and protein expression (neuronal tubulin β3) were all indicative of successful conversion to neurons. The observation of lowered APOE mRNA upon differentiation is consistent with the notion that neurons generally do not express ApoE. Robust levels of ApoE mRNA and protein had been reported in human embryonic stem cells, but not in the Ngn2-neurons differentiated from them (132). ApoE expression is instead expected to increase in neurons when they are exposed to stressed conditions and, the hypothesis being, neuronal ApoE expression would then be stimulated for reasons of neuroprotection or repair (194).

It was promising to note that iNs expressed GRIA3 and GRM1 glutamate receptor mRNA suggesting the potential that these cells could develop sensitivity to glutamate, as I intended to eventually evaluate responses to glutamate-induced excitotoxicity in this platform. In keeping with a view towards *APP* as playing pathologic roles in AD, I evaluated its transcription, and it was interesting to observe the lack of increased *APP* transcription in iN cells. Increased *APP* has been documented in mouse neurogenesis and human iPSCs (195). However, a publication has contradicted the other reports and described no significant changes in *APP* mRNA expression between undifferentiated iPSCs and the neurons differentiated from them (196). Differing results probably stem from different culture systems or neuronal maturation stage or human variability in genetic background.

3.5.2 Rethinking the CRISPR-based genome editing approach

Despite functional incorporation of the selectable markers, I was unable to isolate a single recombination event that evidenced desired stable inducible-NGN2 integration. Puromycin resistance of candidate single cell clones and detection of the puromycin N-acetyltransferase protein which underpins puromycin resistance evidenced some form of integrant of the donor template DNA into the genome. PCR analysis of these candidate clones designed to selectively identify the predicted integration at the AAVS 1 junction did not detect the anticipated PCR amplification products. This suggests a confounding insertion outside of the AAVS1 site. The donor DNA template was transfected into the iPSCs via electroporation, a method that has also been shown to promote random transgene integration in primary cells in general (197). In other transgenic approaches transient transfection, via electroporation, of conventional plasmids can indeed generate cell lines harboring multiple random integrations (198, 199).

Failure of doxycycline treatment to convert mis-integrated transgenic puromycin resistant candidate iPSCs to neurons could suggest silencing of the inducible NGN2 portion of the

transgene cassette. A high frequency of transgene silencing produced by the positional effects at the integration site is a known confound when genetically editing stem cells. Indeed, this issue is the reason behind targeting the silencing resistant AAVS1 locus in the first place (186, 200). An alternative explanation for the lack of neuronal differentiation in the face of retention of puromycin resistance could be that there was only partial insertion of the donor template DNA. It has been reported that insert knock-in effectiveness is influenced by the format of the donor DNA template. Besides a circular plasmid (which I have used), linearized plasmid (double stranded DNA) or single-stranded DNA oligonucleotides (ssDNA) can be also used. Some researchers observed that linearized plasmid is more effective than circular plasmids and suggested that circular DNA can be intracellularly broken randomly at unwanted locations, compromising important parts of the transgene or possibly resulting in incomplete integration of the full transgene (201, 202).

My colleagues' development of the iNGN2-iPSC control line, as well as other successful AAVS1 targeted CRISPR-mediated insertional editing examples in the literature had influenced my rationale. Circular DNA plasmids have been favored by some groups as they allow for efficacious introduction of the transforming DNA (200, 203).

I went back to the literature as well as conducted discussions with CRISPR and stem cell experts, and found, in retrospect, this editing approach is much more complicated than I originally envisioned. After the CRISPR system generates a programmable DSB, the repair function that cells choose to fix this damage is not under the control of the experimenter. Herein lies an important limitation of the technique. Successful homologous recombination-dependent insertion of the donor DNA sequence relies on the low frequency HDR pathway. Different cell lines show differing HDR rates and integration efficiencies, moreover, longer templates, such as entire sets of genes, integrate far less efficiently than shorter sequences carrying point mutations (personal communications with members of the Harvard Stem Cell core and Feng Lab at the Broad Inst.) (204).

An investigation of the full diversity of repair results in CRISPR-based knock-in studies reported that template DNA integration is highly heterogeneous and condition-dependent and that repair pathways needed for integration are more cell- and donor-type dependent than previously appreciated in the field (202). Unexpectedly, *bona fide* HDR made up the minority of integration events (202). Interestingly, the scientists discovered unintentional HDR donor template plasmid bacterial backbone sequences resulting from mis-integration into the genome of CRISPR-engineered cattle, reinforcing the complexities surrounding the HDR (205).

Another underappreciated element of Cas9 is the extent that concentration can affect nuclease specificity and activity strength. One study showed that a 5-fold drop in concentration generated a 7-fold increase in the specificity of the nuclease, but with a concurrent ~2-fold decrease in on-target efficiency (206). The targeting efficacy of the same gRNA can be different amongst different cell lines and the optimal template DNA amount also requires suitable customization (200, 203). I had underestimated the need to optimize the HDR template DNA electroporation concentrations and gRNA efficacy to adjust for specificity and efficacy for every given cell line. I could now pursue steps towards optimization of my CRISPR approach, but my limited success achieved using this method led me to consider alternative and potentially more efficient approaches to introducing the NGN2 into the many APOE stem cells lines with which I had planned to work.

Furthermore, I noticed that a separate line of emerging reports is beginning to question the actual "safety" of the AAVS1 safe harbor in iPSCs. Expression of a calcium indicator reporter transgene inserted at the AAVS1 locus in iPSCs was highly variable across several clones. Furthermore, upon differentiation of the higher expressed clones (to cardiomyocytes) the transgene was silenced (207). A separate study evaluated different myeloid specific promoters in iPSCs that were integrated into the AAVS1 locus and observed differential promoter performance with one promoter being prone to silencing (208). These publications illustrate the possibility that what has been accepted to be a dependable transgene integration locus is not necessarily as perfect as thought for iPSCs.

I concluded that it would not be practical, in terms of time constraints, to further this approach; especially since I aimed to engineer 8 independent cell lines. Rather than spend the rest of the PhD time generating CRISPR-edited clonal lines, I pivoted towards a quicker editing approach, based on lentiviral delivery of inducible-Ngn2 to the iPSCs. This change in strategy allowed me the opportunity to get to some APOE genotype functional data within the doctoral degree timeframe. The next chapter discusses my lentiviral-mediated genetic editing approach and ends with my performing yet another pivot regarding my intended strategy because the engineers of the lines in Figure 3.11, realized that CRISPR editing created unintended insertions rendering disruptions in one allele each of the $\varepsilon 2/\varepsilon 3/\varepsilon 4$ variants (Section 4.5).

Chapter 4 Lentiviral-mediated genetic editing approach for generating an Ngn2-induced neuronal (iN) platform

In the previous chapter, I investigated homologous recombination of an inducible NGN2-containing, 9 kb long genetic cassette into the AAVS1 locus of iPSC lines of interest. I used a CRISPR-assisted genome editing method which colleagues had demonstrated could successfully generate a stably integrated NGN2-iPSC line (which I validated in Section 3.2). After screening 475 derivative monoclonal cultures per iPSC line and evaluating putative positively edited clones, I was not able to isolate NGN2 integrated genomes. In face of the challenges with my preferred CRISPR-assisted insertion of the inducible NGN2 transgene, I considered another approach to generate the desired platform, namely, a suite of human stem cells capable of neuronal induction in which the genetic background variation is limited only to the *APOE* genotype. I switched to a lentiviral-mediated genetic editing strategy because this procedure has been used successfully and repeatedly by different research groups (151, 182).

4.1 Lentiviral mediated iN platform validation

An overview of my approach for generating a lentiviral mediated iN platform is diagrammed in Figure 4.1. I transduced each of the 8 originating iPSC lines (listed in Table 2.1) with and without an inducible-EGFP lentiviral vector (LV-iEGFP) that served as a monitoring control (details of the lentivirus constructs are in Section 2.4.1 and Figure 2.8). In other words, transductions occurred in 2 formats, either: (1) only the 2 vectors necessary for neuronal induction: inducible-NGN2 and puromycin resistance gene lentiviral vector (LV-iNgn2/pac) and constitutive reverse tetracycline transactivator lentiviral vector (LV-rtTA) (A and B in Figure 4.1), or (2) all 3 viral vectors (A, B, and C in Figure 4.1).

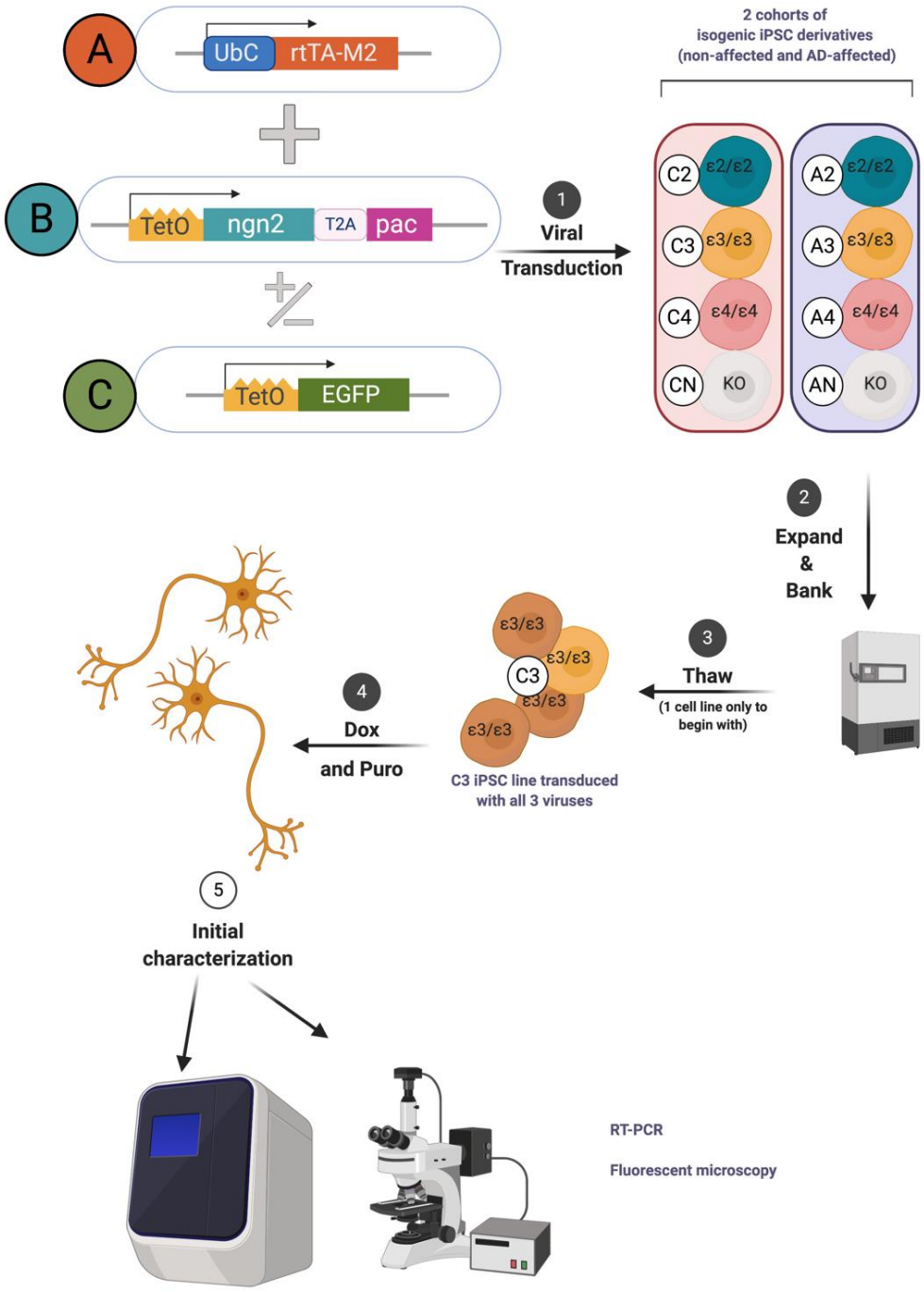

Figure 4.1 Workflow for lentiviral-assisted stable integration of inducible Ngn2.

I co-transduced 8 iPSC lines with lentiviral vectors driving expression of rtTA (A) and inducible Ngn2 and puromycin resistance (B), and/or inducible EGFP (C) (step 1). The resultant 16 transduced cultures were expanded then cryopreserved (step 2). The next steps were to thaw (step 3), treat with doxycycline and puromycin (step 4) and characterize iNs via microscopy and transcriptional profiling (step 5).

Thus, I simultaneously generated a total of 16 derivative transduced lines (via method detailed in Section 2.4.2). The lines comprised of a set of iPSCs engineered to express doxycycline-inducible Ngn2 and puromycin resistance with a matching set that, additionally, expresses doxycycline-

inducible EGFP. All 16 cell lines were expanded for several passages then cryopreserved as iPSCs (not iNs) and are identified as "Banked potential neuron source" in Table 4.1.

Table 4.1 Potential neuron sources for my platform for studying neuronal ApoE.

Original iPSC	Derivative	APOE status	Inducible Ngn2 transduction	Inducible EGFP transduction	New iPSC line name	Banked potential neuron source
BIONi010-C (APOE 3/4; non-demented subject)	BIONi010-C-3	KO	✓	✗	CKO-Ngn2	✓
			✓	✓	CKO-Ngn2-G	✓
	BIONi010-C-6	E2/E2	✓	✗	C22-Ngn2	✓
			✓	✓	C22-Ngn2-G	✓
	BIONi010-C-2	E3/E3	✓	✗	C33-Ngn2	✓
			✓	✓	C33-Ngn2-G	✓
	BIONi010-C-4	E4/E4	✓	✗	C44-Ngn2	✓
			✓	✓	C44-Ngn2-G	✓
UKBi011-A (APOE 4/4; patient with AD)	UKBi011-A-1	KO	✓	✗	AKO-Ngn2	✓
			✓	✓	AKO-Ngn2-G	✓
	UKBi011-A-2	E2/E2	✓	✗	A22-Ngn2	✓
			✓	✓	A22-Ngn2-G	✓
	UKBi011-A-3	E3/E3	✓	✗	A33-Ngn2	✓
			✓	✓	A33-Ngn2-G	✓
	UKBi011-A	E4/E4	✓	✗	A44-Ngn2	✓
			✓	✓	A44-Ngn2-G	✓

4.2 Characterization of iN differentiation in a triple transduced Ngn2-iPSC line

The general procedure to drive neuronal induction for the lentiviral platform cells is like that used for CRISPR-edited iNGN2-iPSC control line (demonstrated in Section 3.2.2, with methods detailed in Section 2.2.11 and variations documented in Section 2.4.3) and a schematic of the lentiviral-mediated protocol is shown in Figure 4.2. For one of the 16 lines from Section 4.1, in addition to banking frozen aliquots of transduced cells, I also replated some and took them forward for validation of neuronal differentiation. The line which I tested was the triple transduced C33-Ngn2-G iPSC line (3/3 genotype from the non-AD individual). The yellow stars in Figure 4.2 represent

progression points along the process at which cells are exposed to (A) doxycycline for 2 days and eventually to (B) a combination of doxycycline (5 days) and puromycin (3 days). It is at these points, A and B, that I assessed neuronal conversion of the C33-Ngn2-G line via microscopy and transcriptional profiling, in a similar manner as was performed in Section 3.2.3.

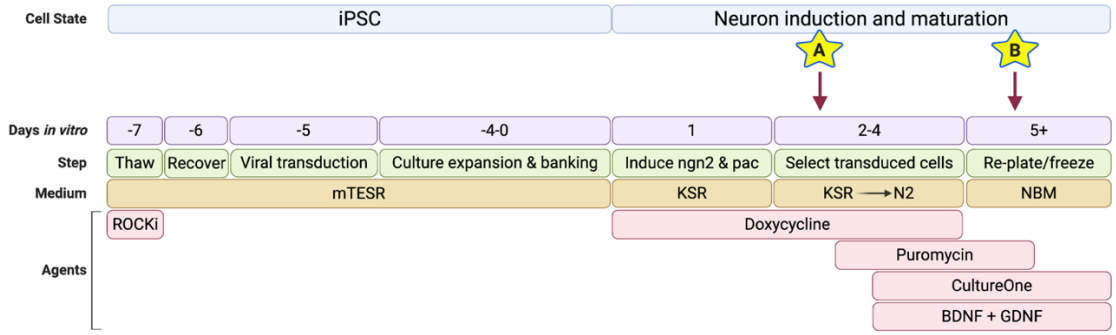

Figure 4.2 Schematic delineating iPSC viral transduction, banking, and iN conversion.

In the first week upon thawing of iPSC stocks, I transduced iPSCs with lentiviral vectors, expanded, then froze them down in their undifferentiated state. When generating iN cultures, Day 0 represents addition of doxycycline to transduced iPSCs triggering Ngn2 expression and neuronal induction. Two days later, puromycin is to be added while progressively switching to neuronal media by 5 days following doxycycline exposure. Agents that either support neuronal maturation (BDNF and GDNF) or suppress proliferation of potentially remaining progenitors (CultureOne supplement) are to be added at this point. The yellow stars A and B represent the points at which I took the photomicrographs shown in Figure 4.3 and harvested cells to yield the data in Figure 4.4 during my first test of the system using C33-Ngn2-G iPSCs.

4.2.1 Morphological characterization

Within 48 hours of doxycycline exposure, I observed clear EGFP expression in a subset of cells which suggested successful viral transduction and incorporation of the vectors (Figure 4.3, panel A). By 5 days of doxycycline exposure, the culture uniformly showed cells with pyramidal cell bodies from which neurite processes were emerging (Figure 4.3, panel B); consistent with neuronal induction and suggesting that the inducible Ngn2/pac cassette was functioning properly. Addition of puromycin to the cultures had caused cell death amongst cells that did not exhibit neuronal morphology; further providing confidence that the system was working as expected.

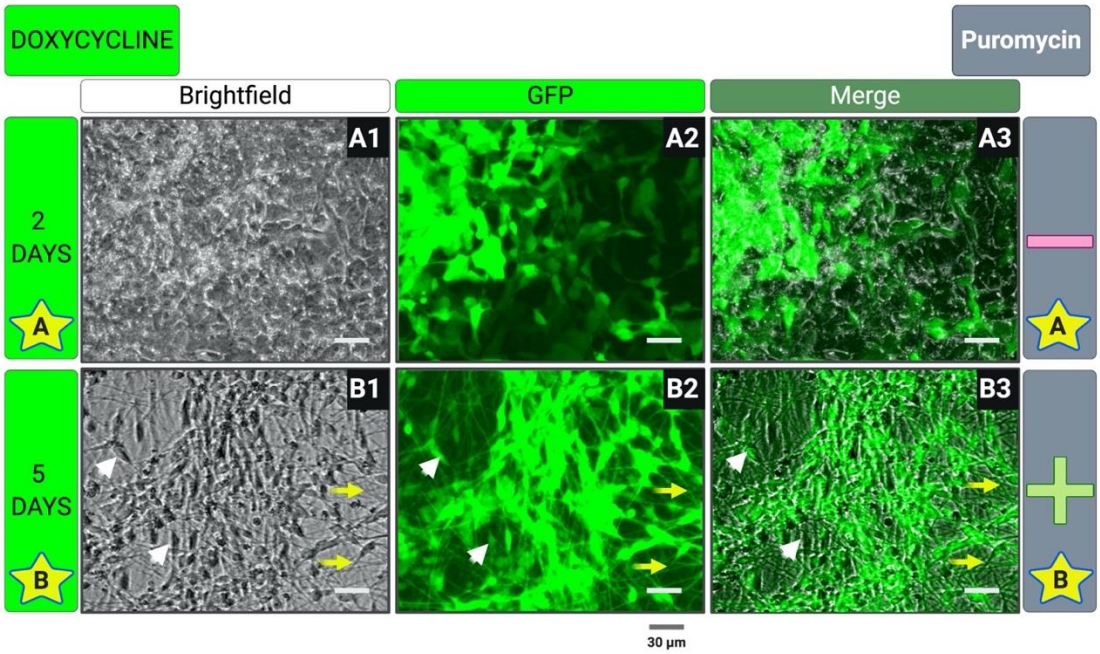

Figure 4.3 Inducible neurons from an iNgn2-iPSC line (APOE3/3).

Panels A and B correspond to timepoints A and B in Figure 4.2, respectively. Panel A shows the C33-Ngn2-G line (from Table 4.1) treated with doxycycline for 2 days in the absence of puromycin. Fluorescence microscopy in the GFP channel (A2) showed that a subset of cells expressed EGFP. Panel B shows the same culture after 5 days of doxycycline with puromycin co-treatment during the latter 3 days. At this point, the culture homogenously consisted of EGFP-expressing cells and these cells also uniformly show neuronal morphology (B2). White arrow heads point to pyramidal cell bodies and yellow arrows point to neurites (B1, B2, B3). Appendix I shows zoomed out images of these cultures.

4.2.2 Transcriptional characterization

I next performed RT-PCR on mRNA extracted from the C33-Ngn2-G line exposed to 2 different treatments shown in Figure 4.3, namely, doxycycline administration at: (A) 2 days and (B) 5 days with co-administration of puromycin during the last 3 days. I quantified the relative expression of several transcripts that support the induced expression of neuronal genes (similar transcriptional profiling as to what I had done in the Section 3.2.3). Transcript levels of the genes encoding the pan-neuronal markers *GAP43* and *MAP2*, as well as, synapse associated transcripts, *SV2B* and *SYP*, increased in a time-dependent manner (Figure 4.4, a). All of them increased in the range of 32- and 64-fold by the 5-day timepoint. The glutamate ionotropic and metabotropic receptor subunits, *GRIA3*, *GRM1*, *GRIK1*, and *GRIN2D* were assessed. *GRM1* and *GRIK1* showed at least 2-fold upregulated levels, compared to progenitors, by 5 days of doxycycline treatment while GRIA3 and *GRIN2D* did not show appreciable changes (Figure 4.4, b). MAPT levels increased in a time-dependent manner while the *APP* transcript showed no change at 2 days then a marked increase of over 4000-fold at 5 days (Figure 4.4, c). *APOE* transcript levels decreased by about 80% in the neuronal context by 5 days (Figure 4.4, d). There was no obvious change in LRP1 transcription (d).

The data are representative of one culture passage in which the mRNA was isolated from three separate wells of a 6-well plate.

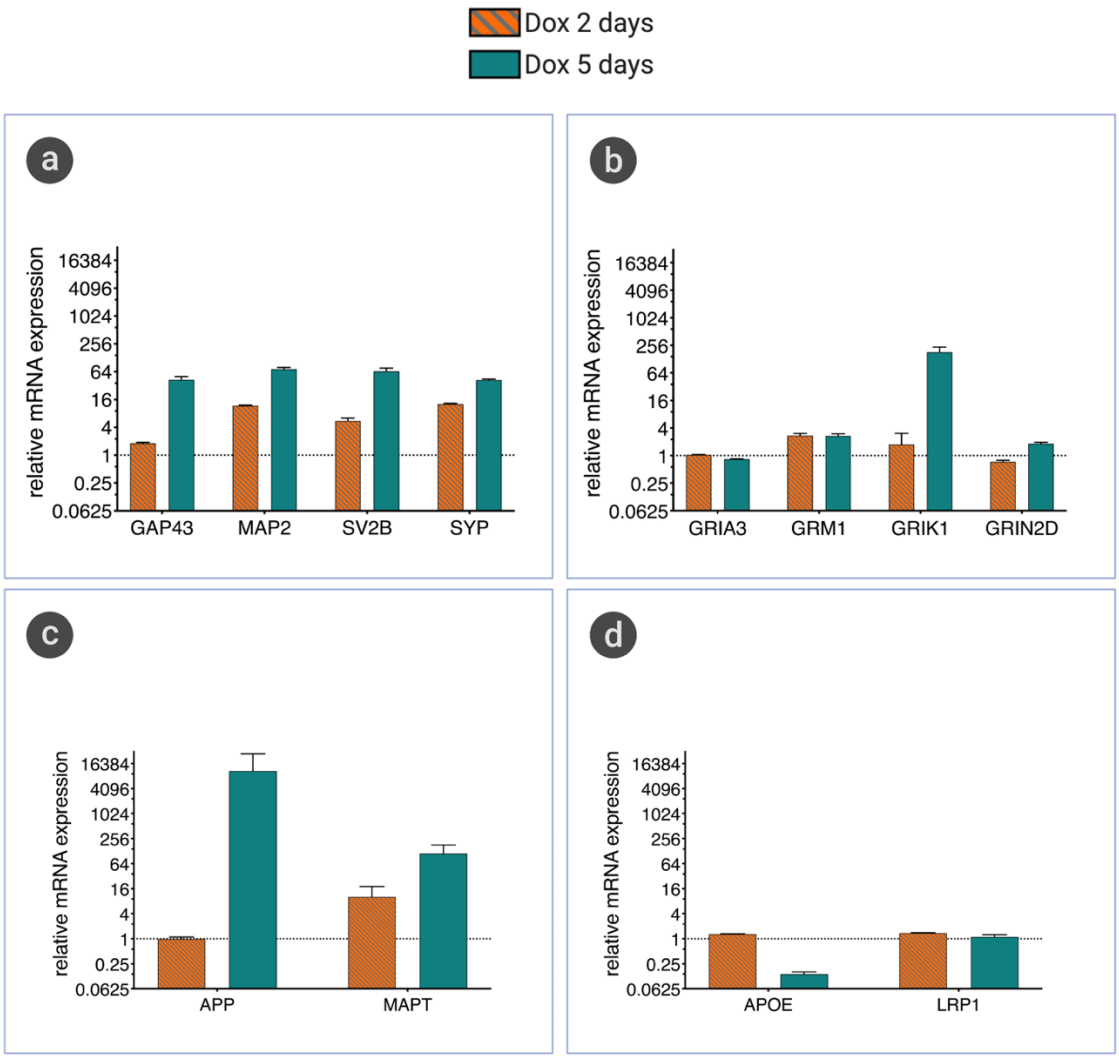

Figure 4.4 Transcriptional profiling of C33-Ngn2-G cultures after exposure to doxycycline.

Real time PCR results of several neuronal transcripts compared to the undifferentiated state which is designated as baseline (dotted line) at two days doxycycline (striped bars) and at five days with doxycycline with puromycin co-administered in the last 3 days (solid bars). *GAP43*, *MAP2*, *SV2B*, and *SYP* all increased (a). GRM1 and GRIK1both increased while there was no change in GRIA3 or GRIND2D levels (b). By five days, MAPT and *APP* transcripts both increased (c). APOE transcript decreased while LRP1 transcription rate remained unchanged (d). Error bars are the SD from three separate wells of a 6-well plate (3 technical replicates; only 1experiment).

I also evaluated two markers for glutamatergic neurons, transcripts that had not been assessed in my earlier work on the CRISPR-edited iNGN2-iPSC control line, encoded by the solute carrier family 17 member 6 (*SLC17A6*) and member 7 (*SLC17A7*) genes, which code for VGLUT2 and VGLUT1 respectively. Both transcripts showed robust time-dependent induction of expression. At the 2-day timepoint, *SLC17A6* levels exhibited 4-fold greater amount than that observed in progenitor cells and these levels rose to over a 250-fold induction at day 5 (Figure 4.5). *SLC17A7*

levels at the 2-day timepoint were 15-fold greater than levels observed in progenitor cells and further increased to over 32-fold at day 5 (Figure 4.5).

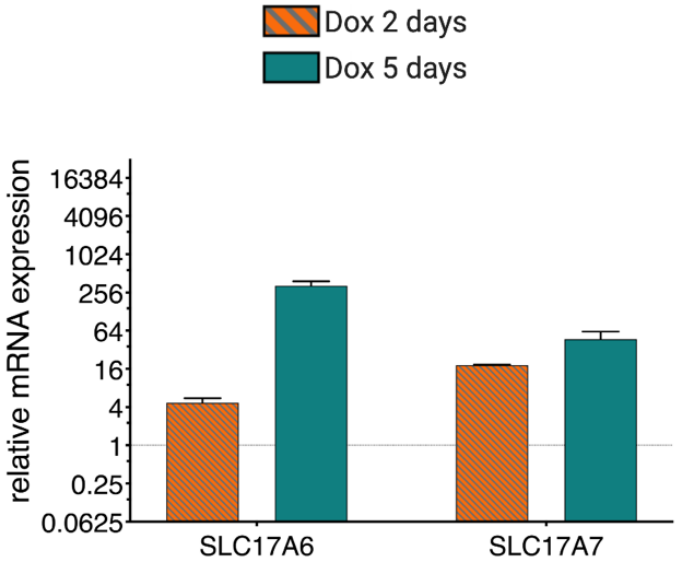

Figure 4.5 Transcriptional confirmation of glutamatergic markers in iN cultures.

Real time RT-PCR evaluation of expression of both *SLC17A6* and *SLC17A7*, the genes encoding VGLUT2 and VGLUT1, respectively, at both two (striped bars) and five (solid bars) days of doxycycline administration in the C33-Ngn2-G line (from Table 4.1). Error bars are the SD from three separate wells of a 6-well plate (3 technical replicates; only 1experiment).

4.3 Transcriptional comparison between iNs from the two genome editing approaches

Having at this point in my project collected transcriptional data on two independent (non-isogenic) *APOE* ε3/ε3 iN cultures (both from non-AD donors) that were generated using distinct genomic editing strategies, I compared the data sets to each other. The directionality of most transcripts was concordant. The classic neuronal and synaptic genes, GAP3, *MAP2*, *SV2B*, and *SYP* all increased ≥ 8-fold (Figure 4.6, a). The glutamate receptor subunit, *GRM1*, consistently increased 2-fold of their respective parental line, while *GRIA3* increased only in one of the 2 lines (Figure 4.6, b). Regarding the genes associated with AD-related pathology, *MAPT* exhibited increased magnitude of expression in both cases (≥ 16-fold induction), whereas *APP* increased over 4000-fold in the lentiviral-generated line and remained unaltered in the CRISPR-generated line (Figure 4.6, c). This difference could be downstream of a human specific genetic background factor. In both iN cultures, *APOE* was reduced while *LRP1* transcript levels remained stable compared to their stem cell stage (Figure 4.6, d).

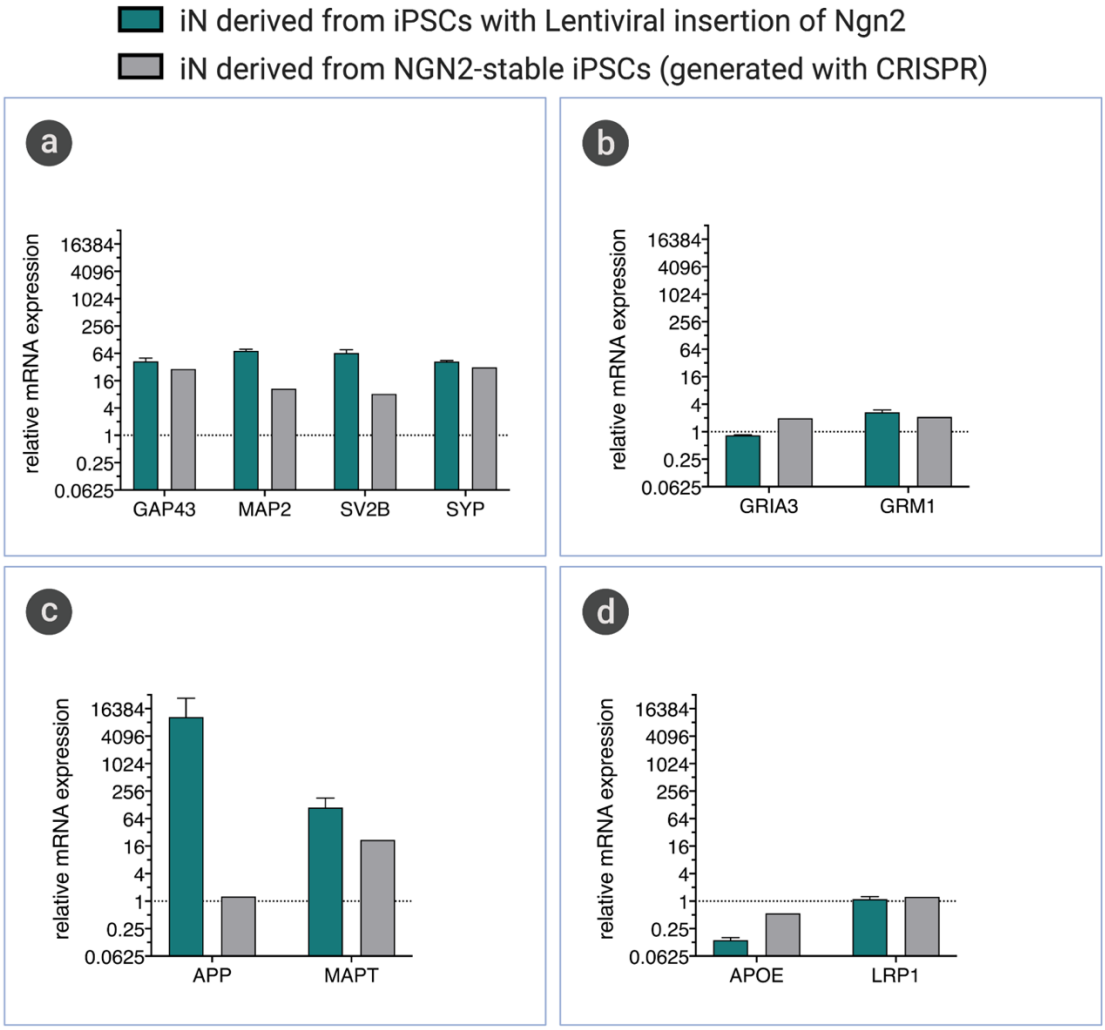

Figure 4.6 Comparison of transcriptional profile between APOE3/3 iN cultures.

RT-PCR analysis of neuronal transcripts in iNs from two different genetic backgrounds and editing approaches showed similar transcript profiles, for the most part. Expression levels are expressed as a ratio of the respective parental line (which was set to 1, dotted line). Error bars for the blue columns represent mean and SD from 3 culture dishes (technical replicates) while the data for the grey columns was from a single dish.

4.4 APOE genotype verification

I decided to doublecheck the APOE variant of the iPSC lines prior to embarking on the biological questions I aimed to investigate. I extracted genomic DNA from the triple lentiviral-transduced cells I had banked (Table 4.1) and conducted PCR using commercial primer and probe sets that specifically recognize the two SNPs associated with the three APOE alleles. This genotyping method is described in the Section 2.5.3. I found that the ε22 and ε33 derivative lines from the control donor, C22-Ngn2-G and C33-Ngn2-G, did not show the expected genotypes (Table 4.2). All the lines derived from the donor with AD matched up with their purported APOE allele homozygosity (Samples 5, 6, 7, and 8 in Table 4.2).

Table 4.2 Interpretation of the APOE SNP genotyping assay results.

ID	Sample #	Rs429358 Automated Call (Expected call)	Rs7412 Automated Call (Expected call)	Genotype Observed
C22-Ngn2-G	1	Homozygous C/C (T/T)	Homozygous T/T (T/T)	unknown
C33-Ngn2-G	2	Homozygous C/C (T/T)	Homozygous C/C (C/C)	e4e4
C44-Ngn2-G	3	Homozygous C/C (C/C)	Homozygous C/C (C/C)	e4e4
CKO-Ngn2-G	4	Heterozygous C/T (C/T)	Homozygous C/C (C/C)	e3e4
A22-Ngn2-G	5	Homozygous T/T (T/T)	Homozygous T/T (T/T)	e2e2
A33-Ngn2-G	6	Homozygous T/T (T/T)	Homozygous C/C (C/C)	e3e3
A44-Ngn2-G	7	Homozygous C/C (C/C)	Homozygous C/C (C/C)	e4e4
AKO-Ngn2-G	8	Homozygous C/C (C/C)	Homozygous C/C (C/C)	e4e4
No Template	9	Undetermined	Undetermined	none

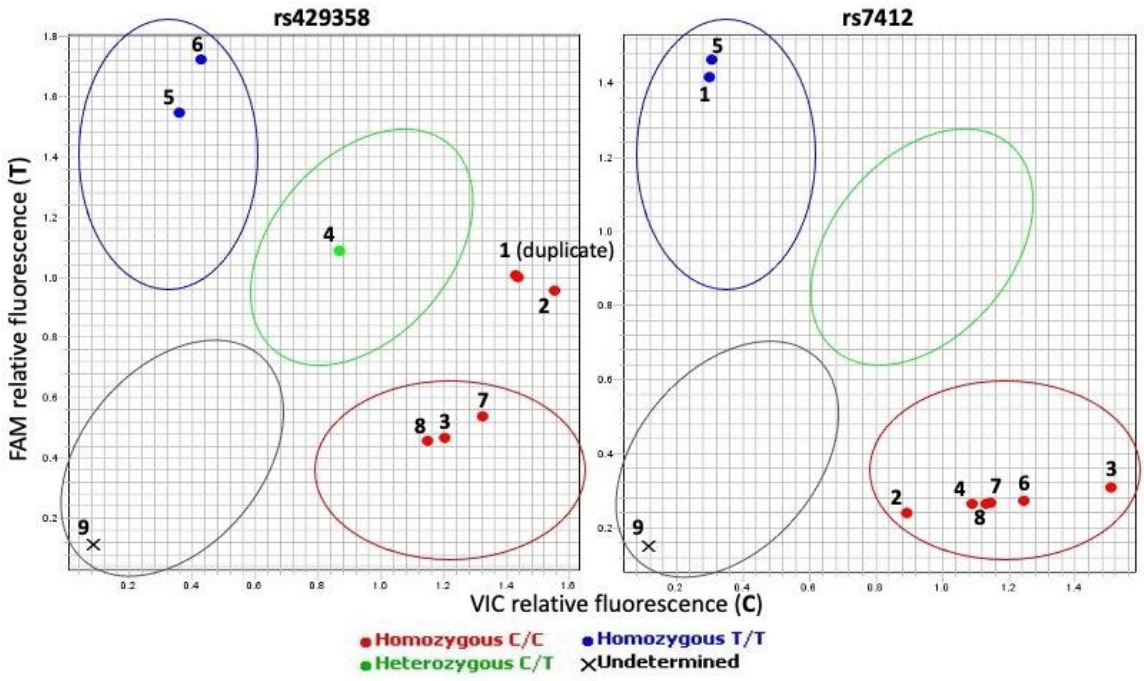

Figure 4.7 *APOE* allelic discrimination plot for 8 iPSC lines.

The relative fluorescent signals from the *APOE* SNP PCR are shown for the 2 sets of *APOE*-variant, inducible-Ngn2 carrying isogenic sets of iPSC lines that were intended for differentiation and maturation investigation. The numbers depict the lines identified in Table 4.2. Lines 1 to 4 were derived from the individual without AD while Lines 5 to 8 originated from the donor with AD and sample number 9 represents the no template PCR control. The assay results for the SNP ID rs429358 are shown on the left and results for SNP ID rs7412 are plotted on the right plot. The interpretation of APOE variant based on the fluorescent signals is shown in column "Genotype Observed" of Table 4.2. All except lines 1 and 2 matched the expected APOE genotype. The relative fluorescence for lines 1 and 2 in the rs429358 assay did not fall into a clearly identifiable segment of the plot and the automated SNP calling method of the software grouped these as homozygous C/C, whereas they were expected to be homozygous T/T but they did not fall anywhere near this threshold. All other samples showed clear results that matched expectations.

4.5 Discussion

I used double and triple lentiviral vector transductions to generate morphologically tractable inducible-Ngn2 iPSCs. This was verified by treatment of the C33-Ngn2-G iPSC line (Table 4.1) with doxycycline which showed time-dependent induction of neuronal morphology. While not required for neuronal differentiation, inducible EGFP provided for inducible cytoplasmic expression of fluorescence as an opportunity to monitor and track viral transduction efficiency and cell morphology. The EGFP reporter helped visualize the emergence of neuronal morphology and highlighted the neuronal homogeneity of the culture validating that puromycin killed off all non-transduced cells.

Transcriptional profiling of neuronal markers further validated that conversion to neurons was successfully taking place. Amplification of the designated gene transcripts confirmed induced expression of neuronal markers upon doxycycline treatment compared to the parental, undifferentiated state (no doxycycline exposure). My studies confirmed that by 5 days of induction, the pan-neuronal markers, *GAP43* and *MAP2*, as well as, the synapse associated transcripts, *SV2B* and *SYP*, robustly increased. Glutamate ionotropic and metabotropic receptor subunit markers, GRM1 and GRIK1, both increased as well did the MAPT and *APP* transcripts. The literature indicates that iN cultures generated by Ngn2 overexpression are reminiscent of cortical excitatory neurons (151). For these reasons I decided to also evaluate transcript levels of markers for glutamatergic neurons: vesicular glutamate transporter 1 (VGLUT1; whose gene name is *SLC17A7*) and vesicular glutamate transporter2 (VGLUT2; whose gene name is *SLC17A6*). As their names suggest, they function in the uptake of glutamate into synaptic vesicles at the presynaptic nerve terminals of excitatory neurons. Both were strongly induced by 5 days of doxycycline exposure.

Consistent with a recent publication (as well as the previous observations in the CRISPR-edited iNGN2-iPSC control line) the *APOE* transcript decreased upon neuronal induction (209). I also gathered side-by-side data for the other common transcripts I had analyzed between these 2 iN cultures. Most transcripts changed in a similar manner except for the *APP* mRNA, which was strikingly different. There was no change in the CRISPR-generated line and a robust induction in the lentiviral-mediated line. The reason for this difference is unknown. Interestingly, both observations have been reported for neuronal cultures differentiated from iPSCs. For example, in a study using culture-driven neuronal differentiation protocol of 120 days of differentiation in 2 independent iPSC lines, no significant change in *APP* mRNA expression was observed even though mature neuronal phenotypes were documented (196). The difference could also arise from other factors like genetic background of different donors or whether cell density affects neuronal rate of conversion and maturation. One limitation of my study is that these samples were collected from a single round of differentiations each.

My SNP genotyping assays aimed at verifying the samples before embarking on the next phase of experiments alerted me to mismatches in the expected *APOE* genotype of the iPSC line characterized in this chapter. Subsequent literature reports confirmed this finding, as well as CRISPR-related discrepancies in lines derived from the individual without AD. Although initially both the APOE2/E2 BIONi010-C-6 and the APOE3/E3 BIONi010-C-2 lines passed all quality controls, the authors afterwards discovered two unexpected CRISPR-editing related abnormalities: 1) Both BIONi010-C-6 and BIONi010-C-2 lines contained one disrupted *APOE* SNP, in one allele, owing to aberrant partial insertion (3.4 kb) of the plasmid used as the cloning

backbone for the sgRNA; 2) BIONi010-C-4 (APOE e4/e4) contained a 5.4 kb insertion of the cloning plasmid that disrupted one SNP in one of the two APOE alleles (173). These issues rendered these 3 lines as having one functioning and correct *APO*E allele. To avoid confounds from these *APOE* hypomorphs, I decided to move forward with the other cohort of iPSCs generated from the donor with AD as they all showed expected *APOE* genotypes and were since validated as having the correct CRISPR editing upon deeper characterization (personal communication with the group that performed the editing experiments).

Chapter 5 Ontogeny of Neuronal Development from iPSCs Harboring Distinct *APOE* Genotypes

5.1 Introduction

While astrocytes are the major source of ApoE in the brain, neurons express ApoE when stressed or injured (Section 1.10.2.1). The extent to which neuronal ApoE impacts neuronal function or contributes to AD pathogenesis remains poorly understood (Section 1.10). My project is driven by the question as to whether the neuronal expression of ApoE and, by extension, its distinct isoforms have differential effects on neuron form and function. Developing a platform to address this will further allow me to probe whether these variants contribute differently to neuronal resilience under stress states that may ultimately translate to differential impact on neurodegeneration underpinning diseases like AD.

Chapter 4 described how I developed a platform suitable for evaluating the neuron autonomous effects of ApoE in pure populations of human cortical neurons. I validated and optimized a workflow in which insertion of inducible NGN2 and GFP genes allowed iPSCs to convert into neurons while simultaneously displaying a fluorescent marker to visually track morphological changes. I had frozen down several iPSC lines after transducing them with the lentiviral vectors that enabled doxycycline inducible NGN2 and GFP (Table 4.1).

Here, I investigate the *APOE*-variant impact on neuronal differentiation and subsequent maturation using the isogenic iPSC lines originating from the donor with AD. Again, they are already engineered for: homozygosity of the three key *APOE* alleles and inducible NGN2 and inducible EGFP genes. For clarity, the iPSC lines used in this investigation are listed in Table 5.1. Although the *APOE* KO line could have served as a loss-of-function comparator that could help reveal the ApoE function in neurons, I chose to not move forward with it now in because of resource limitations. The option to evaluate this line in the future remains.

Table 5.1 Cell lineages for evaluating *APOE* status on iN culture development

EBiSC iPSC Line Name (210)	APOE Genotype	Inducible NGN2 and GFP edited iPSC name (CROSSREF Chap 4)	Short Name in Chapters 5 and 6
UKBi011-A-2	$\varepsilon 2/\varepsilon 2$	A22-NGN2-G	22
UKBi011-A-3	$\varepsilon 3/\varepsilon 3$	A33-NGN2-G	33
UKBi011-A	$\varepsilon 4/\varepsilon 4$	A44-NGN2-G	44

I assessed potential differential phenotypes by comparing, in parallel, culture morphology, viability, and transcriptional landscape. I analyzed transcripts in 3 stages: (1) early time point verification of crucial transcripts (*NGN2* and *APOE*), (2) longitudinal assessment over four weeks of targeted transcripts (Methods Section 2.5.4) that benchmark neuronal development and (3) endpoint assessment, at 28 days post-induction of neurons, of a broad set of >700 genes associated with neuropathology (Methods Section 2.4.3.2). Figure 5.1 is a schematic of these experiments.

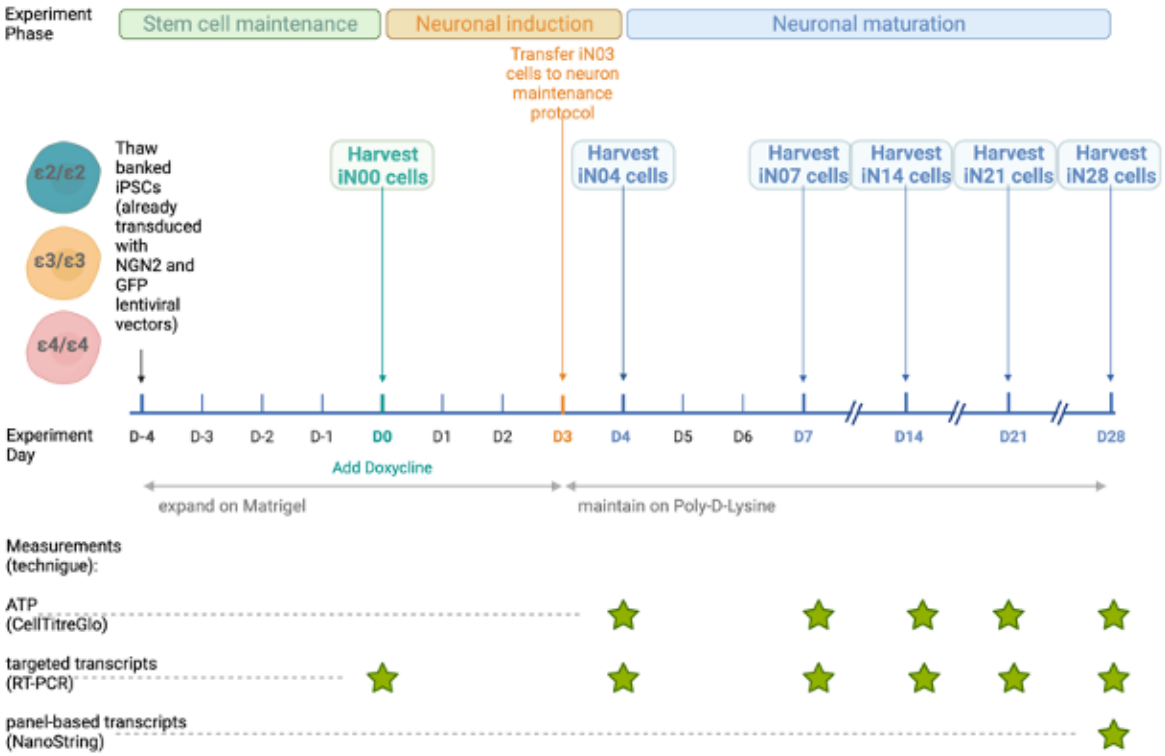

Figure 5.1 Experiment timeline and intersecting sampling points to map functional and transcriptional readouts across neuron culture development.

Summary of the steps for induced neuron generation from isogenic iPSCs homozygous for the different *APOE* alleles and maturation to 28 days, in parallel. Stars demarcate the days at which cultures were monitored for: ATP levels, a small set of targeted transcripts via RT-PCR (longitudinal assessment), and 760 panel-based transcripts via NanoString Technology (endpoint assessment).

5.2 All three APOE-variant iPSC isogenic lines showed similar levels of NGN2 induction

Forced expression of NGN2 triggered the conversion of iPSCs to neurons (Section 4.1). I compared mRNA levels of *NGN2* via RT-PCR in iPSCs (iN00) and four days after doxycycline exposure (iN04)

in the three *APOE*-variant isogenic lines. Results, shown in Figure 5.2, indicated *NGN2*, though not detected in the stem cell condition (iN00), was clearly detected in the induced neurons (iN04) at similar levels for each *APOE*-variant line.

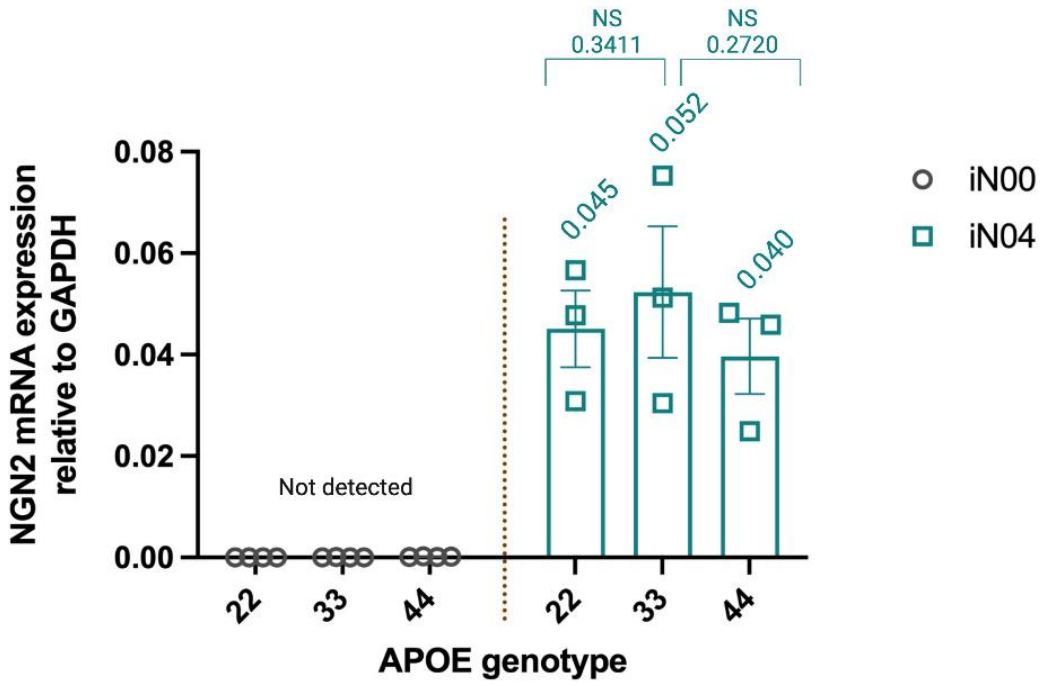

Figure 5.2 *NGN2* expression in iN00 versus iN04 cultures with distinct *APOE* genotypes.

NGN2 mRNA relative to *GAPDH* expression is shown in iPSCs (iN00, left side) and Day 4 induced neurons (iN04; right). The X-axis depicts the *APOE*-variant lines: 22, 33, and 44. Each data point is the mean of three technical replicates from one independent differentiation round. Shown is the mean (annotated above each bar) +/- SEM of the three independent experiments. *GAPDH* levels were robust in all cases, including the iN00 conditions. Paired t test indicated no significant (NS) difference of *NGN2* levels between 33 and 22 or 33 and 44 cells (P values over horizontal brackets).

5.3 *APOE* transcript levels decreased upon neuronal induction

APOE expression in human stem cells is not well documented and expression in neurons is expected to be low (209). I quantified the relative expression of *APOE* transcript in the isogenic stem cells versus the induced neurons using RT-PCR (Section 2.5.2). As seen in Figure 5.3, all three genotype lines showed readily detectible and equivalent *APOE* mRNA expression in the stem cell stage (iN00) which decreased, regardless of genotype, after the cultures began neuronal differentiation (iN04).

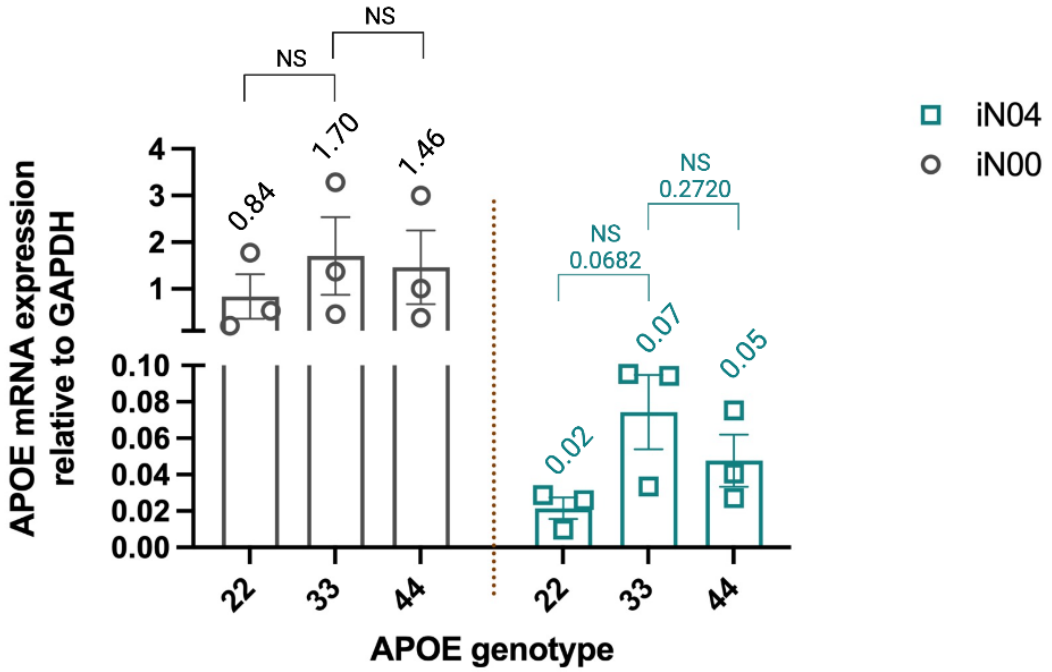

Figure 5.3 ***APOE*** **mRNA expression in stem cell (iN00) versus induced neuronal (iN04) cultures with the distinct APOE genotypes.**

APOE mRNA relative to *GAPDH* expression is shown in iPSCs (iN00, left side) and Day 4 induced neurons (iN04; right). The X-axis depicts the *APOE*-variant lines. Each data point indicates the mean of three technical replicates from one independent differentiation round. Shown is the mean (annotated above each bar) +/- SEM of the three experiments. *GAPDH* levels were robust in all cases. Paired t test between 33 iPSCs or 33 iN04 cells and the corresponding cellular stages of the other genotypes (horizontal brackets) indicated no genotype-related significant differences (NS) in *APOE* transcript. The level of *APOE* transcript in iN04 versus iPSC stages was significantly lower showing a p value of 0.0195 upon 2-way ANOVA.

5.4 *APOE*-variant iPSCs revealed no morphological differences

Daily, I monitored parallel cultures under a microscope (Section 2.2.11). The APOE-variant iPSC cultures exhibited morphology like I saw in Section 3.4.1 and did not look different from each other. For example, Figure 5.4 depicts similar recovery from thawing for each genotype. On the left panels, 4x magnification shows characteristically dense cell colonies with distinct edges. On the right side, 10x magnification shows all cultures had similar iPSCs with characteristic high nucleus:cytoplasm ratio, prominent nucleoli, and scant cytoplasm.

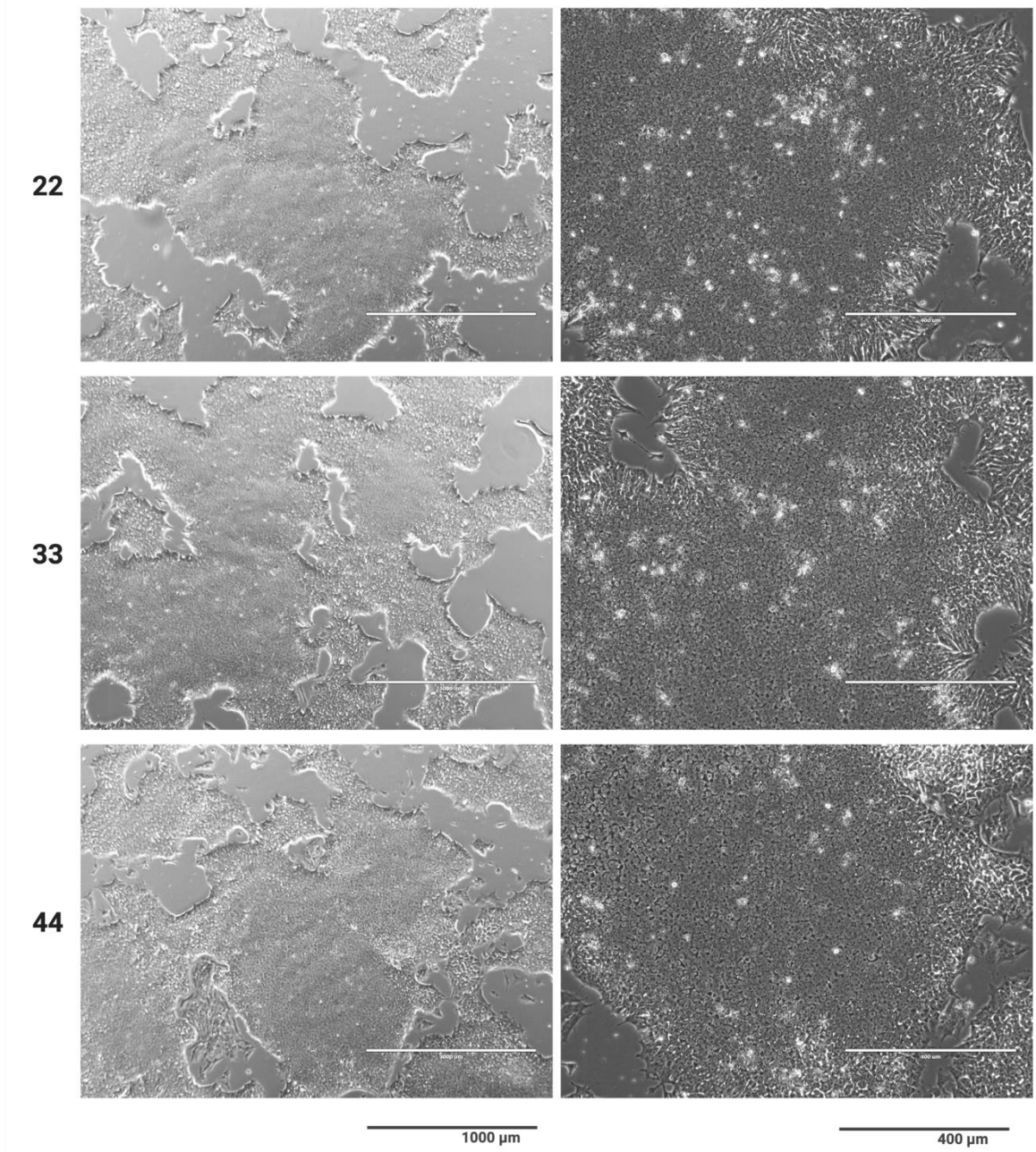

Figure 5.4 Morphology of distinct *APOE*-variant iPSCs three days after thawing.

Brightfield microscope images depicting the isogenic set of 22 (top), 33 (middle), and 44 (bottom) iPSCs. Scale bars on the left panels represent 1,000 µm and those on the right represent 400 µm.

5.5 Doxycycline-induced conversion to neurons yielded qualitatively similar morphology

Triggering the conversion to neurons with doxycycline-inducible NGN2 was marked by the doxycycline-induced expression of EGFP (like I saw in Section 4.2.1) which I assessed using fluorescence microscopy. EGFP expression was evident within 24 hours of doxycycline exposure in each APOE line (Panels B in Figure 5.5, Figure 5.6, and Figure 5.7). Three days after doxycycline

exposure, encompassing puromycin treatment in the latter 48 hours, yielded cultures in which most surviving cells expressed EGFP, their cell bodies appeared pyramidal, and neurites could be seen (Panels C in Figure 5.5, Figure 5.6, and Figure 5.7). This suggested that the inducible NGN2/pac cassette was functioning with equivalent potency in all three cultures of distinct *APOE* genotypes.

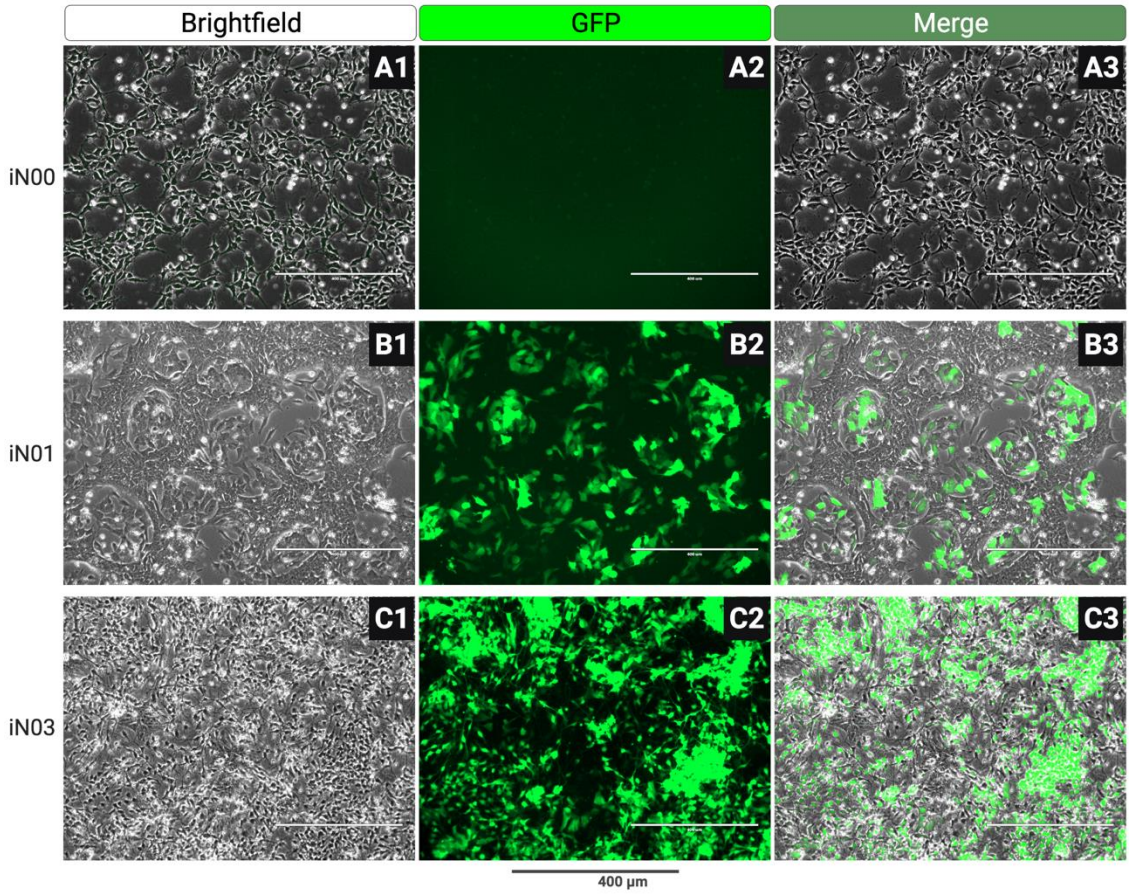

Figure 5.5 Inducible EGFP expression for the APOE22 cells at iN00, iN01 and iN03.

Panel A shows the APOE22 line 18 hours after plating as single cell iPSCs prior to administration of doxycycline (iN00). Panel A2 is the view in the GFP fluorescence channel and Panel A3 shows the overlay of Panels A1 and A2. Panel B shows the same culture at iN01 (24 hours of doxycycline treatment). Fluorescence microscopy (B2) shows that a subset of cells now express EGFP. Panel C depicts the culture at iN03 (3 days of doxycycline treatment) in which the last 48 hours included puromycin co-treatment; showing almost all puromycin-surviving cells are GFP positive. Scale bar in each image represents 400 µm.

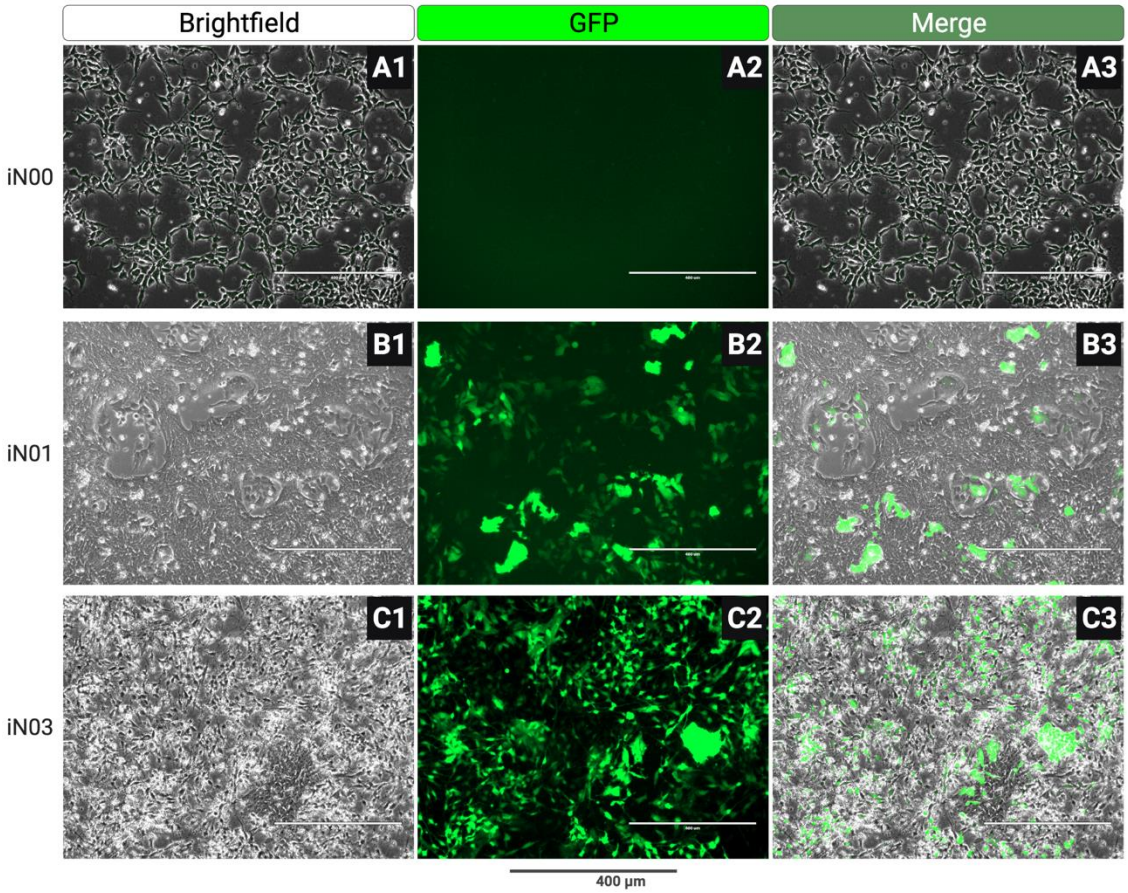

Figure 5.6 Inducible EGFP expression for APOE33 cells at iN00, iN01 and iN03.

Panel A shows the APOE33 line 18 hours after plating as single cell iPSCs prior to administration of doxycycline (iN00). Panel A2 is the view in the GFP fluorescence channel and Panel A3 shows the overlay of Panels A1 and A2. Panel B shows the same culture at iN01 (24 hours of doxycycline). Fluorescence microscopy (B2) shows that a subset of cells now express EGFP. Panel C depicts the culture at iN03 (3 days doxycycline) in which the last 48 hours included puromycin co-treatment; showing almost all puromycin-surviving cells are GFP positive. Scale bar in each image represents 400 µm.

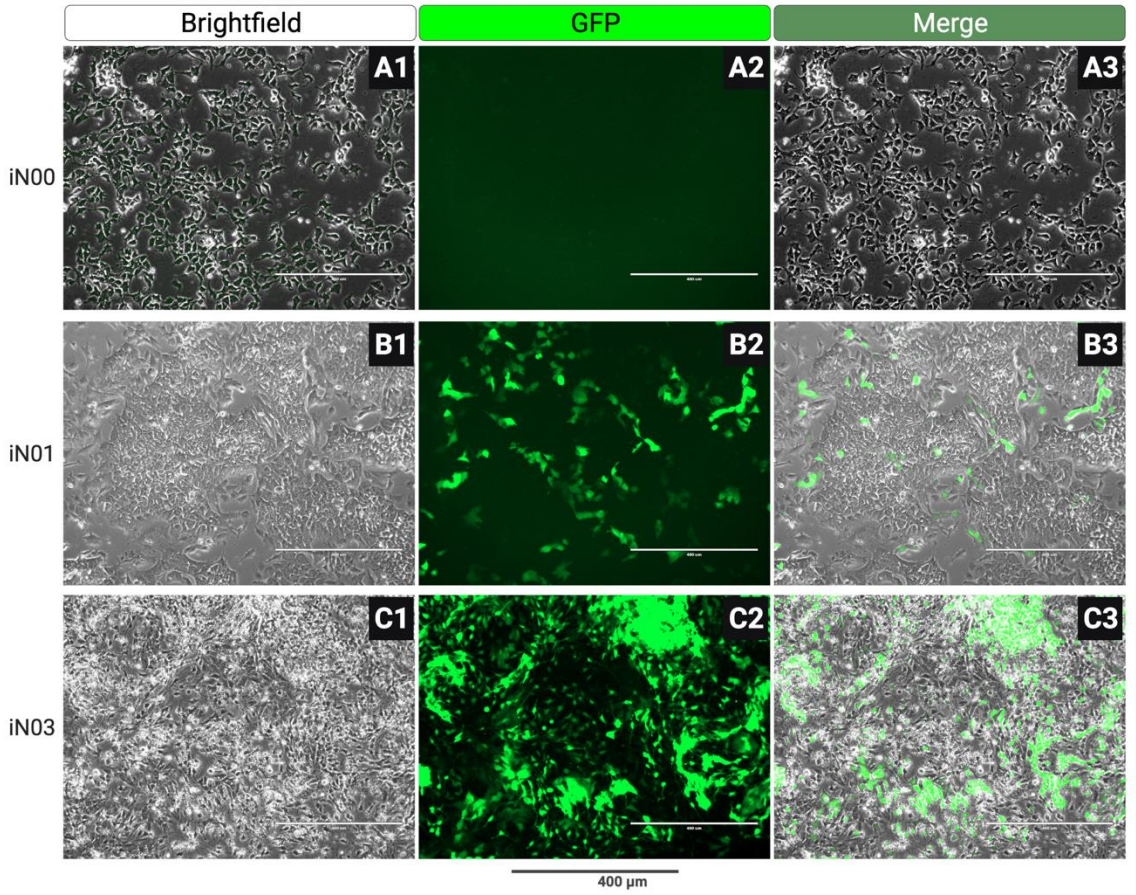

Figure 5.7 Inducible EGFP expression for APOE44 cells at iN00, iN01 and iN03.

Panel A shows the APOE44 line 18 hours after plating as single cell iPSCs prior to administration of doxycycline (iN00). Panel A2 is the view in the GFP fluorescence channel and Panel A3 shows the overlay of Panels A1 and A2. Panel B shows the same culture at iN01 (24 hours of doxycycline). Fluorescence microscopy (B2) shows that a subset of cells now express EGFP. Panel C depicts the culture at iN03 (3 days doxycycline) in which the last 48 hours included puromycin co-treatment; showing almost all puromycin-surviving cells are GFP positive. Scale bar in each image represents 400 µm.

5.6 Maturing *APOE*-variant neuronal cultures showed qualitatively similar morphology

To follow their progressive maturation and assess possible *APOE*-allele driven differences, the iN03 cultures were dissociated and neurons re-plated on growth substrate more conducive to neuronal maintenance (Section 2.4.3.2). I monitored the development of the cultures up until iN28 via fluorescence and brightfield microscopy. Representative images of the morphological progression for the 22, 33, and 44 neurons are shown in Figure 5.8, Figure 5.9, and Figure 5.10, respectively. No overt differences in the cultures developed from the distinct *APOE*-genotypes. In all cases, there was a time-dependent increase in neurite extension, elaboration, and complexity (reminiscent of observations in Section 4.2.1). By iN28, fasciculation of neurites bestowed

prominent rope-like features in the cultures (arrows in Panels E1 in Figure 5.8,Figure 5.9Figure 5.10).

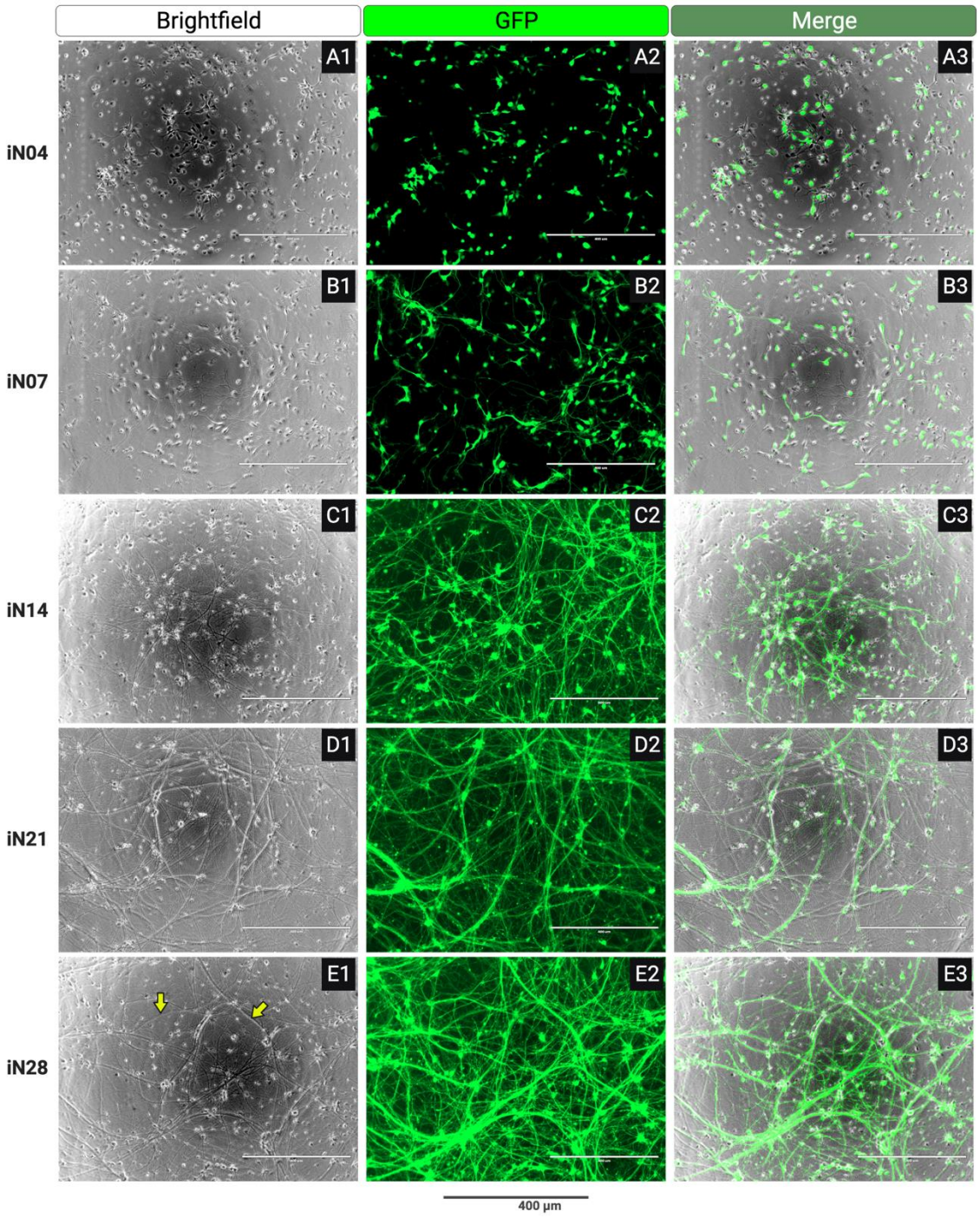

Figure 5.8 Ontogeny of neuronal architecture in APOE22 iNs from day 4 to 28.

Panel A shows the 22 line 18 hours after transferring iN03 cells from Matrigel-coated 6-well plates to PDL-coated 96-well plates. A1 depicts a brightfield view of iN04; A2 is the view in the fluorescence channel; A3 shows their overlay. Panels B, C, D, and E likewise, respectively, show representative cultures at iN07, iN14, iN21, and iN28. Yellow arrows point to fasciculated (bundled) neurites (Panel E1). Scale bar in each image = 400 µm.

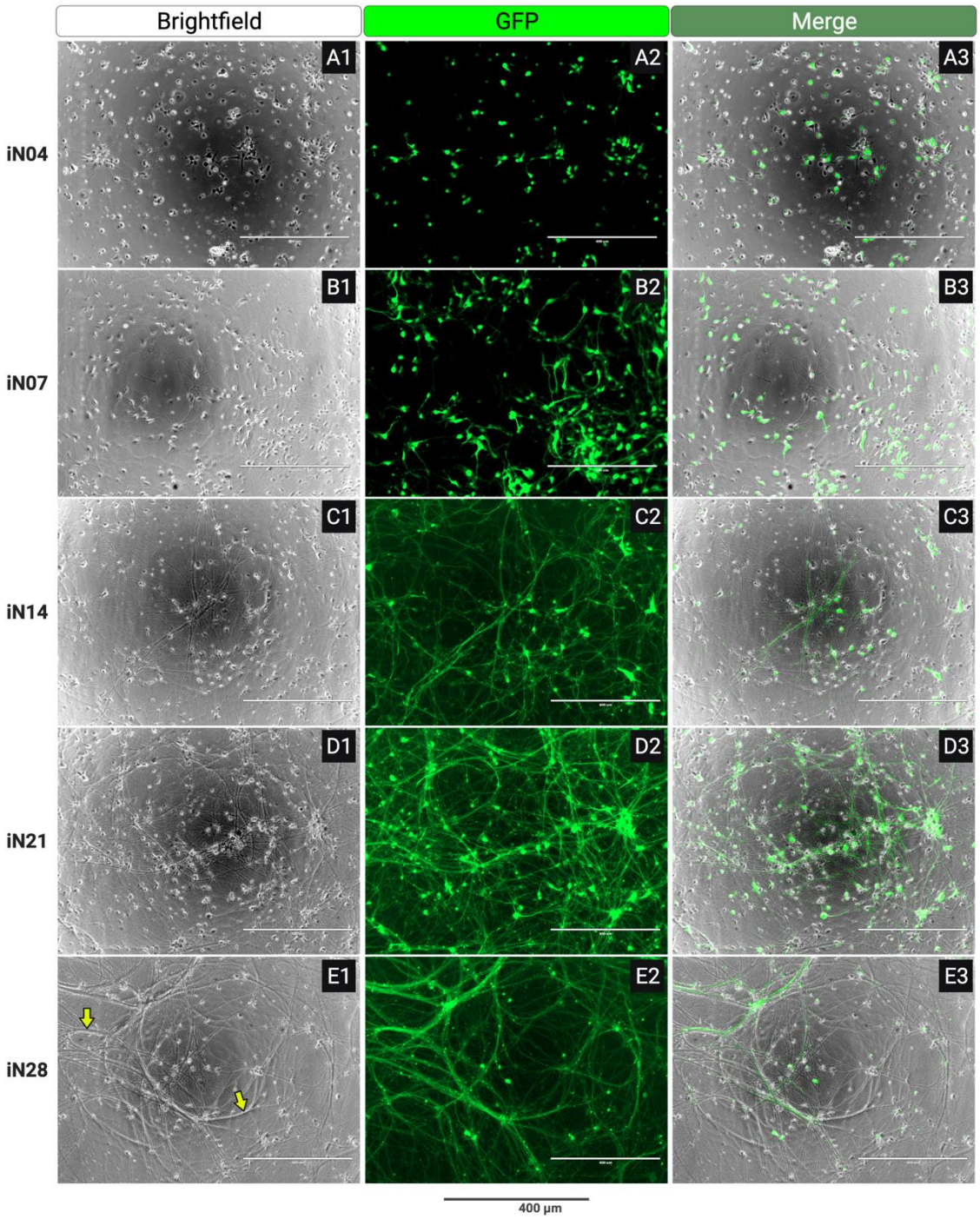

Figure 5.9 Ontogeny of neuronal architecture in APOE33 iNs from day 4 to 28.

Panel A shows the 33 line 18 hours after transferring iN03 cells from Matrigel-coated 6-well plates to PDL-coated 96-well plates. A1 depicts a brightfield view of iN04; A2 is the view in the fluorescence channel; A3 shows their overlay. Panels B, C, D, and E likewise, respectively, show representative cultures at iN07, iN14, iN21, and iN28. Yellow arrows point to fasciculated (bundled) neurites (Panel E1). Scale bar in each image = 400 µm.

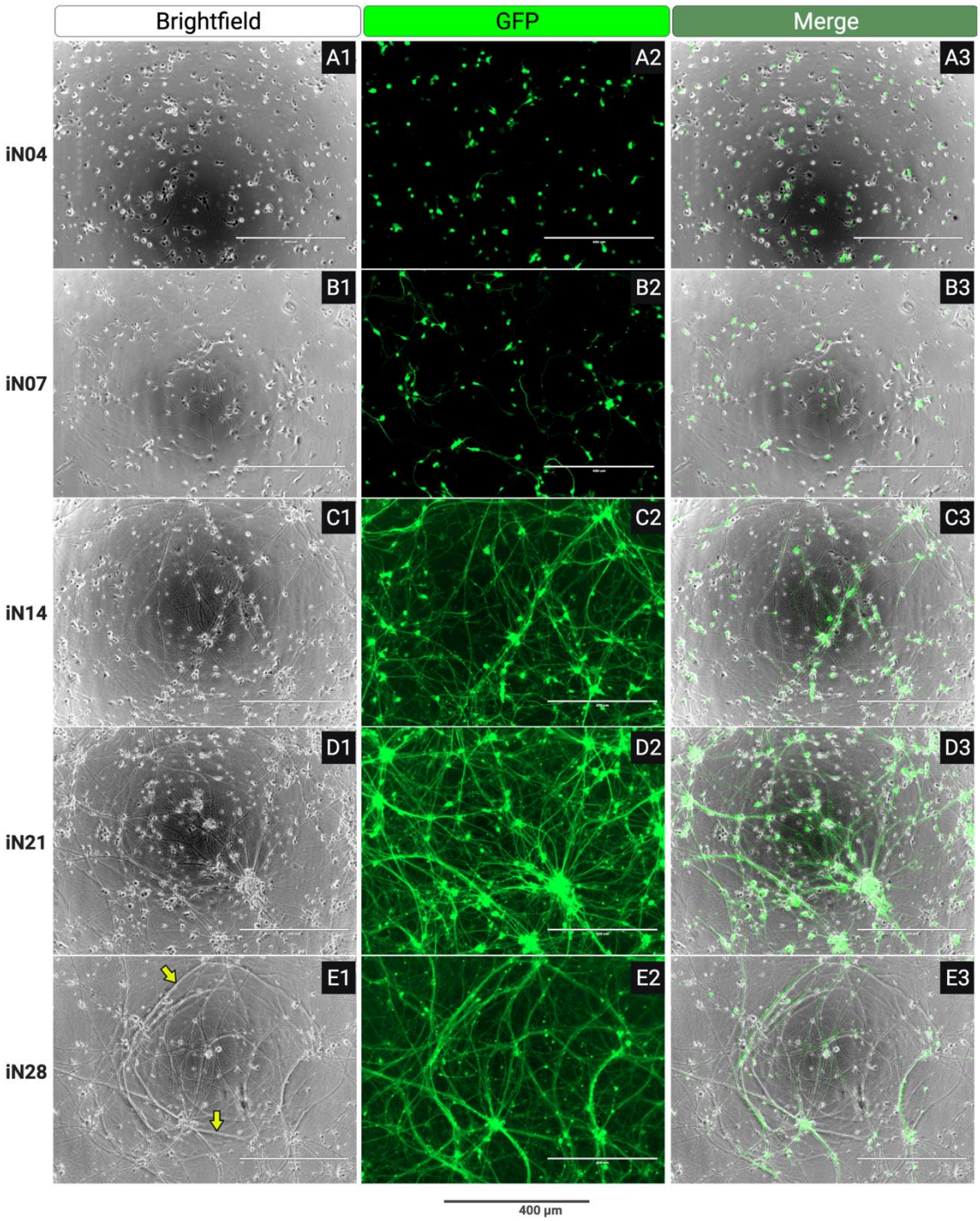

Figure 5.10 Ontogeny of neuronal architecture in APOE44 iNs from day 4 to 28.

Panel A shows the 44 line 18 hours after transferring iN03 cells from Matrigel-coated 6-well plates to PDL-coated 96-well plates. A1 depicts a brightfield view of iN04; A2 is the view in the fluorescence channel; A3 shows their overlay. Panels B, C, D, and E likewise, respectively, show representative cultures at iN07, iN14, iN21, and iN28. Yellow arrows point to fasciculated (bundled) neurites (Panel E1). Scale bar in each image = 400 µm.

5.7 *APOE*-variant cultures were of comparable health

To support the above morphological comparisons, I monitored culture vitality by measuring ATP levels at the same culture stages shown in Section 5.6. Within each time point, no differences in ATP levels based on genotype were evident (Figure 5.11), suggesting *APOE* genotype did not overtly influence culture health.

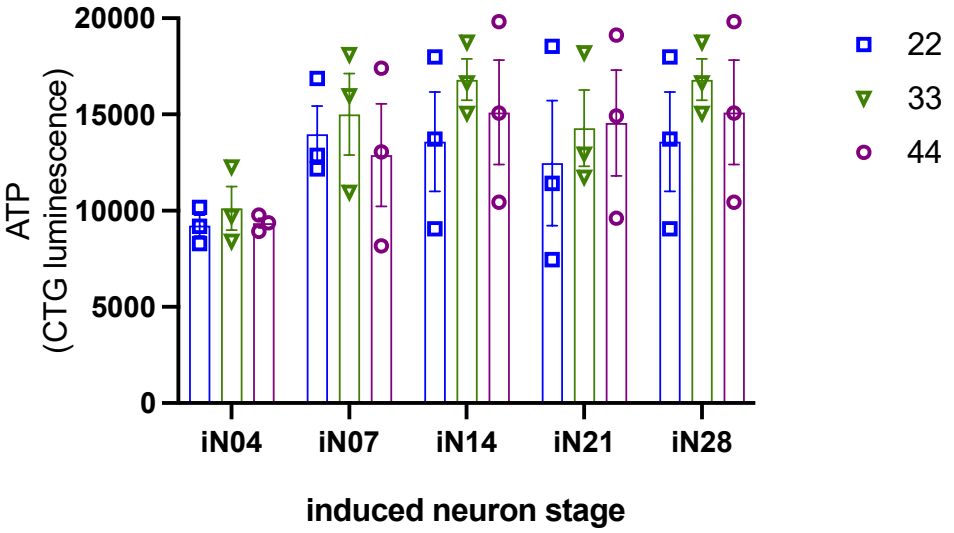

Figure 5.11 Adenosine triphosphate (ATP) in the *APOE*-variant induced neurons at 5 stages of maturation.

ATP levels measured as luminescence from the Cell Titer Glo assay (arbitrary units) are indicated for each culture genotype (error bars = mean with SEM of 3 independent differentiation experiments [each with 3 replicate cultures]). In each sub-grouping, the left, middle, and right bars represent 22, 33, and 44 iNs, respectively. Upon 2-way ANOVA, a significant interaction between time and ATP levels was revealed but not with genotype.

5.8 Pan-neuronal markers were unaffected by APOE genotype

I assessed the expression of two classic pan-neuronal markers over time via RT-PCR. Figure 5.12 (A) documents that *GAP43* increased from iN04 to iN14 then plateaued and this trajectory was the same regardless of APOE genotype. *MAP2*, shown in Figure 5.12 (B), followed a similar pattern of time-dependent increased expression as *GAP43*, which was not influenced by genotype; in fact, 22 and 33 culture expression superimposed on each other identically.

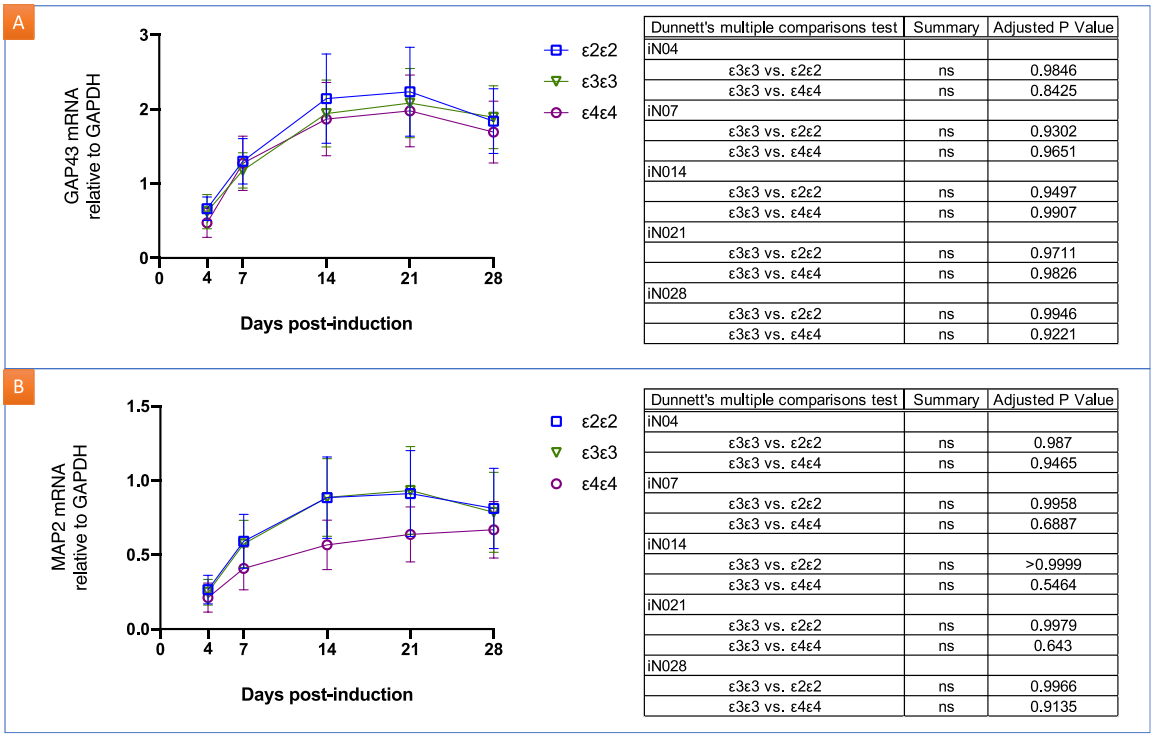

Dunnett's multiple comparisons test	Summary	Adjusted P Value
iN04		
ε3ε3 vs. ε2ε2	ns	0.9846
ε3ε3 vs. ε4ε4	ns	0.8425
iN07		
ε3ε3 vs. ε2ε2	ns	0.9302
ε3ε3 vs. ε4ε4	ns	0.9651
iN014		
ε3ε3 vs. ε2ε2	ns	0.9497
ε3ε3 vs. ε4ε4	ns	0.9907
iN021		
ε3ε3 vs. ε2ε2	ns	0.9711
ε3ε3 vs. ε4ε4	ns	0.9826
iN028		
ε3ε3 vs. ε2ε2	ns	0.9946
ε3ε3 vs. ε4ε4	ns	0.9221

Dunnett's multiple comparisons test	Summary	Adjusted P Value
iN04		
ε3ε3 vs. ε2ε2	ns	0.987
ε3ε3 vs. ε4ε4	ns	0.9465
iN07		
ε3ε3 vs. ε2ε2	ns	0.9958
ε3ε3 vs. ε4ε4	ns	0.6887
iN014		
ε3ε3 vs. ε2ε2	ns	>0.9999
ε3ε3 vs. ε4ε4	ns	0.5464
iN021		
ε3ε3 vs. ε2ε2	ns	0.9979
ε3ε3 vs. ε4ε4	ns	0.643
iN028		
ε3ε3 vs. ε2ε2	ns	0.9966
ε3ε3 vs. ε4ε4	ns	0.9135

Figure 5.12 Temporal transcriptional profile of *GAP43* and *MAP2* in induced neurons carrying distinct *APOE* genotypes.

(A) *GAP43* and (B) *MAP2* expression (via RT-PCR) in the *APOE*-variant iNs at the following timepoints after NGN2 induction (days) are shown: 4, 7, 14, 21, and 28. *APOE* 22, 33, and 44 induced neurons are represented by the square, triangle, or circle symbols, respectively. Error bars are the SEM from 3 independent rounds of differentiations (each with n=3 biological replicates). Tables show p values of comparisons to the neutral genotype, 33, after 2-way ANOVA analysis which indicated an interaction between time and expression levels but not genotype.

5.9 *APOE*-genotype impacted the transcription of select synapse-associated genes

I assessed select transcripts encoding synaptic vesicle membrane proteins that are functionally important in neurotransmission and are established markers of neuronal identity: *VGLUT2* (*SLC17A6*), belonging to a synaptic vesicle that is a terminal differentiation marker for glutamatergic transmission; *SYP*, encoding a generic protein found in synaptic vesicles in almost all neurons; and *SV2B*, marking a synaptic vesicle partially restricted to glutamatergic neurons. The mRNA for all three genes was detectable at iN04.

VGLUT2 showed increasing expression consistent with the glutamatergic phenotype associated with culture conditions. The increased expression of *VGLUT2* across ontogeny was not genotype related (Figure 5.13 [A]).

SYP levels in the 44 cultures started out lower and continued on a lowered trend compared to 33 cultures from the first to the last timepoint (Figure 5.13 [B]). However, all the while, the shape of the expression curves in all the APOE variants mirrored each other with measurements of the 33 and 22 cultures overlapping starting at iN14.

SV2B mRNA levels progressively increased with time in a way that was similar for 22 and 33, and divergent in 44, cultures. The 44 iNs showed progressively enhanced *SV2B* expression above that of the other *APOE*-variant lines such that, by the last time point, they displayed highly significant, 2-fold increased levels over that measured in 33 iNs (Figure 5.13 [C, Day 28]).

Together, the data for these synapse-associated genes suggest that, although organelles are developing in common, *APOE* genotype distinctly influences the transcriptional program of some synaptic components; though not necessarily in the same direction.

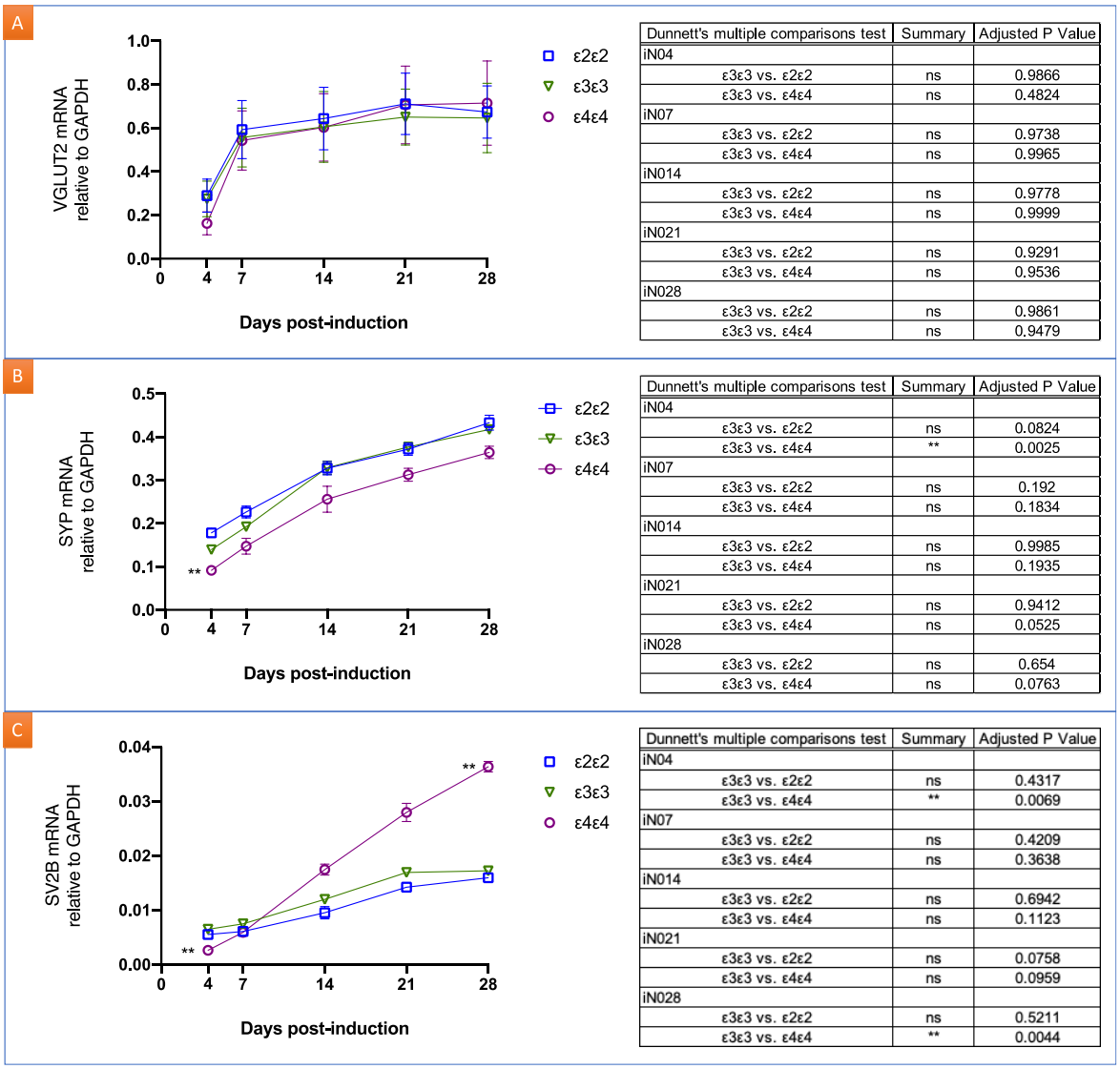

Dunnett's multiple comparisons test	Summary	Adjusted P Value
iN04		
ε3ε3 vs. ε2ε2	ns	0.9866
ε3ε3 vs. ε4ε4	ns	0.4824
iN07		
ε3ε3 vs. ε2ε2	ns	0.9738
ε3ε3 vs. ε4ε4	ns	0.9965
iN014		
ε3ε3 vs. ε2ε2	ns	0.9778
ε3ε3 vs. ε4ε4	ns	0.9999
iN021		
ε3ε3 vs. ε2ε2	ns	0.9291
ε3ε3 vs. ε4ε4	ns	0.9536
iN028		
ε3ε3 vs. ε2ε2	ns	0.9861
ε3ε3 vs. ε4ε4	ns	0.9479

Dunnett's multiple comparisons test	Summary	Adjusted P Value
iN04		
ε3ε3 vs. ε2ε2	ns	0.0824
ε3ε3 vs. ε4ε4	**	0.0025
iN07		
ε3ε3 vs. ε2ε2	ns	0.192
ε3ε3 vs. ε4ε4	ns	0.1834
iN014		
ε3ε3 vs. ε2ε2	ns	0.9985
ε3ε3 vs. ε4ε4	ns	0.1935
iN021		
ε3ε3 vs. ε2ε2	ns	0.9412
ε3ε3 vs. ε4ε4	ns	0.0525
iN028		
ε3ε3 vs. ε2ε2	ns	0.654
ε3ε3 vs. ε4ε4	ns	0.0763

Dunnett's multiple comparisons test	Summary	Adjusted P Value
iN04		
ε3ε3 vs. ε2ε2	ns	0.4317
ε3ε3 vs. ε4ε4	**	0.0069
iN07		
ε3ε3 vs. ε2ε2	ns	0.4209
ε3ε3 vs. ε4ε4	ns	0.3638
iN014		
ε3ε3 vs. ε2ε2	ns	0.6942
ε3ε3 vs. ε4ε4	ns	0.1123
iN021		
ε3ε3 vs. ε2ε2	ns	0.0758
ε3ε3 vs. ε4ε4	ns	0.0959
iN028		
ε3ε3 vs. ε2ε2	ns	0.5211
ε3ε3 vs. ε4ε4	**	0.0044

Figure 5.13 Temporal transcriptional profile of *VGLUT2*, *SYP*, and *SV2B* in induced neurons of distinct *APOE* genotypes.

(A) VGLUT, (B) *SYP*, and (C) *SV2B* mRNA expression (via RT-PCR) in the *APOE*-variant iNs at the following timepoints after induction (days) are shown: 4, 7, 14, 21, and 28. *APOE* 22, 33, and 44 neurons are represented by the square, triangle, or circle symbols, respectively. Error bars are the SEM from 3 independent rounds of differentiations (each with n=3 technical replicates). Tables show p values when, at each timepoint, comparisons were made to the 33 cultures after 2-way ANOVA analysis which indicated an interaction between time and expression levels.

5.10 No *APOE* genotype effect on synaptic activity marker gene, FOS

Another important element of maturation is synaptic connectivity. My morphological analysis suggested the cultures are maturing (arrows mark intertwined neurites in Figure 5.8, Figure 5.9 and Figure 5.10). To confirm development of active synapses, I assessed FOS as a transcriptional reporter as it is an immediate-early gene (IEG) that increases with synaptic activity (211). I observed the expected time-dependent increase in FOS expression suggesting the neurons were

becoming excitable as the cultures matured (Figure 5.14). All three APOE-variant cultures showed an incremental induction of FOS up to 21 days that dramatically spiked by 3-fold increases between day 21 to day 28. The overlapping trajectory of FOS induction in the three *APOE*-variant cultures implied that FOS expression was unaffected by *APOE* allele.

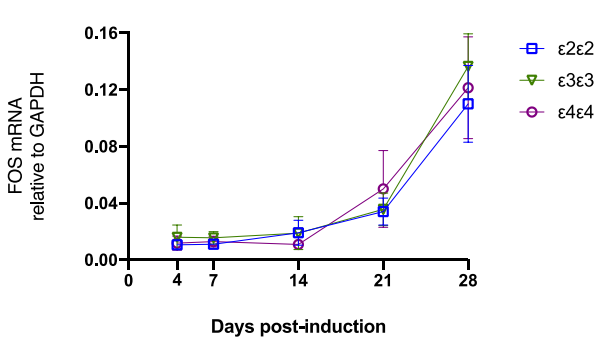

Dunnett's multiple comparisons test	Summary	Adjusted P Value
iN04		
ε3ε3 vs. ε2ε2	ns	0.8046
ε3ε3 vs. ε4ε4	ns	0.8966
iN07		
ε3ε3 vs. ε2ε2	ns	0.6214
ε3ε3 vs. ε4ε4	ns	0.8649
iN014		
ε3ε3 vs. ε2ε2	ns	0.9999
ε3ε3 vs. ε4ε4	ns	>0.9999
iN021		
ε3ε3 vs. ε2ε2	ns	0.9916
ε3ε3 vs. ε4ε4	ns	0.8516
iN028		
ε3ε3 vs. ε2ε2	ns	0.7037
ε3ε3 vs. ε4ε4	ns	0.9155

Figure 5.14 Temporal transcriptional profile of FOS in induced neurons carrying distinct *APOE* genotypes.

Expression of FOS (via RT-PCR) in *APOE*-variant iN cultures at the following timepoints after NGN2 induction (days) is shown: 4, 7, 14, 21, and 28. *APOE* 22, 33, and 44 neurons are represented by the square, triangle, or circle symbols, respectively. Error bars are the SEM from 3 independent differentiation timeline experiments. Table shows p values when, at each timepoint, comparisons were made to the 33 cultures after 2-way ANOVA analysis, which indicated an interaction between time and expression levels, but not genotype.

5.11 No effect of *APOE*-genotype on the expression of MAPT and *APP*

Seeing that tau and Aβ pathophysiology are central to AD, I included their coding genes in my transcriptional profiling timecourse study and measured the expression of MAPT and *APP* mRNA over time. MAPT levels increased steadily from iN4 to iN21 after which expression rates slowed (Figure 5.15; A). *APP* levels increased from iN4 to iN14 and levelled off thereafter (Figure 5.15; B). During iN maturity, neither gene transcription was influenced by *APOE* genotype.

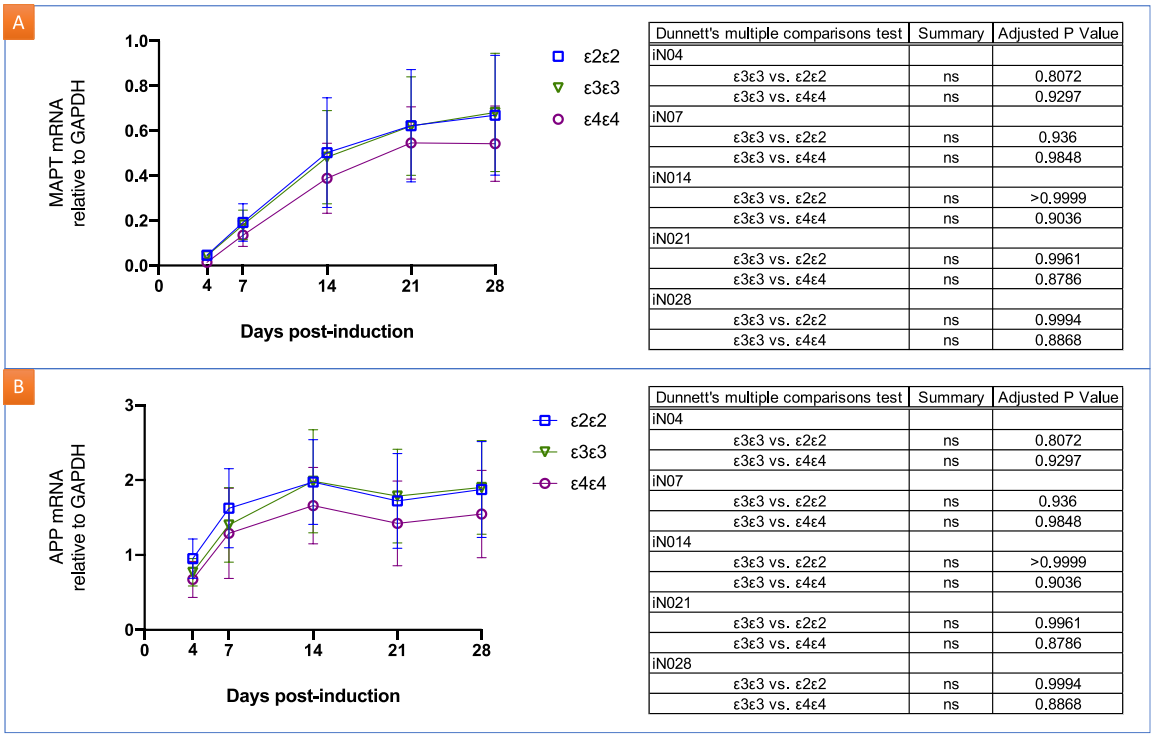

Dunnett's multiple comparisons test	Summary	Adjusted P Value
iN04		
ε3ε3 vs. ε2ε2	ns	0.8072
ε3ε3 vs. ε4ε4	ns	0.9297
iN07		
ε3ε3 vs. ε2ε2	ns	0.936
ε3ε3 vs. ε4ε4	ns	0.9848
iN014		
ε3ε3 vs. ε2ε2	ns	>0.9999
ε3ε3 vs. ε4ε4	ns	0.9036
iN021		
ε3ε3 vs. ε2ε2	ns	0.9961
ε3ε3 vs. ε4ε4	ns	0.8786
iN028		
ε3ε3 vs. ε2ε2	ns	0.9994
ε3ε3 vs. ε4ε4	ns	0.8868

Dunnett's multiple comparisons test	Summary	Adjusted P Value
iN04		
ε3ε3 vs. ε2ε2	ns	0.8072
ε3ε3 vs. ε4ε4	ns	0.9297
iN07		
ε3ε3 vs. ε2ε2	ns	0.936
ε3ε3 vs. ε4ε4	ns	0.9848
iN014		
ε3ε3 vs. ε2ε2	ns	>0.9999
ε3ε3 vs. ε4ε4	ns	0.9036
iN021		
ε3ε3 vs. ε2ε2	ns	0.9961
ε3ε3 vs. ε4ε4	ns	0.8786
iN028		
ε3ε3 vs. ε2ε2	ns	0.9994
ε3ε3 vs. ε4ε4	ns	0.8868

Figure 5.15 Temporal transcriptional profile of MAPT and *APP* in induced neurons carrying distinct APOE genotypes.

Transcript expression of (A) MAPT and (B) *APP* in *APOE*-variant iN cultures at the following timepoints after NGN2 induction (days) are shown: 4, 7, 14, 21, and 28. *APOE* 22, 33, and 44 induced neurons are represented by the square, triangle, and circle, respectively. Error bars are the SEM from 3 independent differentiation timeline experiments. Table shows p values when, at each timepoint, comparisons were made to the 33 cultures after 2-way ANOVA analysis; which indicated an interaction between time and expression levels, but not genotype.

5.12 No genotype effect on transcripts related to the lipid-associated genes

The central gene of my study, APOE, plummeted in expression during transition from stem cell to neuronal stage (Figure 5.3). Extending analysis to the full time range clarified that expression of APOE was maintained at low but detectable levels as the neuronal cultures aged. Figure 5.16 (A) shows that APOE expression levels at iN04 (replotted from Figure 5.3) became less variable (smaller error bars) and decreased to iN14, then stabilized. No significant differences in the APOE transcript levels were detected when the distinct genotypes were compared although levels in 22 cultures trended lower than those of 33.

The most well-known function of ApoE is facilitation of lipid transport between cells. This general function is shared with other lipid handling molecules including clusterin whose gene, CLU, has been implicated by GWAS studies as a risk factor for LOAD (Section 1.3.2). LRP1 is not only the major neuronal receptor associated with ApoE function but is also implicated in AD pathogenesis

via Aβ related mechanisms (Sections 1.6.1 and 1.10.3). As such, I assessed these gene transcripts during my study. No differences in CLU or LRP1 expression amongst the APOE-variant cultures emerged at any point of the time course (Figure 5.16, (B) and (C), respectively).

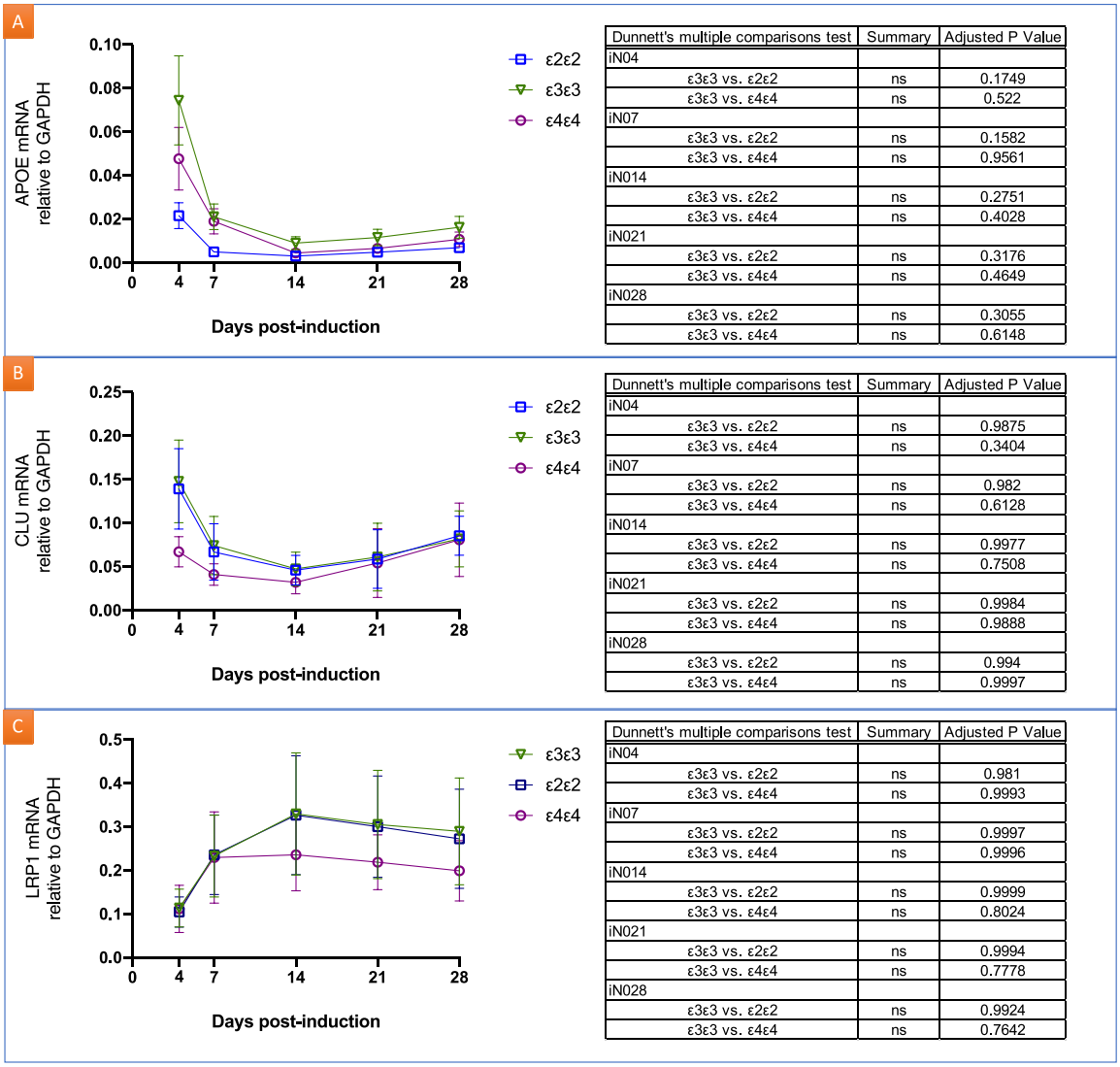

Dunnett's multiple comparisons test	Summary	Adjusted P Value
iN04		
ε3ε3 vs. ε2ε2	ns	0.1749
ε3ε3 vs. ε4ε4	ns	0.522
iN07		
ε3ε3 vs. ε2ε2	ns	0.1582
ε3ε3 vs. ε4ε4	ns	0.9561
iN014		
ε3ε3 vs. ε2ε2	ns	0.2751
ε3ε3 vs. ε4ε4	ns	0.4028
iN021		
ε3ε3 vs. ε2ε2	ns	0.3176
ε3ε3 vs. ε4ε4	ns	0.4649
iN028		
ε3ε3 vs. ε2ε2	ns	0.3055
ε3ε3 vs. ε4ε4	ns	0.6148

Dunnett's multiple comparisons test	Summary	Adjusted P Value
iN04		
ε3ε3 vs. ε2ε2	ns	0.9875
ε3ε3 vs. ε4ε4	ns	0.3404
iN07		
ε3ε3 vs. ε2ε2	ns	0.982
ε3ε3 vs. ε4ε4	ns	0.6128
iN014		
ε3ε3 vs. ε2ε2	ns	0.9977
ε3ε3 vs. ε4ε4	ns	0.7508
iN021		
ε3ε3 vs. ε2ε2	ns	0.9984
ε3ε3 vs. ε4ε4	ns	0.9888
iN028		
ε3ε3 vs. ε2ε2	ns	0.994
ε3ε3 vs. ε4ε4	ns	0.9997

Dunnett's multiple comparisons test	Summary	Adjusted P Value
iN04		
ε3ε3 vs. ε2ε2	ns	0.981
ε3ε3 vs. ε4ε4	ns	0.9993
iN07		
ε3ε3 vs. ε2ε2	ns	0.9997
ε3ε3 vs. ε4ε4	ns	0.9996
iN014		
ε3ε3 vs. ε2ε2	ns	0.9999
ε3ε3 vs. ε4ε4	ns	0.8024
iN021		
ε3ε3 vs. ε2ε2	ns	0.9994
ε3ε3 vs. ε4ε4	ns	0.7778
iN028		
ε3ε3 vs. ε2ε2	ns	0.9924
ε3ε3 vs. ε4ε4	ns	0.7642

Figure 5.16 Temporal transcriptional profile of *APOE*, *CLU*, and *LRP1* in induced neurons iNs carrying distinct *APOE* genotypes.

RT-PCR evaluation of expression of (A) *APOE*, (B) CLU and (C) LRP1, in APOE-variant induced neurons at the following timepoints after NGN2 induction (days) are shown: 4, 7, 14, 21, and 28. *APOE* 22, 33, and 44 iNs are represented by the square, triangle, and circle, respectively. Error bars are the SEM from 3 independent differentiation timeline experiments. Table shows p values when, at each timepoint, comparisons were made to the 33 cultures after 2-way ANOVA analysis; which indicated an interaction between time and expression levels, but not genotype.

5.13 Comparison of transcriptional landscape in mature neurons using NanoString

The data above highlighted the ability to probe the development and functional potential of the iNs by assessing mRNA transcription. To extend this, I profiled the mRNA of a library of 760 candidate genes hypothesized to serve as a signature of CNS dysfunction and/or homeostasis using a hybridization-based technology that counts mRNA molecules, NanoString. The library, designed by NanoString Technologies Inc and is called the nCounter® Human Neuropathology Panel, had representation of prioritized neuronal, as well as disease-related, genes (full list copy/pasted in Appendix A). I rationalized that iN28 represented mature neurons such that any accumulated phenotype derived from development and specific to a distinct ApoE isoform would be revealed. In the context of my neuronal development platform, by iN28, the increased induction of the *FOS* and synaptic vesicle markers, plateaued expression of *GAP34*, and microscopy observations suggested this was a time-point reflective of neuronal network connectivity. As such, I interrogated datasets gleaned from two independent rounds of isogenic iN28 cultures and comparisons were based on the relative expression to 33 cultures, which harbor the neutral allele for AD (Section 2.5.6 covers NanoString methodology and Appendix C shows housekeeping gene counts).

5.13.1 Benchmarking of NanoString against RT-PCR

For the comparison between NanoString and RT-PCR, I plotted the genes common to both technologies side-by-side. To compare like datasets, only the iN28 data points from the RT-PCR (replotted from the longitudinal studies above [Figure 5.12 to Figure 5.16, inclusive]) were analyzed alongside NanoString outputs. Owing to the differences in technologies (one quantifies the absolute number of mRNA particles while the other quantifies the relative amplification signal of the target to GAPDH mRNA), the data on the Y-axes are thus different, however what I am interested in observing is whether the pattern or relationship between the genotypes is the similar. Figure 5.17 confirmed *APOE* mRNA was readily detected via NanoString in these neurons. Since the Nanostring data came from separate cultures than those used to generate RT-PCR data, this is additional verification that the differences I observed are indeed valid.

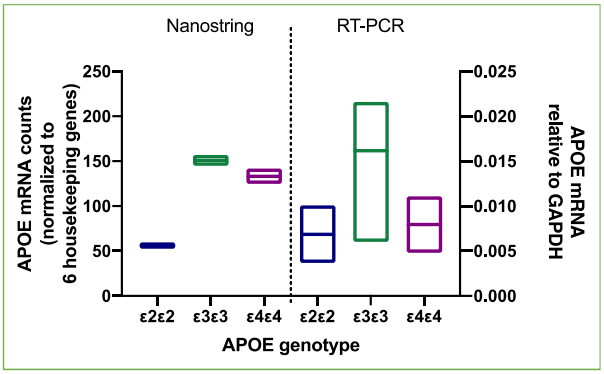

Figure 5.17 ***APOE*** **mRNA across isogenic APOE-variant iN28 cultures quantified by NanoString and RT-PCR.**

Floating bar (min to max) plots with line at the mean for APOE mRNA detected via NanoString (left) and RT-PCR (right) across *APOE* 22, 33, and 44 iNs at day 28. NanoString data is from 2, while RT-PCR is from 3, independent rounds of iN28 differentiations.

Likewise, the other genes relating to lipid biology and neuron identity, shown in Figure 5.18: LRP1, CLU, *MAP2*, and *VGLUT2* in panels (A), (B), (C), and (D), respectively, showed similar patterns of expression relative to the *APOE*-variant cultures. Figure 5.19, likewise, shows the similarity in profile of genes associated with AD neuropathology: *APP* (top) and *MAPT* (bottom). Finally, this consistency held for synaptic activity marker *FOS*, shown in Figure 5.20. The NanoString data faithfully recapitulated the RT-PCR data therefore validating the technology, and so I moved forward with more in-depth analysis of the NanoString datasets.

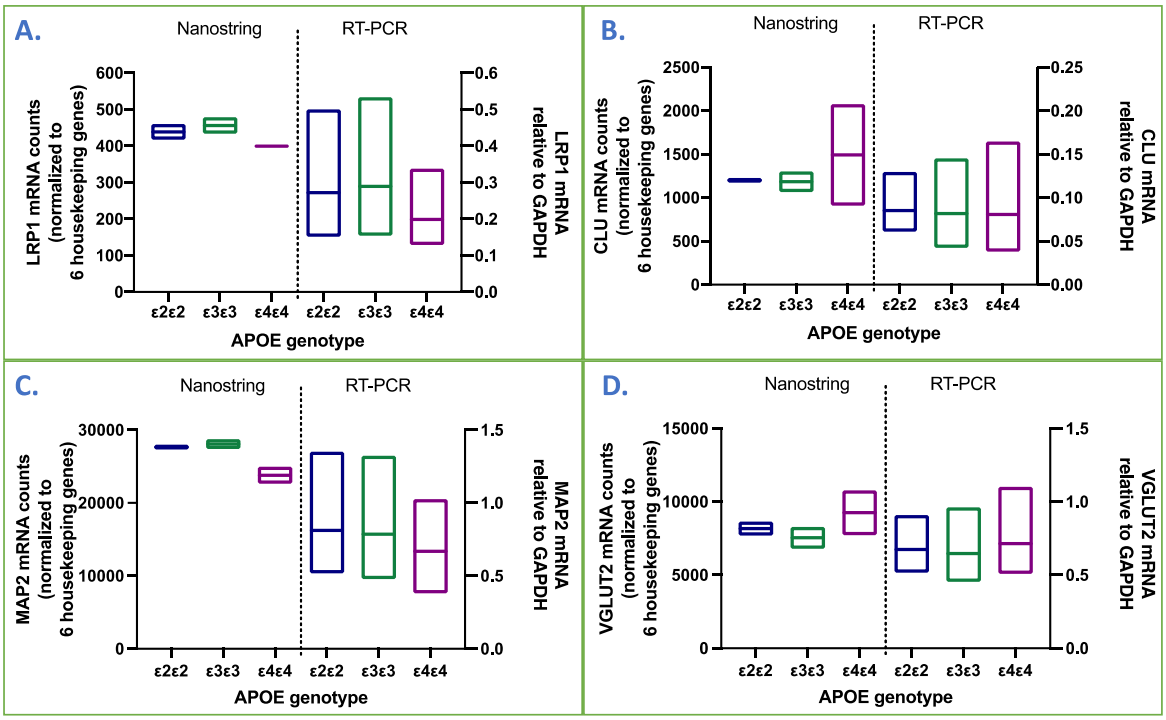

Figure 5.18 Transcript expression across isogenic *APOE*-variant iN28 cultures quantified by NanoString and RT-PCR for: *LRP1*, *CLU*, *MAP2*, and *VGLUT2*.

Floating bar (min to max) plots with line at the mean for mRNA detected via NanoString and RT-PCR across *APOE* 22, 33, and 44 iNs at day 28 for the following transcripts: *LRP1* (A), *CLU* (B), *MAP2* (C), and *VGLUT2* (D). Each panel shows NanoString plotted on the left and RT-PCR on the right Y-axis. NanoString data is from 2, while RT-PCR is from 3, independent rounds of iN28 differentiations.

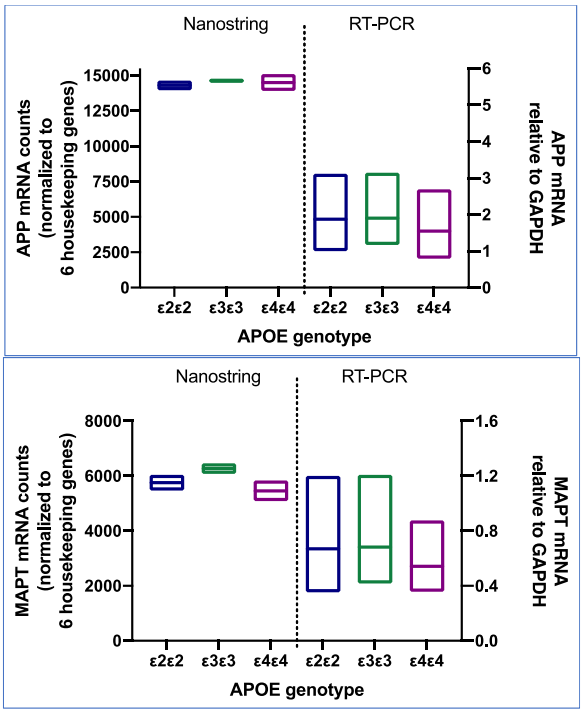

Figure 5.19 Technology comparison showing transcript expression across isogenic *APOE*-variant iN28 cultures quantified by NanoString and RT-PCR for: *APP* and *MAPT*.

Floating bar (min to max) plots with line at the mean for mRNA detected via NanoString and RT-PCR across *APOE* 22, 33, and 44 iNs at day 28 for: *APP* (top) and *MAPT* (bottom). Each panel shows NanoString plotted on the left and RT-PCR on the right Y-axis. NanoString data is from 2, while RT-PCR is from 3, independent rounds of iN28 differentiations.

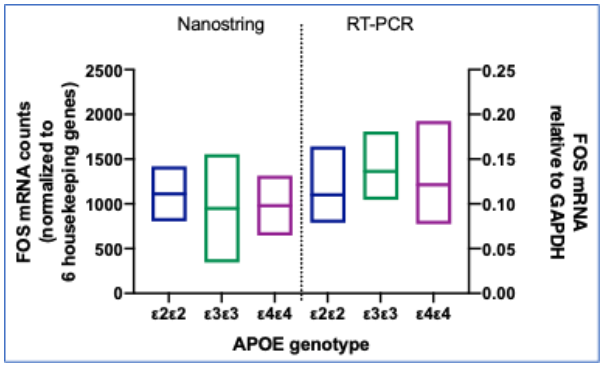

Figure 5.20 Technology comparison showing transcript expression across isogenic *APOE*-variant iN28 cultures quantified by NanoString and RT-PCR for *FOS*.

Floating bar (min to max) plots with line at the mean for *FOS* mRNA detected via NanoString (left) and RT-PCR (right) across *APOE* 22, 33, and 44 iNs at day 28. NanoString data is from 2, while RT-PCR is from 3, independent rounds of iN28 differentiations.

5.13.2 Global transcriptional profiling of 760 genes across the APOE 22, 33 and 44 neurons via NanoString

I next visualized the results of the 760 genes on the NanoString panel in terms of their mRNA counts ordered highest to lowest; represented as a rolling bar in Figure 5.21. Essentially this plot allows the counts for 760 genes to be displayed from most to least abundant and the cutoff for undetectable expression is shown. This cutoff is defined by 2 standard deviations above the average of the negative controls, i.e., probes included in the library for which no target exists as designed by External RNA Controls Consortium (ERCC; https://www.nist.gov/programs-projects/external-rna-controls-consortium). In the analysis of the NanoString dataset from iN28 neurons, NEFL was the most abundant (highest counts) transcript and the cutoff for detection fell at counts overlapping with those of FAS. The 8 genes compared with RT-PCR analysis (Section 5.13.1) are labelled, with *MAP2*, *APP*, *VGLUT/SLC17A6*, *MAPT*, and *FOS* all falling amongst the top 100 most abundantly expressed genes. The least abundant of previously investigated by RT-PCR genes was APOE which showed low but readily detectable counts at 2-fold higher than the negative control defined undetectable cut off. Importantly, the data reinforces the neuronal identity of the cultures with very little other cell types based on the undetectable scoring for GFAP and other nonneuronal genes (Appendix B.1).

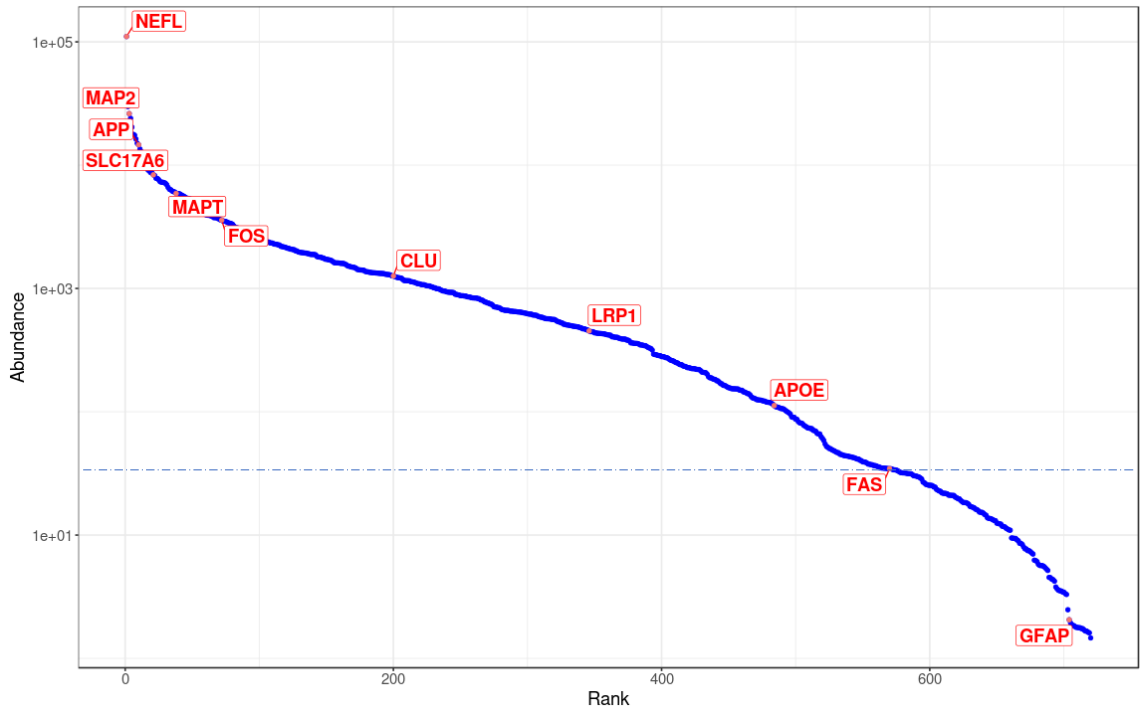

Figure 5.21 Rank abundance curve of genes in iN28 neurons detected via NanoString.

The mRNA extracted from iN28 cultures were probed against the 760 genes on the nCounter® Human Neuropathology panel (using NanoString) and the output expressed as mRNA counts normalized to 6 housekeeping genes. These counts are used to rank the relative abundance of the profiled genes (1 being the most, and 760 being the least, abundant) on the X-axis relative to their abundance (in counts) on the Y-axis. The 8 genes previously analyzed in similar cultures by RT-PCR (Section 5.13.1) are highlighted on the plot plus 3 others: *NEFL* (the most abundant mRNA), *FAS* (whose counts fell at the detection threshold), and *GFAP* (whose counts were well below the detection limit). The dotted line running through *FAS* (34 counts) represents the detection threshold. Also labelled are the 8 genes that were also analyzed in prior RT-PCR experiments. *APOE* counts fell clearly above the undetectable cut off.

I next used the nCounter software from the NanoString manufacturer to compare gene expression between *APOE*-variant iN28 cultures. Comparisons were done in pairs: 33 versus 22 and 33 versus 44. Genes fulfilling my criteria of differential expression of 50% lower or higher (i.e., 1.5-fold decrease or increase) with adjusted p-value <0.05 compared to that of the neutral genotype, 33, were extracted as differentially expressed genes (DEGs).

5.13.3 Differentially expressed genes between APOE 22 and 33 neurons

The volcano plot in Figure 5.22 shows that *APOE* (top left corner) was the only mRNA that reached DEG criteria; its fold change was 0.335 in 22 compared to 33 cultures (p-value = 0.0024). *APOE* lies to the left of 0.0 on the X-axis (which is in log2 units) which further indicates that it is less expressed in 22 versus 33 cultures. *APOE* mRNA counts are depicted above in Figure 5.17. Of

note, *APOE* mRNA levels in 22 cultures trended lower than those in 33 cultures in the prior RT-PCR study (Figure 5.3).

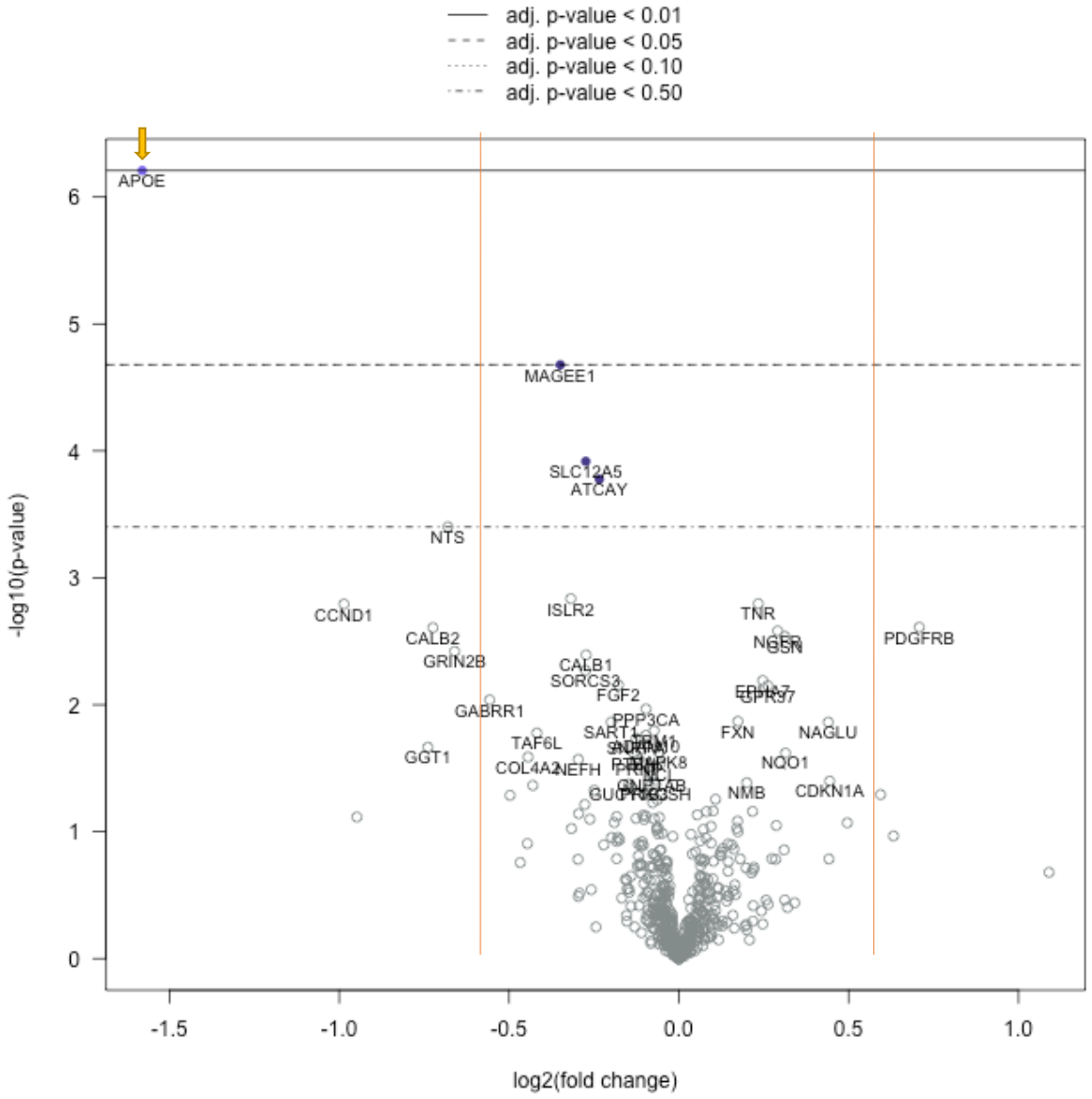

Figure 5.22 NanoString defined relative gene expression between APOE 22 and 33 iN28s.

Volcano plot representing nCounter® Human Neuropathology panel when comparing mRNA from 22 versus 33 iN28 neurons, (n = 2 independent sets of iN differentiation and maturation samples per genotype in a single NanoString run). Each circle represents an mRNA target that was detected. Solid circles depict targets that showed a difference with adjusted p-values < 0.2. The left and right vertical lines depict linear 1.5-fold thresholds for (log2 fold change of 0.585) decreased or increased expression, respectively. One mRNA target, *APOE* (arrow), met criteria for DEG.

5.13.4 Differentially expressed genes between APOE 44 and 33 neurons

When the NanoString based comparison was made between 33 and 44 genotype neurons, 18 genes were defined as having at least a 50% change in expression, in either direction. This quantification is shown on the volcano plot in Figure 5.23 and the DEGs are indicated with arrows.

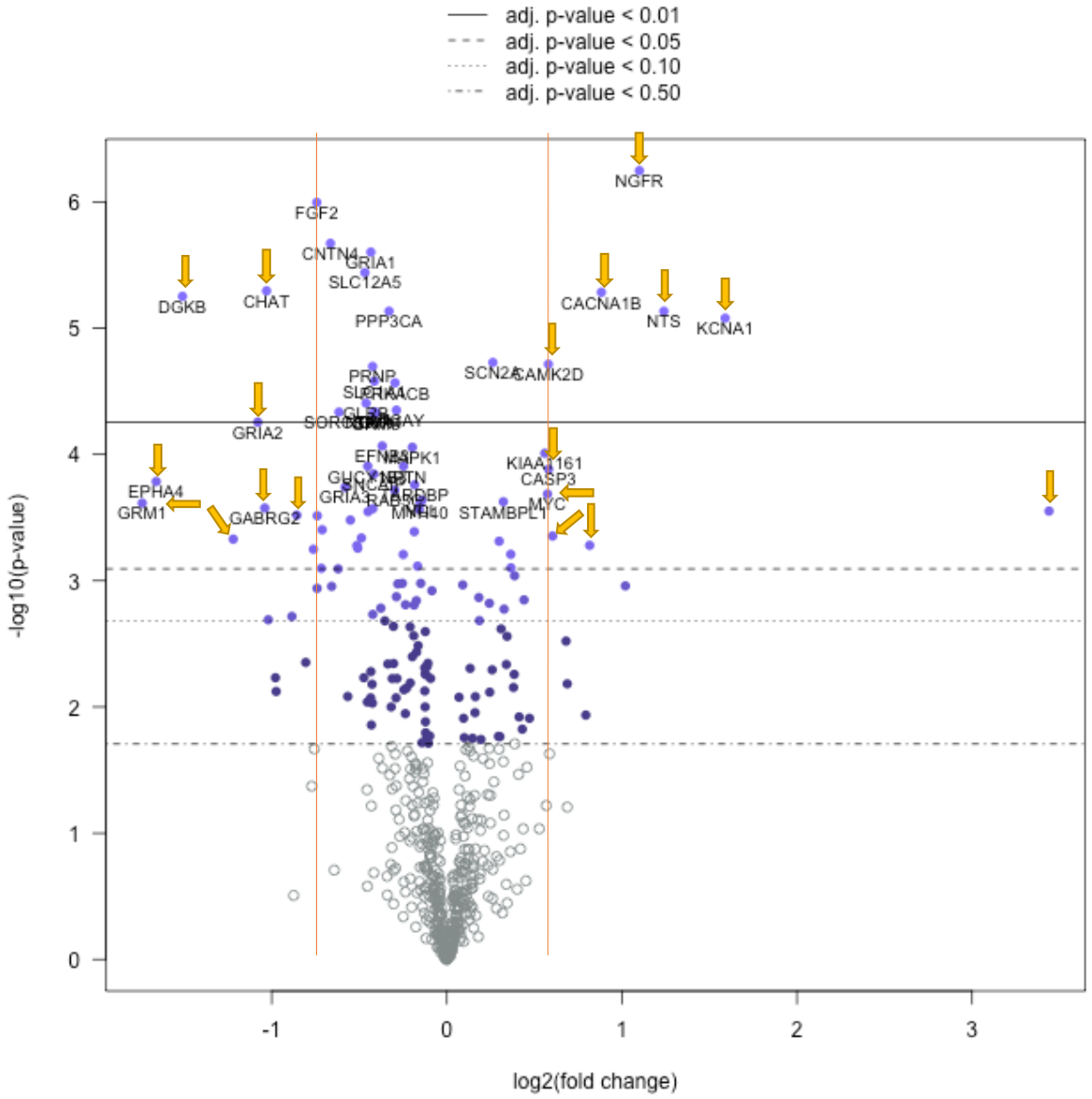

Figure 5.23 NanoString defined relative gene expression between APOE 33 and 44 iN28 neurons.

Volcano plot representing nCounter® Human Neuropathology panel when comparing mRNA from 44 versus 33 iN28 neurons, (n = 2 independent sets of iN differentiation and maturation samples per genotype in a single NanoString run). Each circle represents an mRNA target that was detected. Solid circles depict targets that showed a difference with adjusted p-values < 0.5. The left and right vertical lines depict linear 1.5-fold thresholds for (log2 fold change of 0.585) decreased or increased expression, respectively. Genes meeting criteria for DEG are indicated with arrows.

The heatmap in Figure 5.24 visualizes all DEGs in terms of mRNA counts (log2) while Table 5.2 lists the linear fold-changes alongside adjusted p values for the individual two samples from two independent iN28 neurons for each *APOE*-variant line, i.e., the iPSC lines used in this NanoString investigation are those listed in Table 5.1.

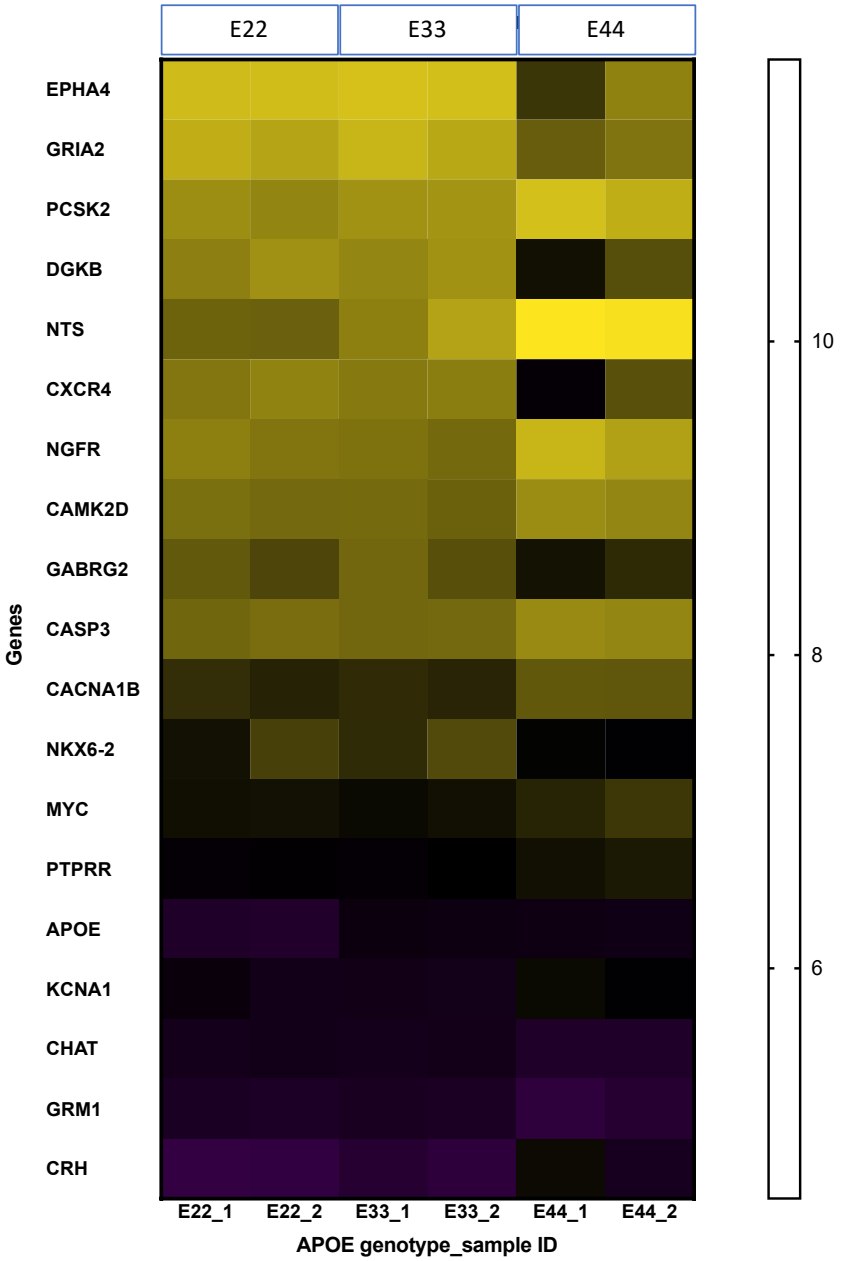

Figure 5.24 Heatmap listing the 19 differentially expressed genes amongst the APOE-variant iN28 cultures and calibrated according to their NanoString mRNA counts.

Heatmap showing all 19 DEGs extracted from the nCounter® Human Neuropathology panel calibrated along mRNA counts (log2) for each pair of samples for 22, 33, and 44 neurons (mRNA from 2 independently differentiated cultures per genotype loaded into a common NanoString run). The gene list is ranked from top to bottom as highest- to lowest-expressing when averaged across all cultures. The color calibration bar indicates that yellow, black, and purple hues are associated with higher, mid-range, and lower counts respectively.

Table 5.2 Full gene names of the DEGs and their fold changes from the APOE33 condition

Gene Symbol	Gene Full Name	22 versus 33			44 versus 33		
		Log2 fold change	Linear fold change	adj. p value	Log2 fold change	Linear fold change	adj. p value
APOE	apolipoprotein E	-1.580	0.34	0.0024	-0.103	0.93	1.0000
CACNA1B	calcium voltage-gated channel subunit alpha1 B			> 0.05	0.883	1.84	0.0027
CAMK2D	calcium/calmodulin-dependent protein kinase II delta			> 0.05	0.580	1.49	0.0054
CASP3	caspase 3			> 0.05	0.581	1.50	0.0171
CHAT	choline O-acetyltransferase			> 0.05	-1.030	0.49	0.0027
CRH	corticotropin releasing hormone			> 0.05	3.440	10.80	0.0245
CXCR4	chemokine (C-X-C motif) receptor 4			> 0.05	-1.220	0.43	0.0342
DGKB	diacylglycerol kinase beta			> 0.05	-1.510	0.35	0.0027
EPHA4	EPH receptor A4			> 0.05	-1.660	0.32	0.0200
GABRB2	gamma-aminobutyric acid type A receptor gamma2 subunit			> 0.05	-1.040	0.49	0.0245
GRIA2	glutamate ionotropic receptor AMPA type subunit 2			> 0.05	-1.080	0.47	0.0092
GRM1	glutamate receptor, metabotropic 1			> 0.05	-1.740	0.30	0.0238
KCNA1	potassium voltage-gated channel subfamily A member 1			> 0.05	1.590	3.01	0.0029
MYC	v-myc avian myelocytomatosis viral oncogene homolog			> 0.05	0.575	1.49	0.0223
NGFR	nerve growth factor receptor			> 0.05	1.100	2.14	0.0019
NKX6-2	NK6 homeobox 2			> 0.05	-0.857	0.55	0.0252
NTS	neurotensin			> 0.05	1.240	2.36	0.0028
PCSK2	proprotein convertase subtilisin/kexin type 2			> 0.05	0.604	1.52	0.0337
PTPRR	protein tyrosine phosphatase, receptor type R			> 0.05	0.816	1.76	0.0364

5.13.5 Differentially expressed pathways

Figure 5.25 shows the DEGs categorized based on NanoString Technologies Inc gene ontology annotations. Of the 23 pathways plus “Disease Association” annotated in the nCounter® Human Neuropathology panel, those reported on with the highest frequencies were: “Axon and Dendrite Structure”, “Vesicle Trafficking”, and “Transmitter Release and Neural Connectivity” which, together, mapped onto two (of six) themes: “Neurotransmission and Compartmentalization” and “Structural integrity”. Notably, seven pathways did not show up, suggesting a degree of specificity to my finding of 19 DEGs. Table 5.3 shows the gene annotations used to generate Figure 5.25.

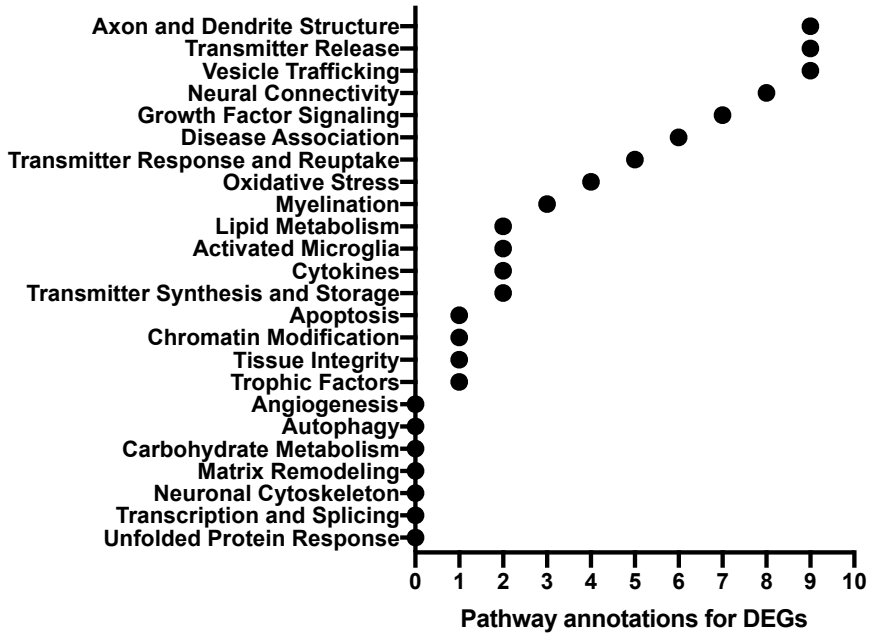

Figure 5.25 Pathway annotations of differentially expressed genes from the Neuropathology panel.

Scatter plot illustrating the distribution of pathway annotations for the DEGs. The top 4 most represented pathways can be linked to neural connectivity. Seven pathways were not represented at all.

Table 5.3 Neuropathology panel pathway annotations for each DEG

Gene	nCounter® Human Neuropathology Panel - Pathway Annotation															
	Activated Microglia	Apoptosis	Axon and Dendrite Structure	Chromatin Modification	Cytokines	Growth Factor Signaling	Lipid Metabolism	Myelination	Neural Connectivity	Oxidative Stress	Tissue Integrity	Transmitter Release	Transmitter Response and Reuptake	Transmitter Synthesis and Storage	Trophic Factors	Vesicle Trafficking
APOE	+		+							+						+
CACNA1B			+			+			+			+	+	+		+
CAMK2D			+	+		+			+			+	+		+	
CASP3		+				+				+		+				
CHAT							+		+			+		+		+
CRH			+									+	+			+
CXCR4	+				+			+								
DGKB							+									
EPHA4			+			+			+		+					
GABRB2									+			+	+			+
GRIA2									+			+	+			+
GRM1			+						+			+	+			+
KCNA1			+						+			+				+
MYC						+										
NGFR					+	+		+		+					+	+
NKX6-2											+					
NTS									+							
PCSK2				+												
PTPRR						+										

5.14 Discussion

In the face of limited investigation of the role played by neuron expressed ApoE, my system of pure neuronal cultures allowed a platform to investigate its function. Here, I leveraged human

isogenic cell lines with identical genetic backgrounds that only differ with respect to *APOE* alleles to definitively describe genotype-to-phenotype relationships regarding ontogeny of neuron development from iPSCs. I approached the question of how do neutral, protective, and detrimental alleles of *APOE* (in the context of AD), in a cell-type autonomous fashion, impact the differentiation and development of neurons - the most vulnerable cell type in AD? I deemed it important to include the *APOE ε2* variant in my comprehensive study to help fill the gap linking ApoE2 function with protective mechanisms against AD; almost all reports using isogenic iPSC lines to study ApoE function investigate only toxic functions of ApoE4, leaving ApoE2 underexplored (135).

NGN2 induction was equally robust in all three lines and thus did not confound my findings. *APOE* transcript reduction correlated with neuronal induction and culture maturity as I had anticipated because, in a mouse model, ApoE was expressed in neural precursors and *APOE*-null mice showed a depletion of NSCs, suggesting that ApoE is important in stem cell maintenance (212). Of note, I did not observe morphology or obvious differences when working with the APOE null iPSC (Figure 3.11). A recent report showed that *APOE* levels dramatically drop from undifferentiated human iPSCs stage compared with neural cultures differentiated from them (209). My analysis also reinforced that human neurons in culture maintain low, clearly detectable levels of *APOE* transcript expression. That *APOE ε2* expression was lower compared to *APOE* ε3 was surprising because *APOE ε2* carriers have higher levels of CSF and plasma ApoE, so I expected the opposite (95). However, analysis of bioinformatic sets (personal communication) indicated that individuals homozygous for *APOE*2/2, compared to *APOE*3/3, showed lower *APOE* mRNA was as well. The discrepancy could lie in either sample number (ε2 homozygotes are rare in the general population and the reports show data for ε2/ε3 genotypes) or endpoint measurements (transcript versus protein) or sample type (neuronal ApoE likely contributes minimally to CSF or plasma ApoE).

My study supported the endogenous expression of ApoE in mature neurons, though meanwhile, the functional significance of neuronal ApoE is poorly defined. Although Lin *et al.* 2018 reported baseline (meaning unperturbed cells) differential gene expression between isogenic iPSC-derived neurons harboring ε3/ε3 and ε4/ε4 genotypes (predicting some differences could emerge), I hypothesized based on my data there would be little to no developmental impact of *APOE* genotype and that it would be the interaction with genotype and stress or injury that would uncover functional cell-autonomous differences of the variants (134).

I characterized the conversion of neurons from iPSCs and their subsequent maturation by longitudinally tracking the cultures in terms of specific gene transcripts (via RT-PCR), health (ATP levels and microscopy), and morphology (microscopy). Additionally, when cells progressed to a

level of neuronal connectivity where they morphologically displayed fasciculated neurites (*in vitro* correlates of axonal tracts) accompanied by FOS induction, I analyzed them against a wider range of gene transcripts (213). Altogether, transcript profiling revealed the iPSCs developed into glutamatergic neurons as evidenced by induction, then progressively increased expression, of relevant markers. Furthermore, the induced neuronal cultures did not contain astrocytes, the cell type most known for ApoE production in the brain, because the astrocytic marker, GFAP, was not detected.

In the oldest cultures, to access desired additional transcripts in a scalable manner, I used NanoString technology and the nCounter® Human Neuropathology Panel containing 760 genes covering pathways grouped into the following six biological domains: (1) Neuroplasticity, Development & Aging, (2) Neuroinflammation, (3) Neuron-glia interaction, (4) Metabolism, (5) Neurotransmission, and (6) Compartmentalization and Structural integrity. NanoString revealed NEFL (from the gene that encodes Neurofilament Light Chain) as the most abundantly expressed transcript in the cultures and that makes sense; the gene product is a component of the neuronal cytoskeleton. Astrocytic markers, like GFAP, and other non-neuronal cell type markers were below the detection limit, again confirming the lack of astrocytes and adding confidence to the purely neuronal identity of the culture.

5.14.1 Stable transcriptional profile

The induction of neuronal phenotype and maturation recapitulates important developmental steps implemented by profound transcriptional cascades across development and these changes are both large and dynamic. My analyses of marker genes across time and the global transcription by NanoString at the endpoint recapitulated this neuronal ontology. Performing the time course allowed me to gain insight into the complexity of the structure of the cultures, for example, sharp induction of FOS expression from 3 to 4 weeks. My data showed that the transcription program that maps onto neuronal birth and maturation including synapse formation is relatively unperturbed by *APOE* genotype. My data also suggested that perturbing factors, including any impact of *APOE* genotype, would be detectable using this approach.

My clearly robust experiments allowed a precise dissection of differential gene expression between APOE genotypes. While transcriptional response is relatively robust with neuron conversion and aging, there were only subtle, but intriguing differences that emerged based on *APOE* allele. While there is almost no differential in gene expression between mature cultures of 22 and 33 genotypes, this was not the case when I compared 33 and 44 cultures, where 18 of 760

NanoString-profiled genes varied. Importantly, the ontology of one third of these genes converged onto biological roles related to synaptic function and/or neuronal connectivity.

5.14.2 Subtle transcriptional regulation of synaptic function and connectivity

The explicit role of ApoE in general, and neuronal ApoE in particular, in disease risk is not understood, but my NanoString studies hinted at a change in transcription of some synaptic determinants. This is solidified by my targeted investigation of *SV2B*, a major constituent of transmitter release dynamics. SV2B has been studied in the context of neurodegeneration. Brains from patients with AD showed reduced SV2B levels compared to controls (214). Furthermore, ε4, compared to ε3, was linked with down-regulation of SV2B in patients with AD (215). *SV2B* mRNA was shown to increase when rat neuroblastoma cells were stressed with Aβ toxic species (216). *In vivo*, SV2B knockout mice showed standard learning and memory functioning and, when stressed (injected) with Aβ species, were protected against harmful effects of the Aβ oligomers on synaptic function (217). In my study, neuronal 44 cultures showed increased SV2B (and decreased SYP) mRNA levels compared to both 22 and 33 culture variants. SV2B and SYP differential expression showed a time- and genotype-dependent interaction. Interestingly, SYP binds cholesterol during formation of synaptic vesicles (218).

Lin *et al.* 2018 showed a 30% differential increase in synapse number (via SYP and PSD95 immunostaining) in 44 over 33 iNs (also an NGN2-induced isogenic neuron approach; but cultured in conditioned media from 33 astrocytes). They did not pull out *SV2B*, nor *SYP*, in their transcriptomic study (182). They evaluated only one timepoint and interpreted their data as neuronal 44 genotype causing neurons to *overall* mature faster than 33, hence enhanced synaptic activity, but they could not rule out a contribution of astrocytic ApoE coming from the conditioned media in which they maintained the iNs. In their system, it could also be another factor (not ApoE) in the astrocyte conditioned media to which the neurons respond differentially in a genotype-dependent fashion. My data, however, suggest that neuronal 44 versus 33 has a synapse-specific effect; since both E33 and E44 iNs mature at the same rate, as assessed by no differential in *MAP2* and *GAP43* expression during development. Furthermore, E22 (which was not assessed by Lin *et al.* 2018), despite being the protective variant, does not change these synaptic transcripts compared to E33.

A subtle synaptic transcriptional change is consistent with underlying AD disease progression for decades before onset of overt cognitive impairment. Early stages of AD are associated with subtle loss of synaptic structures (56). Also, the degree of cognitive decline in subjects with MCI correlated with presynaptic vesicle SYP immunostaining which was reduced 25% compared with

age-matched, cognitively normal controls (56). Furthermore, subtle alterations in synapse function have been detected in E4 versus non-E4 carriers (56). Considering that synaptic function is affected in AD, slight differences in synaptic function related to changes in synaptic gene expression, as suggested by mRNA expression of these iN cultures, could be a clue of early drivers of disease. My work adds to the theory that neuronal ApoE4 could contribute or drive synaptic dysfunction.

My robust data clearly shows that human neurons in culture develop and functionally connect in a way that is not readily distinguished by *APOE* allele status. Similarly, a head-to-head comparison of a broad transcriptional landscape suggested small shifts in the otherwise similar cultures. These altered transcriptional signatures are striking for two reasons. Firstly, they hint at a shifted synapse-specific development in these cultures. Secondly, there is a significant impact on molecular pathways that underpin neuron signaling.

At this point, the ontogeny of morphology indicated that *APOE* genotype did not impact the neuronal conversion and maturation of the cultures. The different *APOE*-variant cultures showed equally healthy networks reinforced by the surrogate of metabolism, ATP. Importantly, transcription of pan-neuronal neuronal markers and the induction of *FOS* expression showed that maturation was associated with network activity in a neuronal ApoE isoform independent manner. Major neuronal developmental was not impacted by *APOE* genotype.

My findings provide more evidence that ApoE from neurons may influence synaptic development and that the ε4 allele alters synaptic development, compared to ε3, while ε2 does not. *SV2B* was the gene showing the most significant and robust modulation. This encouraged the use of an approach that, compared to RT-PCR, facilitated a more scalable comparison, and retained sufficient sensitivity for detecting shifting transcription.

That most genes were unchanged was not surprising because, while the risk of AD is different for each of the genotypes, the more robust risk is advanced age, so I did not expect a developmental phenotype. My hypothesis is that neuronal ApoE is important in stressed conditions, such as aging or injury. Basically, nothing changed apart from the select synaptic readouts. Even so, the functional outcome is unpredictable because the synaptic transcripts I focused on during the development of the neurons were not universally altered in the same direction despite the fact that they all can pertain to synaptic vesicles involved in glutamatergic neurotransmission, i.e. via RT-PCR, one strikingly went up (*SV2B*), one trended down (*SYP*), and one was unchanged (VGLUT).

Thus, having established this cellular model in which my results indicate successful development from iPSCs to cortical neurons that are mature enough to show synaptic activity, I was now poised

to address my hypothesis that neuronal ApoE mediates response to stress in an isoform-dependent manner such that E2 enhances, while E4 diminishes neuron resilience.

Chapter 6 Response to excitotoxic stress in neurons of different *APOE* genotypes

6.1 Introduction

In the previous chapter I established a human cellular system consisting of a set of isogenic neurons carrying homozygosity for the three major *APOE* alleles. The neurons matured to a point where they exhibited fasciculated neurites reminiscent of neural tracts accompanied by induction of the activity marker, *FOS*, thus suggesting connectivity. I identified readily detectable, albeit low, levels of *APOE* transcript in all neuronal cultures. There was no overt differential effect of *APOE* genotype related to integrity and metabolism. However, a small shift in transcriptional profile hinted at a developmental impact of the AD susceptibility allele, *APOE* ε4. I had now established a platform that allows for testing my hypothesis: neuronal ApoE mediates response to stress in an isoform-dependent manner. The basis for this premise emerges from concepts reviewed in the introduction that: ε2 enhances, while ε4 diminishes, AD resilience (Section 1.4). Hence, I extended my approach of directly comparing the *APOE*-variant neurons under stress conditions and perturbed neuronal homeostasis.

6.2 Testing neuronal resilience

Several groups have demonstrated that neuronal ApoE is upregulated upon Kainic Acid (KA) mediated excitotoxicity in rat and mouse models (Section 1.10.2.1) which inspired me to explore a KA treatment paradigm for stressing human neurons *in vitro* (126, 219). KA, like excitotoxic glutamate, can cause death of susceptible neurons in the CNS in *in vivo* models that simulate neurodegeneration in humans (220). Excitotoxicity is multifaceted but basically prolonged- or over-stimulation of glutamate (which include kainate) receptors results in the degeneration of axons and dendrites and the cell dies (220, 221). In the culture dish, degeneration induced by excitotoxicity can be evidenced by swelling and disintegration of neurites; a phenomenon clearly visualized when GFP-expressing neuron cultures were treated with excess glutamate (Figure 6.1) (221).

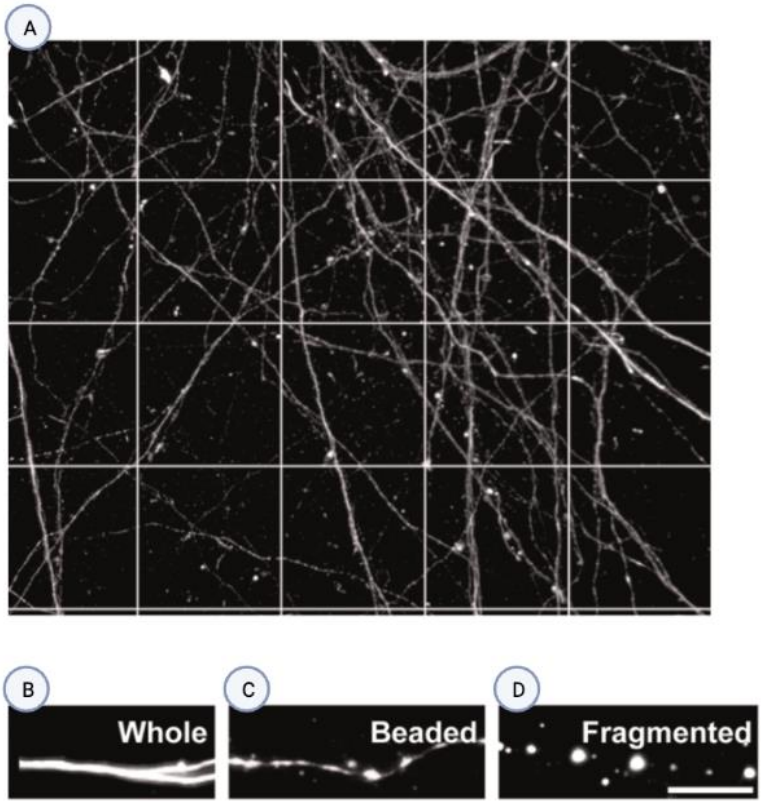

Figure 6.1 Excitotoxicity-induced neurodegeneration in cultured neurons by Hosie *et al.* (221).

A mature (11 days in vitro) primary neuronal culture from transgenic GFP mice (which readily allows morphological examination of neuronal processes) is shown with a superimposed grid helpful for scoring neurodegeneration (A). Excitotoxicity was induced by adding glutamate (to a final concentration of 100 µM) to the culture medium and axons were scored as whole (B) or degenerated, by displaying beaded (discrete swellings connected by sections of axon) (C) or fragmented (disconnected swellings) (D) morphologies. Scale bar = 5 µm. Adapted from Hosie *et al.* (221).

Dysregulated opening of kainate receptor channels upon excessive exposure to KA causes overabundant Ca^{2+} influx across the plasma membrane and triggers increased ROS (Figure 1.4) (220). Perilous levels of ROS lead to mitochondrial dysfunction and membrane lipid peroxidation (220). The main role of mitochondria is energy production in the form of adenosine triphosphate (ATP) via oxidative phosphorylation through the mitochondrial respiratory chain. Since most of a neuron's ATP use is for electrogenic activity, ample energy from mitochondria, which accumulate at synapses to support their high energy demand, is essential for neuronal excitability and survival (220). As such, one way to measure changes in mitochondrial function that presage cell death is to monitor ATP levels in neuronal cultures and lowered levels suggest a negative impact on cell health.

As part of their role in regulating energy metabolism, mitochondria constantly signal to the nucleus and, upon stress, can trigger the nucleus to activate adaptive responses. Activating transcription factor 4, ATF4, is a key effector of mitochondrial stress signaling and promotes

upregulation of protective genes (222, 223). Mitochondrial dysfunction and Ca^{2+} imbalances can stimulate several cellular stress response pathways, like the unfolded protein response (UPR) and the integrated stress response (ISR). The UPR, which also triggers, ATF4 is reported to be activated in several neurodegenerative diseases (223). For example, ATF4 is increased 1.9-fold in brains from patients with AD compared to age matched controls (224). As such, I chose *ATF4* as a readout of stress.

I deemed it important to pick a "Goldilocks" stress condition, wherein, cells are to experience enough strain to mount a stress response, but not too much that they are overwhelmed to the point of irreversible degeneration or death. That is, I wanted to capture responses that drove resilience to, rather than perishing from, stress. As such, I planned to first run exploratory experiments schematized in Figure 6.2, Cartoon 1. Different KA concentrations over a time range would be evaluated and those that elicited stress, and/or decline in culture health, would be revealed as measured by *ATF4* transcription, ATP levels, and gross morphology. Outcomes from these three measurements would then help establish the stress condition for a follow-on study, depicted by Figure 6.2, Cartoon 2. This plan involved subjecting the mature (iN28) neuronal cultures of different *APOE* genotypes to the excitotoxic stress (a single timepoint and concentration of KA determined from experiments represented in Figure 6.2, Cartoon 1) and analyzing the mRNA expression of the set of genes in the NanoString Neuropathology Panel (like was done in untreated neurons in Section 5.13.2)

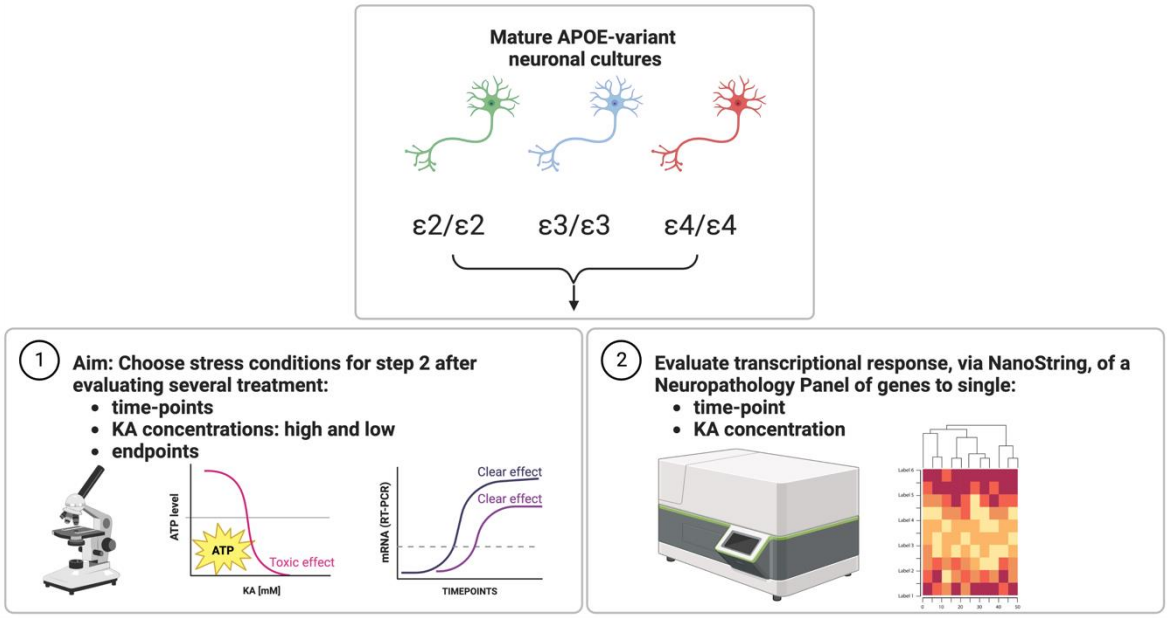

Figure 6.2 Schematic of stress induction experiments.

To identify an optimal kainic acid (KA) concentration and timepoint with which to stress the *APOE*-variant iN28 neuronal cultures, experiments were done as schematized in ①. Parallel cultures were incubated with two KA concentrations and analyzed for health and structural integrity via microscopy and metabolism (ATP levels) at 18 hours. Furthermore, the induction of activity- and stress-associated transcripts were quantified. Results of ① then informed the single KA concentration and timepoint I chose for the next step, represented in ②: comparison of mRNA copy numbers of genes in the Neuropathology Panel (NanoString) in the *APOE*-variant neurons exposed to the finalized stress conditions.

6.3 Select kainic acid receptor subunits are expressed

I checked whether genes encoding components of the ligand-gated kainate family of glutamate receptors, mediators of excitotoxicity in my paradigm, were being upregulated during the conversion to neurons. I tested mRNA expression of glutamate receptor ionotropic kainate 1 (*GRIK1*) and glutamate receptor ionotropic kainate 2 (*GRIK2*) via RT-PCR from samples generated in the last Chapter (Section 5.5). As expected, both receptor subunits were strongly upregulated from being almost undetectable in the iPSC stage to being clearly expressed after neuronal induction, as shown in Figure 6.3. The upregulation was not affected by *APOE* genotype.

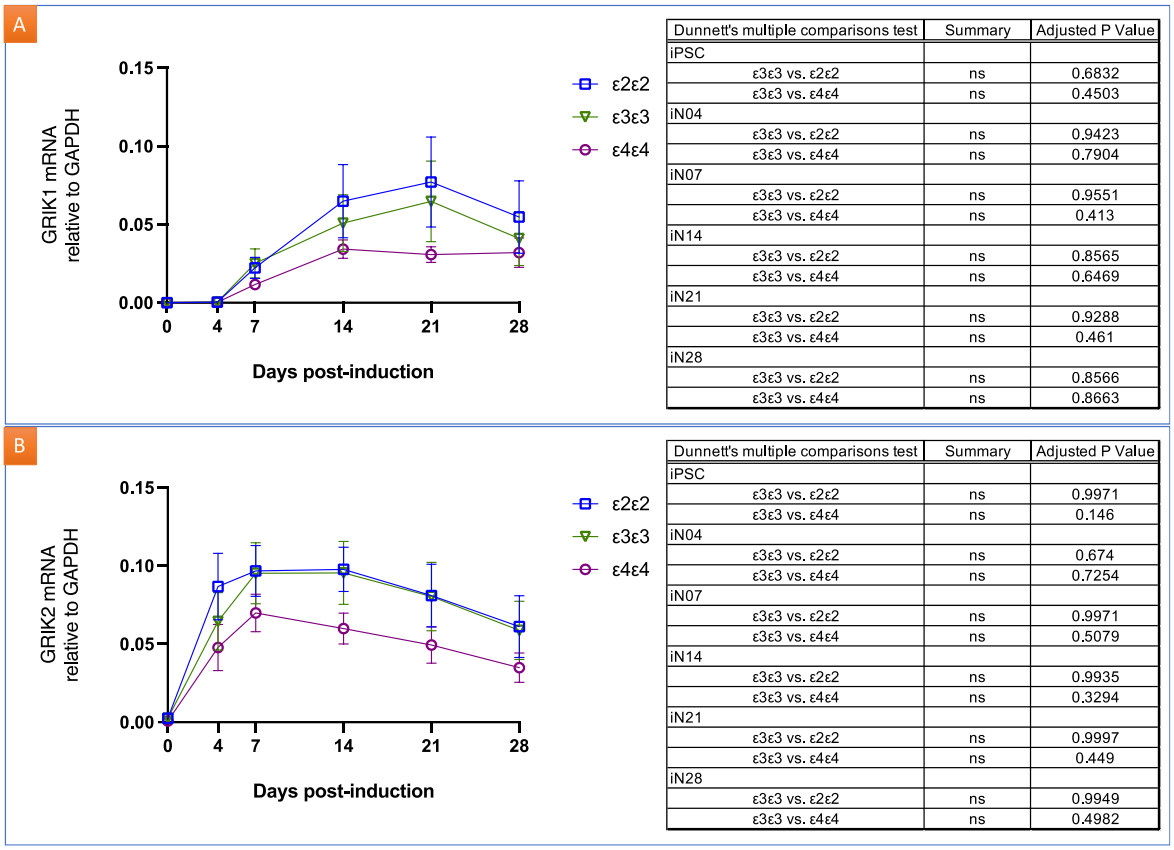

Dunnett's multiple comparisons test	Summary	Adjusted P Value
iPSC		
ε3ε3 vs. ε2ε2	ns	0.6832
ε3ε3 vs. ε4ε4	ns	0.4503
iN04		
ε3ε3 vs. ε2ε2	ns	0.9423
ε3ε3 vs. ε4ε4	ns	0.7904
iN07		
ε3ε3 vs. ε2ε2	ns	0.9551
ε3ε3 vs. ε4ε4	ns	0.413
iN14		
ε3ε3 vs. ε2ε2	ns	0.8565
ε3ε3 vs. ε4ε4	ns	0.6469
iN21		
ε3ε3 vs. ε2ε2	ns	0.9288
ε3ε3 vs. ε4ε4	ns	0.461
iN28		
ε3ε3 vs. ε2ε2	ns	0.8566
ε3ε3 vs. ε4ε4	ns	0.8663

Dunnett's multiple comparisons test	Summary	Adjusted P Value
iPSC		
ε3ε3 vs. ε2ε2	ns	0.9971
ε3ε3 vs. ε4ε4	ns	0.146
iN04		
ε3ε3 vs. ε2ε2	ns	0.674
ε3ε3 vs. ε4ε4	ns	0.7254
iN07		
ε3ε3 vs. ε2ε2	ns	0.9971
ε3ε3 vs. ε4ε4	ns	0.5079
iN14		
ε3ε3 vs. ε2ε2	ns	0.9935
ε3ε3 vs. ε4ε4	ns	0.3294
iN21		
ε3ε3 vs. ε2ε2	ns	0.9997
ε3ε3 vs. ε4ε4	ns	0.449
iN28		
ε3ε3 vs. ε2ε2	ns	0.9949
ε3ε3 vs. ε4ε4	ns	0.4982

Figure 6.3 Kainic acid (KA) receptor subunits, GRIK1 and GRIK2, are expressed in the induced neurons.

RT-PCR data for transcript levels of two KA subunits, (A) *GRIK1* and (B) *GRIK2*, relative to the housekeeping gene, *GAPDH* are shown for the 3 APOE-variant lineages at the following timepoints after NGN2 induction (days): 0, 4, 7, 14, 21, and 28. Neuronal cultures derived from isogenic iPSCs homozygous for E2, E3 or E4 are represented by the square, triangle, or circle symbols, respectively. Error bars are SEM from 3 independent rounds of differentiations (each n=3 bioreps). Two-way ANOVA analysis indicated there was an interaction between time and expression level and there was no interaction with *APOE* allele status. The tables show respective p values of comparisons to the neutral genotype, E3, after 2-way ANOVA analysis, which indicated an interaction between time and expression levels.

6.4 Defining the kainic acid stress condition (time and concentration)

To find a concentration and timepoint that would inform the stress conditions for the follow-on experiments, I tested two concentrations of KA (a high and a low concentration: 300 and 30 µM, respectively) over a time course ranging from 30 minutes to 18 hours, based on published data for rodent primary neurons (221). I confirmed KA-induced neuronal excitability and stress by evaluating *FOS* and *ATF4* transcript levels respectively, as well as morphology.

6.4.1 Kainate induced neuronal activity in all cultures: no *APOE*-dependent effect

Fos protein is induced by neuronal activity, including KA–induced seizures, acting as a switch between appropriate neuronal excitability and protection from potential excitotoxicity (225). Upon 30 µM KA treatment over 0.5, 1, 2, 4, 6, and 18 hours, *FOS* expression showed a rapid induction reaching significant levels relative to vehicle treatment by 4 hours (statistics table in Appendix D), peaking at the 6-hour timepoint, after which, the level of expression fell by 18 hours (Figure 6.4). There was no genotype-related difference when comparing neuronal responses in the E22 or E44 with that of E33 cultures for the 30 µM treatment (Figure 6.4 left). Treatment with 300 µM KA induced a significant differential *FOS* response when comparing E33 with E44 iN28s at the 6-hour time-point. Meanwhile, the parallel comparison between E33 and E22 cultures was not significant (Figure 6.4 right).

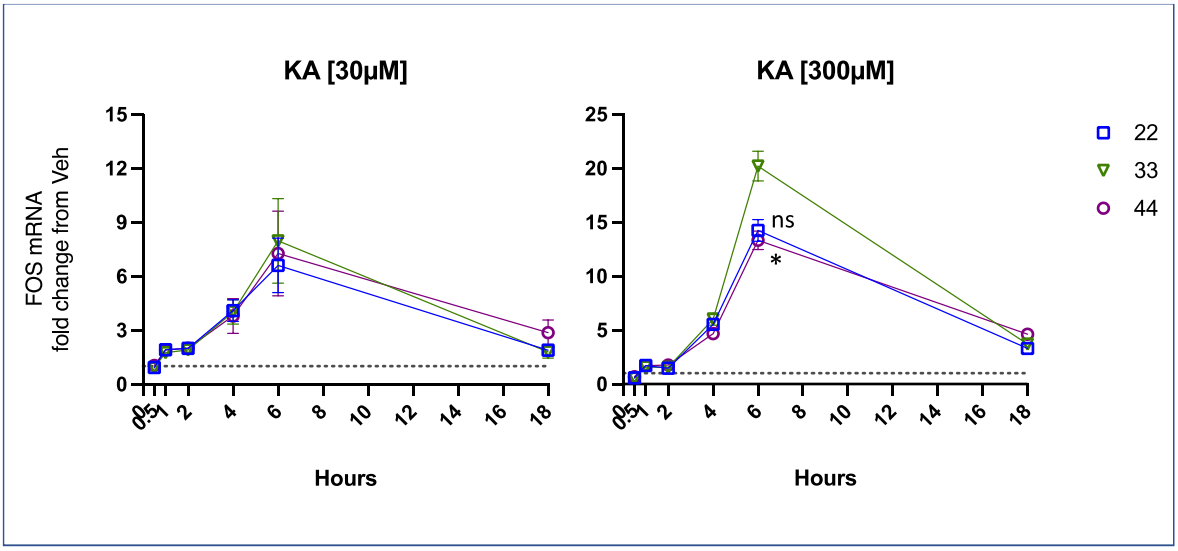

Figure 6.4 *FOS* mRNA response to kainic acid (KA) exposure over time in *APOE*-variant iN28 neurons.

Time course (0.5, 1, 2, 4, 6, and 18 hours) of *FOS* transcript induction in response to 30 (left) or 300 (right) µM KA treatments, for the indicated APOE-genotype. Square, triangle, and circle depict E22, E33, and E44 iN28s, respectively. Data is shown as fold-change from the respective vehicle control, set at 1 (dotted line). * E33 vs. E44 adjusted P value = 0.0382; ns = E33 vs. E22 adjusted P value = 0.0569 (2-way ANOVA with Sidak's multiple comparisons). Error bars = SEM from 3 independent experiments (each with n=3 technical replicates). 2-way ANOVA indicated an interaction between time and expression levels.

Taken together, these *FOS* data suggest robust induction of neuronal activity in the neurons regardless of APOE genetic status, which peaked at 6 hours. The magnitude of the response was more consistent for the different cultures when used at the lower rather than the higher concentration.

6.4.2 Kainate induced stress in all cultures: slight delay in *APOE ε4* neurons

To compare how KA treatment elicited stress in the human neuronal *APOE*-variant cultures, I assessed the stress-response gene, *ATF4*. This analysis saw a genotype-differential induction at the 2-hour mark with the 30 µM treatment. At this point *ATF4* levels in the E44 cultures remained close to baseline while E22 and E33 cultures experienced increased (both by 16%) *ATF4* transcription. At 4, 6 and 18 hours, all three cultures, irrespective of *APOE* genotype, showed overlapping *ATF4* induction levels. At the high KA concentration (Figure 6.5 [right]), the response pattern in the E44 curve also implies a delayed *ATF4* induction compared to the E22 and E33 cultures (though not statistically significant). Overall, ATF*4* levels remained elevated from 6 to 18 hours.

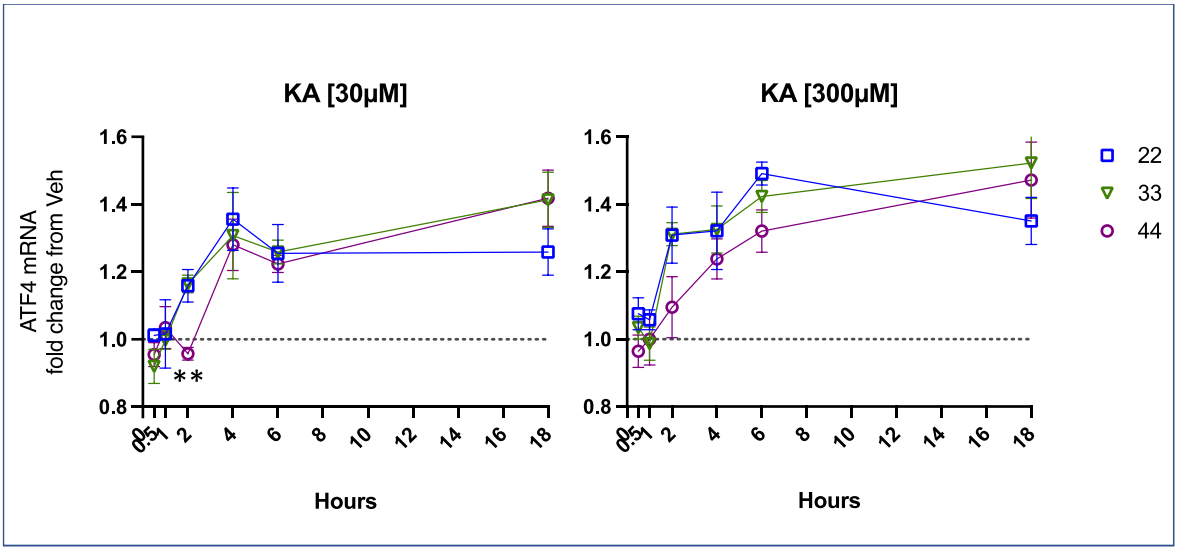

Figure 6.5 *ATF4* mRNA response to kainic acid exposure over time in *APOE*-variant iN28 neurons.

Time course (0.5, 1, 2, 4, 6, and 18 hours) of *ATF4* expression in response to 30 (left) and 300 (right) µM KA treatments in distinct different *APOE*-variant. Square, triangle, and circle depict E22, E33, and E44 iN28s, respectively. Data is shown as fold-change from the respective vehicle control, set at 1 (dotted line). ** E33 vs. E44 adjusted P value = 0.0085 (2-way ANOVA with Sidak's multiple comparisons). Error bars = SEM from 3 independent experiments (each with n=3 technical replicates). 2-way ANOVA indicated an interaction between time and expression levels.

These *ATF4* kinetic profiles suggest E44 neurons at 2 hours failed to mount an initial response to 30 µM KA. However, although delayed in responding to stress, the E44 neurons eventually caught up to the other cultures and this profile is distinct to *ATF4* as the *FOS* response (Section 6.4.1) did not show this lag. Overall, the response at 30 µM reached maximal levels at 4 hours and did not decline but plateaued thereafter, in contrast to FOS, that declined after peaking at 6 hours.

6.4.3 *APOE* transcription remained unchanged following kainate-induced stress

I next measured *APOE* mRNA in these same samples described above (Section 6.4.1). I predicted *APOE* would be induced by excitotoxic stress from KA exposure based on experiments in mouse models (126). Overall, *APOE* transcription was not altered by either KA concentration or timepoint. This indicated that, although present, neuronal *APOE* was not responsive to this stress paradigm. Any differences in stress response would thus be connected to basal ApoE levels and underpinning synaptic developmental differences owing to genotype.

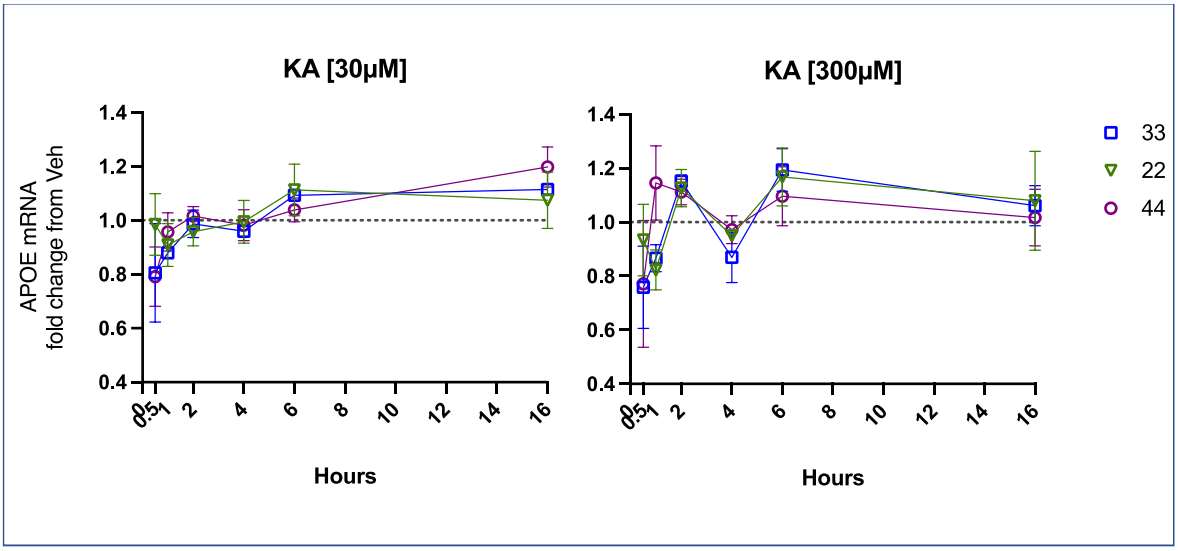

Figure 6.6 *APOE* mRNA response to kainic acid exposure over time in *APOE*-variant neurons.

Time course (0.5, 1, 2, 4, 6, and 18 hours) of *APOE* transcript induction in response to 30 (left) and 300 (right) µM KA treatments, for the different *APOE*-variant iN28 cultures. Data is shown as fold-change from the respective vehicle control, set at 1 (dotted line). Error bars = SEM from 3 independent experiments (each with n=3 technical replicates). 2-way ANOVA did not indicate an interaction between time and expression levels.

6.4.4 High kainic acid concentration impaired culture health

I had collected photomicrographs across the time course at which cultures developed. These indicated that there was no clear difference in the appearance of the cultures (Figure 5.8, Figure 5.9 and, Figure 5.10). In a similar way, just prior to conducting an assay to assess ATP levels in neurons treated with or without kainate, I collected images to investigate neuronal structural integrity – both endpoints as proxies for neuron health.

6.4.4.1 Neurodegeneration after KA treatment; independent of *APOE* genotype

Figure 6.7 depicts E33 neurons after 18 hours of exposure to 30 and 300 µM concentrations of KA. Visualization of the 300 µM treatment revealed that some neurites acquired a fragmented appearance and GFP was extensively aggregated, reminiscent of the reports shown in Figure 6.1,

and suggests neurons were degenerating. I enlarged the dotted outlined boxes to create Figure 6.8; showing the degenerating neurites and blebbing GFP. Corresponding observations were made in the other two *APOE*-variant neuronal cultures at the 300 µM KA conditions; Figure 6.9 and Figure 6.10 depict the E22 and E44 cultures, respectively.

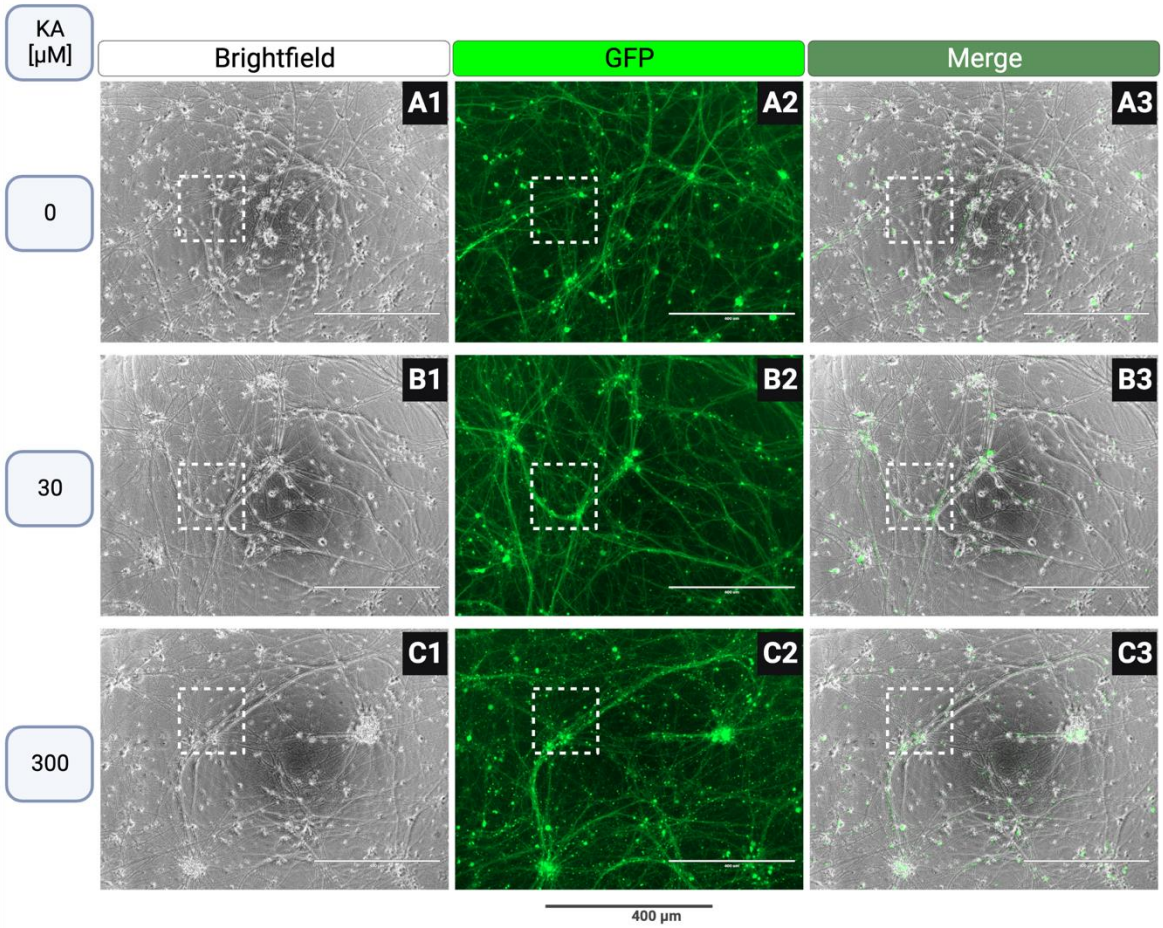

Figure 6.7 Appearance of *APOE* E33 iN28 upon kainic acid (KA) treatment for 18 hours.

Representative photomicrographs of E33 cultures at iN28 after 18 hours of the indicated KA treatment. Images from brightfield, GFP, and merge of the two views are shown in the left, middle and right columns, respectively. Top row (A) shows cultures that were controls not exposed to KA (0 µM). Middle (B) and bottom (C) rows show cultures treated with 30 and 300 µM KA, respectively. The dotted box outlines the parts of the images that are blown up below (Figure 6.8). Scale bars represent 400 µm.

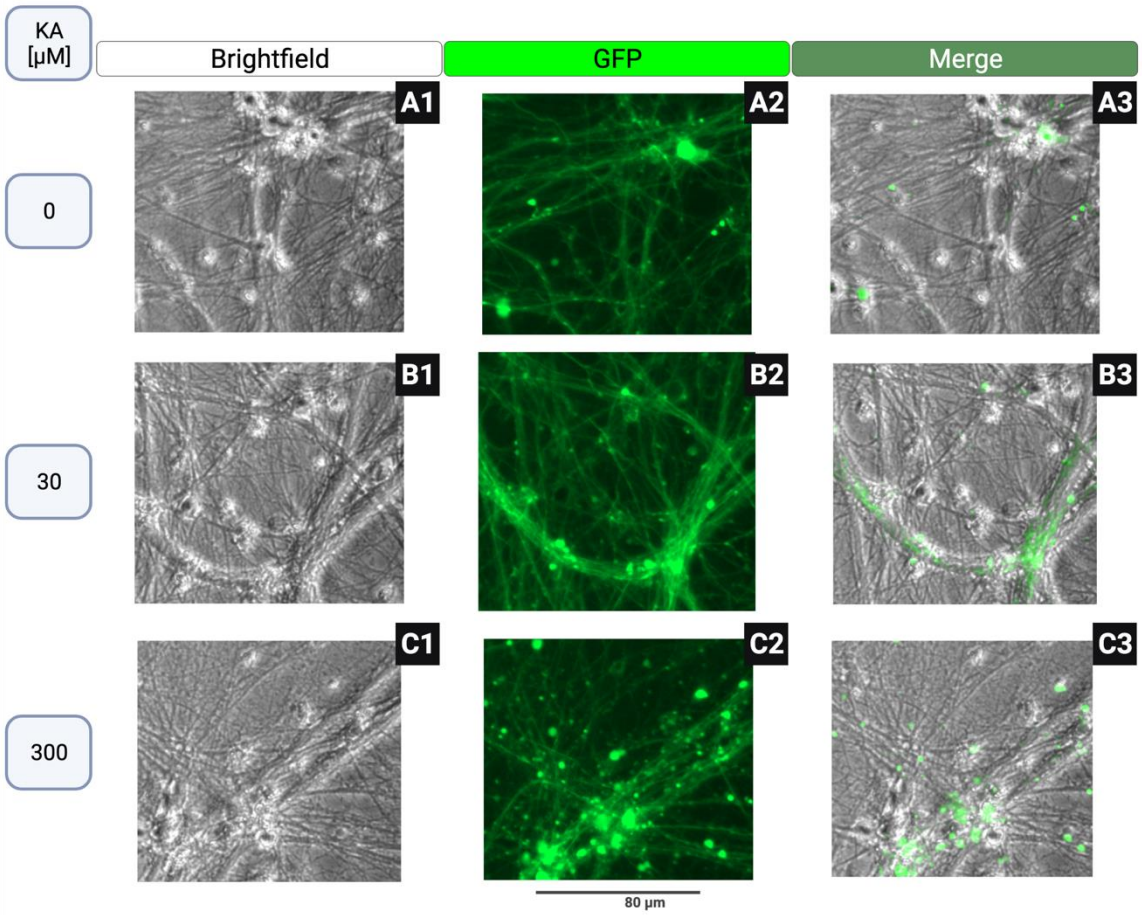

Figure 6.8 Enlarged sections from Figure 6.7: *APOE* E33 iN28 treated with kainic acid.

Enlarged portions within the dotted area of images in Figure 6.7 are shown. The GFP channel (middle panels) clearly reveals high levels of GFP aggregation (C2) upon exposure to KA [300 µM]. Scale bars represent about 80 µm.

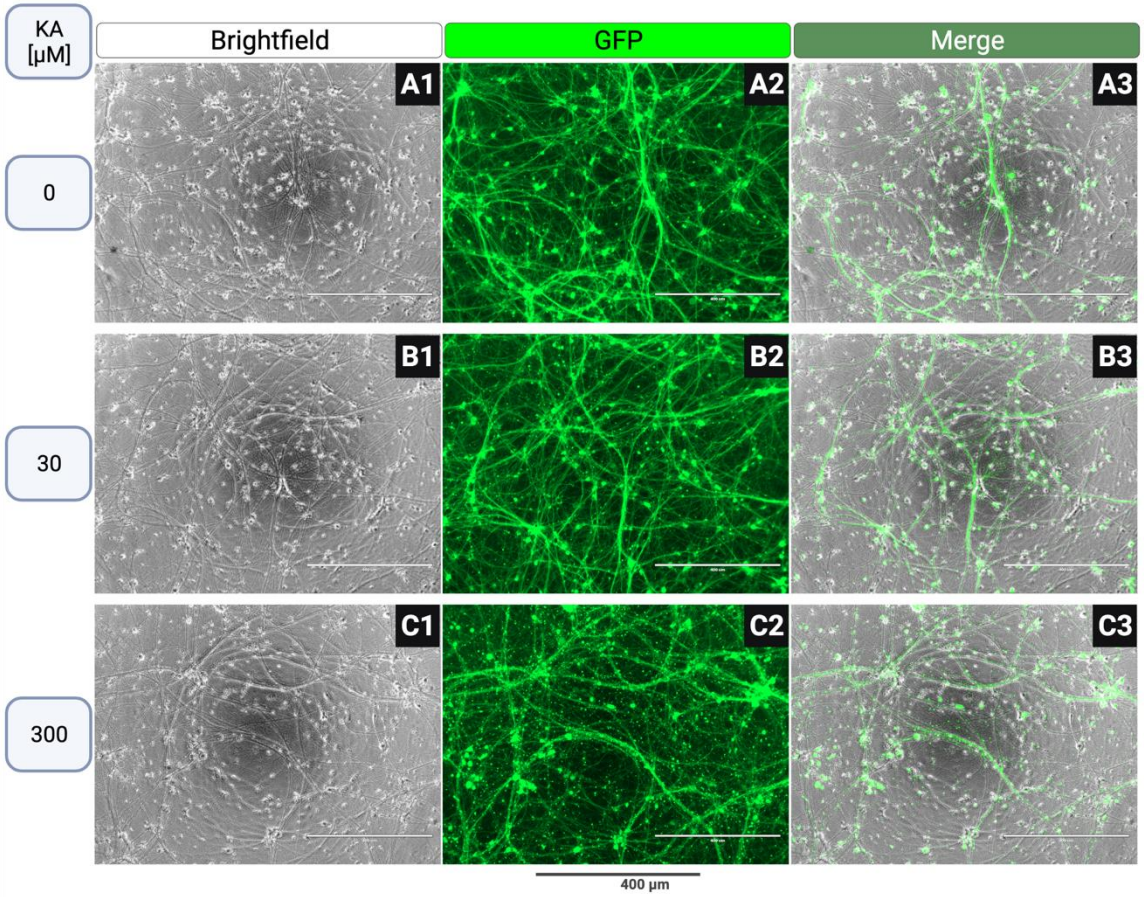

Figure 6.9 Appearance of *APOE* E22 iN28 upon KA treatment.

Representative photomicrographs of E22 cultures at iN28 after 18 hours of the indicated KA treatment. Images from brightfield, GFP, and merge of the two views are shown in the left, middle and right columns, respectively. Top row (A) shows cultures that were not exposed to KA (0 µM). Middle (B) and bottom (C) rows show cultures treated with 30 and 300 µM KA, respectively. The punctate appearance of GFP in C2 compared to A2 is indicative of neurodegeneration. Scale bars represent 400 µm.

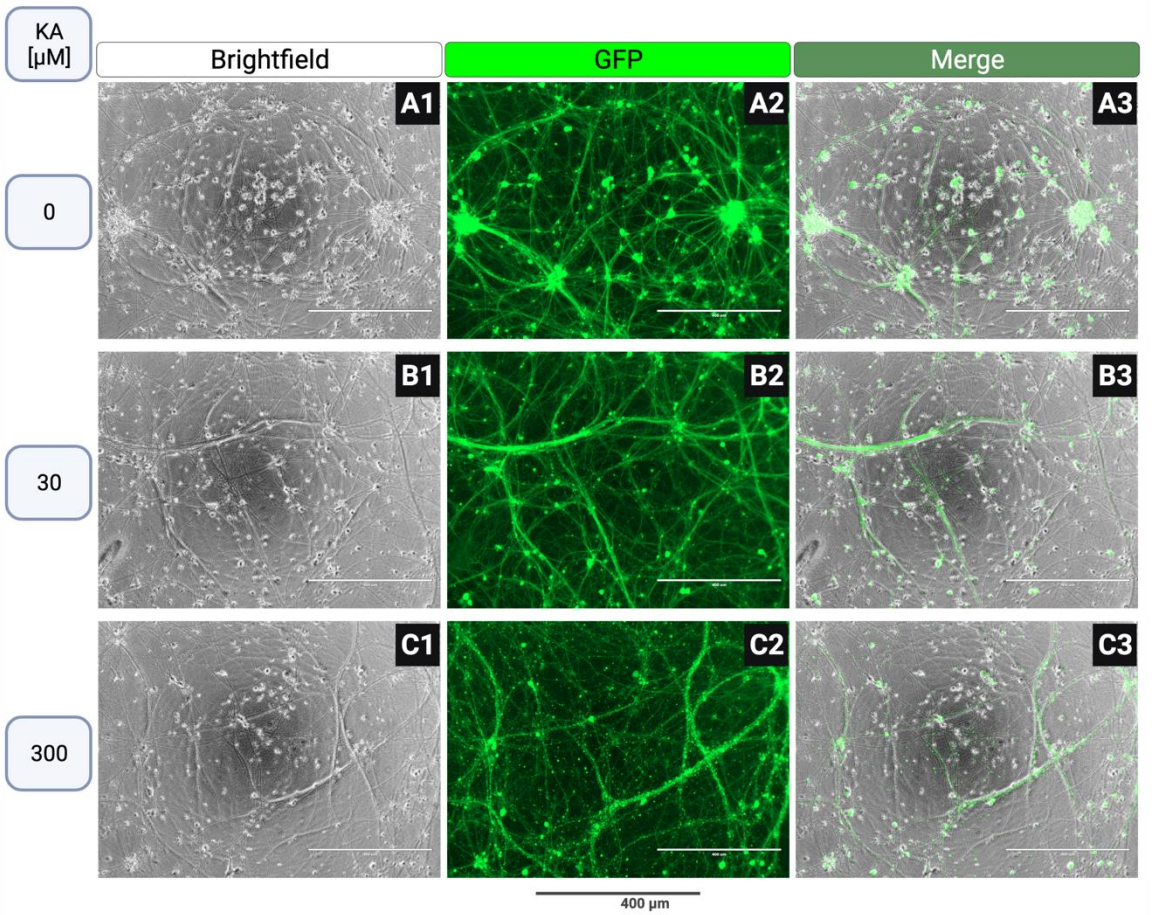

Figure 6.10 Appearance of *APOE* E44 iN28 upon KA treatment.

Representative photomicrographs of E44 cultures at iN28 after 18 hours of the indicated KA treatment. Images from brightfield, GFP, and merge of the two views are shown in the left, middle, and right columns, respectively. Top row (A) shows cultures that were not exposed to KA (0 µM). Middle (B) and bottom (C) rows show cultures treated with 30 and 300 µM KA, respectively. The punctate appearance of GFP in C2 compared to A2 is indicative of neurodegeneration. Scale bars represent 400 µm.

6.4.4.2 Lowered mitochondrial respiration; independent of *APOE* genotype

I next evaluated ATP levels with the CellTiter-Glo® Luminescent Cell Viability Assay in the cultures described above 18 hours after KA exposure (method described in Section 2.5.5). In the vehicle-treated cultures there was an equivalent luminescence emission implying the metabolism was equally intact in the control cultures from each genotype. In contrast, 30 µM KA treatment caused a drop in the ATP levels for all cultures. Figure 6.11 shows ATP levels in the E22, E33, and E44 cultures fell by 10%, 13%, and 13%, respectively, compared to their vehicle-matched controls. At the 300 µM KA concentration, ATP levels decreased further; by 45%, 46%, and 50% in the E22, E33, and E44 cultures, respectively. The robust drop in ATP suggested 300 µM KA for 18 hours negatively impacts cellular health. The datasets largely overlapped amongst the various neuron types indicating a lack of *APOE* allele-specific, differential vulnerability.

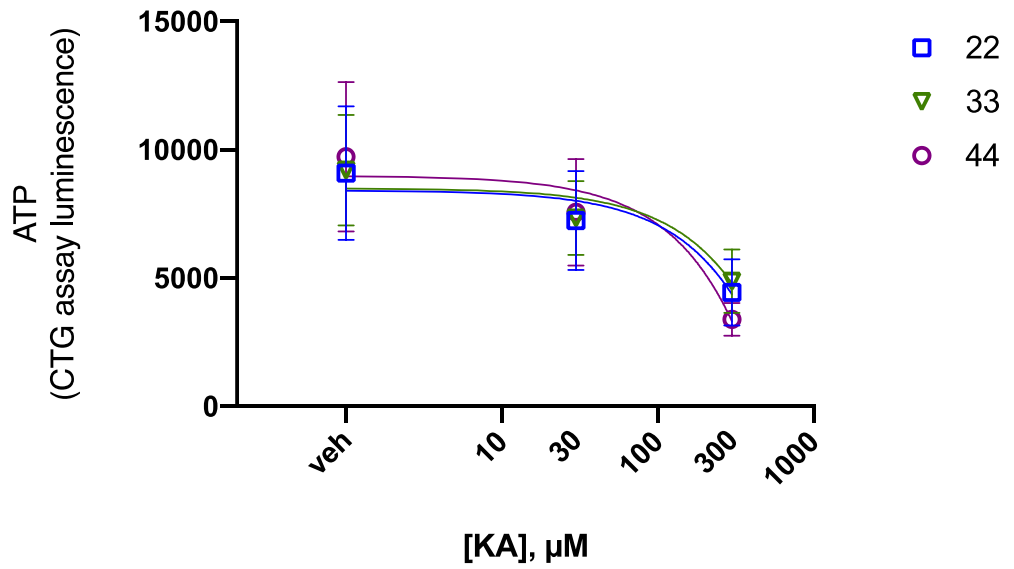

Figure 6.11 Adenosine triphosphate (ATP) levels in *APOE*-variant iN28s treated with kainic acid (KA).

ATP levels in the iN28 cultures carrying the three *APOE* genotypes after 18-hour exposures to 30 and 300 µM KA. Error bars = SEM from 3 independent experiments each with 3 culture replicates. CTG = CellTiter-Glo® Luminescent Cell Viability Assay. ANOVA indicated a significant interaction with KA concentration (P value = 0.0055) and no significant interaction with *APOE*-variant culture (p value = 0.9988).

6.5 Gene expression analysis (NanoString) upon excitotoxic stress

My results indicated that this experimental paradigm was sensitive enough to capture conditions in which neurons showed a transcriptional response encompassing activity dependent and stress induced genes while at the same time the cells remained healthy (no negative impacts on ATP and neurite structural morphology). Subjected to 300 µM KA for 18 hours, a clear negative impact was demonstrated as measured by ATP reduction and by blebbing of neurites. My analysis of *ATF4* expression indicated this paradigm was able to detect a distinct response to the stressor based on genotype; E44 neurons had a lagged response, implying a shift in kinetics rather than in absolute response. For this reason, using this paradigm to perform a deeper characterization of the response to excitotoxicity seemed reasonable. I purified RNA from 2 independent rounds of experiments in which iN28 neurons of each of the three *APOE* genotypes were treated with KA at 30 µM or vehicle for 6 hours, in parallel. The resultant samples were subjected to the nCounter® Human Neuropathology NanoString Panel comprising 760 genes linked to neurodegeneration pathways plus internal reference housekeeping genes for normalizing transcript counts (Section 5.13 shows panel results in nontreated neurons).

6.5.1 NanoString results corroborated those of earlier RT-PCR for *FOS*, *ATF4*, and *APOE*

My initial analyses of the NanoString data determined whether the *FOS*, *ATF4*, and *APOE* mRNA readouts were consistent with the experiments in Sections 6.4.1, 6.4.2, and 6.4.3, which had used RT-PCR to quantify three different rounds of differentiation. Data from NanoString came from two rounds of differentiation and was consistent with data gleaned via RT-PCR. Figure 6.12 shows 6-, 7-, and 6-fold inductions of *FOS* mRNA counts for the E22, E33, and E44 cultures respectively for NanoString results, which are similar to the fold-inductions reported in Figure 6.4 (left side). NanoString shows that *ATF4* mRNA was induced by 33%, 31% and 26% in the E22, E33, and E44 cultures respectively (Figure 6.13). For reference, extracting the 6-hour 30 µM KA treatment time point from the RT-PCR results from Figure 6.5, *ATF4* mRNA was induced in a similar range; by 26%, 27% and 23% in the E22, E33, and E44 cultures respectively. Figure 6.14 illustrates that although *APOE* counts were low, they clearly fell above the threshold cut-off of expression (Section 2.5.6). The level of *APOE* in the E22 samples was lower than those in the E33 and E44 samples, an observation consistent with the RT-PCR readouts for both undifferentiated iPS and neuron-differentiated cells (Figure 5.3, Figure 5.16, and Figure 5.17). However, in all cases, *APOE* levels remained unchanged following KA exposure, as was also seen in the RT-PCR experiments above (Figure 6.6). The correlation of the *ATF4*, *FOS,* and *APOE* results in the two distinct technologies and independent rounds of differentiation from iPSCs systems validated the overall robustness of the data and platform.

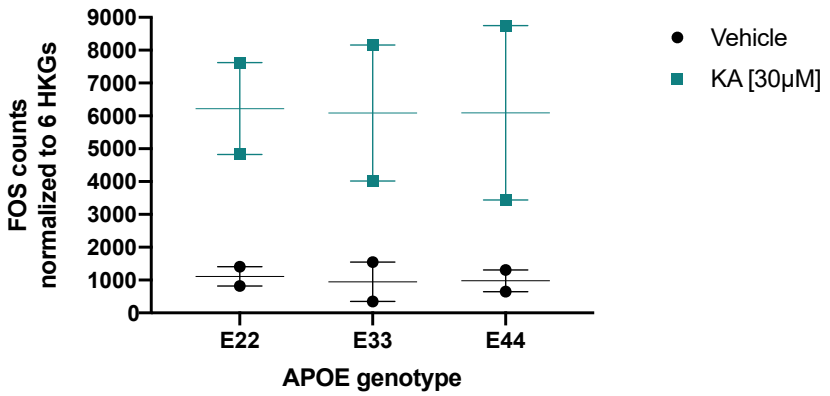

Figure 6.12 NanoString data shows kainic acid (KA) treatment induced *FOS* transcription.

FOS mRNA counts extracted from the nCounter® Human Neuropathology panel normalized to 6 housekeeping genes (HKG) for APOE-variant iN28s at 6 hours of 30 µM KA or vehicle treatments. Error bars = SD from 2 independent experiments. The horizontal line between a pair of samples marks their average.

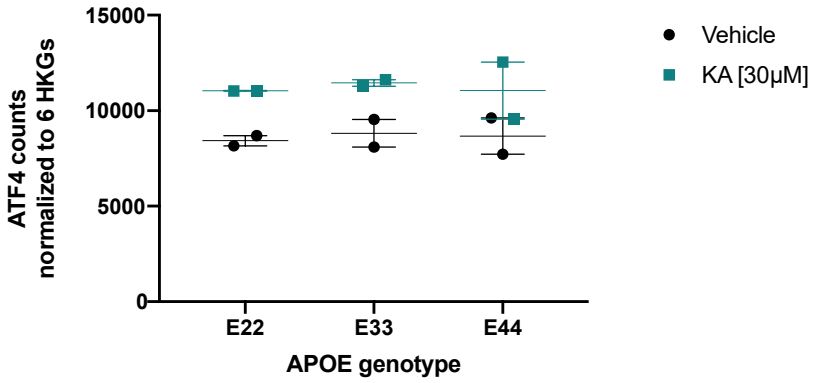

Figure 6.13 NanoString data shows kainic acid (KA) treatment induced *ATF4* transcription.

ATF4 mRNA counts extracted from the nCounter® Human Neuropathology panel normalized to 6 housekeeping genes (HKG) for APOE-variant iN28s at 6 hours of 30 µM KA or vehicle treatments. Error bars = SD from 2 independent experiments. The horizontal line between a pair of samples marks their average.

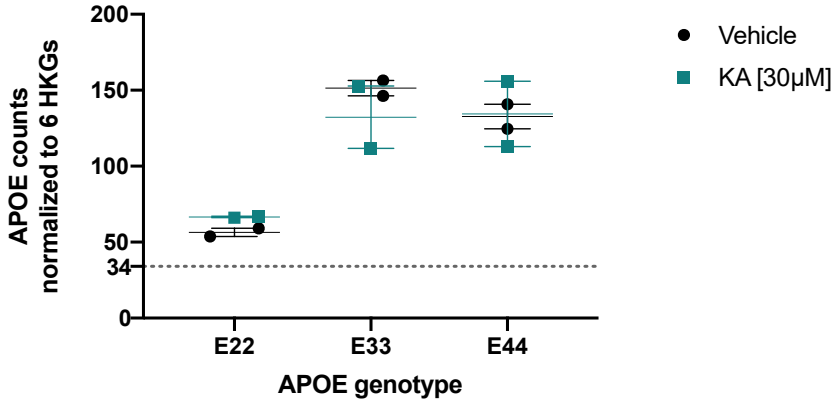

Figure 6.14 NanoString data shows *APOE* transcript levels were unaffected by kainic acid (KA).

APOE mRNA counts extracted from the nCounter® Human Neuropathology panel normalized to 6 housekeeping genes (HKG) for APOE-variant iN28s at 6 hours of 30 µM KA or vehicle treatments. Error bars = SD from 2 independent experiments. The horizontal line between a pair of samples marks their average. Dotted line represents the background (below 34 counts) threshold.

6.5.2 Transcriptional response to KA stress was in an *APOE* genotype-agnostic manner

Total mRNA extracted from control and kainate-treated cultures were probed against the nCounter® Human Neuropathology panel using NanoString technology. Of the 760 investigational transcripts, only 12 were differentially regulated upon KA-induced stress. My analysis of the NanoString data identified, in addition to *ATF4* and *FOS*, 10 genes in which baseline expression showed a significant change upon KA administration (per criteria set out in Section 2.5.6). These genes appear in the heatmap in Figure 6.15 as the absolute expression (normalized to housekeeping genes) with vehicle samples on the left half and KA-treated samples on the right. The color calibration bar indicates that yellow, black, and purple hues are associated with higher,

mid-range, and lower counts respectively. Across the left 6 (untreated) and right 6 (treated) groups in Figure 6.15, a differential expression induced by KA can be perceived by the color change. Interestingly within this set of genes there is no variation in their expression from the distinct *APOE* genotypes under the control vehicle condition. From this global heatmap I highlighted interesting sets of genes as individual scatter plots in the following sections.

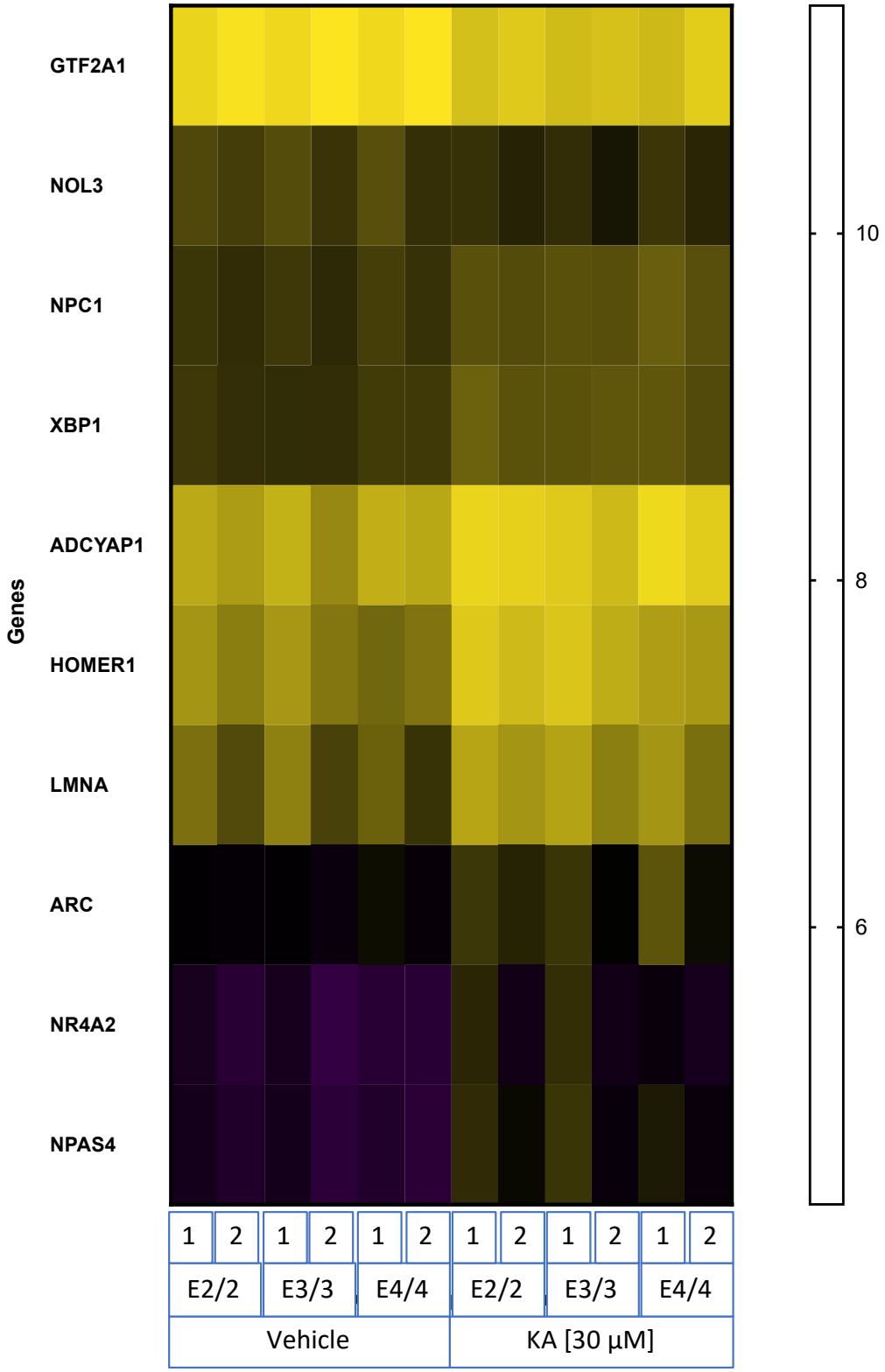

Figure 6.15 Heatmap of genes that were sensitive to excitotoxicity.

Heatmap showing 10 transcripts (besides *ATF4* and *FOS*) responding to kainic acid-induced excitotoxity extracted from the nCounter® Human Neuropathology panel and calibrated along mRNA counts (log2) for each sample (mRNA from 2 independently differentiated and treated cultures per genotype was loaded into a common NanoString cartridge of 12 slots) representing the 3 *APOE* genotypes. The gene list is ranked from top to bottom as highest- to lowest-expressing when averaged across all cultures. The color calibration bar indicates that yellow, black, and purple hues are associated with higher, mid-range, and lower counts respectively.

6.5.2.1 Upregulated genes

Extracting from the DEGs listed in Figure 6.15, I noted that network activity responsive genes like the immediate early genes *NPAS4* and *NR4A2/NURR1* were induced upon KA treatment. Their upregulation is charted in a more granular level (compared to the heatmap) in Figure 6.16. Likewise, late-response genes, *HOMER1* and *ADCYAP1* (also known as *PACAP*), were upregulated and further charted in Figure 6.17. Together, these gene inductions further suggested stimulation of neuronal excitability by KA.

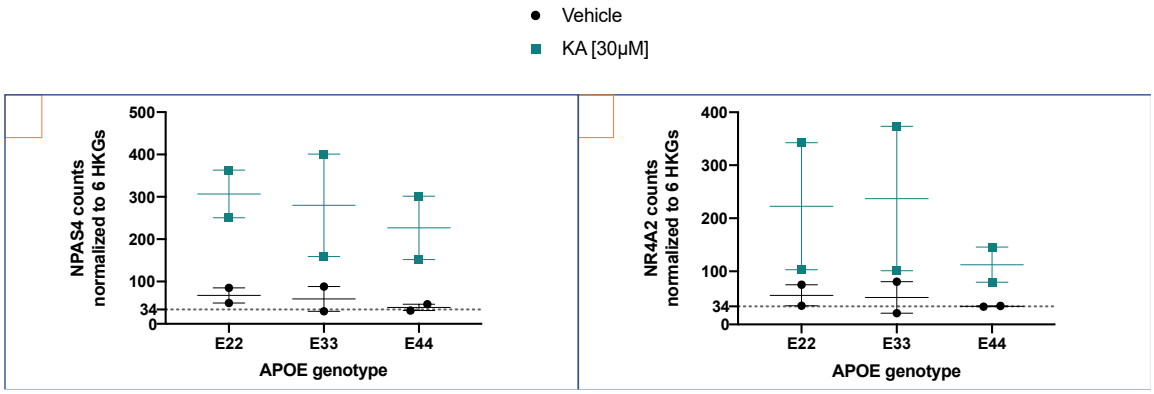

Figure 6.16 Immediate early genes, *NPAS4* and *NR4A2,* responded to kainic acid induced stress.

(A) *NPAS4* and (B) *NR4A2* mRNA counts extracted from the nCounter® Human Neuropathology panel normalized to 6 housekeeping genes (HKG) for APOE-variant iN28s at 6 hours of 30 µM KA or vehicle treatments. Error bars = SD from 2 independent experiments. The horizontal line between a pair of samples marks their average. Dotted line represents the background (below 34 counts) threshold.

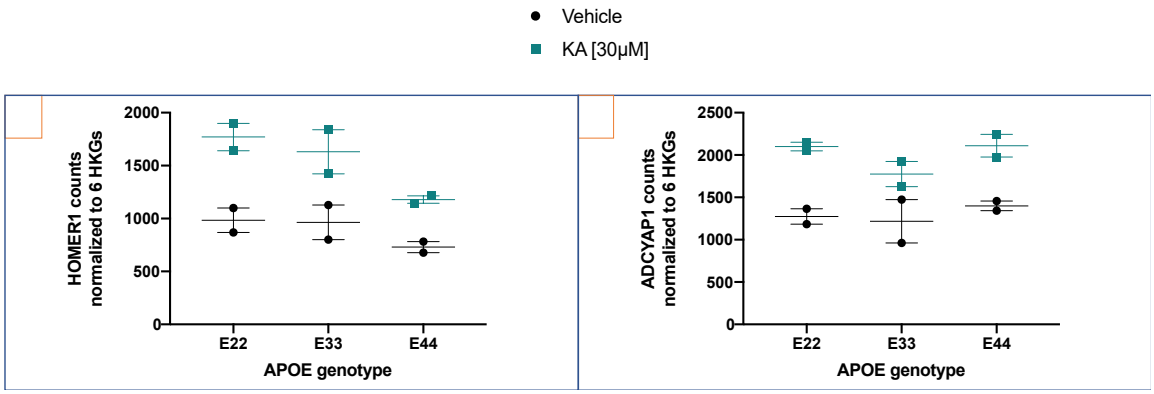

Figure 6.17 Late-response genes, *HOMER1* and *ADCYAP1,* responded to kainic acid-stress.

(A) *HOMER1* and (B) *ADCYAP1* mRNA counts extracted from the nCounter® Human Neuropathology panel normalized to 6 housekeeping genes (HKG) for APOE-variant iN28s at 6 hours of 30 µM KA or vehicle treatments. Error bars = SD from 2 independent experiments. The horizontal line between a pair of samples marks their average.

The *XBP1* mRNA transcript, encoding a factor known to regulate the UPR and connected with cellular stress response, was induced upon KA-mediated stress (Figure 6.18). Notably, spliced versus unspliced *XBP1* was not distinguished by the NanoString probe set.

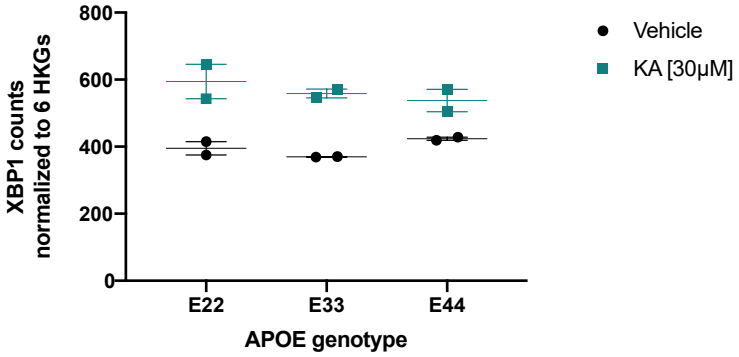

Figure 6.18 *XBP1*, a stress response transcript, increased with kainic acid exposure.

XBP1 mRNA counts extracted from the nCounter® Human Neuropathology panel normalized to 6 housekeeping genes (HKG) for APOE-variant iN28s at 6 hours of 30 µM KA or vehicle treatments. Error bars = SD from 2 independent experiments. The horizontal line between a pair of samples marks their average.

The influence of KA excitotoxic stress on NPC1 gene expression is detailed in Figure 6.19. The clear upregulation of this gene is interesting because the product of NPC1 transports cholesterol within cells (Section 1.6.1).

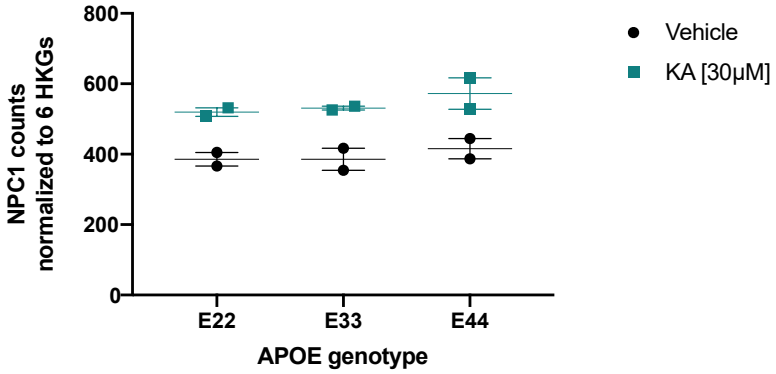

Figure 6.19 *NPC1* transcript responded to kainic acid induced stress.

NPC1 mRNA counts extracted from the nCounter® Human Neuropathology panel normalized to 6 housekeeping genes (HKG) for *APOE*-variant iN28s at 6 hours of 30 µM KA or vehicle treatments. Error bars = SD from 2 independent experiments. The horizontal line between a pair of samples marks their average.

6.5.2.2 Downregulated genes

Two of the 12 DEGs showing sensitivity to KA were downregulated and they are independently graphed in Figure 6.20. *GTF2A1* also known as *TFIIA*, encodes a subunit of the RNA polymerase II transcriptional machinery. *NOL3* encodes an anti-apoptotic protein.

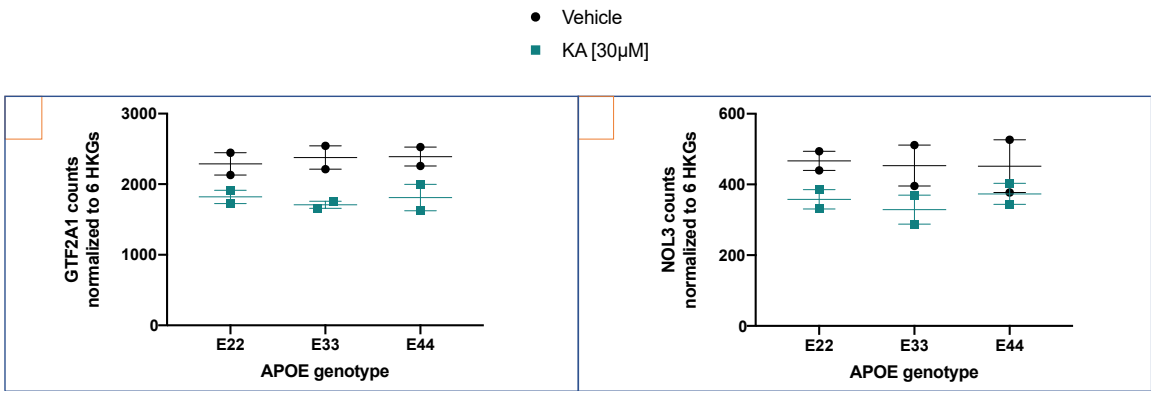

Figure 6.20 *GTF2A1* and *NOL3* were downregulated upon kainic acid induced stress.

(A) *GTF2A1* and (B) *NOL3* mRNA counts extracted from the nCounter® Human Neuropathology panel normalized to 6 housekeeping genes (HKG) for APOE-variant iN28s at 6 hours of 30 μM KA or vehicle treatments. Error bars = SD from 2 independent experiments. The horizontal line between a pair of samples marks their average.

6.5.3 *APOE* allele-associated differentially expressed genes were insensitive to stress

None of the DEGs extracted in the previous Chapter (Figure 5.24) that focused on the ontogeny of the *APOE*-variant neurons surfaced as stress responsive. I nonetheless analyzed scatter plots of several that overlapped with the DEGs described in a report from another group that compared E33 and E44 iNs: EPHA4, KCNA1, PTPRR, NKX6-2, and NTS (182). Figure 6.21 illustrates that KA-induced stress had no impact on their expression.

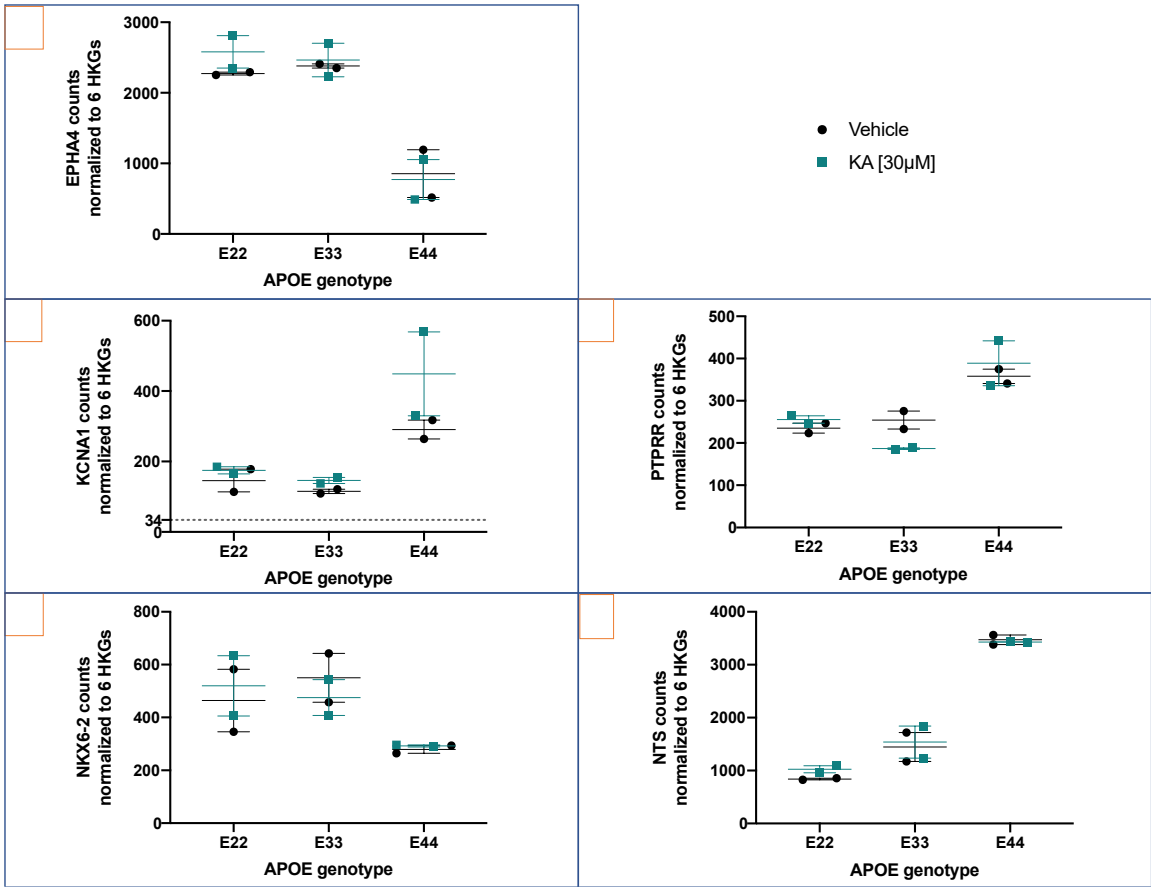

Figure 6.21 NanoString data plotted for *APOE*-genotype-dependent differentially expressed genes I uncovered in the untreated neurons (Figure 5.24).

NanoString mRNA counts extracted from the nCounter® Human Neuropathology panel normalized to 6 housekeeping genes (HKG) for APOE-variant iN28s at 6 hours of 30 μM KA or vehicle treatments. Data plotted for several interesting genes differentially expressed between E33 and E44 iN28 neurons, both in this study and a published study: (A) EPHA4, (B) KCNA1, (C) PTPRR, (D) NKX6-2, and (E) NTS (182). Error bars = SD from 2 independent experiments. The horizontal line between a pair of samples marks their average. All vehicle data correspond to heatmap in the previous Chapter (Figure 5.24).

6.6 Discussion

Excitotoxicity puts neurons in danger of dysfunction and degeneration. They can mount adaptive responses to protect themselves against this stress-induced injury to some extent. Neuron-expressed ApoE has been implicated in response to excitotoxic stress. During neuronal hyperactivity, ROS can cause peroxidation of fatty acids (FAs) found in cell membranes (226). Upon challenge with NMDA to induce excitotoxicity, rodent primary hippocampal neuronal cultures generated apoE-positive lipoprotein particles that mobilized these toxic FAs and released them into the culture media. In a co-culture setup, the apoE-positive lipoprotein particles secreted by neurons were take up via endocytosis by neighboring astrocytes, a cell type with greater capacity than neurons to detoxify such lipids (89).

Neuronal ApoE's role in FA efflux from neurons was shown when, expressed in neurons versus astrocytes, ApoE4 had decreased lipid binding and secretion efficiency and increased toxicity, compared to ApoE3 (219). Neurons harboring ε4 may not expel FAs as efficiently as those with ε3, and thus may be exposed to increased injury owing to lipid peroxidation or lipotoxicity. Stress-induced upregulation of ApoE is likely to be a neuron's rapid response to counter stress-induced increases in toxic FAs and get rid of them. In fact, Buttini *et al.* 2010 showed that upon excitotoxic stress, it was more detrimental for neurons to express ApoE4 than to have no ApoE at all, concordant with other data suggesting that ApoE4 displays a toxic gain-of-function compared to ApoE3 and ApoE2 (219). Neuronal ApoE, therefore, may be crucial for keeping neurons healthy in the face of stress and injury by acting as a chaperone routing damaging FAs away. Such a cell autonomous neuronal ApoE mechanism during excitotoxicity could form the basis for potential differential vulnerability as assessed here.

Most of the cellular investigation of neuron derived ApoE and its role in stress resilience is done in rodents. These studies highlight the upregulation of neuronal ApoE upon excitotoxic challenge and put forward potential roles in neutralizing lipotoxicity. Nevertheless, what is missing is evidence in human neurons and this is important in bridging the translatability gap of any AD treatments developed from laboratory observations. This chapter was designed to overcome some of these limitations. I designed the experiments to investigate (1) an ApoE isoform specific neuronal response to hyperactivity induced stress (2) in human neurons. Precedent in several labs utilized the analog of glutamate, KA, in animal models to induce neuronal ApoE expression under excitotoxic stress, so I investigated this compound as the stressor in my system (219).

An initial important observation from my previous work is that there is low level gene expression of APOE transcript in each of the characterized iPSC-derived neuronal cultures regardless of the APOE genotype. This genotype-phenotype comparison identified no differences in morphology, metabolism, or classic pan-neuronal transcript expression. In the case of the underpinning transcriptional program, this approach revealed important but subtle differences that hint at a disruptive effect of APOE4 in the development of the synapse.

Because prior studies have shown that neuronal susceptibility to excitotoxicity requires neuronal maturity and expression of glutamate receptor subunits, it was important to confirm the iNs in my study expressed KA receptor subunits and demonstrated activity dependent gene induction which reinforced that the cultures were connected and likely synaptically active (221). My initial experiments helped define KA conditions that would induce modest, but not excessive, stress. Neuronal activity was confirmed by increased *FOS* transcription and evidence that the KA administration induced stress was confirmed by *ATF4* induction.

6.6.1 *APOE* mRNA expression was not altered upon KA administration

Results demonstrated that KA led to concentration- and time-dependent inductions of the neural activity marker, *FOS*, as well as the stress response marker, *ATF4.* Furthermore, by 18 hours of treatment, the 300 µM concentration of KA induced degeneration as shown by neurite blebbing highlighted with GFP that correlated with dramatic reductions in ATP production. However, throughout the time course of both high and low concentrations of KA treatments, at no point were changes in *APOE* levels detected in any of the cultures, irrespective of *APOE* genotype.

I concluded that *APOE* is not an excitotoxic stress response gene in this model. One possible reason could be that perhaps the iNs generated were not the specific neuron type that responds to stress by inducing *APOE*. KA-induced apoE-immunoreactivity was not universally apparent in all neurons and was regionally restricted in the brain or, in human RNAseq studies demonstrating neuronal expression, it was only a specific subset of neurons that expressed *APOE* (124, 219). Another possible explanation for the discrepancy between *in vivo* studies and my study's lack of *APOE* upregulation upon excitotoxic stimulation is the reduced nature of the culture system. I used neuron-only cultures to decipher whether a neuronal cell type associated mechanism of ApoE4 could be an important contributor to AD. However, since most of ApoE in the CNS comes from astrocytes as well as activated microglia, perhaps crosstalk from these other cell types must be present to generate a neuronal ApoE response to injury (2). Culture media from astrocytes was shown to stimulate synthesis of apoE in neurons, illuminating a "cross-talk" between these cell types that was tied to an injury response in a mouse neuroblastoma cell culture system; this has yet to be validated in a human system (227).

Another possibility is that human neurons do not utilize neuronal ApoE like mouse neurons, accentuating the value of expanding the platforms used for the investigation of human-only diseases. Compared to unaffected people, subjects with MCI or early AD experience increased frequency of epileptic seizures lending relevance to the excitotoxicity associated stressor here (12). However, perhaps, the role of neuronal ApoE, that is generated during injury and stress such as advanced aging (the strongest risk factor for AD) requires using a different (e.g., toxic Aβ oligomers) stressor to induce the APOE response to injury in human neurons.

Even though *APOE* was not regulated by KA mediated excitotoxicity, I opted to continue my study on the effect of KA-induced stress because potential differences in stress response would be interpreted as a consequence of the already existing basal ApoE levels and/or underpinning developmental differences owing to distinct *APOE* allele expression.

One limitation of my study is that I probed only the mRNA levels and ApoE protein levels could be tested in future studies – to rule out possibility of posttranslational regulation of ApoE protein in response to KA-induced stress. Although I do not have direct evidence for this for ApoE, per se, axonal damage can initiate the rapid engagement of already existing mRNA and translation machinery to synthesize neuroprotective proteins locally in the axons as needed (222). Xu *et al.* published on an intriguing way that apoE protein in neurons could be staged for rapid production (228). ApoE mRNA, but not protein, was detected in healthy neurons. The neuronal mRNA was expressed containing an intron that prevented its translation (astrocytes meanwhile expressed an intron-lacking correlate transcript and astrocytic protein was abundantly produced). After KA injury in this *in vivo* study, neuronal intron retention was released, resulting in mature apoE mRNA being transferred out of the nucleus for apoE protein production. Remarkably, the intron retention mechanism was uniquely neuronal so not detected in other apoE-synthesizing cells types (228).

6.6.2 APOE ε4 was associated with delayed start in ATF4 response upon KA stress

Compared to that of *FOS,* the shape of the *ATF4* induction time-response curve was delayed and occurred in a sustained manner, suggesting that, with time, neuronal excitation escalated to hyperactivity-induced, excitotoxic stress. A key finding of my study is that *ATF4* induction was further delayed for the 44 compared to 22 and 33 cultures. The implication of this disparity in ε4/ε4 neurons having slower adaptive kinetics in response to stress is that, over a lifetime, this could propagate to impact cellular homeostasis progressively negatively with advancing age and trigger a cascade of pathogenic events.

6.6.3 *APOE* genotype was not associated with DEGs from the NanoString panel of genes

My interest is in the adaptive rather than pro-degenerative stage of the response to stress, and I did not want to risk excessively stressing the cultures beyond recovery. As such, I chose to run my NanoString experiment using the low KA concentration because in my exploratory study it did not impact cell health in a major way, according to the ATP and morphological evaluations. My design focused on low concentration effects which also showed some evidence of inducing stress-related genes. Any change in genes might inform on wider issues of neuronal homeostasis. For >700 genes probed, I identified a small subset of KA-responsive genes; but none did so in an *APOE*-allele dependent fashion.

Although *FOS* and *ATF4* mRNA expression were regulated by KA, I found little differential sensitivity with respect to the *APOE* variant of the cultures. In my prior work, I had discovered

clear but subtle *APOE* ε4-dependent changes in genes linked to synaptic function, like *SV2B* and *SYP* (Section 5.9), as well as others have reported on differential synaptic density and activity between isogenic iN cultures harboring ε3/3 versus ε4/4 genotypes (182). However, such pre-existing synaptic phenotypes did not differentially pre-dispose these cultures to respond differently to KA-induced stress— at least not on the genes represented on the NanoString panel.

Amongst the KA treatment related DEGs extracted from the NanoString analysis, some were upregulated compared to vehicle (not *APOE*-dependent changes). For instance, NPAS4 and NR4A2/NURR1, which have been described as activity responsive genes in previous literature, served as confirmatory (229). Furthermore, the relevance of NR4A2 in AD contexts is a new area of study: for example, NR4A2 was diminished in autopsied human brains from patients with AD, compared to those of controls (230). Other upregulated transcripts revealed by my study such as late-response genes, *HOMER1* and *ADCYAP1* (which is specific to excitatory neurons) and *XBP1* which regulates the UPR are in line with expectations of increased excitability and/or stress, and therefore validated my neuronal hyperexcitability/excitotoxic stress platform.

6.6.4 NPC1 induction in the face of KA-induced stress

What has not been previously reported is that excitotoxic stress induces *NPC1* expression. Although *APOE* transcription was unaltered when the neurons were stressed, another gene associated with intracellular FAs and cholesterol transport showed clear induction (Figure 1.8). It is tempting to speculate that in these cultures KA could have induced FAs that were then redistributed via NPC1-mediated mechanisms, in a manner like what was described for ApoE-mediated redistribution of FAs (89). Alternatively, since cholesterol and lipid dynamics are important in synaptic plasticity, NPC1 induction in this paradigm may be reporting on network activation, not necessarily stress (231). Whether NPC1 upregulation in these studies connects to neuronal excitability or excitotoxicity, is an intriguing question and worth following up on. Of note, mutations in NPC1 cause the autosomal recessive neurodegenerative disorder Niemann-Pick type C disease known for excessive accumulation of FAs and cholesterol in the brain (231).

6.6.5 Conclusion

In conclusion, excitotoxic stimulation of the cultures induced a clear stress response as evidenced by transcriptional upregulation of stress markers like *ATF4* and *XBP1*. Contrary to my expectation, upregulation of *APOE* in neurons after excitotoxic stress was not evident. Intriguingly, a different intracellular lipid transport gene, *NPC1*, was induced and if this upregulation is connected to recovery of neurons after stress or injury per se, perhaps it compensated for the hypothesized

mechanism by which ApoE would have acted to promote resilience to stress. My study does not rule out whether other stressors could elucidate neuronal ApoE as a driver of adaptive response to other AD-related stressors, such as ageing, amyloid β, or NFTs. My study does suggest that *APOE* variants set up a developmental foundation that allows for a subtle intrinsic differential way in which neurons respond to KA-induced excitotoxic stress. While neurons carrying the ε2 and ε3 alleles responded with the same timeline, neurons with ε4 had a delay in activating the *ATF4* genetic cascade. This finding warrants further investigation as the mechanism of this *APOE* ε4 neuron-specific delay in activation of the stress response potentially offers clues to constructing a therapeutic strategy aimed at improving neuronal resilience to injury and delaying or preventing the dyshomeostasis of AD.

Chapter 7 Concluding Remarks

7.1 Why this study?

APOE alleles are well-established genetic risk and protective factors for LOAD; ε4 confers major risk and ε2 is protective compared to the "neutral" ε3. More deeply understanding the cellular and molecular mechanisms of the allele-specific effects could elucidate targets for more effective therapeutic interventions. Furthermore, since the cellular source of ApoE impacts its function, understanding which cell-specific role has the most crucial influence on AD is critical. Isolating the role of ApoE specifically from neurons is relatively understudied, especially in the human context and so I focused on this area for my PhD project, which I based on human neurons in the laboratory dish. Another gap in the field is in-depth investigation into ε2 is disproportionally low relative to ε4, so I included ε2 in my studies. I was keen to observe, in parallel, clues as to whether its neuroprotective effect would overlap in the same pathways as ε4's detrimental effects. Figure 7.1 summarizes my process.

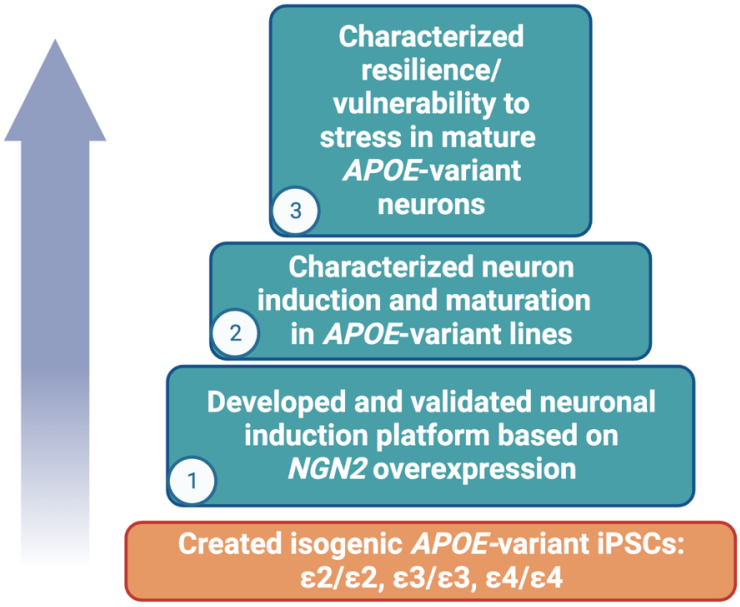

Figure 7.1 Summary of my process to generate deeper understanding of APOE genotype impact on neuron form and function.

This figure depicts that, building on a foundation of *APOE*-variant isogenic iPSC lines created by the ADAPTED consortium (bottom blocks), I (1) constructed a platform to convert them to neurons then performed detailed characterization of (2) neuronal differentiation and maturation, (3) followed by response to excitotoxic stress.

7.2 Discussion of key findings

No dramatic *APOE* genotype-associated difference was observed. However, subtle differences emerged from my analysis and were associated with the ε4 allele. Figure 7.2 tabulates my key findings. The left side focuses on six groupings of analyses during the longitudinal neuronal ontogeny, after forced expression of *NGN2* in the iPSCs, and an endpoint evaluation of over 700 genes in 4-week-old neurons. During the developmental time course, no significant genotype-specific differences were seen in morphology, or classic neuronal (e.g., *MAP2*) or activity (*FOS*) marker genes. Hence, the graphic shows no indication of changes in these parameters. During the developmental timeline, the ε4/ε4 genotype had a small but striking modulation of genes linking with synapse function, especially *SV2B*. Interestingly, two other synapse-associated (*GRIK1* and *GRIK2*) trended lower in ε4/ε4 compared to ε3/ε3 cultures but did not reach statistical significance (Figure 6.3). Increasing the statistical power with more independent experimental replicates would possibly reveal a significant difference. If this is the case, it would strengthen the finding that neuronal ApoE4 modulated the synaptic transcriptional profile during neuronal development. (I could not conduct a power calculation beforehand because I did not know what to expect regarding the magnitude of the differences, if any, amongst the *APOE*-variant cultures. I had thus run my neuronal induction and differentiation studies with three biological replicates (n=3), as is the convention for cell-based assays.) At the 4-week endpoint assessment of the scaled-up number of genes, further DEGs (a very small percentage) associated with ε4. Taken together, these DEGs largely associated with synapse or network connectivity functions and did not occur with uniform directionality, thus marked by arrows pointing in two directions in the bottom row in Figure 7.2.

My data suggests that ε4 selectively impacts transcription of select genes, but the exact molecular mechanism underlying this is to be determined. Possibly, *APOE* genetic status in the stem cell stage influenced neuronal differentiation and phenotype as ApoE has been implicated to play a role in neurogenesis (1). It would be interesting to investigate whether transcriptional regulation of the two other SV family members, SV2A and SV2C, was affected. Interestingly, a public- private-sector pre-competitive consortium, announced October 2022, is validating whether SV2A positron emission tomography (PET) imaging can be used as a prognostic biological marker or "biomarker" of synapse function that precedes neuronal death and symptom onset or progression or monitor the efficacy of treatments in people with AD (232). Considering that the DEGs did not move in the same direction, it is difficult to predict the outcome of these changes. The synaptic difference lends evidence to reports that ablation of neuronal ε4, more so than ε3, robustly impacted synaptic hyperexcitability *in vivo* (Section 1.10.2.2) (130). In a somewhat related sense, my data

connects to a study showing that ApoE applied to neurons in culture could have different effects on excitability depending on whether the source was neuronal or astrocytic (233).

It is important to reiterate that, *APOE* expression is present in this cell type, based on careful mRNA measurements in two distinct technologies. *APOE* was then the sole DEG detected in the 22 compared to the 33 neurons (Figure 7.2, top row). Lower *APOE* levels were detected as a trend in the ε2 context from the very start, in the iPSCs stage, and remained a pattern throughout the neuronal stages (RT-PCR analyses) and it was detected as a lowered DEG (NanoString analyses). A biological impact of this lowered *APOE* transcription (by ~30%) did not emerge in this study and in all other respects, the 22 behaved no differently than the 33 cultures with regards to the endpoints measured in my investigations.

The right side of Figure 7.2 depicts six sets of parameters measured during the Stress Response experiments. Analysis of the stress response during a time course of KA exposure showed a clear delay in 44, compared to the 33, neurons to induce *ATF4* (Figure 7.2, downward arrow, bottom row). It is important to note this was a transient phenomenon and the delay resolved itself later in the time course. Therefore, *ATF4* which can support a protective stress response program is present and only the kinetics is delayed. It would be interesting to expose the cultures to repeated stress and test whether this blunted *ATF4* response in 44 relative to the other two genotypes leads to a worsened outcome after multiple insults over time (224).

In my single-timepoint KA treatment stress paradigm in which a scaled-up set of over 700 genes were evaluated, some genes were generically modulated by KA across genotypes. However, the outcome of the KA cytotoxic stress study is there was no differential response between genotypes (Figure 7.2, last column, labelled “DEGs”). Intriguingly, one generically modulated gene unexpectedly upregulated by the excitotoxic stress was *NPC1*. This gene is associated with intracellular cholesterol transport function, suggesting that the hyperactive neurons experienced accumulation of lipids and NPC1 (shown in Figure 1.8) was shuttling them throughout the cell, akin to a mechanism described for ApoE (89). Future studies could confirm whether FA and cytotoxic lipids were generated by the KA-induced stress and whether they are different and need to be addressed by a different lipid transporter.

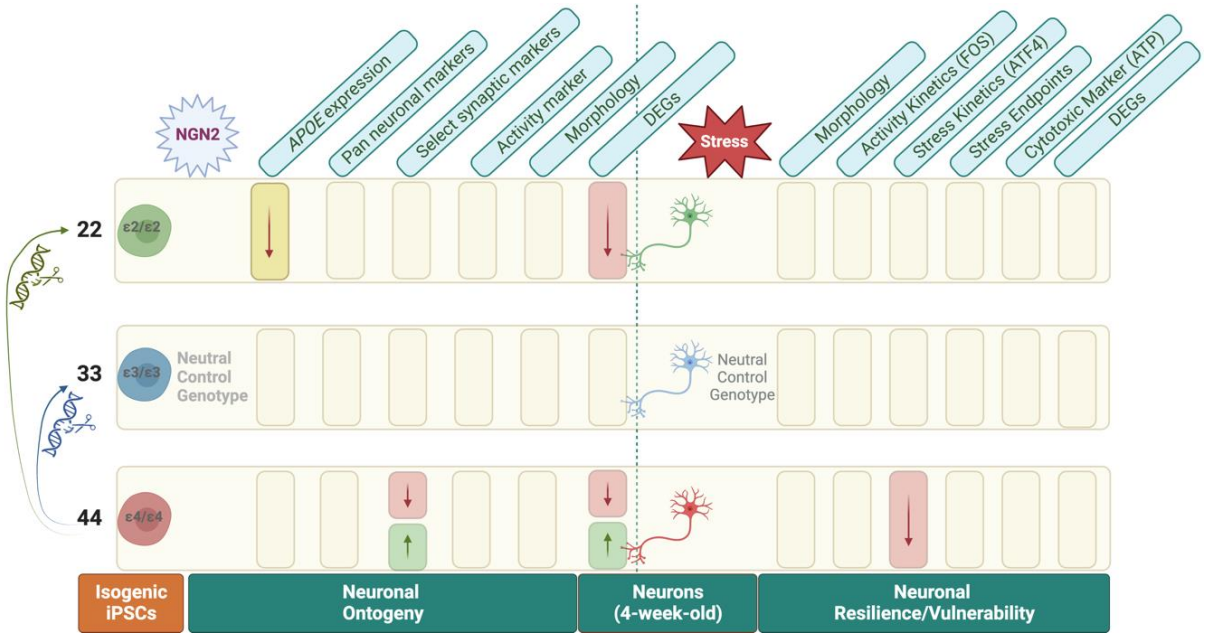

Figure 7.2 Summary of findings.

This graphic provides an overview of my key findings. The left side of the dotted line focuses on the results of the Neuronal Ontogeny, while the right side depicts those for the Stress Response, experiments. Six groups of endpoints were analyzed during the conversion and maturation of neurons from iPSCs and another six groups of endpoints were analyzed upon stressing 4-week-old neurons from each *APOE*-variant line. In all analyses, each of 2 lines (22 and 44) were consistently compared to the neutral control line, 33. Empty cells, devoid of arrows, indicate there was no change from the neutral genotype. The first key finding was endogenous neuronal ApoE isoforms have little impact on neuronal development, although subtle, but clear, changes were observed. Lower *APOE* expression was seen in the 22 line (top row) compared to the 33 line. A small percentage of differentially expressed genes (DEGs) emerged in the 44 compared to 33 neurons during their development and again at the endpoint analyses of a panel of over 700 genes. These DEGs largely associated with synapse or network connectivity function and did not occur with uniform directionality, thus marked by arrows pointing in two directions in the bottom row. Analysis of the stress response showed a clear delay in the 44 neurons to activate the ATF4 pathway (downward arrow, bottom row).

7.3 Implications

One reasonable and consistent interpretation of my data is the $\varepsilon 4$ carrying neurons closely resemble those carrying $\varepsilon 3$ in how they differentiate and develop except that they have slightly different levels of genes associated with the synapse and connectivity. The first symptom of AD has to do with synapses and connectivity, i.e., patients lose their capacity to make new memories - first of minor and then of meaningful life events. This insidious loss of the ability to learn new information occurs in someone who is otherwise neurologically intact (56). Progressively, memory is overwhelmingly incapacitated and reasoning abilities and language slip away. My findings point to the possibility that a developmental compromise like altered neural circuit formation could occur early in life in people harboring $\varepsilon 4$. This raises the possibility that while these perturbations

are subtle and do not meaningfully affect cognition and memory in early adulthood, they may increase the risk of neurodegeneration and cognitive decline in the setting of chronic stressors with advancing age, which predisposes them to develop LOAD.

My results also imply that these small circuitry changes occur in a backdrop of small stress response alterations. The blunted response of *ATF4* in E44 neurons, not in absolute terms but in terms of kinetics, will be useful information for the field and this set of observations warrants publication. ATF4 is a transcription factor that puts in place a program in which the metabolic requirement of the cell is dampened for the period that the insult is present and afterwards the cells enter recovery (or programmed death) (224). If the time from base to peak response is slow, it could cause more damage and, in case of multiple insults consistently, not reach maximum homeostasis as quickly as in the other *APOE*-allele contexts. This might lead to accumulated damage over repeated stress over time. Together, the data suggests ε4 to some extent impacts stress induced transcriptional response without affecting synapse activity in terms of *FOS* response. Because the modest effect on *ATF4* is so clear, it could be that the determinants of AD from neurons might be small but does not rule out that they are not clinically meaningful over a lifetime. The strength of the data allows me to put forth this argument and repeated stress experiments would need to be investigated to see if this is truly the case.

I had wanted to see if a converse protective impact of ε2 would emerge. My results imply that the mechanisms by which ε2 bestows neuroprotection do not overlap with those by which ε4 bestows risk. The effect of ε2 was not an opposite modulation of the same pathways; not unlike interpretations put forth by Reiman *et al.* and in contrast to the assumption that the functional properties of E2 often display the opposite of that of E4 (73, 77). Continued work using this platform perhaps with other AD-related challenges, like cytotoxic Aβ oligomers, could potentially highlight ε2-mediated mechanisms of neuroprotection.

Carrying the ε4 allele is not 100% penetrant for LOAD which points to the contribution of human genetic variability. It is important to investigate, within the same genetic background, to what extent the *APOE* alleles change phenotype. And, an extension of what I have done here, would be to check whether these observations persist across other genetic backgrounds; sadly, the donor of these cells did succumb to AD. Examining several other sets of isogenic neurons from other people (including age-matched individuals without dementia, and of different sexes) is worth doing to understand the variability of these phenotypes uncovered.

Overall, I provide evidence that there are some determinants within neurons important to the overall outcome of sAD from an *APOE*-variant perspective. Although an association between *APOE* genotype and KA-induced excitotoxity was not observed, this study pointed to an intrinsic

difference in expression of genes associated with synapse function associated with ε4. Increasing our knowledge on how synapses reach their demise in the complex setting of the AD brain may generate novel ideas and targets for the development of neuroprotective therapeutic interventions. In conclusion, I propose a neuron source specific effect of ApoE whereby neuronal ApoE4 induces subtle effects on neuronal connectivity during development. In addition, neuronal ApoE4 potentially induces a delay in mounting protective stress responses by delaying activation of *ATF4*. Further research is required to understand the underpinning molecular mechanisms in both AD and non-AD situations. These findings contribute to increased understanding of neuronal ApoE, the major genetic risk factor for AD, in human neuronal network development. This may have implications for early stages of AD and help with new insights for future AD therapeutics surrounding ApoE4, neuronal dysfunction, and response to stress. Designing cell type-specific therapeutics might be challenging however learning the cell-type-specific impact of ApoE is important in developing targeted and nuanced therapies, especially if the field uncovers cell-type specific mechanisms that could highlight new targets.

Bibliography

1. Moller HJ, Graeber MB. The case described by Alois Alzheimer in 1911. Historical and conceptual perspectives based on the clinical record and neurohistological sections. Eur Arch Psychiatry Clin Neurosci. 1998;248(3):111-22.
2. World_Health_Organization. World failing to address dementia challenge 2021 [updated 2 September 2021. Available from: https://www.who.int/news/item/02-09-2021-world-failing-to-address-dementia-challenge.
3. Europe A. Dementia in Europe Yearbook 2019 2019 [updated 2019. Available from: https://www.alzheimer-europe.org/sites/default/files/alzheimer_europe_dementia_in_europe_yearbook_2019.pdf.
4. 2023 Alzheimer's disease facts and figures. Alzheimers Dement. 2023.
5. Ward A, Tardiff S, Dye C, Arrighi HM. Rate of conversion from prodromal Alzheimer's disease to Alzheimer's dementia: a systematic review of the literature. Dement Geriatr Cogn Dis Extra. 2013;3(1):320-32.
6. Scheltens P, De Strooper B, Kivipelto M, Holstege H, Chetelat G, Teunissen CE, et al. Alzheimer's disease. Lancet. 2021;397(10284):1577-90.
7. Prince M, Wimo A, Guerchet M, Ali G-C, Wu Y-T, Prina M, et al. World Alzheimer Report 2015 “The global impact of dementia: An analysis of prevalence, incidence, cost and trends”: Published by Alzheimer’s Disease International (ADI), London.; 2015 [
8. Gustavsson A, Norton N, Fast T, Frolich L, Georges J, Holzapfel D, et al. Global estimates on the number of persons across the Alzheimer's disease continuum. Alzheimers Dement. 2023;19(2):658-70.
9. 2022 Alzheimer's disease facts and figures. Alzheimers Dement. 2022;18(4):700-89.
10. Sengoku R. Aging and Alzheimer's disease pathology. Neuropathology. 2020;40(1):22-9.
11. Soria Lopez JA, González HM, Léger GC. Chapter 13 - Alzheimer's disease. In: Dekosky ST, Asthana S, editors. Handbook of Clinical Neurology. 167: Elsevier; 2019. p. 231-55.
12. Hampel H, Hardy J, Blennow K, Chen C, Perry G, Kim SH, et al. The Amyloid-beta Pathway in Alzheimer's Disease. Mol Psychiatry. 2021;26(10):5481-503.
13. Zolezzi JM, Bastías-Candia S, Santos MJ, Inestrosa NC. Alzheimer's disease: relevant molecular and physiopathological events affecting amyloid-β brain balance and the putative role of PPARs. Front Aging Neurosci. 2014;6:176.
14. Müller UC, Zheng H. Physiological functions of APP family proteins. Cold Spring Harb Perspect Med. 2012;2(2):a006288.
15. Jang SS, Chung HJ. Emerging Link between Alzheimer's Disease and Homeostatic Synaptic Plasticity. Neural Plast. 2016;2016:7969272.
16. Hardy J, Selkoe DJ. The amyloid hypothesis of Alzheimer's disease: progress and problems on the road to therapeutics. Science. 2002;297(5580):353-6.
17. Kummer MP, Heneka MT. Truncated and modified amyloid-beta species. Alzheimers Res Ther. 2014;6(3):28.
18. Haass C, Kaether C, Thinakaran G, Sisodia S. Trafficking and proteolytic processing of APP. Cold Spring Harb Perspect Med. 2012;2(5):a006270.
19. Bossy-Wetzel E, Schwarzenbacher R, Lipton SA. Molecular pathways to neurodegeneration. Nat Med. 2004;10 Suppl:S2-9.
20. Tu S, Okamoto S-i, Lipton SA, Xu H. Oligomeric Aβ-induced synaptic dysfunction in Alzheimer’s disease. Molecular Neurodegeneration. 2014;9(1):48.
21. Selkoe DJ, Hardy J. The amyloid hypothesis of Alzheimer's disease at 25 years. EMBO Mol Med. 2016;8(6):595-608.
22. Ballard C, Gauthier S, Corbett A, Brayne C, Aarsland D, Jones E. Alzheimer's disease. The Lancet. 2011;377(9770):1019-31.
23. Kepp KP, Robakis NK, Høilund-Carlsen PF, Sensi SL, Vissel B. The amyloid cascade hypothesis: an updated critical review. Brain. 2023.

24. Brody DL, Magnoni S, Schwetye KE, Spinner ML, Esparza TJ, Stocchetti N, et al. Amyloid-beta dynamics correlate with neurological status in the injured human brain. Science. 2008;321(5893):1221-4.
25. Oe T, Ackermann BL, Inoue K, Berna MJ, Garner CO, Gelfanova V, et al. Quantitative analysis of amyloid beta peptides in cerebrospinal fluid of Alzheimer's disease patients by immunoaffinity purification and stable isotope dilution liquid chromatography/negative electrospray ionization tandem mass spectrometry. Rapid Commun Mass Spectrom. 2006;20(24):3723-35.
26. Saido T, Leissring MA. Proteolytic degradation of amyloid β-protein. Cold Spring Harb Perspect Med. 2012;2(6):a006379.
27. Tatulian SA. Challenges and hopes for Alzheimer's disease. Drug Discov Today. 2022;27(4):1027-43.
28. van Dyck CH, Swanson CJ, Aisen P, Bateman RJ, Chen C, Gee M, et al. Lecanemab in Early Alzheimer's Disease. N Engl J Med. 2023;388(1):9-21.
29. Budd Haeberlein S, Aisen PS, Barkhof F, Chalkias S, Chen T, Cohen S, et al. Two Randomized Phase 3 Studies of Aducanumab in Early Alzheimer's Disease. J Prev Alzheimers Dis. 2022;9(2):197-210.
30. Cummings J, Apostolova L, Rabinovici GD, Atri A, Aisen P, Greenberg S, et al. Lecanemab: Appropriate Use Recommendations. The Journal of Prevention of Alzheimer's Disease. 2023;10(3):362-77.
31. Braak E, Braak H, Mandelkow EM. A sequence of cytoskeleton changes related to the formation of neurofibrillary tangles and neuropil threads. Acta Neuropathol. 1994;87(6):554-67.
32. Cho H, Choi JY, Hwang MS, Kim YJ, Lee HM, Lee HS, et al. In vivo cortical spreading pattern of tau and amyloid in the Alzheimer disease spectrum. Ann Neurol. 2016;80(2):247-58.
33. Ghoshal N, García-Sierra F, Wuu J, Leurgans S, Bennett DA, Berry RW, et al. Tau conformational changes correspond to impairments of episodic memory in mild cognitive impairment and Alzheimer's disease. Exp Neurol. 2002;177(2):475-93.
34. Jouanne M, Rault S, Voisin-Chiret AS. Tau protein aggregation in Alzheimer's disease: An attractive target for the development of novel therapeutic agents. Eur J Med Chem. 2017;139:153-67.
35. Wang Y, Mandelkow E. Tau in physiology and pathology. Nat Rev Neurosci. 2016;17(1):5-21.
36. Mandelkow EM, Mandelkow E. Biochemistry and cell biology of tau protein in neurofibrillary degeneration. Cold Spring Harb Perspect Med. 2012;2(7):a006247.
37. Qiang L, Sun X, Austin TO, Muralidharan H, Jean DC, Liu M, et al. Tau Does Not Stabilize Axonal Microtubules but Rather Enables Them to Have Long Labile Domains. Curr Biol. 2018;28(13):2181-9.e4.
38. Holtzman DM, Herz J, Bu G. Apolipoprotein E and apolipoprotein E receptors: normal biology and roles in Alzheimer disease. Cold Spring Harb Perspect Med. 2012;2(3):a006312.
39. Frandemiche ML, De Seranno S, Rush T, Borel E, Elie A, Arnal I, et al. Activity-dependent tau protein translocation to excitatory synapse is disrupted by exposure to amyloid-beta oligomers. J Neurosci. 2014;34(17):6084-97.
40. Violet M, Delattre L, Tardivel M, Sultan A, Chauderlier A, Caillierez R, et al. A major role for Tau in neuronal DNA and RNA protection in vivo under physiological and hyperthermic conditions. Front Cell Neurosci. 2014;8:84.
41. Ramaswami M, Taylor JP, Parker R. Altered ribostasis: RNA-protein granules in degenerative disorders. Cell. 2013;154(4):727-36.
42. Meier S, Bell M, Lyons DN, Rodriguez-Rivera J, Ingram A, Fontaine SN, et al. Pathological Tau Promotes Neuronal Damage by Impairing Ribosomal Function and Decreasing Protein Synthesis. J Neurosci. 2016;36(3):1001-7.
43. Chang CW, Shao E, Mucke L. Tau: Enabler of diverse brain disorders and target of rapidly evolving therapeutic strategies. Science. 2021;371(6532).
44. Jack CR, Jr., Knopman DS, Jagust WJ, Petersen RC, Weiner MW, Aisen PS, et al. Tracking pathophysiological processes in Alzheimer's disease: an updated hypothetical model of dynamic biomarkers. Lancet Neurol. 2013;12(2):207-16.

45. Seeley WW, Crawford RK, Zhou J, Miller BL, Greicius MD. Neurodegenerative diseases target large-scale human brain networks. Neuron. 2009;62(1):42-52.
46. Holmes C. Genotype and phenotype in Alzheimer's disease. Br J Psychiatry. 2002;180:131-4.
47. Franzmeier N, Neitzel J, Rubinski A, Smith R, Strandberg O, Ossenkoppele R, et al. Functional brain architecture is associated with the rate of tau accumulation in Alzheimer's disease. Nature Communications. 2020;11(1):347.
48. Holmes BB, Diamond MI. Prion-like properties of Tau protein: the importance of extracellular Tau as a therapeutic target. J Biol Chem. 2014;289(29):19855-61.
49. Florian H, Wang D, Arnold SE, Boada M, Guo Q, Jin Z, et al. Tilavonemab in early Alzheimer's disease: results from a phase 2, randomized, double-blind study. Brain. 2023;146(6):2275-84.
50. Mignon L, Kordasiewicz H, Lane R, Smith A, Miller T, Narayanan P, et al. Design of the First-in-Human Study of IONIS-MAPTRx, a Tau-lowering Antisense Oligonucleotide, in Patients With Alzheimer Disease (S2.006). Neurology. 2018;90(15 Supplement):S2.006.
51. Graham DL, Gray AJ, Joyce JA, Yu D, O'Moore J, Carlson GA, et al. Increased O-GlcNAcylation reduces pathological tau without affecting its normal phosphorylation in a mouse model of tauopathy. Neuropharmacology. 2014;79:307-13.
52. Bartolome-Nebreda JM, Trabanco AA, Velter AI, Buijnsters P. O-GlcNAcase inhibitors as potential therapeutics for the treatment of Alzheimer's disease and related tauopathies: analysis of the patent literature. Expert Opin Ther Pat. 2021;31(12):1117-54.
53. Park J, Ha HJ, Chung ES, Baek SH, Cho Y, Kim HK, et al. O-GlcNAcylation ameliorates the pathological manifestations of Alzheimer's disease by inhibiting necroptosis. Sci Adv. 2021;7(3):eabd3207.
54. Mummery CJ, Börjesson-Hanson A, Blackburn DJ, Vijverberg EGB, De Deyn PP, Ducharme S, et al. Tau-targeting antisense oligonucleotide MAPTRx in mild Alzheimer's disease: a phase 1b, randomized, placebo-controlled trial. Nature Medicine. 2023;29(6):1437-47.
55. Tzioras M, McGeachan RI, Durrant CS, Spires-Jones TL. Synaptic degeneration in Alzheimer disease. Nat Rev Neurol. 2023;19(1):19-38.
56. Selkoe DJ. Alzheimer's disease is a synaptic failure. Science. 2002;298(5594):789-91.
57. Langille JJ, Brown RE. The Synaptic Theory of Memory: A Historical Survey and Reconciliation of Recent Opposition. Front Syst Neurosci. 2018;12:52.
58. Lee A, Kondapalli C, Virga DM, Lewis TL, Koo SY, Ashok A, et al. Aβ42 oligomers trigger synaptic loss through CAMKK2-AMPK-dependent effectors coordinating mitochondrial fission and mitophagy. Nature Communications. 2022;13(1):4444.
59. Lasagna-Reeves CA, Castillo-Carranza DL, Sengupta U, Clos AL, Jackson GR, Kayed R. Tau oligomers impair memory and induce synaptic and mitochondrial dysfunction in wild-type mice. Mol Neurodegener. 2011;6:39.
60. Usenovic M, Niroomand S, Drolet RE, Yao L, Gaspar RC, Hatcher NG, et al. Internalized Tau Oligomers Cause Neurodegeneration by Inducing Accumulation of Pathogenic Tau in Human Neurons Derived from Induced Pluripotent Stem Cells. J Neurosci. 2015;35(42):14234-50.
61. Anstey KJ, Lipnicki DM, Low LF. Cholesterol as a risk factor for dementia and cognitive decline: a systematic review of prospective studies with meta-analysis. Am J Geriatr Psychiatry. 2008;16(5):343-54.
62. Reiss AB, Voloshyna I. Regulation of cerebral cholesterol metabolism in Alzheimer disease. J Investig Med. 2012;60(3):576-82.
63. Glöckner F, Ohm TG. Tau pathology induces intraneuronal cholesterol accumulation. J Neuropathol Exp Neurol. 2014;73(9):846-54.
64. Farrer LA, Cupples LA, Haines JL, Hyman B, Kukull WA, Mayeux R, et al. Effects of age, sex, and ethnicity on the association between apolipoprotein E genotype and Alzheimer disease. A meta-analysis. APOE and Alzheimer Disease Meta Analysis Consortium. Jama. 1997;278(16):1349-56.
65. Mamun AA, Uddin MS, Bin Bashar MF, Zaman S, Begum Y, Bulbul IJ, et al. Molecular Insight into the Therapeutic Promise of Targeting APOE4 for Alzheimer's Disease. Oxid Med Cell Longev. 2020;2020:5086250.

66. Brickell KL, Steinbart EJ, Rumbaugh M, Payami H, Schellenberg GD, Van Deerlin V, et al. Early-onset Alzheimer disease in families with late-onset Alzheimer disease: a potential important subtype of familial Alzheimer disease. Arch Neurol. 2006;63(9):1307-11.
67. Ertekin-Taner N. Genetics of Alzheimer's disease: a centennial review. Neurol Clin. 2007;25(3):611-67, v.
68. Zis P, Strydom A. Clinical aspects and biomarkers of Alzheimer's disease in Down syndrome. Free Radic Biol Med. 2018;114:3-9.
69. Martiskainen H, Herukka SK, Stančáková A, Paananen J, Soininen H, Kuusisto J, et al. Decreased plasma β-amyloid in the Alzheimer's disease APP A673T variant carriers. Ann Neurol. 2017;82(1):128-32.
70. Gatz M, Reynolds CA, Fratiglioni L, Johansson B, Mortimer JA, Berg S, et al. Role of genes and environments for explaining Alzheimer disease. Arch Gen Psychiatry. 2006;63(2):168-74.
71. Corder EH, Saunders AM, Strittmatter WJ, Schmechel DE, Gaskell PC, Small GW, et al. Gene dose of apolipoprotein E type 4 allele and the risk of Alzheimer's disease in late onset families. Science. 1993;261(5123):921-3.
72. Robinson M, Lee BY, Hane FT. Recent Progress in Alzheimer's Disease Research, Part 2: Genetics and Epidemiology. J Alzheimers Dis. 2017;57(2):317-30.
73. Corbo RM, Scacchi R. Apolipoprotein E (APOE) allele distribution in the world. Is APOE*4 a 'thrifty' allele? Ann Hum Genet. 1999;63(Pt 4):301-10.
74. Barnes LL, Arvanitakis Z, Yu L, Kelly J, De Jager PL, Bennett DA. Apolipoprotein E and change in episodic memory in blacks and whites. Neuroepidemiology. 2013;40(3):211-9.
75. Kaup AR, Nettiksimmons J, Harris TB, Sink KM, Satterfield S, Metti AL, et al. Cognitive resilience to apolipoprotein E ε4: contributing factors in black and white older adults. JAMA Neurol. 2015;72(3):340-8.
76. Rajabli F, Beecham GW, Hendrie HC, Baiyewu O, Ogunniyi A, Gao S, et al. A locus at 19q13.31 significantly reduces the ApoE ε4 risk for Alzheimer's Disease in African Ancestry. PLoS Genet. 2022;18(7):e1009977.
77. Reiman EM, Arboleda-Velasquez JF, Quiroz YT, Huentelman MJ, Beach TG, Caselli RJ, et al. Exceptionally low likelihood of Alzheimer's dementia in APOE2 homozygotes from a 5,000-person neuropathological study. Nat Commun. 2020;11(1):667.
78. Shi Y, Yamada K, Liddelow SA, Smith ST, Zhao L, Luo W, et al. ApoE4 markedly exacerbates tau-mediated neurodegeneration in a mouse model of tauopathy. Nature. 2017;549(7673):523-7.
79. Sepulveda-Falla D, Sanchez JS, Almeida MC, Boassa D, Acosta-Uribe J, Vila-Castelar C, et al. Distinct tau neuropathology and cellular profiles of an APOE3 Christchurch homozygote protected against autosomal dominant Alzheimer's dementia. Acta Neuropathol. 2022;144(3):589-601.
80. Bu G. APOE targeting strategy in Alzheimer's disease: lessons learned from protective variants. Mol Neurodegener. 2022;17(1):51.
81. Liu CC, Murray ME, Li X, Zhao N, Wang N, Heckman MG, et al. APOE3-Jacksonville (V236E) variant reduces self-aggregation and risk of dementia. Sci Transl Med. 2021;13(613):eabc9375.
82. Raffai RL, Dong LM, Farese RV, Jr., Weisgraber KH. Introduction of human apolipoprotein E4 "domain interaction" into mouse apolipoprotein E. Proc Natl Acad Sci U S A. 2001;98(20):11587-91.
83. Brecht WJ, Harris FM, Chang S, Tesseur I, Yu GQ, Xu Q, et al. Neuron-specific apolipoprotein e4 proteolysis is associated with increased tau phosphorylation in brains of transgenic mice. J Neurosci. 2004;24(10):2527-34.
84. Zhao N, Liu CC, Qiao W, Bu G. Apolipoprotein E, Receptors, and Modulation of Alzheimer's Disease. Biol Psychiatry. 2018;83(4):347-57.
85. Martens YA, Zhao N, Liu CC, Kanekiyo T, Yang AJ, Goate AM, et al. ApoE Cascade Hypothesis in the pathogenesis of Alzheimer's disease and related dementias. Neuron. 2022;110(8):1304-17.
86. Giau VV, Bagyinszky E, An SS, Kim SY. Role of apolipoprotein E in neurodegenerative diseases. Neuropsychiatr Dis Treat. 2015;11:1723-37.
87. Feingold KR. Introduction to Lipids and Lipoproteins. In: Feingold KR, Anawalt B, Blackman MR, Boyce A, Chrousos G, Corpas E, et al., editors. Endotext. South Dartmouth (MA): MDText.com, Inc.

88. Boyles JK, Pitas RE, Wilson E, Mahley RW, Taylor JM. Apolipoprotein E associated with astrocytic glia of the central nervous system and with nonmyelinating glia of the peripheral nervous system. J Clin Invest. 1985;76(4):1501-13.
89. Ioannou MS, Jackson J, Sheu SH, Chang CL, Weigel AV, Liu H, et al. Neuron-Astrocyte Metabolic Coupling Protects against Activity-Induced Fatty Acid Toxicity. Cell. 2019;177(6):1522-35 e14.
90. Björkhem I, Meaney S. Brain cholesterol: long secret life behind a barrier. Arterioscler Thromb Vasc Biol. 2004;24(5):806-15.
91. Dietschy JM, Turley SD. Thematic review series: brain Lipids. Cholesterol metabolism in the central nervous system during early development and in the mature animal. J Lipid Res. 2004;45(8):1375-97.
92. Benarroch EE. Brain cholesterol metabolism and neurologic disease. Neurology. 2008;71(17):1368-73.
93. Reilly M, Rader DJ. Apolipoprotein E and coronary disease: a puzzling paradox. PLoS Med. 2006;3(6):e258.
94. Wahrle SE, Shah AR, Fagan AM, Smemo S, Kauwe JS, Grupe A, et al. Apolipoprotein E levels in cerebrospinal fluid and the effects of ABCA1 polymorphisms. Mol Neurodegener. 2007;2:7.
95. Cruchaga C, Kauwe JS, Nowotny P, Bales K, Pickering EH, Mayo K, et al. Cerebrospinal fluid APOE levels: an endophenotype for genetic studies for Alzheimer's disease. Hum Mol Genet. 2012;21(20):4558-71.
96. Liu M, Kuhel DG, Shen L, Hui DY, Woods SC. Apolipoprotein E does not cross the blood-cerebrospinal fluid barrier, as revealed by an improved technique for sampling CSF from mice. Am J Physiol Regul Integr Comp Physiol. 2012;303(9):R903-8.
97. Linton MF, Gish R, Hubl ST, Bütler E, Esquivel C, Bry WI, et al. Phenotypes of apolipoprotein B and apolipoprotein E after liver transplantation. J Clin Invest. 1991;88(1):270-81.
98. Andersson M, Elmberger PG, Edlund C, Kristensson K, Dallner G. Rates of cholesterol, ubiquinone, dolichol and dolichyl-P biosynthesis in rat brain slices. FEBS Lett. 1990;269(1):15-8.
99. Petrov AM, Kasimov MR, Zefirov AL. Brain cholesterol metabolism and its defects: Linkage to neurodegenerative diseases and synaptic dysfunction. Acta Naturae. 2016;8(1):58-73.
100. Jurevics H, Morell P. Cholesterol for synthesis of myelin is made locally, not imported into brain. J Neurochem. 1995;64(2):895-901.
101. Yassine HN, Feng Q, Chiang J, Petrosspour LM, Fonteh AN, Chui HC, et al. ABCA1-Mediated Cholesterol Efflux Capacity to Cerebrospinal Fluid Is Reduced in Patients With Mild Cognitive Impairment and Alzheimer's Disease. J Am Heart Assoc. 2016;5(2).
102. Wahrle SE, Jiang H, Parsadanian M, Hartman RE, Bales KR, Paul SM, et al. Deletion of Abca1 increases Abeta deposition in the PDAPP transgenic mouse model of Alzheimer disease. J Biol Chem. 2005;280(52):43236-42.
103. Tokuda T, Calero M, Matsubara E, Vidal R, Kumar A, Permanne B, et al. Lipidation of apolipoprotein E influences its isoform-specific interaction with Alzheimer's amyloid beta peptides. Biochem J. 2000;348 Pt 2(Pt 2):359-65.
104. Kanekiyo T, Bu G. The low-density lipoprotein receptor-related protein 1 and amyloid-beta clearance in Alzheimer's disease. Front Aging Neurosci. 2014;6:93.
105. Lane-Donovan C, Philips GT, Herz J. More than cholesterol transporters: lipoprotein receptors in CNS function and neurodegeneration. Neuron. 2014;83(4):771-87.
106. Schmechel DE, Saunders AM, Strittmatter WJ, Crain BJ, Hulette CM, Joo SH, et al. Increased amyloid beta-peptide deposition in cerebral cortex as a consequence of apolipoprotein E genotype in late-onset Alzheimer disease. Proc Natl Acad Sci U S A. 1993;90(20):9649-53.
107. Tiraboschi P, Hansen LA, Masliah E, Alford M, Thal LJ, Corey-Bloom J. Impact of APOE genotype on neuropathologic and neurochemical markers of Alzheimer disease. Neurology. 2004;62(11):1977-83.
108. Strittmatter WJ, Saunders AM, Schmechel D, Pericak-Vance M, Enghild J, Salvesen GS, et al. Apolipoprotein E: high-avidity binding to beta-amyloid and increased frequency of type 4 allele in late-onset familial Alzheimer disease. Proc Natl Acad Sci U S A. 1993;90(5):1977-81.

109. LaDu MJ, Falduto MT, Manelli AM, Reardon CA, Getz GS, Frail DE. Isoform-specific binding of apolipoprotein E to beta-amyloid. J Biol Chem. 1994;269(38):23403-6.
110. Namba Y, Tomonaga M, Kawasaki H, Otomo E, Ikeda K. Apolipoprotein E immunoreactivity in cerebral amyloid deposits and neurofibrillary tangles in Alzheimer's disease and kuru plaque amyloid in Creutzfeldt-Jakob disease. Brain Research. 1991;541(1):163-6.
111. Irizarry MC, Rebeck GW, Cheung B, Bales K, Paul SM, Holzman D, et al. Modulation of A beta deposition in APP transgenic mice by an apolipoprotein E null background. Ann N Y Acad Sci. 2000;920:171-8.
112. Wisniewski T, Frangione B. Apolipoprotein E: a pathological chaperone protein in patients with cerebral and systemic amyloid. Neurosci Lett. 1992;135(2):235-8.
113. Drummond E, Wisniewski T. Alzheimer's disease: experimental models and reality. Acta Neuropathologica. 2017;133(2):155-75.
114. Nathan BP, Chang KC, Bellosta S, Brisch E, Ge N, Mahley RW, et al. The inhibitory effect of apolipoprotein E4 on neurite outgrowth is associated with microtubule depolymerization. J Biol Chem. 1995;270(34):19791-9.
115. Espeseth T, Westlye LT, Fjell AM, Walhovd KB, Rootwelt H, Reinvang I. Accelerated age-related cortical thinning in healthy carriers of apolipoprotein E epsilon 4. Neurobiol Aging. 2008;29(3):329-40.
116. Reiman EM, Uecker A, Caselli RJ, Lewis S, Bandy D, de Leon MJ, et al. Hippocampal volumes in cognitively normal persons at genetic risk for Alzheimer's disease. Ann Neurol. 1998;44(2):288-91.
117. Bondi MW, Houston WS, Eyler LT, Brown GG. fMRI evidence of compensatory mechanisms in older adults at genetic risk for Alzheimer disease. Neurology. 2005;64(3):501-8.
118. Bookheimer SY, Strojwas MH, Cohen MS, Saunders AM, Pericak-Vance MA, Mazziotta JC, et al. Patterns of brain activation in people at risk for Alzheimer's disease. N Engl J Med. 2000;343(7):450-6.
119. Chen Y, Durakoglugil MS, Xian X, Herz J. ApoE4 reduces glutamate receptor function and synaptic plasticity by selectively impairing ApoE receptor recycling. Proc Natl Acad Sci U S A. 2010;107(26):12011-6.
120. Buttini M, Yu GQ, Shockley K, Huang Y, Jones B, Masliah E, et al. Modulation of Alzheimer-like synaptic and cholinergic deficits in transgenic mice by human apolipoprotein E depends on isoform, aging, and overexpression of amyloid beta peptides but not on plaque formation. J Neurosci. 2002;22(24):10539-48.
121. Steele OG, Stuart AC, Minkley L, Shaw K, Bonnar O, Anderle S, et al. A multi-hit hypothesis for an APOE4-dependent pathophysiological state. Eur J Neurosci. 2022;56(9):5476-515.
122. Xu PT, Gilbert JR, Qiu HL, Ervin J, Rothrock-Christian TR, Hulette C, et al. Specific regional transcription of apolipoprotein E in human brain neurons. Am J Pathol. 1999;154(2):601-11.
123. Aoki K, Uchihara T, Sanjo N, Nakamura A, Ikeda K, Tsuchiya K, et al. Increased expression of neuronal apolipoprotein E in human brain with cerebral infarction. Stroke. 2003;34(4):875-80.
124. Zalocusky KA, Najm R, Taubes AL, Hao Y, Yoon SY, Koutsodendris N, et al. Neuronal ApoE upregulates MHC-I expression to drive selective neurodegeneration in Alzheimer's disease. Nat Neurosci. 2021;24(6):786-98.
125. Xu PT, Schmechel D, Rothrock-Christian T, Burkhart DS, Qiu HL, Popko B, et al. Human apolipoprotein E2, E3, and E4 isoform-specific transgenic mice: human-like pattern of glial and neuronal immunoreactivity in central nervous system not observed in wild-type mice. Neurobiol Dis. 1996;3(3):229-45.
126. Xu Q, Bernardo A, Walker D, Kanegawa T, Mahley RW, Huang Y. Profile and regulation of apolipoprotein E (ApoE) expression in the CNS in mice with targeting of green fluorescent protein gene to the ApoE locus. J Neurosci. 2006;26(19):4985-94.
127. Horsburgh K, Nicoll JA. Selective alterations in the cellular distribution of apolipoprotein E immunoreactivity following transient cerebral ischaemia in the rat. Neuropathol Appl Neurobiol. 1996;22(4):342-9.

128. Shi Y, Manis M, Long J, Wang K, Sullivan PM, Remolina Serrano J, et al. Microglia drive APOE-dependent neurodegeneration in a tauopathy mouse model. Journal of Experimental Medicine. 2019;216(11):2546-61.
129. Wang C, Xiong M, Gratuze M, Bao X, Shi Y, Andhey PS, et al. Selective removal of astrocytic APOE4 strongly protects against tau-mediated neurodegeneration and decreases synaptic phagocytosis by microglia. Neuron. 2021;109(10):1657-74.e7.
130. Koutsodendris N, Blumenfeld J, Agrawal A, Traglia M, Grone B, Zilberter M, et al. Neuronal APOE4 removal protects against tau-mediated gliosis, neurodegeneration and myelin deficits. Nature Aging. 2023;3(3):275-96.
131. Dekroon RM, Armati PJ. Synthesis and processing of apolipoprotein E in human brain cultures. Glia. 2001;33(4):298-305.
132. Huang YA, Zhou B, Wernig M, Sudhof TC. ApoE2, ApoE3, and ApoE4 Differentially Stimulate APP Transcription and Abeta Secretion. Cell. 2017;168(3):427-41 e21.
133. Wang C, Najm R, Xu Q, Jeong DE, Walker D, Balestra ME, et al. Gain of toxic apolipoprotein E4 effects in human iPSC-derived neurons is ameliorated by a small-molecule structure corrector. Nat Med. 2018;24(5):647-57.
134. Lin YT, Seo J, Gao F, Feldman HM, Wen HL, Penney J, et al. APOE4 Causes Widespread Molecular and Cellular Alterations Associated with Alzheimer's Disease Phenotypes in Human iPSC-Derived Brain Cell Types. Neuron. 2018;98(6):1141-54 e7.
135. Brookhouser N, Raman S, Frisch C, Srinivasan G, Brafman DA. APOE2 mitigates disease-related phenotypes in an isogenic hiPSC-based model of Alzheimer's disease. Molecular Psychiatry. 2021;26(10):5715-32.
136. Engle SJ, Blaha L, Kleiman RJ. Best Practices for Translational Disease Modeling Using Human iPSC-Derived Neurons. Neuron. 2018;100(4):783-97.
137. Penney J, Ralvenius WT, Tsai L-H. Modeling Alzheimer's disease with iPSC-derived brain cells. Molecular Psychiatry. 2020;25(1):148-67.
138. de Leeuw S, Tackenberg C. Alzheimer's in a dish - induced pluripotent stem cell-based disease modeling. Transl Neurodegener. 2019;8:21.
139. Takahashi K, Yamanaka S. Induction of pluripotent stem cells from mouse embryonic and adult fibroblast cultures by defined factors. Cell. 2006;126(4):663-76.
140. Yu J, Vodyanik MA, Smuga-Otto K, Antosiewicz-Bourget J, Frane JL, Tian S, et al. Induced pluripotent stem cell lines derived from human somatic cells. Science. 2007;318(5858):1917-20.
141. Farkhondeh A, Li R, Gorshkov K, Chen KG, Might M, Rodems S, et al. Induced pluripotent stem cells for neural drug discovery. Drug Discov Today. 2019;24(4):992-9.
142. Mungenast AE, Siegert S, Tsai LH. Modeling Alzheimer's disease with human induced pluripotent stem (iPS) cells. Mol Cell Neurosci. 2016;73:13-31.
143. Israel MA, Yuan SH, Bardy C, Reyna SM, Mu Y, Herrera C, et al. Probing sporadic and familial Alzheimer's disease using induced pluripotent stem cells. Nature. 2012;482(7384):216-20.
144. Wadhwani AR, Affaneh A, Van Gulden S, Kessler JA. Neuronal apolipoprotein E4 increases cell death and phosphorylated tau release in alzheimer disease. Ann Neurol. 2019;85(5):726-39.
145. Wang C, Ward ME, Chen R, Liu K, Tracy TE, Chen X, et al. Scalable Production of iPSC-Derived Human Neurons to Identify Tau-Lowering Compounds by High-Content Screening. Stem Cell Reports. 2017;9(4):1221-33.
146. Kazim SF, Chuang SC, Zhao W, Wong RK, Bianchi R, Iqbal K. Early-Onset Network Hyperexcitability in Presymptomatic Alzheimer's Disease Transgenic Mice Is Suppressed by Passive Immunization with Anti-Human APP/Abeta Antibody and by mGluR5 Blockade. Front Aging Neurosci. 2017;9(MAR):71.
147. Wilkinson G, Dennis D, Schuurmans C. Proneural genes in neocortical development. Neuroscience. 2013;253:256-73.
148. Bertrand N, Castro DS, Guillemot F. Proneural genes and the specification of neural cell types. Nat Rev Neurosci. 2002;3(7):517-30.
149. Pang ZP, Yang N, Vierbuchen T, Ostermeier A, Fuentes DR, Yang TQ, et al. Induction of human neuronal cells by defined transcription factors. Nature. 2011;476(7359):220-3.

150. Busskamp V, Lewis NE, Guye P, Ng AH, Shipman SL, Byrne SM, et al. Rapid neurogenesis through transcriptional activation in human stem cells. Mol Syst Biol. 2014;10(11):760.
151. Zhang Y, Pak C, Han Y, Ahlenius H, Zhang Z, Chanda S, et al. Rapid single-step induction of functional neurons from human pluripotent stem cells. Neuron. 2013;78(5):785-98.
152. Chanda S, Ang CE, Davila J, Pak C, Mall M, Lee QY, et al. Generation of induced neuronal cells by the single reprogramming factor ASCL1. Stem Cell Reports. 2014;3(2):282-96.
153. Thoma EC, Wischmeyer E, Offen N, Maurus K, Sirén AL, Schartl M, et al. Ectopic expression of neurogenin 2 alone is sufficient to induce differentiation of embryonic stem cells into mature neurons. PLoS One. 2012;7(6):e38651.
154. Sun S, Zhu XJ, Huang H, Guo W, Tang T, Xie B, et al. WNT signaling represses astrogliogenesis via Ngn2-dependent direct suppression of astrocyte gene expression. Glia. 2019;67(7):1333-43.
155. Dennis DJ, Han S, Schuurmans C. bHLH transcription factors in neural development, disease, and reprogramming. Brain Res. 2019;1705:48-65.
156. Yuan L, Hassan BA. Neurogenins in brain development and disease: an overview. Arch Biochem Biophys. 2014;558:10-3.
157. Shimojo H, Ohtsuka T, Kageyama R. Dynamic expression of notch signaling genes in neural stem/progenitor cells. Front Neurosci. 2011;5:78.
158. Hand R, Bortone D, Mattar P, Nguyen L, Heng JI-T, Guerrier S, et al. Phosphorylation of Neurogenin2 Specifies the Migration Properties and the Dendritic Morphology of Pyramidal Neurons in the Neocortex. Neuron. 2005;48(1):45-62.
159. Patsali P, Kleanthous M, Lederer CW. Disruptive Technology: CRISPR/Cas-Based Tools and Approaches. Mol Diagn Ther. 2019;23(2):187-200.
160. Saito M, Xu P, Faure G, Maguire S, Kannan S, Altae-Tran H, et al. Fanzor is a eukaryotic programmable RNA-guided endonuclease. Nature. 2023.
161. Tycko J, Myer VE, Hsu PD. Methods for Optimizing CRISPR-Cas9 Genome Editing Specificity. Mol Cell. 2016;63(3):355-70.
162. Kotin RM, Linden RM, Berns KI. Characterization of a preferred site on human chromosome 19q for integration of adeno-associated virus DNA by non-homologous recombination. Embo j. 1992;11(13):5071-8.
163. Smith JR, Maguire S, Davis LA, Alexander M, Yang F, Chandran S, et al. Robust, persistent transgene expression in human embryonic stem cells is achieved with AAVS1-targeted integration. Stem Cells. 2008;26(2):496-504.
164. Lombardo A, Cesana D, Genovese P, Di Stefano B, Provasi E, Colombo DF, et al. Site-specific integration and tailoring of cassette design for sustainable gene transfer. Nat Methods. 2011;8(10):861-9.
165. Ogata T, Kozuka T, Kanda T. Identification of an insulator in AAVS1, a preferred region for integration of adeno-associated virus DNA. J Virol. 2003;77(16):9000-7.
166. Xia X, Zhang Y, Zieth CR, Zhang SC. Transgenes delivered by lentiviral vector are suppressed in human embryonic stem cells in a promoter-dependent manner. Stem Cells Dev. 2007;16(1):167-76.
167. Das AT, Tenenbaum L, Berkhout B. Tet-On Systems For Doxycycline-inducible Gene Expression. Curr Gene Ther. 2016;16(3):156-67.
168. Zhou X, Vink M, Klaver B, Berkhout B, Das AT. Optimization of the Tet-On system for regulated gene expression through viral evolution. Gene Ther. 2006;13(19):1382-90.
169. Gossen M, Freundlieb S, Bender G, Müller G, Hillen W, Bujard H. Transcriptional activation by tetracyclines in mammalian cells. Science. 1995;268(5218):1766-9.
170. Loew R, Heinz N, Hampf M, Bujard H, Gossen M. Improved Tet-responsive promoters with minimized background expression. BMC Biotechnol. 2010;10:81.
171. USDoHaH. <Services Manual .pdf>. In: Services USDoHaH, editor. 2009.
172. Schmid B, Prehn KR, Nimsanor N, Garcia BIA, Poulsen U, Jorring I, et al. Generation of a set of isogenic, gene-edited iPSC lines homozygous for all main APOE variants and an APOE knock-out line. Stem Cell Res. 2019;34:101349.

173. Schmid B, Prehn KR, Nimsanor N, Garcia BIA, Poulsen U, Jorring I, et al. Corrigendum to "Generation of a set of isogenic, gene-edited iPSC lines homozygous for all main APOE variants and an APOE knock-out line" [Stem Cell Res. 34/1873-5061 (2019) 101349-55]. Stem Cell Res. 2020;48:102005.
174. Schmid B, Holst B, Clausen C, Bahnassawy L, Reinhardt P, Bakker MHM, et al. Generation of a set of isogenic iPSC lines carrying all APOE genetic variants (E2/E3/E4) and knock-out for the study of APOE biology in health and disease. Stem Cell Res. 2021;52:102180.
175. Abruzzese R, Fekete R, Kephart D. Cells-to-CT Kits: Next Generation Gene Expression Analysis Workflows that Eliminate Sample Purification. JALA: Journal of the Association for Laboratory Automation. 2010;15(5):362-8.
176. nanoString. Gene Expression Data Analysis Guidelines [Manual]. [nCounter differential gene expression data analysis manual]. Available from: https://nanostring.com/wp-content/uploads/Gene_Expression_Data_Analysis_Guidelines.pdf.
177. Vignon A, Salvador-Prince L, Lehmann S, Perrier V, Torrent J. Deconstructing Alzheimer's Disease: How to Bridge the Gap between Experimental Models and the Human Pathology? Int J Mol Sci. 2021;22(16).
178. Kim H, Yoo J, Shin J, Chang Y, Jung J, Jo DG, et al. Modelling APOE ε3/4 allele-associated sporadic Alzheimer's disease in an induced neuron. Brain. 2017;140(8):2193-209.
179. Duan L, Bhattacharyya BJ, Belmadani A, Pan L, Miller RJ, Kessler JA. Stem cell derived basal forebrain cholinergic neurons from Alzheimer's disease patients are more susceptible to cell death. Mol Neurodegener. 2014;9:3.
180. Huang YA, Zhou B, Nabet AM, Wernig M, Sudhof TC. Differential Signaling Mediated by ApoE2, ApoE3, and ApoE4 in Human Neurons Parallels Alzheimer's Disease Risk. J Neurosci. 2019;39(37):7408-27.
181. Fang EF, Hou Y, Palikaras K, Adriaanse BA, Kerr JS, Yang B, et al. Mitophagy inhibits amyloid-β and tau pathology and reverses cognitive deficits in models of Alzheimer's disease. Nat Neurosci. 2019;22(3):401-12.
182. Lin YT, Seo J, Gao F, Feldman HM, Wen HL, Penney J, et al. APOE4 Causes Widespread Molecular and Cellular Alterations Associated with Alzheimer's Disease Phenotypes in Human iPSC-Derived Brain Cell Types. Neuron. 2018;98(6):1141-54.e7.
183. Birnbaum JH, Wanner D, Gietl AF, Saake A, Kündig TM, Hock C, et al. Oxidative stress and altered mitochondrial protein expression in the absence of amyloid-β and tau pathology in iPSC-derived neurons from sporadic Alzheimer's disease patients. Stem Cell Res. 2018;27:121-30.
184. Qian K, Huang CT, Chen H, Blackbourn LWt, Chen Y, Cao J, et al. A simple and efficient system for regulating gene expression in human pluripotent stem cells and derivatives. Stem Cells. 2014;32(5):1230-8.
185. Baron U, Bujard H. Tet repressor-based system for regulated gene expression in eukaryotic cells: principles and advances. Methods Enzymol. 2000;327:401-21.
186. Du ZW, Hu BY, Ayala M, Sauer B, Zhang SC. Cre recombination-mediated cassette exchange for building versatile transgenic human embryonic stem cells lines. Stem Cells. 2009;27(5):1032-41.
187. Consensus guidance for banking and supply of human embryonic stem cell lines for research purposes. Stem Cell Rev Rep. 2009;5(4):301-14.
188. Wakao S, Kitada M, Kuroda Y, Ogura F, Murakami T, Niwa A, et al. Morphologic and gene expression criteria for identifying human induced pluripotent stem cells. PLoS One. 2012;7(12):e48677.
189. Nagasaka R, Matsumoto M, Okada M, Sasaki H, Kanie K, Kii H, et al. Visualization of morphological categories of colonies for monitoring of effect on induced pluripotent stem cell culture status. Regenerative Therapy. 2017;6:41-51.
190. Rodin S, Antonsson L, Hovatta O, Tryggvason K. Monolayer culturing and cloning of human pluripotent stem cells on laminin-521-based matrices under xeno-free and chemically defined conditions. Nat Protoc. 2014;9(10):2354-68.
191. Benowitz LI, Perrone-Bizzozero NI. The expression of GAP-43 in relation to neuronal growth and plasticity: when, where, how, and why? Prog Brain Res. 1991;89:69-87.

192. Denny JB. Molecular mechanisms, biological actions, and neuropharmacology of the growth-associated protein GAP-43. Curr Neuropharmacol. 2006;4(4):293-304.
193. Goparaju SK, Kohda K, Ibata K, Soma A, Nakatake Y, Akiyama T, et al. Rapid differentiation of human pluripotent stem cells into functional neurons by mRNAs encoding transcription factors. Sci Rep. 2017;7:42367.
194. Mahley RW, Huang Y. Apolipoprotein e sets the stage: response to injury triggers neuropathology. Neuron. 2012;76(5):871-85.
195. Nicolas M, Hassan BA. Amyloid precursor protein and neural development. Development. 2014;141(13):2543-8.
196. Bergström P, Agholme L, Nazir FH, Satir TM, Toombs J, Wellington H, et al. Amyloid precursor protein expression and processing are differentially regulated during cortical neuron differentiation. Scientific Reports. 2016;6(1):29200.
197. Gonzalez F, Barragan Monasterio M, Tiscornia G, Montserrat Pulido N, Vassena R, Batlle Morera L, et al. Generation of mouse-induced pluripotent stem cells by transient expression of a single nonviral polycistronic vector. Proc Natl Acad Sci U S A. 2009;106(22):8918-22.
198. Si-Tayeb K, Noto FK, Sepac A, Sedlic F, Bosnjak ZJ, Lough JW, et al. Generation of human induced pluripotent stem cells by simple transient transfection of plasmid DNA encoding reprogramming factors. BMC Dev Biol. 2010;10:81.
199. Stuchbury G, Munch G. Optimizing the generation of stable neuronal cell lines via pre-transfection restriction enzyme digestion of plasmid DNA. Cytotechnology. 2010;62(3):189-94.
200. Oceguera-Yanez F, Kim SI, Matsumoto T, Tan GW, Xiang L, Hatani T, et al. Engineering the AAVS1 locus for consistent and scalable transgene expression in human iPSCs and their differentiated derivatives. Methods. 2016;101:43-55.
201. Song F, Stieger K. Optimizing the DNA Donor Template for Homology-Directed Repair of Double-Strand Breaks. Mol Ther Nucleic Acids. 2017;7:53-60.
202. Canaj H, Hussmann J, Li H, Beckman K, Goodrich L, Cho N, et al. Deep profiling reveals substantial heterogeneity of integration outcomes in CRISPR knock-in experiments. bioRxiv; 2019.
203. Mali P, Yang L, Esvelt KM, Aach J, Guell M, DiCarlo JE, et al. RNA-guided human genome engineering via Cas9. Science. 2013;339(6121):823-6.
204. Skryabin BV, Kummerfeld DM, Gubar L, Seeger B, Kaiser H, Stegemann A, et al. Pervasive head-to-tail insertions of DNA templates mask desired CRISPR-Cas9-mediated genome editing events. Sci Adv. 2020;6(7):eaax2941.
205. Norris AL, Lee SS, Greenlees KJ, Tadesse DA, Miller MF, Lombardi HA. Template plasmid integration in germline genome-edited cattle. Nature Biotechnology. 2020;38(2):163-4.
206. Hsu PD, Scott DA, Weinstein JA, Ran FA, Konermann S, Agarwala V, et al. DNA targeting specificity of RNA-guided Cas9 nucleases. Nature Biotechnology. 2013;31(9):827-32.
207. Bhagwan JR, Collins E, Mosqueira D, Bakar M, Johnson BB, Thompson A, et al. Variable expression and silencing of CRISPR-Cas9 targeted transgenes identifies the AAVS1 locus as not an entirely safe harbour. F1000Res. 2019;8:1911.
208. Klatt D, Cheng E, Hoffmann D, Santilli G, Thrasher AJ, Brendel C, et al. Differential Transgene Silencing of Myeloid-Specific Promoters in the AAVS1 Safe Harbor Locus of Induced Pluripotent Stem Cell-Derived Myeloid Cells. Hum Gene Ther. 2020;31(3-4):199-210.
209. Lee H, Nowosiad P, Dutan Polit LM, Price J, Srivastava DP, Thuret S. Apolipoprotein E expression pattern in human induced pluripotent stem cells during in vitro neural induction. F1000Res. 2020;9:353.
210. Peitz M, Bechler T, Thiele CC, Veltel M, Bloschies M, Fliessbach K, et al. Blood-derived integration-free iPS cell line UKBi011-A from a diagnosed male Alzheimer's disease patient with APOE varepsilon4/varepsilon4 genotype. Stem Cell Res. 2018;29:250-3.
211. Minatohara K, Akiyoshi M, Okuno H. Role of Immediate-Early Genes in Synaptic Plasticity and Neuronal Ensembles Underlying the Memory Trace. Front Mol Neurosci. 2015;8:78.
212. Yang CP, Gilley JA, Zhang G, Kernie SG. ApoE is required for maintenance of the dentate gyrus neural progenitor pool. Development. 2011;138(20):4351-62.

213. Frotscher M, Zafirov S, Heimrich B. Development of identified neuronal types and of specific synaptic connections in slice cultures of rat hippocampus. Prog Neurobiol. 1995;45(6):vii-xxviii.
214. Bartholome O, Van den Ackerveken P, Sánchez Gil J, de la Brassinne Bonardeaux O, Leprince P, Franzen R, et al. Puzzling Out Synaptic Vesicle 2 Family Members Functions. Front Mol Neurosci. 2017;10:148.
215. Xu PT, Li YJ, Qin XJ, Scherzer CR, Xu H, Schmechel DE, et al. Differences in apolipoprotein E3/3 and E4/4 allele-specific gene expression in hippocampus in Alzheimer disease. Neurobiol Dis. 2006;21(2):256-75.
216. Stout KA, Dunn AR, Hoffman C, Miller GW. The Synaptic Vesicle Glycoprotein 2: Structure, Function, and Disease Relevance. ACS Chem Neurosci. 2019;10(9):3927-38.
217. Detrait E, Maurice T, Hanon E, Leclercq K, Lamberty Y. Lack of synaptic vesicle protein SV2B protects against amyloid-beta(2)(5)(-)(3)(5)-induced oxidative stress, cholinergic deficit and cognitive impairment in mice. Behav Brain Res. 2014;271:277-85.
218. White DN, Stowell MHB. Room for Two: The Synaptophysin/Synaptobrevin Complex. Front Synaptic Neurosci. 2021;13:740318.
219. Buttini M, Masliah E, Yu GQ, Palop JJ, Chang S, Bernardo A, et al. Cellular source of apolipoprotein E4 determines neuronal susceptibility to excitotoxic injury in transgenic mice. Am J Pathol. 2010;177(2):563-9.
220. Wang Q, Yu S, Simonyi A, Sun GY, Sun AY. Kainic acid-mediated excitotoxicity as a model for neurodegeneration. Mol Neurobiol. 2005;31(1-3):3-16.
221. Hosie KA, King AE, Blizzard CA, Vickers JC, Dickson TC. Chronic Excitotoxin-Induced Axon Degeneration in a Compartmented Neuronal Culture Model. ASN Neuro. 2012;4(1):AN20110031.
222. Baleriola J, Walker CA, Jean YY, Crary JF, Troy CM, Nagy PL, et al. Axonally synthesized ATF4 transmits a neurodegenerative signal across brain regions. Cell. 2014;158(5):1159-72.
223. Quirós PM, Prado MA, Zamboni N, D'Amico D, Williams RW, Finley D, et al. Multi-omics analysis identifies ATF4 as a key regulator of the mitochondrial stress response in mammals. J Cell Biol. 2017;216(7):2027-45.
224. Wei N, Zhu L-Q, Liu D. ATF4: a Novel Potential Therapeutic Target for Alzheimer's Disease. Molecular Neurobiology. 2015;52(3):1765-70.
225. Zhang J, Zhang D, McQuade JS, Behbehani M, Tsien JZ, Xu M. c-fos regulates neuronal excitability and survival. Nature Genetics. 2002;30(4):416-20.
226. Sultana R, Perluigi M, Butterfield DA. Lipid peroxidation triggers neurodegeneration: A redox proteomics view into the Alzheimer disease brain. Free Radical Biology and Medicine. 2013;62:157-69.
227. Harris FM, Tesseur I, Brecht WJ, Xu Q, Mullendorff K, Chang S, et al. Astroglial regulation of apolipoprotein E expression in neuronal cells. Implications for Alzheimer's disease. J Biol Chem. 2004;279(5):3862-8.
228. Xu Q, Walker D, Bernardo A, Brodbeck J, Balestra ME, Huang Y. Intron-3 retention/splicing controls neuronal expression of apolipoprotein E in the CNS. J Neurosci. 2008;28(6):1452-9.
229. Spiegel I, Mardinly AR, Gabel HW, Bazinet JE, Couch CH, Tzeng CP, et al. Npas4 regulates excitatory-inhibitory balance within neural circuits through cell-type-specific gene programs. Cell. 2014;157(5):1216-29.
230. Catala-Solsona J, Minano-Molina AJ, Rodriguez-Alvarez J. Nr4a2 Transcription Factor in Hippocampal Synaptic Plasticity, Memory and Cognitive Dysfunction: A Perspective Review. Front Mol Neurosci. 2021;14:786226.
231. Mitroi DN, Pereyra-Gómez G, Soto-Huelin B, Senovilla F, Kobayashi T, Esteban JA, et al. NPC1 enables cholesterol mobilization during long-term potentiation that can be restored in Niemann-Pick disease type C by CYP46A1 activation. EMBO Rep. 2019;20(11):e48143.
232. Health FftNIo. Pre-competitive Analytical Validation of SV2A PET as a Biomarker of Synaptic Density (SV2A PET Project) https://fnih.org/our-programs/pre-competitive-analytical-validation-of-sv2a-pet-as-a-biomarker-of-synaptic-density-sv2a-pet-project/: FNIH; 2023 [

233. Konings SC, Torres-Garcia L, Martinsson I, Gouras GK. Astrocytic and Neuronal Apolipoprotein E Isoforms Differentially Affect Neuronal Excitability. Front Neurosci. 2021;15:734001.
234. Shipley MM, Mangold CA, Szpara ML. Differentiation of the SH-SY5Y Human Neuroblastoma Cell Line. J Vis Exp. 2016(108):53193.
235. Schaffer S, Lam VY, Ernst IM, Huebbe P, Rimbach G, Halliwell B. Variability in APOE genotype status in human-derived cell lines: a cause for concern in cell culture studies? Genes Nutr. 2014;9(1):364.
236. Krishtal J, Bragina O, Metsla K, Palumaa P, Tougu V. In situ fibrillizing amyloid-beta 1-42 induces neurite degeneration and apoptosis of differentiated SH-SY5Y cells. PLoS One. 2017;12(10):e0186636.
237. Agholme L, Lindström T, Kågedal K, Marcusson J, Hallbeck M. An in vitro model for neuroscience: differentiation of SH-SY5Y cells into cells with morphological and biochemical characteristics of mature neurons. J Alzheimers Dis. 2010;20(4):1069-82.
238. Tagai N, Tanaka A, Sato A, Uchiumi F, Tanuma SI. Low Levels of Brain-Derived Neurotrophic Factor Trigger Self-aggregated Amyloid β-Induced Neuronal Cell Death in an Alzheimer's Cell Model. Biol Pharm Bull. 2020;43(7):1073-80.
239. Lee M, McGeer E, McGeer PL. Activated human microglia stimulate neuroblastoma cells to upregulate production of beta amyloid protein and tau: implications for Alzheimer's disease pathogenesis. Neurobiol Aging. 2015;36(1):42-52.
240. Jamsa A, Hasslund K, Cowburn RF, Backstrom A, Vasange M. The retinoic acid and brain-derived neurotrophic factor differentiated SH-SY5Y cell line as a model for Alzheimer's disease-like tau phosphorylation. Biochem Biophys Res Commun. 2004;319(3):993-1000.
241. Ferrari A, Hoerndli F, Baechi T, Nitsch RM, Gotz J. beta-Amyloid induces paired helical filament-like tau filaments in tissue culture. J Biol Chem. 2003;278(41):40162-8.
242. Chambers SM, Fasano CA, Papapetrou EP, Tomishima M, Sadelain M, Studer L. Highly efficient neural conversion of human ES and iPS cells by dual inhibition of SMAD signaling. Nature Biotechnology. 2009;27(3):275-80.
243. Ulrich JD, Burchett JM, Restivo JL, Schuler DR, Verghese PB, Mahan TE, et al. In vivo measurement of apolipoprotein E from the brain interstitial fluid using microdialysis. Mol Neurodegener. 2013;8:13.
244. Fryer JD, Demattos RB, McCormick LM, O'Dell MA, Spinner ML, Bales KR, et al. The low density lipoprotein receptor regulates the level of central nervous system human and murine apolipoprotein E but does not modify amyloid plaque pathology in PDAPP mice. J Biol Chem. 2005;280(27):25754-9.
245. Hera C, Jeffrey AH, Han L, Kyle AB, Leeanne G, Nathan HC, et al. Deep profiling reveals substantial heterogeneity of integration outcomes in CRISPR knock-in experiments. bioRxiv. 2019:841098.

Appendix A

A.1 nCounter® Neuropathology Panel Gene List

nCounter® Neuropathology Panel Gene List															
AARS1	ATM	CALB1	CHMP2B	CYP4X1	EPO	GNAI3	HIF1A	KATNA1	MGMT	NMNAT2	PHF19	PRKACB	SCN2A	SRC	TNFRSF1B
ABAT	ATP13A2	CALB2	CHRM5	DAGLA	ERBB3	GNAO1	HLA-DRA	KCNA1	MMP12	NOL3	PHF2	PRKACG	SEC23A	SRI	TNR
ABL1	ATP2B3	CALM1	CHRNA7	DBH	ERG	GNAQ	HMGB1	KCNB1	MMP14	NOS1	PHF21A	PRKCA	SERPINB6	SRSF4	TOR1A
ACAA1	ATP6V0C	CALML5	CHRNB2	DCX	ERLEC1	GNB5	HMOX1	KCNJ10	MMP16	NOS2	PIK3CA	PRKCB	SF3A2	STAB1	TP53
ACHE	ATP6V0D1	CAMK2B	CLDN15	DDC	ESAM	GNG2	HNRNPM	KEAP1	MMP19	NOS3	PIK3CB	PRKCE	SF3B2	STAMBPL1	TPM1
ACIN1	ATP6V0E1	CAMK2D	CLDN5	DDIT3	F2	GNGT1	HOMER1	KEL	MMP2	NOSTRIN	PIK3R1	PRKCG	SF3B4	STAT1	TRADD
ACTN1	ATP6V0E2	CAMK2G	CLN3	DDX23	FA2H	GNPTAB	HPGDS	KIF3A	MMP24	NOTCH1	PINK1	PRKCQ	SGPL1	STAT3	TREM1
ACVRL1	ATP6V1A	CAMK4	CLN8	DES	FAM104A	GNPTG	HRAS	KLK6	MMP9	NOTCH3	PKN1	PRKCSH	SH3TC2	STX1A	TREM2
ADAM10	ATP6V1D	CASP1	CLU	DGKB	FAM126A	GPD1L	HSPA6	KRAS	MMRN2	NOTCH4	PLA2G2A	PRKN	SHANK2	STX1B	TRIM28
ADCY5	ATP6V1E1	CASP3	CNKSR2	DGKE	FAS	GPR37	HSPB1	L1CAM	MNAT1	NOVA1	PLA2G2E	PRL	SHH	STX2	TRIM37
ADCY8	ATP6V1G2	CASP6	CNOT10	DLAT	FASLG	GPR4	HTR1A	LAMA2	MOG	NPAS4	PLA2G2F	PRNP	SIRT1	SUCLA2	TRPM2
ADCY9	ATP6V1H	CASP7	CNR1	DLD	FGF12	GPR84	HTR5A	LAMB2	MPZ	NPC1	PLA2G4A	PRPF3	SIRT2	SUPT7L	TRPV1
ADCYAP1	ATP7A	CASP8	CNTF	DLG3	FGF14	GPRASP1	HTRA2	LAMP1	MSN	NPC2	PLA2G4B	PRPF31	SIRT7	SYNJ1	TSPO
ADORA1	ATP8A2	CASP9	CNTN1	DLG4	FGF2	GRIA1	HTT	LARS1	MTA1	NPTN	PLA2G4C	PSEN1	SLA	SYT1	TWISTNB
ADORA2A	ATRN	CAST	CNTN4	DLGAP1	FLT1	GRIA2	ICAM1	LCLAT1	MTA2	NPY	PLA2G4D	PSEN2	SLC11A1	SYT13	TXNL1
ADRA2A	ATXN2	CCDC127	CNTNAP1	DLL4	FLT4	GRIA3	ICAM2	LDHC	MTHFR	NQO1	PLA2G4E	PSMB8	SLC12A5	SYT4	U2AF2
ADRB2	ATXN3	CCK	CNTNAP2	DLX1	FMR1	GRIA4	IDE	LIF	MTO1	NR4A2	PLA2G4F	PSMB9	SLC17A6	SYT7	UBE2K
AGER	ATXN7	CCL2	COL4A1	DLX2	FN1	GRIK2	IDH1	LMNA	MTOR	NRG1	PLA2G6	PTDSS1	SLC18A2	TADA2B	UBE2N
AIF1	AVP	CCL5	COL4A2	DNAH1	FOS	GRIN1	IGF1	LOX	MUTYH	NRXN1	PLAAT3	PTDSS2	SLC18A3	TAF10	UBE3A
AKT1	B4GALT6	CCND1	COMT	DNAJA2	FRMPD4	GRIN2A	IGF1R	LPAR1	MYC	NSF	PLCB1	PTEN	SLC1A1	TAF4	UBQLN1
AKT1S1	BACE1	CCNH	CP	DNM1L	FUS	GRIN2B	IKBKB	LPO	MYCT1	NTF3	PLCB2	PTGS2	SLC1A2	TAF4B	UCHL1
AKT2	BAD	CCR2	CPLX1	DNM2	FXN	GRIN2C	IL10	LRP1	MYD88	NTNG1	PLCB3	PTPRN2	SLC2A1	TAF6L	UGCG
AKT3	BAX	CCR5	CPT1B	DOT1L	FYN	GRIN2D	IL10RA	LRRC25	MYH10	NTRK1	PLCB4	PTPRR	SLC32A1	TAF9	UGT8
ALDH1L1	BCAS1	CCS	CR1	DRD1	GAA	GRIN3B	IL13RA1	LRRC4	MYORG	NTS	PLCL2	PVALB	SLC4A10	TARDBP	UNC13A
AMIGO1	BCAS2	CD14	CREB1	DRD2	GABRA1	GRM1	IL15RA	LRRK2	MYRF	NWD1	PLEKHO2	RAB2A	SLC6A3	TAZ	USP21
AMPH	BCHE	CD33	CREBBP	DRD4	GABRA4	GRM2	IL1B	LSM2	NAGLU	OLFM3	PLLP	RAB3A	SLC6A4	TBP	USP30
ANG	BCL2	CD34	CRH	EFNA1	GABRB2	GRM5	IL1R1	LSM7	NAPSA	OLIG2	PLS1	RAB3C	SLC8A1	TBPL1	VCP
ANGPT2	BCL2L1	CD4	CRTC2	EFNA5	GABRB3	GRM8	IL4R	LSR	NCAM1	OPA1	PLXNB3	RAC1	SLC9A6	TBR1	VEGFA
AP1S1	BDNF	CD40	CSF1	EFNB3	GABRG2	GRN	IL6	LTBR	NCF1	OPTN	PLXNC1	RAD23B	SLU7	TCERG1	VIP
AP2A2	BECN1	CD44	CSF1R	EFR3A	GABRP	GSK3B	IL6R	LYPLA1	NCL	OSMR	PMP22	RAF1	SMN1	TCIRG1	WFS1
AP2B1	BID	CD68	CSF2RB	EGF	GABRR1	GSN	INA	MAG	NEFH	OXR1	PNKD	RAN	SMPD4	TENM2	XAB2
AP3M2	BNIP3	CD8A	CSNK2A2	EGFL7	GABRR3	GSR	INHBB	MAGEE1	NEFL	P2RX4	POLR2B	RAPGEF2	SMYD1	TF	XBP1
AP3S1	BRMS1L	CD9	CSPG4	EGFR	GAD1	GSS	INPP4A	MAL	NEGR1	P2RX7	POLR2H	RASGRP1	SNAP91	TFAM	XIAP
AP4S1	C3	CDC27	CTNNB1	EGR1	GAD2	GSTP1	INPP5F	MAN2B1	NELFA	P2RY12	POLR2J	RDX	SNCA	TGFB1	XK
APAF1	C5	CDC40	CTNS	EGR2	GAL3ST1	GTF2A1	INS	MAP2	NELL2	PAH	POLR2K	RELA	SNCAIP	TGFBR2	ZNF24
APC	C6	CDK2	CTSE	EHMT1	GALC	GTF2B	INSR	MAP2K1	NEO1	PAK1	POLR2L	RET	SNCB	TH	
APOE	C9orf72	CDK5	CUL1	EIF2S1	GATA2	GTF2H1	IPCEF1	MAP2K2	NES	PALM	PPARGC1A	RHOA	SNRPA	THY1	
APP	CA2	CDK5R1	CUL2	EMCN	GBA	GTF2H3	IRF8	MAPK1	NF1	PARK7	PPM1L	RIMS1	SOD1	TIE1	
AQP4	CAB39	CDK5RAP3	CUL3	EMP2	GDNF	GTF2IRD1	ISLR2	MAPK10	NFE2L2	PARP1	PPP2CA	RING1	SOD2	TLR2	
ARC	CACNA1A	CDK7	CX3CL1	ENG	GDPD2	GUCY1B1	ITGA5	MAPK3	NFKBIA	PCNA	PPP2R5C	RIT2	SORCS3	TLR4	
ARHGAP44	CACNA1B	CDKN1A	CX3CR1	ENTPD2	GFAP	GUSB	ITGA7	MAPK8	NFKBIB	PCSK2	PPP2R5E	RRAS	SORL1	TMEM119	
ARHGEF10	CACNA1C	CDS1	CXCL10	ENTPD4	GFPT1	HAP1	ITGAL	MAPK9	NGF	PDE1B	PPP3CA	RTN4	SOX10	TNC	
ARRB2	CACNA1D	CERS1	CXCL11	EP300	GGA1	HCN1	ITGAM	MAPKAPK2	NGFR	PDE4D	PPP3CB	RYR1	SOX9	TNF	
ARSA	CACNA1F	CERS2	CXCL12	EPHA2	GGT1	HDAC1	ITGAX	MAPT	NINJ2	PDGFRB	PPP3CC	RYR2	SP1	TNFRSF10A	
ASB7	CACNA1S	CERS4	CXCL16	EPHA3	GJB1	HDAC2	ITPR1	MARCO	NKX6-2	PDPK1	PPT1	RYR3	SP100	TNFRSF10B	
ATCAY	CACNB2	CERS6	CXCR4	EPHA4	GLRB	HDAC6	ITPR2	MBP	NLGN4X	PECAM1	PQBP1	S100B	SPAST	TNFRSF10D	
ATF4	CACNB4	CHAT	CXXC1	EPHA5	GLS	HDAC7	ITPR3	MEAF6	NLRP3	PFN1	PRF1	SART1	SPI1	TNFRSF11B	
ATF6	CADM3	CHD4	CYBB	EPHA6	GNAI1	HEXB	JAM3	MECP2	NMB	PGAM1	PRKAA2	SCAMP2	SPTBN2	TNFRSF12A	
ATG5	CADPS	CHL1	CYCS	EPHA7	GNAI2	HGF	JUN	MFN2	NME5	PGK1	PRKACA	SCN1A	SQSTM1	TNFRSF1A	

List of all 770 genes included in my NanoString analysis.

The nCounter® Human Neuropathology Panel features 760 genes targeting neurodegeneration and other nervous system diseases pathways, and 10 housekeeping genes for normalization.

Appendix B

B.1 Confirmed absence of markers that specify cell types other than glutamatergic neurons

I investigated the level of GFAP expression in these cultures and failed to find evidence of expression above limits of sensitivity using either RT-PCR or NanoString technologies. These observations are consistent with absence of astrocytes morphological observations in the cultures (Figure below). The nCounter® Human Neuropathology panel contained probes for markers of cell types other than glutamatergic neurons and they yielded mRNA counts that fell within background levels (crosslink to MATERIALS and METHODS where I describe NanoString background). For example, as shown in the figure in this Appendix, the astrocyte-specific genes, GFAP and GDPD2, the oligodendrocyte markers, SOX10 and BCAS1, the microglia markers, GPR84 and TMEM119, the endothelial associated genes, EMCN and CLDN5, and the inhibitory GABAergic interneurons markers: GAD65 and DXL1 all fell at or below the dotted line representing background threshold.

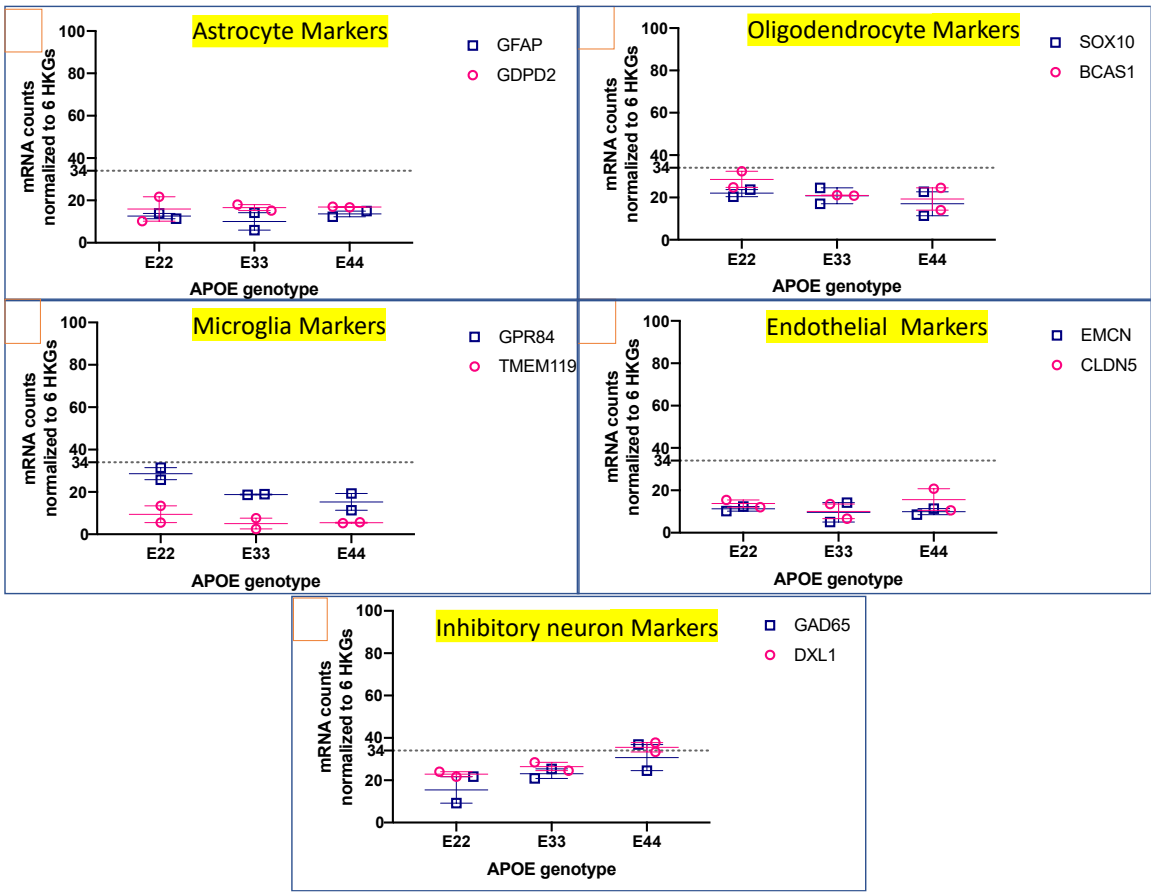

Genes specific for cell type other than glutamatergic neurons were not expressed.

Scatter plots of Nanostring mRNA counts of genes associated with other cell types show they were below the threshold of background of 34 mRNA molecules: (A) Astrocyte-specific genes: GFAP and GDPD2, (B) Oligodendrocyte markers: SOX10 and BCAS1 (C) Microglia markers: GPR84 and TMEM119 (D) Endothelial associated genes: EMCN and CLDN5 and (E) Inhibitory neuron markers: GAD65 and DXL1.

Appendix C

C.1 Raw counts of housekeeping genes in the NanoString

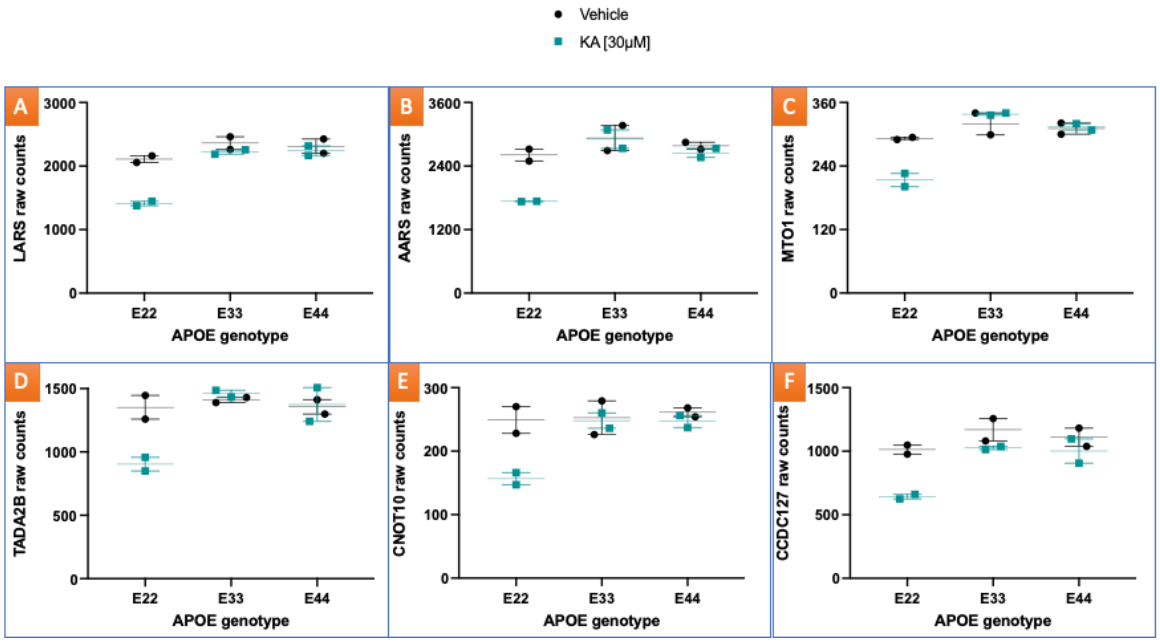

Raw counts of the housekeeping genes used to adjust the NanoString dataset.

Appendix D

D.1 Similar sensitivity and competency to induce FOS expression regardless of APOE genotype.

When considering the broader picture of the entire response pattern (indicated by “Yes” in the column asking whether the adjusted P value is small enough to pass “Below threshold?” set at 0.05), the remarkable similarity in response amongst the cultures treated with 30 µM was revealed further. According to the adjusted P values, significant activity first emerged at the same time point of 4 hours (and all displayed 4-fold induction of *FOS* over vehicle (blue shading)). This table further highlights, in yellow, that the cultures’ peak fold-changes from their vehicle-treated counterpart, were alike, at 7-, 8-, and 7-fold for the ε2, ε3, and ε4 cultures, respectively.

D.1.1 Holm-Sidak multiple comparisons for *APOE*-variant iN28s treated with kainate for FOS levels

[KA]	Genotype	Time (hour)	P value	Geometric mean of ratios	Adjusted P Value	Below threshold?
30 µM	APOE E2/E2	0.5	0.682365	0.9067	0.682365	No
		1	0.014951	1.926	0.058476	No
		2	0.03486	2.074	0.100976	No
		4	0.000656	**4.11**	**0.003929**	**Yes**
		6	0.005593	**6.691**	**0.027655**	**Yes**
		18	0.042936	1.86	0.100976	No
	APOE E3/E3	0.5	0.594439	0.8607	0.594439	No
		1	0.033593	1.756	0.127753	No
		2	0.051106	1.972	0.145616	No
		4	0.000722	**4.071**	**0.004323**	**Yes**
		6	0.001092	**8.289**	**0.00545**	**Yes**
		18	0.093672	1.739	0.17857	No
	APOE E4/E4	0.5	0.975738	0.9951	0.975738	No
		1	0.026803	1.901	0.078272	No
		2	0.015719	2.053	0.06141	No
		4	0.005878	**3.739**	**0.034754**	**Yes**
		6	0.007158	**7.184**	**0.035281**	**Yes**
		18	0.101372	2.802	0.192469	No
300 µM	APOE E2/E2	0.5	0.034405	0.5787	0.099704	No
		1	0.039979	1.72	0.099704	No
		2	0.142527	1.525	0.142527	No
		4	0.012472	5.638	0.060823	No
		6	0.01323	15.06	0.060823	No
		18	0.007268	3.293	**0.042823**	**Yes**
	APOE E3/E3	**0.5**	0.007409	0.5669	**0.0365**	**Yes**
		1	0.071545	1.557	0.13797	No
		2	0.158782	1.588	0.158782	No
		4	0.012122	6.178	0.047614	Yes
		6	0.016151	22.64	**0.047675**	**Yes**
		18	0.004453	3.666	**0.026422**	**Yes**
	APOE E4/E4	0.5	0.094242	0.6817	0.178753	No
		1	0.093773	1.666	0.178753	No
		2	0.020856	1.763	0.067876	No
		4	0.013554	4.874	0.067876	No
		6	0.012816	14.43	0.067876	No
		18	0.011647	4.753	0.067876	No

In the bottom half of the table that pertains to the 300 µM KA versus vehicle treatments, satisfactorily, individual P values were significant in all cases at least 4 hours of treatment and later. This table also iterates that, like the 30 µM KA time course, the peak FOS induction over vehicle-treated conditions occurred at 6 hours. Induction at the higher concentration was of a higher magnitude, at 15-, 23-, and 14-fold for the ε2, ε3, and ε4 cultures, respectively. Interestingly, adjusted P values in the 300 µM response curve, when the overall time course was considered lost the 4-hour statistical significance for all allele-variant cultures, and the 6-hour significance for ε2 and ε4 neurons. APOE ε2 neurons showed significance at only 18 hours; ε3 neurons showed significant reduction of FOS at 0.5 hours and significant increases at 6 and 18 hours (pink shading); ε4 neuronal responses did not become significant at any point.

Put simply, FOS is induced to a significant level at 4 and 6 hours in the 30µM situation and in the 300µM condition the induction was noisier. Nonetheless, there was not difference in the relative induction when compared across ApoE-variant cultures. This highlights the similar sensitivity and competency to induce FOS expression regardless of genotype.

Appendix E

E.1 Material and Methods pertaining to SH-SY5Y cellular model building (0)

E.1.1 HEK293 and SH-SY5Y immortalized cell lines

The immortalized lines were SH-SY5Y (Sigma-Aldrich, catalog # 94030304) and HEK293 (American Type Culture Collection (ATCC) catalog # CRL-1573).

E.1.2 HEK293 and SH-SY5Y cell line maintenance

HEK293 and SH-SY5Y cell lines were grown in Dulbecco's Modified Eagle Medium (DMEM) supplemented with 10% heat-inactivated fetal bovine serum (FBS) and 2mM GlutaMax, in an atmosphere of 5% CO2 and 37°C. Cells were sub-cultured every 4 to 5 days when they reached about 80% confluence. Sub-culturing was performed by aspirating and discarding growth medium, washing the cells once with phosphate-buffered saline (PBS), incubating in 0.25% Trypsin-EDTA for approximately 3 minutes until cells visibly detached from culture vessels, then, inactivating trypsin with fresh DMEM 10% FBS. The cells were resuspended via trituration with a 10 mL serological pipette to achieve homogeneous cell suspensions then reseeded into fresh DMEM 10% FBS in T75 flasks at a 1:10 ratio of cell suspension to medium.

E.1.3 Neuronal differentiation of SH-SY5Ycells

I differentiated SH-SY5Y cells using a protocol modified from Shipley *et al.* (2016) (234). This was conducted over a 2-week timeframe, outlined in Figure E.1.4. On day 0, freshly dissociated cells from ~80% confluent T175 flasks were dissociated into single cells and counted using an automated cell counter (Countess™ II Automated Cell Counter from ThermoFisher Scientific). These were seeded at a density of 6 x 10^5 cells per plate in 100mm dishes in full growth/maintenance media (DMEM 10% FBS). The following day (day 1 of differentiation), all the growth media was removed and replaced with “differentiation media #1” featuring low serum and retinoic acid (RA) (Figure E.1.4 with media recipes in Table E.1.5). On days 3 and 5, the media was fully refreshed by removing and adding again differentiation media #1. On day 7, cells were trypsinized and seeded into plates pre-coated with substrates permissible for neuronal growth; either poly-D-lysine (PDL) or collagen type IV, as indicated. When 96-well PDL-coated plates (Corning® BioCoat™ catalog # 354640) were used, cells were seeded at 4 x 10^4 cells/well into the

central, inner 36 wells with the outer edge wells filled with PBS. When 6-well PDL-coated plates (Corning™ BioCoat™ Poly-D-Lysine #354413) were used, cells were seeded at 1.2 x 10^6 cells/well. When 60mm collagen type IV-coated culture dishes (Corning® BioCoat™ Collagen IV catalog # 354416) were used, cells were plated at a density of 2.4 x 10^4 cells/dish. The plating medium on day 7 remained differentiation media #1. On day 8, the cells were switched to "differentiation media #2" (Figure E.1.4) in a single media change and this formulation was kept for the remainder of the life of the cultures. Representative morphological changes across culture period were documented using the EVOS FL imaging system (ThermoFisher Scientific).

a.

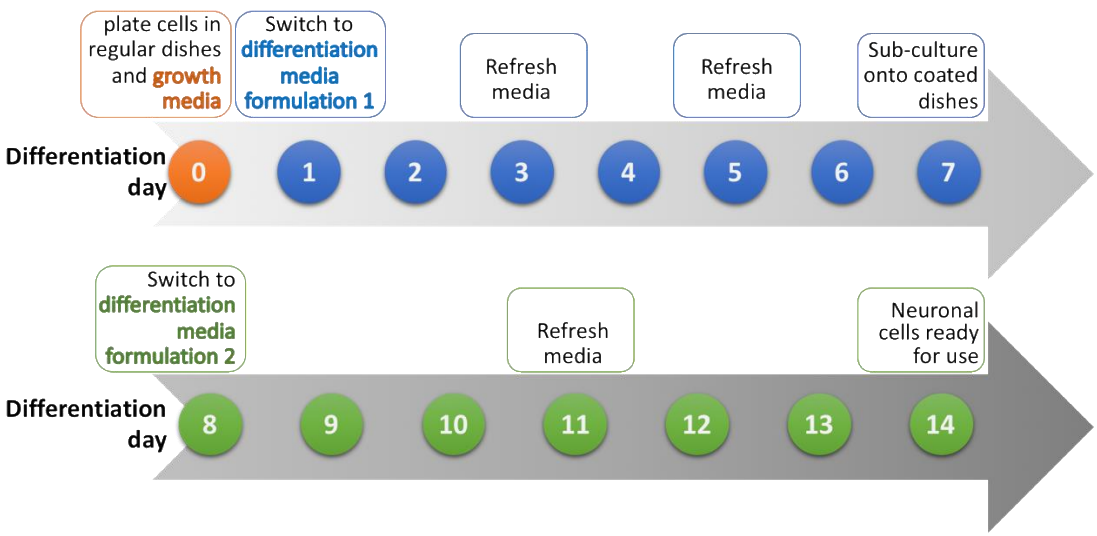

b.

Growth Media	Differentiation Media #1	Differentiation Media #2
DMEM	DMEM	Neurobasal media
fetal bovine serum (10%)	fetal bovine serum (2.5%)	B27 supplement (1x)
GlutaMax (2mM)	GlutaMax (2mM)	GlutaMax (2mM)
	retinoic acid (RA) (10 µM)	retinoic acid (RA) (10 µM)
		KCl (20 mM)
		BDNF (50 ng/mL)
		dibutyryl cyclicAMP (2 mM)

E.1.4 Two-week neuronal differentiation paradigm for SH-SY5Y cells

Schematic depiction of the differentiation timeline highlighting the differentiation media formulation. (a) In Week 1 cells were plated in regular growth medium then, the next morning, were switched to differentiation media #1. At the start of Week 2 (day 8), split cells were placed onto permissible substrate-coated plates, in differentiation media #2. (b.) The sequential exposure to key differentiation factors during the cultural timeline is shown.

E.1.5 Differentiation media recipes and components for SH-SY5Y cells

Differentiation Media #1 (modified from differentiation media #1, Shipley at al.(86))		
Component	**Final Concentration**	**Source (catalog #)**
DMEM (Dulbecco's Modified Eagle Medium)	n/a	ThermoFisher Scientific (11965084)
Fetal Bovine Serum (FBS)	2.5%	ThermoFisher Scientific
Gibco® GlutaMAX™ (100x stock)	2 mM	ThermoFisher Scientific (35050-061)
all trans-retinoic acid (5mM stock dissolved in DMSO; stored in single-use aliquots at -80°C)	10 µM	Sigma (R2625)
Differentiation Media #2 (modified from differentiation media #3, Shipley at al.)		
Component	**Final Concentration**	**Source (catalog #)**
Neurobasal™ Medium	n/a	ThermoFisher Scientific (21103-049)
B-27 Supplement (50X stock)	1x	ThermoFisher Scientific (17504-044)
KCl, 1M solution	20 mM	Millipore (60142)
Gibco® GlutaMAX™ (100x stock)	2 mM	ThermoFisher Scientific (35050-061)
all trans-retinoic acid (5mM stock dissolved in DMSO)	10 µM	Sigma (R2625)
BDNF (human) reconstituted in sterile water at 100µg/ml which and aliquots out and stored at -20°C.	50 ng/ml	Tocris (2837)
dibutyryl cyclic AMP (db-cAMP) (1M stock dissolved in media)	2 mM	StemCell (73882)

E.1.6 Commercial source of purified ApoE protein

Purified recombinant ApoE protein, generated in both bacterial and mammalian expression platforms, was purchased from PeproTech or Origene (Table E.1.7).

E.1.7 Commercial sources of purified recombinant apoE

Description	Expression Host	Final Treatment Concentration	Commercial source (catalog #)
Recombinant apoE2	Escherichia coli (E. coli)	10 µg/mL	Sigma-Aldrich (SRP4760)
Recombinant apoE3	Escherichia coli (E. coli)	10 µg/mL	Sigma-Aldrich (SRP4696)
Recombinant apoE4	Escherichia coli (E. coli)	10 µg/mL	Sigma-Aldrich (A3234)
Recombinant apoE2	Escherichia coli (E. coli)	10 µg/mL	PeproTech (350-12)
Recombinant apoE3	Escherichia coli (E. coli)	10 µg/mL	PeproTech (350-02)
Recombinant apoE4	Escherichia coli (E. coli)	10 µg/mL	PeproTech (350-04)
Recombinant apoE3	HEK293T	10 µg/mL	Origene (TP300395)

E.1.8 Conditioned media from HEK293 overexpression system as source of ApoE

As an alternate to commercially sourced ApoE, I transfected HEK293 with plasmids expressing ApoE of the indicated genotype. I developed mammalian expression DNA vectors in collaboration with GenScript USA Inc (Piscataway, NJ). I selected the APOE3 open reading frame clone (ORF apoE clone ID OHu27296 based on accession number NM_000041) and directed the company to insert this sequence into the multiple cloning site of the pcDNA3.1+/C-(K)DYK base expression vector to create the apoE3 plasmid. Figure E.1.9 diagrams the empty vector where “ORF”

designates the insertion site of the APOE nucleotide sequence wherein the expressed protein would be generated with a FLAG tag at its c-terminus. This backbone was used to engineer the C/T nucleotide base switches in their APOE3 clone according to the positions highlighted in Figure E.1.10. Using a similar approach, APOE2 and APOE4 FLAG-tagged expression cDNA constructs were made. The plasmids, listed in Table E.1.11, were delivered as purified transfection-ready DNA at 1 µg/mL in Tris-EDTA (TE) buffer. These were subjected to in house DNA sequencing (Biogen) which confirmed the authenticity of these constructs (data not shown).

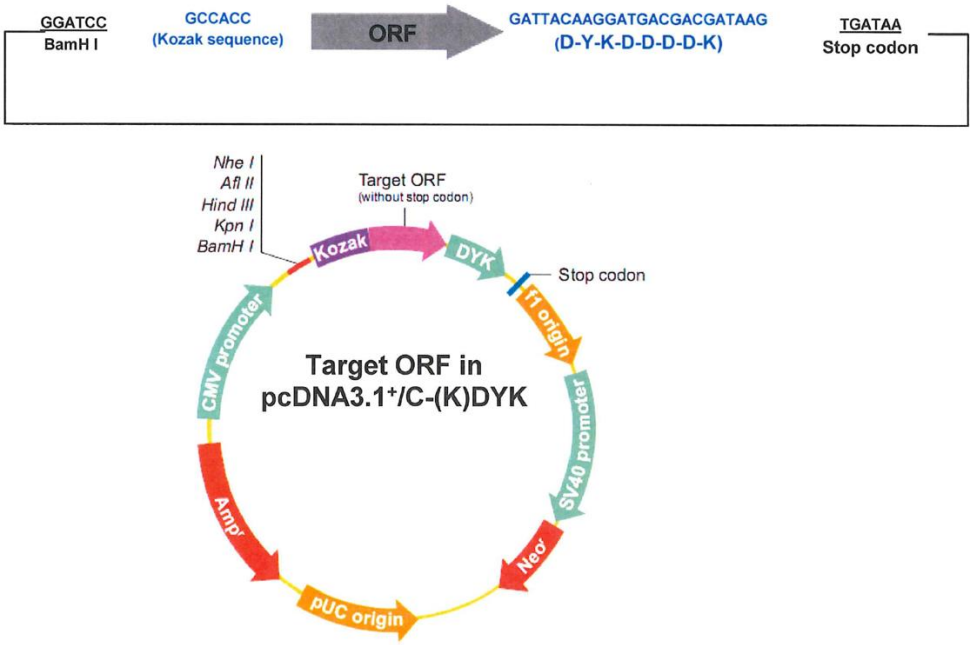

E.1.9 Diagram of the DNA vector backbone for APOE expression vector construction.

The APOE cDNA nucleotide sequences of the designated APOE variants were inserted in the region labelled ORF (open reading frame) of the cloning site.

```
APOE4     ACCCCGGTGGCGGAGGAGACGCGGGCACGGCTGTCCAAGGAGCTGCAGGCGGCGCAGGCC
APOE2     ACCCCGGTGGCGGAGGAGACGCGGGCACGGCTGTCCAAGGAGCTGCAGGCGGCGCAGGCC
APOE3     ACCCCGGTGGCGGAGGAGACGCGGGCACGGCTGTCCAAGGAGCTGCAGGCGGCGCAGGCC
          ************************************************************

APOE4     CGGCTGGGCGCGGACATGGAGGACGTGCGCGGCCGCCTGGTGCAGTACCGCGGCGAGGTG
APOE2     CGGCTGGGCGCGGACATGGAGGACGTGTGCGGCCGCCTGGTGCAGTACCGCGGCGAGGTG
APOE3     CGGCTGGGCGCGGACATGGAGGACGTGTGCGGCCGCCTGGTGCAGTACCGCGGCGAGGTG
          ****************************^*******************************

APOE4     CAGGCCATGCTCGGCCAGAGCACCGAGGAGCTGCGGGTGCGCCTCGCCTCCCACCTGCGC
APOE2     CAGGCCATGCTCGGCCAGAGCACCGAGGAGCTGCGGGTGCGCCTCGCCTCCCACCTGCGC
APOE3     CAGGCCATGCTCGGCCAGAGCACCGAGGAGCTGCGGGTGCGCCTCGCCTCCCACCTGCGC
          ************************************************************

APOE4     AAGCTGCGTAAGCGGCTCCTCCGCGATGCCGATGACCTGCAGAAGCGCCTGGCAGTGTAC
APOE2     AAGCTGCGTAAGCGGCTCCTCCGCGATGCCGATGACCTGCAGAAGTGCCTGGCAGTGTAC
APOE3     AAGCTGCGTAAGCGGCTCCTCCGCGATGCCGATGACCTGCAGAAGCGCCTGGCAGTGTAC
          ********************************************^***************

APOE4     CAGGCCGGGGCCCGCGAGGGCGCCGAGCGCGGCCTCAGCGCCATCCGCGAGCGCCTGGGG
APOE2     CAGGCCGGGGCCCGCGAGGGCGCCGAGCGCGGCCTCAGCGCCATCCGCGAGCGCCTGGGG
APOE3     CAGGCCGGGGCCCGCGAGGGCGCCGAGCGCGGCCTCAGCGCCATCCGCGAGCGCCTGGGG
          ************************************************************
```

E.1.10 Base pair changes to generate APOE2 and APOE4 from the APOE3 ORF.

Mutagenesis of the purchased APOE3 cDNA ORF was performed at the highlighted C/T positions to convert it to the APOE2 and APO4 sequence variants (full length sequences not shown).

E.1.11 Expression plasmids for overexpressing ApoE in HEK293 cells.

Plasmid Name	Working Name	Molecular Description	Function
pcDNA3.1+/C-(K)DYK	Empty vector	Base mammalian expression vector with FLAG tag (Figure 2.2)	Control plasmid for preparing control CM
APOE(NM_000041)_pcDNA3.1+/C-(K)DYK	APOE3-FLAG	APOE(NM_000041) ORF inserted into MCS of pcDNA3.1+/C-(K)DYK	APOE3 expression vector for preparing CM
APOE2_pcDNA3.1+/C-(K)DYK	APOE2-FLAG	APOE(NM_000041) ORF converted to APOE2 variant sequence then cloned into MCS of pcDNA3.1+/C-(K)DYK	APOE2 expression vector for preparing CM
APOE4_pcDNA3.1+/C-(K)DYK	APOE4-FLAG	APOE(NM_000041) ORF converted to APOE4 variant sequence then cloned into MCS of pcDNA3.1+/C-(K)DYK	APOE4 expression vector for preparing CM

APOE plasmids designed to generate HEK293 ApoE protein secreted in the media upon transfection. ORF: open reading frame; MCS: multiple cloning site; CM: conditioned medium.

E.1.12 Transfection of HEK293 cells to produce ApoE conditioned media

HEK293 cells were transfected using the Amaxa™ 4D-Nucleofector™ system (Lonza). Freshly trypsinized cells were washed with PBS, 1.0 x 10^6 cells were aliquoted into a 50mL conical flask and pelleted by centrifugation then resuspended in 100 µL SF 4D nucleofector solution (SF Cell Line 4D-Nucleofector™ X Kit; Lonza Cologne GmbH) and 2 µg of the indicated DNA plasmid was mixed in. Cells were pulsed using program CM-130 in a 100 µL Nucleovette™ then immediately

plated in a 6-well dish in pre-warmed growth media. After cells were attached, the growth medium was fully replaced with media that contained 2%, instead of 10%, FBS.

Approximately 48 hours after transfecting the HEK293 cells with APOE plasmids, conditioned media was collected, filtered (Sigma-Aldrich catalog #CLS431153) and applied to SH-SY5Y cells. A portion of the filtered media was reserved and ApoE protein levels of this conditioned medium was assayed using a human ApoE amplified luminescent proximity homogeneous assay linked immunosorbent assay (alphaLISA®) detection kit (PerkinElmer Inc.) (Section E.1.19).

E.1.13 Treatment of SH-SY5Y with exogenous ApoE

For ApoE treatments in their undifferentiated state, SH-SY5Y cells were plated at either at 1.2 x 10^6 cells/well in a 6-well format or 4.0 x 10^4 cells/well in a 96-well format. The next day the media was switched to serum-free medium (DMEM lacking FBS). ApoE treatments occurred after 24 hours of serum starvation.

For ApoE treatments in the neuronal differentiated state, at differentiation day 8 (Figure E.1.4), SH-SY5Y cells were plated onto permissive substrate-coated plates at the indicated density for each format. For 6-well formats, cells were plated at 1.2 x 10^6 cells/well and for 96-well formats, cells were seeded at 4.0 x 10^4 cells/well, and for 60 mm dishes cells were seeded at 2.4 x 10^6 per dish. Once the 2-week differentiation period was achieved, differentiated cells were maintained in the final differentiation media, with media changes every 3 days, until use in ApoE signaling induction experiments. Two hours before ApoE treatments, media was switched to Neurobasal Medium that did not contain other additives.

Indicated isoforms and source of the ApoE was applied to SH-SY5Y cultures. These were either purified protein from commercial sources (Section E.1.6) or conditioned medium taken from HEK293 cells that overexpressed and secreted ApoE (Section E.1.8). The indicated purified ApoE was spiked into the existing SH-SY5Y media to a final concentration of 10 µg/mL for the indicated timepoints. Alternatively, 7-fold volume of ApoE conditioned media was added onto wells containing 1 volume of existing media (For example, in a 60 mm dish, all but 500µL of existing medium was removed then 3 mL of conditioned media was added). The final concentration of ApoE in the conditioned medium treatments ranged from 6 to 10 ng/mL.

E.1.14 Treatment of SH-SY5Y with PMA

Phorbol-12-myristate-13-acetate (PMA) (Cell Signaling Technology) was resuspended in dimethyl sulfoxide (DMSO; from ATCC) to make 200µM stocks that were stored at -20°C. These were added

to cultures to give a 200 nM final concentration for the indicated periods of time. These incubations acted as positive controls for confirming the test system's ability to respond with downstream kinase activation (MAPK).

E.1.15 Western blot to detect activation of Erk1/2 signaling

SH-SY5Y cells (Section E.1.1) were washed with cold PBS and kept on ice. Cells were then harvested with ice-cold radio-immunoprecipitation assay (RIPA) buffer (Sigma-Aldrich; catalog # R0278) supplemented with a protease and phosphatase inhibitor cocktail (HaltTM Protease and Phosphatase Inhibitor Cocktail; ThermoFisher catalog # 78444). Lysis reactions were vortexed 3 times over a 10-min incubation period on ice then centrifuged at 10,000 × g for 15 minutes at 5°C. Supernatants were transferred to pre-cooled microcentrifuge tubes while the pellets containing RIPA-insoluble material were discarded.

E.1.16 Total protein quantification

Total protein concentrations in the clarified lysates were determined using a bicinchoninic acid assay kit (Pierce BCA Protein Assay Kit; ThermoFisher catalog # 23225) according to the manufacturer's instructions.

E.1.17 Polyacrylamide electrophoresis (SDS-PAGE) and Western blotting

Twenty µg of lysate protein was diluted into NuPAGE LDS sample loading buffer (Thermo Scientific; catalog # NP0007) supplemented with 100 mM Dithiothreitol (DTT) (Thermo Scientific; catalog # A39255) and resolved via SDS-PAGE through 4-12% Bis-Tris polyacrylamide gels (Thermo Fisher Scientific). After electrophoresis, protein was transferred using the iBlot system to a polyvinylidene difluoride (PVDF) membrane of 0.2-µm pore size (Thermo Scientific; iBlot Transfer Stacks). Membranes were blocked with blocking buffer (Licor cat# 927-60001) for 1 hour at room temperature. Primary antibodies were then diluted to the indicated working dilution (Table E.1.18) in blocking buffer with 0.2% Tween 20 and incubated on the blots overnight at 4°C with gentle shaking. Membranes were then washed 3 times in washing buffer (TBS-T 0.1% Tween 20), incubated in secondary antibodies for 1 hour at room temperature, then washed 3 times in washing buffer. Antibodies and dilutions are shown in (Table E.1.18).

Immunoreactivity was quantified by dual-channel scanning and detection of infrared signal from the infrared-labeled secondary antibodies (IRdye 800 and IRdye 680) using an Odyssey Infrared Imager CLX (LI-COR Biosciences). The average background around individual Western blot bands was subtracted using Image Studio software (LI-COR Biosciences) and background-corrected

signal intensity values were graphed with Prism 7 software (GraphPad, CA, USA). Target phosphoprotein signals were normalized to total protein signals probed on the same blots.

E.1.18 Antibody information

Antibody	Source (catalog #)	Application	Stock Concentration	Working Dilution	Incubation time (temperature)
anti-phospho-pErk1/2 (Thr202/Tyr204)	Cell Signaling Technology (4696)	Immunoblot	94.0 µg/ml	1:1000	overnight (4°C)
anti-Erk1/2	Cell Signaling Technology (4695)	Immunoblot		1:1000	overnight (4°C)
IRDye® 800 anti-mouse IgG	LiCor (926-32210)	Immunoblot	1.0 mg/mL	1:20,000	1 hour (room temp)
IRDye® 680 anti-rabbit IgG	LiCor (926-68021)	Immunoblot	1.0 mg/mL	1:20,000	1 hour (room temp)
anti-Tubulin β 3 (TUBB3; TUJ1)	BioLegend (801202; previously, Covance # MMS-435P)	Immunocytochemistry	1.0 mg/ml	1:1000	overnight (4°C)

E.1.19 AlphaLISA quantification of apoE

ApoE was quantified using a bead- and proximity-based amplified luminescent proximity homogeneous assay-linked immunosorbent assay (alphaLISA). The ApoE alphaLISA kit (PerkinElmer, USA) utilizes antibodies against different epitopes on ApoE and which are conjugated with either biotin or alphaLISA acceptor beads. The anti-ApoE acceptor beads and the biotinylated anti-ApoE antibodies were independently diluted in assay buffer to a concentration of and 25 µg/mL and 2.5 nM, respectively. Just prior to use, equal volumes of the diluted antibodies were mixed and 10 µL of this antibody mix was added to each well of a 384-well plate. Conditioned media and standard controls (2.5 µL of each) were added per well and plates were incubated for 1 hour. Streptavidin donor beads were freshly diluted in assay buffer (80 µg/mL) and 12.5 µL was added to each well and plates were incubated in the dark for 30 minutes. All incubations were performed at room temperature and plates were read using an EnVision® Reader (PerkinElmer). An apoE calibration curve was generated using the optical density values from serially diluted human ApoE protein which was provided in the kit. The concentration of ApoE in the experimental samples were extrapolated from this standard curve.

Appendix F

F.1 Investigating the SH-SY5Y cell model of neurons as a probe to APOE sensitivity

I questioned whether the SH-SY5Y neuroblastoma cell line would prove a useful model for investigating the contribution of neuron-expressed ApoE variants in the context of neurodegeneration. Therefore, I modelled a set of experiments to explore whether this cell line would recapitulate ApoE mediated changes that Huang et al. (2017) reported for ESC derived neurons (132). The APOE genotype of SH-SY5Y cells is E3/E3 (235). After characterization, if I deemed these cells suitable for building the model platform, I expected to then engineer their genome to generate derivative lines expressing the additional distinct APOE genotypes of interest.

F.2 Investigation of ApoE responsivity in undifferentiated SH-SY5Y cells

I focused my initial experiments on undifferentiated SH-SY5Y cells.

F.2.1 Assessment of ApoE-mediated induction of *APP* transcription

I treated SH-SY5Y cultures with a concentration range (1, 3, 10, and 30 μg/mL) of exogenous ApoE variants for 24 and 48 hours then assessed the effect on *APP* transcription using RT-PCR methods. *APP* levels were normalized to the reference, housekeeping gene, Glyceraldehyde-3-Phosphate Dehydrogenase (GAPDH), then represented as fold-change from the average of all vehicle-treated baseline controls. *APP* mRNA was detected in all samples and ApoE treatment did not alter their relative levels in a clear concentration dependent manner (Figure F.2.2).

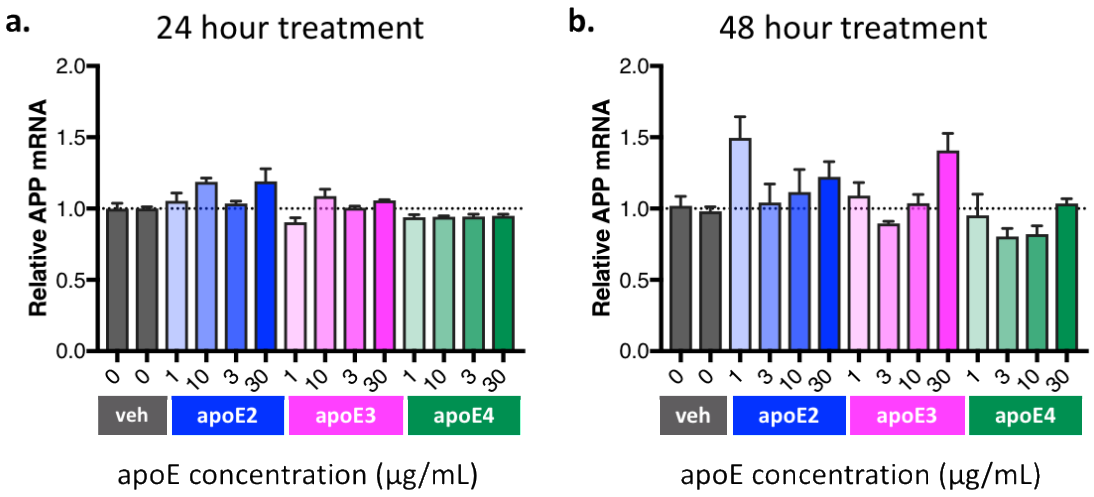

F.2.2 *APP* transcript levels upon 24- and 48-hour exposure to ApoE

SH-SY5Y cells were treated with indicated concentrations 3 ApoE isoforms for 24 (a) and 48 (b) hours. *APP* transcript levels are graphed relative to the vehicle control wells. Error bars are SEM from 3 wells from a 96-well sample.

I repeated this experiment using new ApoE reagents sourced from a different manufacturer. The results of the second independent experiment were like those of the first in that no effect on *APP* mRNA levels was detected subsequent to ApoE exposures (Appendix A). In the second experiment I had included a retinoic acid (RA) treatment arm to serve as a positive control. While RA induced *APP* transcript levels after 48 hours by 2-fold, it showed no effect at the 24-hour timepoint (Appendix A) thus was not a robust inducer of *APP* transcription. I next decided to switch to a different method (also used by Huang *et al.*) for monitoring responsivity to ApoE.

F.2.3 Assessing ApoE-mediated induction of ERK1/2 phosphorylation

I treated SH-SY5Y cells with 3 ApoE isoforms in a final concentration of 10 µg/mL then harvested them at 10-minute and 2-hour exposure time points. I then assessed ERK1/2 phosphorylation status by probing cell extracts with a phospho-specific antibody that detects p44 and p42 MAP Kinase (ERK1 and ERK2) when phosphorylated either individually or dually at Thr202 and Tyr204 of ERK1 (Thr185 and Tyr187 of ERK2). The antibody does not immunoreact with non-phosphorylated ERK1/2. I simultaneously subjected the blots to an antibody that detects total p44/42 MAP kinase (ERK1/ERK2) protein. Figure F.2.4 shows the Western blot results. Immunoreactivity of phospho-ERK1/2 (Thr202/Tyr204) (green) was normalized to that of total ERK1/2 (42 kDa/44 kDa; red). Normalized band intensities illustrated a lack of phosphorylation response upon ApoE treatments as the signals from all ApoE treated wells did not differ from those of baseline conditions (Figure F.2.4; b). Baseline levels of phospho-ERK1/2 were

demonstrated by PBS and DMSO neutral and vehicle controls, respectively. Treatment with the positive control, PMA [200 nM], indicated the system could mount a response as phosphorylation levels increased 6-fold (10 min) and 4-fold (2 hours) above baseline (Figure F.2.4; b).

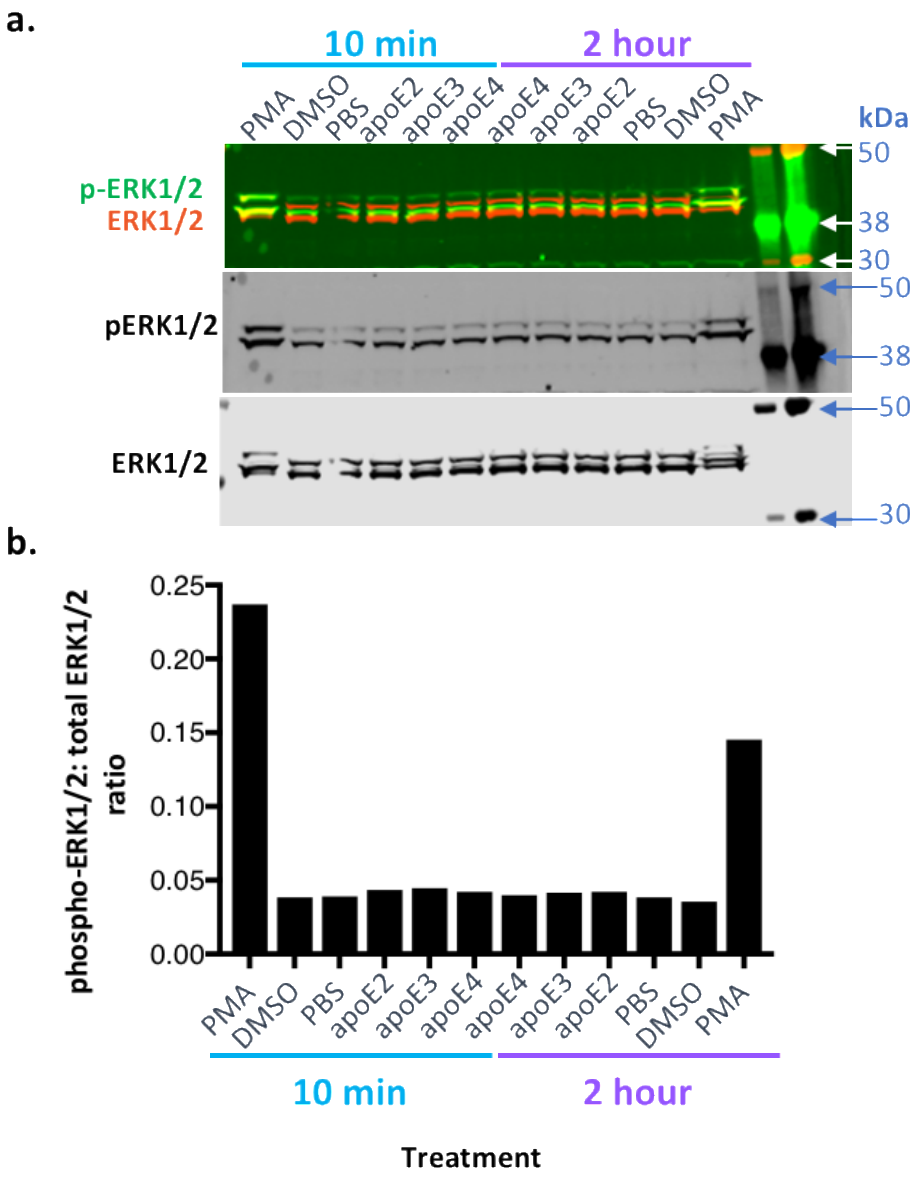

F.2.4 Western blot analysis of phosphorylated ERK1/2 after ApoE treatment

(a) Immunoblot showing phospho-ERK1/2 (Thr202/Tyr204) (green) and total ERK1/2 (red) for undifferentiated SH-SY5Y cells treated with the 3 ApoE isoforms for 10 minutes and 2 hours. Each lane represents 1 well of a 6-well plate. PBS and DMSO showed baseline levels while PMA increased phosphorylation. (b.) Quantification of the bands was done by plotting the ratio of the signals from the phosphorylated- to the total-ERK1/2 bands.

Thus far, the recombinant ApoE I had been adding to the cells had been generated in *E. Coli*. I next obtained recombinant human ApoE3 generated in a mammalian-recombinant expression system (Section E.1.8) and used it to again treat undifferentiated SH-SY5Y cultures at a concentration of

10 µg/mL for 10 minutes and 2 hours. I subsequently evaluated ERK1/2 phosphorylation in a similar manner as I did before. The result, seen in Figure F.2.5, was similar to what I originally observed, despite having switched the ApoE3 reagent. ApoE3 did not induce a detectable ERK1/2 phosphorylation response at either 10 minutes or 2 hours of administration (meanwhile, PMA yielded 4- and 3-fold increased phosphorylation at 10 minutes and 2 hours, respectively).

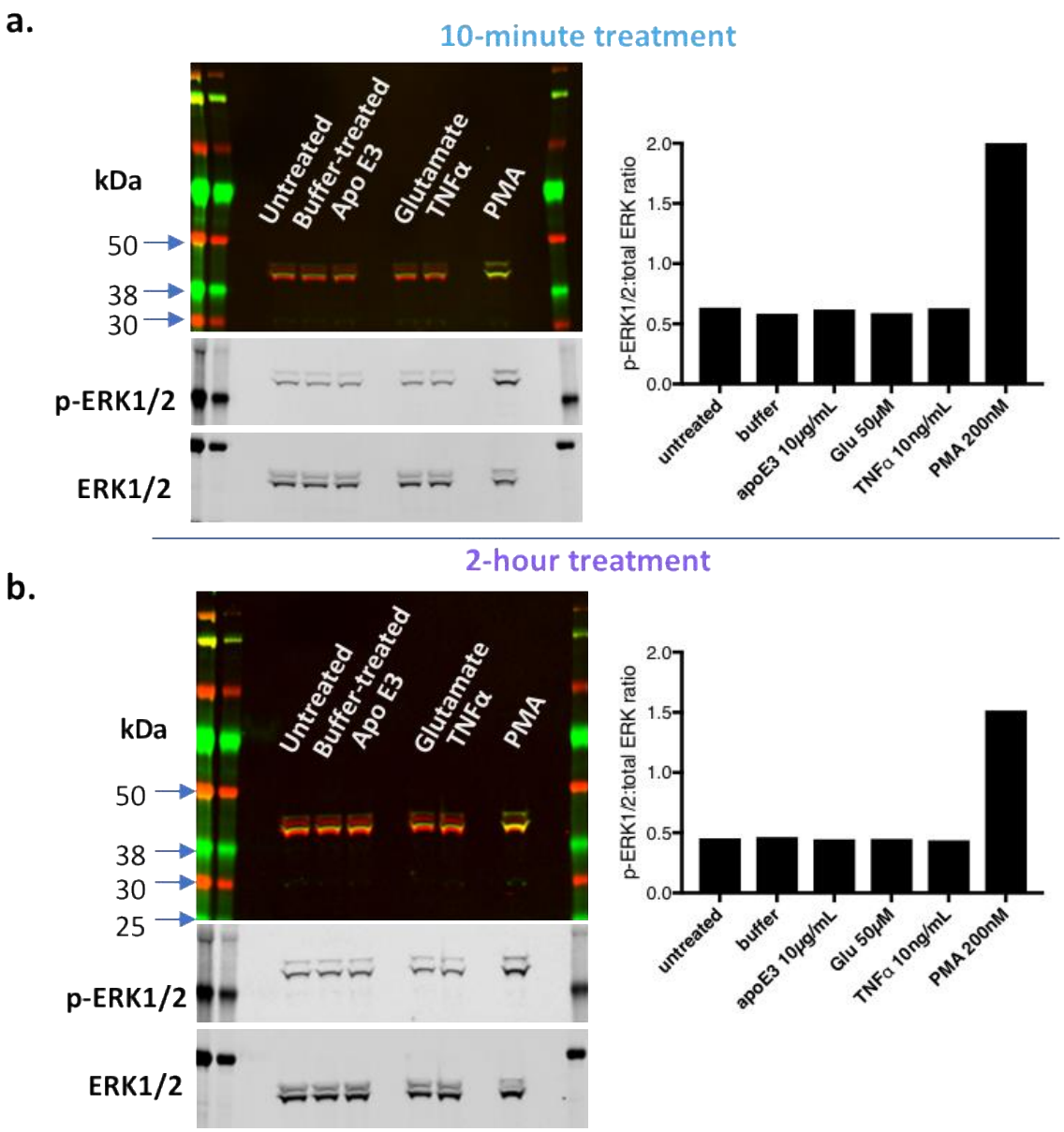

F.2.5 Undifferentiated SH-SY5Y treated with mammalian recombinant ApoE3

Immunoblots of phospho-ERK1/2 (Thr202/Tyr204) (green) and total ERK1/2 (red) for undifferentiated SH-SY5Y cells treated with mammalian-recombinant ApoE3. Each lane represents 1 well of a 6-well plate. Untreated and buffer (PBS) treated samples were baseline controls and PMA-treated samples were the positive controls. Graphs show quantification of the bands on the left. Panel (a) shows a 10-minute treatment while (b) shows a 2-hour treatment time point.

I next designed my own ApoE isoform expression plasmids and contracted an outside research organization to perform the molecular biology steps to build them. I received 4 transfection-ready DNA plasmids (representing 3 ApoE isoforms and a control empty-vector plasmid) (Section E.1.8). When I transfected them into HEK293 cells, I noted that the different ApoE plasmids did not elicit any gross effects in the HEK293 cultures (Appendix B). I harvested conditioned media (CM) containing secreted ApoE (presumably lipidated though I did not have an assay to confirm this) from the HEK293 transfectants and applied this to undifferentiated SHSY5Y cells for 10-minute and 2-hour time points. I then analyzed ERK1/2 phosphorylation via Western blot in a similar manner as was performed earlier. No effect on ERK1/2 phosphorylation was evident at either the 10-minute (Figure F.2.6; a) or the 2 -hour (Figure F.2.6; b) treatments with the ApoE from HEK293 CM.

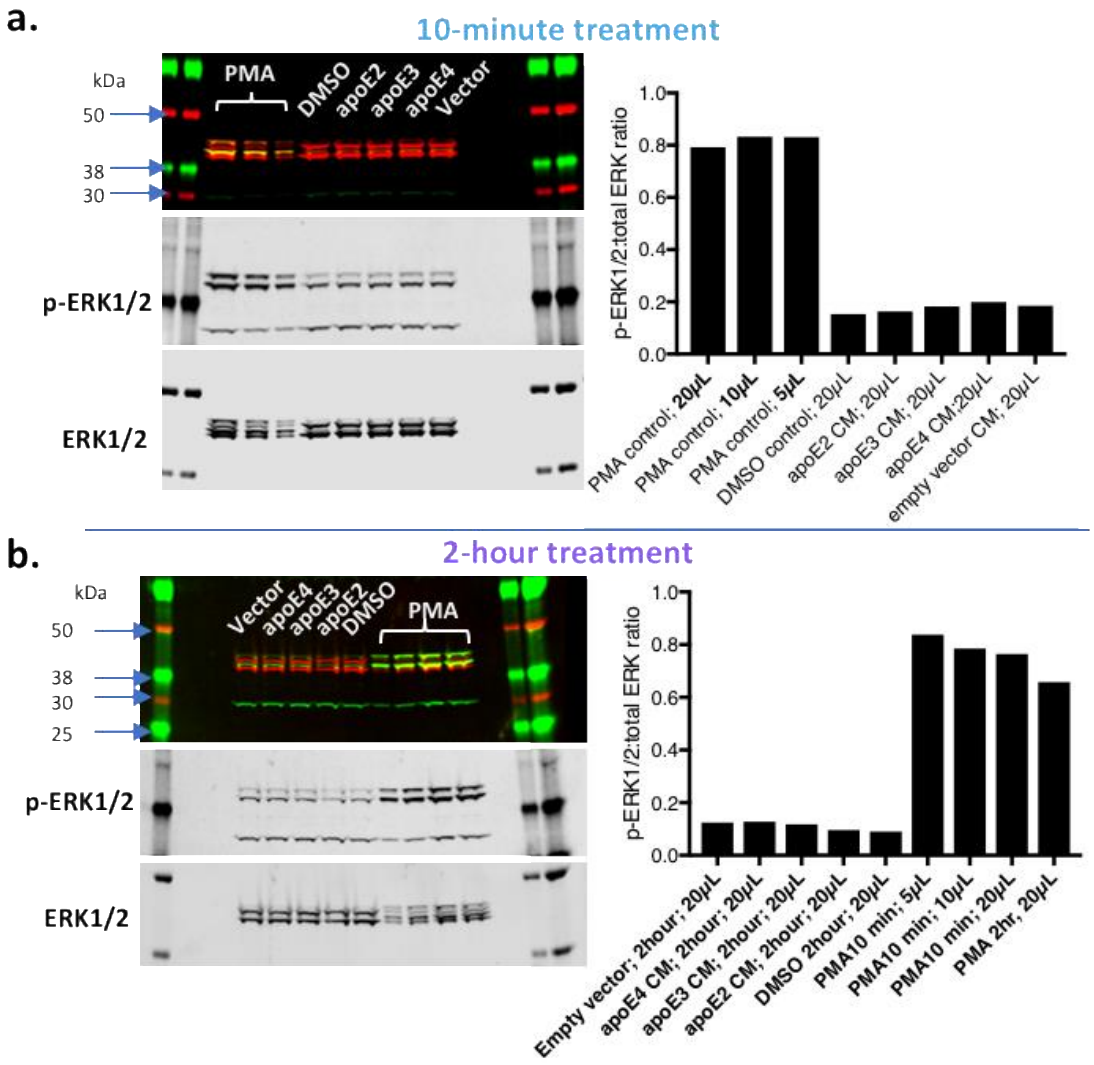

F.2.6 Western blot analysis of phospho-ERK1/2 after ApoE CM treatment

Immunoblots of phospho-pErk1/2 (Thr202/Tyr204) (green) and total ERK1/2 (red) for extracts from undifferentiated SH-SY5Y cells treated with the 3 mammalian-recombinant, secreted ApoE variants in the form of HEK293 ApoE CM. Each lane represents 1 well of a 6-well plate. DMSO (vehicle) and Empty Vector represent baseline controls and PMA [200 nM] samples were positive controls, loaded at varying amounts of extract (20, 10, and 5 µL). Graphs show quantification of the phosphorylation of the bands on its left. Panel (a) shows the 10-minute treatment (and is the same blot pictured in Figure F.2.7) while (b) shows the 2-hour treatment time point. The PMA-treated samples titrated by loading various amounts (µL), reported concordant pERK1/2:totalERK1/2 ratios.

In this iteration of the Western blot experiment, I had loaded varying amounts of the PMA [200nM] signal activation control lysate on the gels in order to verify that I was working within the linear range of quantification. The raw infra-red signals corresponding to the Western blot in Figure F.2.6 (panel a) are graphed Figure F.2.7. The serial dilution of 20, 10, and 5 µL PMA-treated lysate (corresponding to 20, 10, and 5 µg of total protein per lane, respectively) showed the expected stepwise reduction in signal strength, for both antibodies. The gel from this experiment

was stained for total protein and showed protein levels per lane corresponded with the dilution series, as well as indicated similar levels of total protein loading was the equivalent (20 µL; 20 µg) lanes across samples Appendix C.

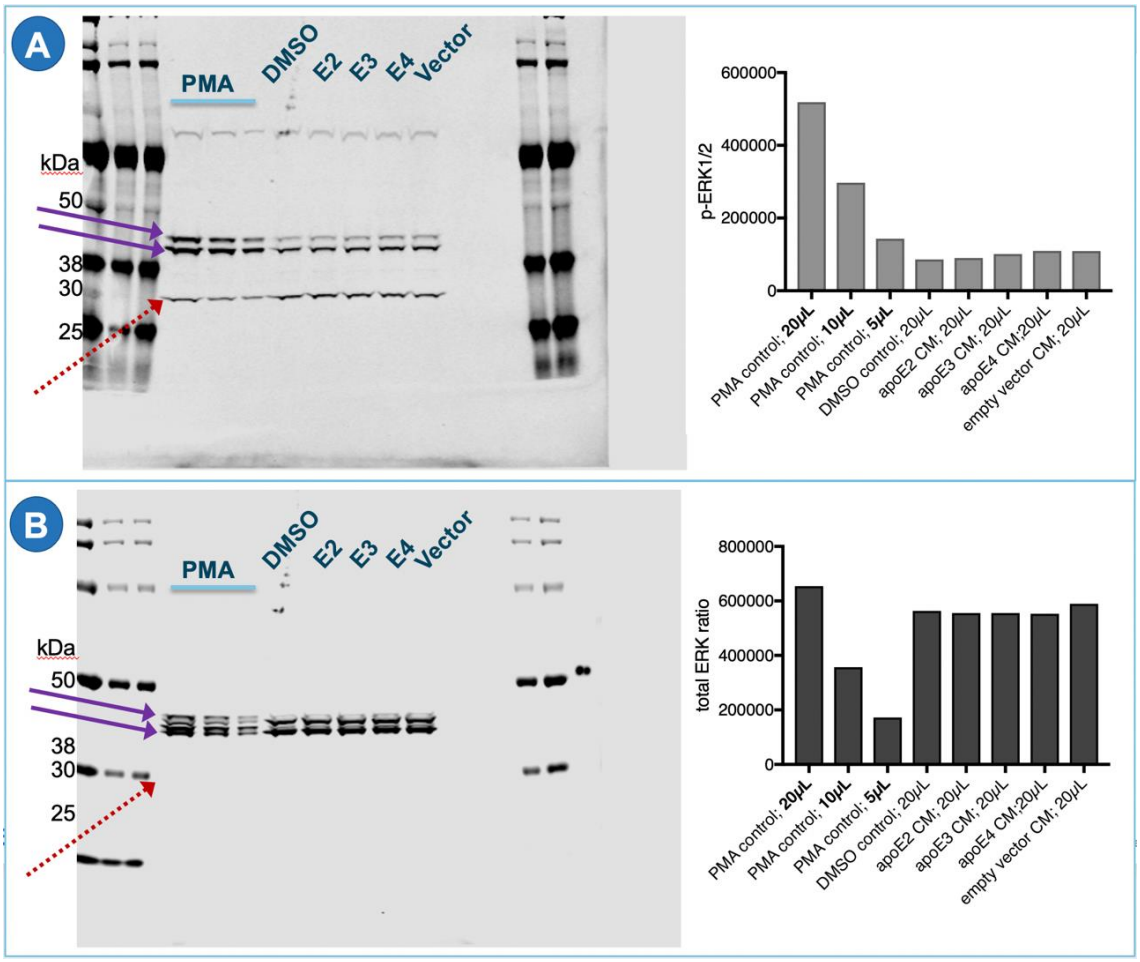

F.2.7 Raw infrared Western blot signals validate assay linearity

A range of PMA-treated samples was loaded (20, 10, and 5 µL) which corresponds to 20, 10, and 5 µg of total protein per lane. All other samples were loaded at 20 µL each (equivalent to 20 µg of total protein). For each antibody, corresponding raw infrared signal values were plotted in the graph to its the right. A. Immunoblot using a primary antibody that detects both phosphorylated and un-phosphorylated ERK1/2 (total ERK1/2) which yield 44 and 42 kDa banding pattern (solid arrows). The dotted arrow points to unspecific bands. B. shows the phosphorylated ERK1/2 protein (p-ERK1/2) result (arrows). The dotted arrow points to a blank area that corresponds to the blot in A.

F.2.8 ApoE levels in the CM from HEK293 transfectants

I next quantified ApoE levels within the treatment CM, using an alphaLISA assay (Section E.1.19). The ApoE2 concentration in my preparation was 12 ng/mL while the ApoE3 and ApoE4 concentrations were about 2-fold less, at 8 and 7 ng/mL, respectively (Figure F.2.9).

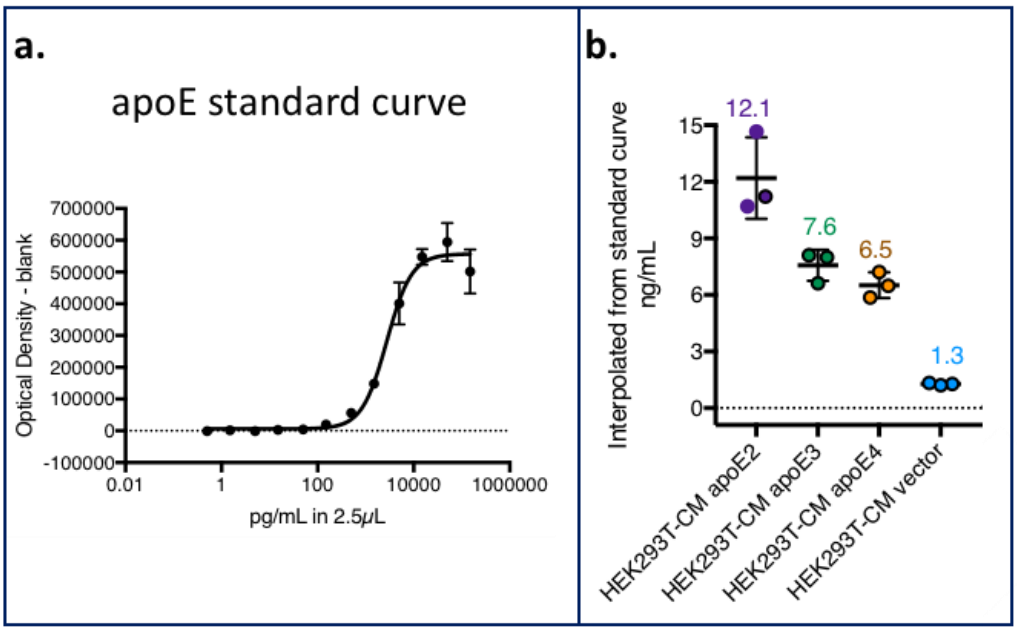

F.2.9 Quantification of ApoE in the CM from HEK293 transfectants

ApoE levels in the HEK293 conditioned media (CM) were determined via alphaLISA assay. A standard curve (a) allowed for interpolating absolute values for ApoE concentrations in the indicated preparations (b). Each point is a technical alphaLISA replicate from a single biological sample.

F.3 Investigation of ApoE responsivity in differentiated SH-SY5Y cells

Rather than trying to optimize secreted ApoE yields from HEK293 transfectants to then re-treat undifferentiated SH-SY5Y cells, I decided to test whether differentiated cultures would show responsivity to the various ApoE reagents I had by now amassed.

F.3.1 SH-SY5Y neuronal differentiation and characterization

I established a differentiation procedure based on reducing the serum content in the media and supplementation with RA and BDNF (236-241). My finalized differentiation paradigm, shown in Section E.1.3, was an optimized and accelerated version of an 18-day protocol which I modified into a 14-day workflow (234). As differentiation progressed, cultures no longer became confluent and did not require passaging, reminiscent of post-mitotic primary neuronal cultures thus suggesting cell proliferation became suppressed. In contrast, sister-plate controls maintained in the normal growth media, initially seeded at the same time with the same cell densities, continued becoming fully confluent at about every 5 days and required consistent passaging. By 10 days from the start of the differentiation procedure (Figure F.3.2), SH-SY5Ys adopted increased neuronal morphology evidenced by elongation and branching of neurites which also frequently

connected neighboring cells to form networks (Figure F.3.2; a). By day 15 from the start of the differentiation procedure, neurite extensions and network became even more elaborated taking on a pattern reminiscent of mature primary neuronal cultures (rodent) with which I have had extensive prior experience (Figure F.3.2; b).

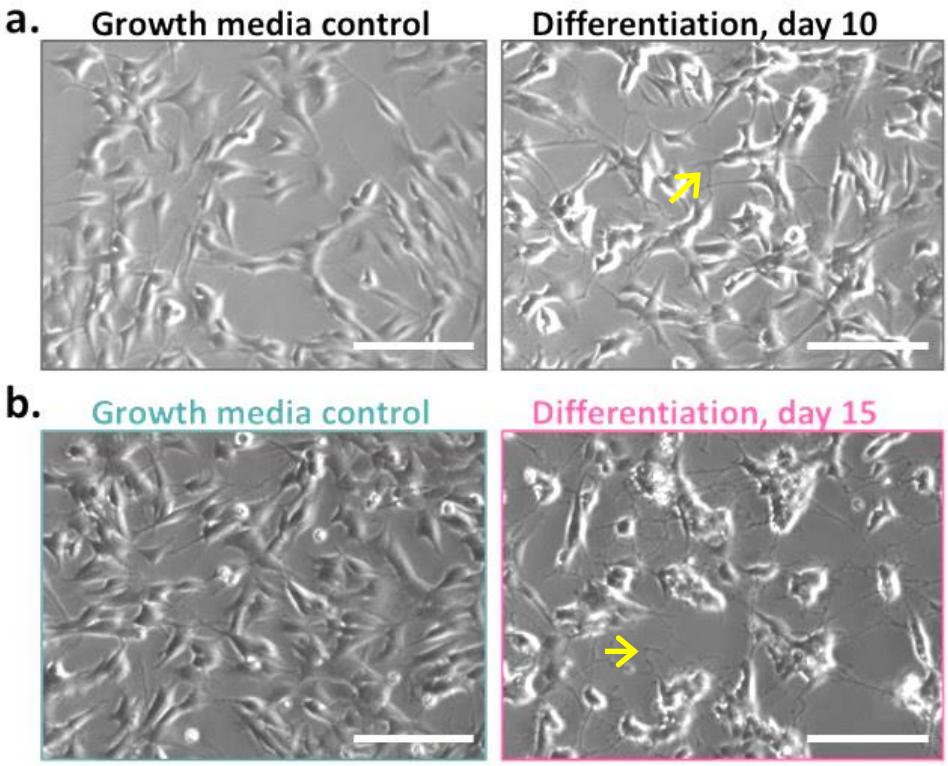

F.3.2 Differentiating SH-SY5Y cells

Phase-contrast micrographs illustrating SH-SY5Y cells displaying increased neuronal morphology over time. Morphology differences between parental cells and differentiated cells became evident by day 10. Compared to undifferentiated cells in regular growth media (a, left), neurites were more branched and elongated (yellow arrow) in cells exposed to differentiation media (a, right). By 15 days in differentiation media, compared to growth media conditions (b, left) neurites became even more elaborate (b, right, yellow arrow). (The growth media control cells had been passaged and re-plated between the 2 time-points pictured while in the differentiating conditions, cells did not become confluent over the 15-day period and were not passaged; indicating adoption of a post-mitotic nature). Scale bars=50 µm.

To independently ascertain that *bona fide* neuronal differentiation underpinned morphological transformation, I compared the mRNA expression level of typical neuron marker gene transcripts, as well as *APP* and MAPT, between cultures maintained in normal growth versus differentiation conditions. All transcriptional evaluations for the genes I chose to assess were performed using cells that were harvested at day 15 of neuronal differentiation which corresponds to Figure F.3.2, panel b.

MAPT and *APP* transcript levels both increased by at least 3-fold (Figure F.3.3). Synaptophysin (*SYP*) and synaptic vesicle glycoprotein 2B (*SV2B*) synaptic markers robustly increased by 10- and 90-fold, respectively (Figure F.3.3). The transcript encoded by the growth associated protein 43 (*GAP43*) gene increased 3-fold in differentiating cultures (Figure F.3.3). The microtubule associated protein 2 (MAP 2) gene transcript doubled in differentiated versus undifferentiated conditions (Figure F.3.3) while nerve growth factor receptor (NGFR) was upregulated by 12-fold (Figure F.3.3).

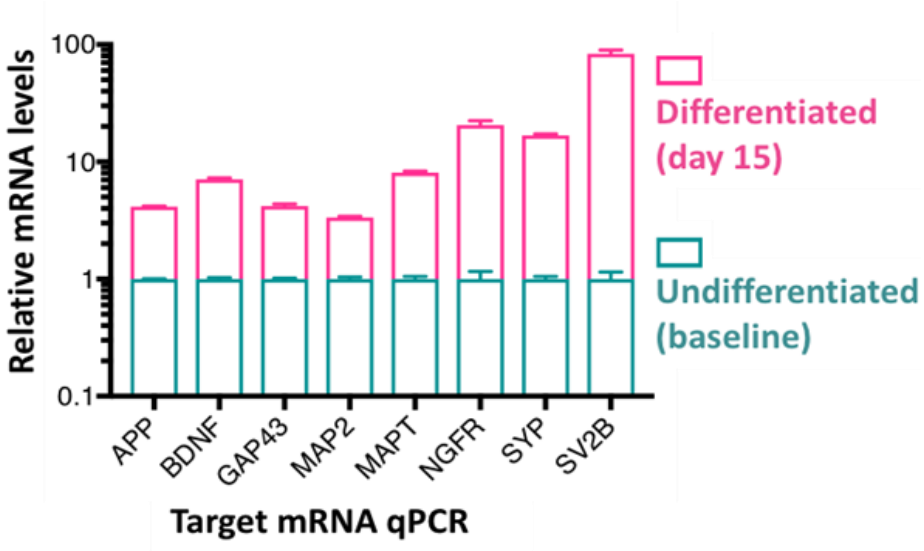

F.3.3 Differentiating SH-SY5Y cells showed enhanced neuronal transcriptional markers

Transcriptional profile of select neuronal markers using mRNA extracted from undifferentiated versus day 15 differentiated cells. Data is representative of 2 independent experiments. Each bar represents 4 technical RT-PCR replicates from a single culture dish (60mm plate) and error bars are SEM. Data are normalized to the housekeeping gene, GAPDH, then represented as fold-change from baseline (where baseline is defined as cells maintained in typical growth medium). *GAP43*: Growth Associated Protein 43; *MAP2*: Microtubule Associated Protein 2; MAPT: Microtubule Associated Protein Tau; NGFR: Nerve Growth Factor Receptor; *SYP*: Synaptophysin; *SV2B*: Synaptic Vesicle Glycoprotein 2B.

F.3.4 Assessing ApoE-mediated induction of phospho-ERK1/2

I next subjected differentiated SH-SY5Y cells to similar ApoE treatments used in the earlier undifferentiated contexts. For the 10-minute time point, I treated cells with *E. Coli* produced ApoE3 (n=2) and ApoE4 (n=1), each at 10 µg/mL (and 1 plate with the PMA control). For the 2-hour timepoint, I administered *E. Coli* produced ApoE3 (10 µg/mL), commercial, non-secreted HEK293 produced ApoE3 (10 µg/mL), my preparation of HEK293 produced, secreted ApoE3 (45 ng/mL; fresh batch Appendix E).

I next extracted total protein from the cells and performed Western immunoblotting analyses as before. The differentiated, more neuronal version of the SH-SY5Y cells still did not yield detectable responses to ApoE exposure, regardless of isoform or treatment source (Figure F.3.5). Variability in signals between the 2 separate plates treated with *E. Coli* produced ApoE3 for 10-minutes was negligible (Figure F.3.5, b, marked by stars).

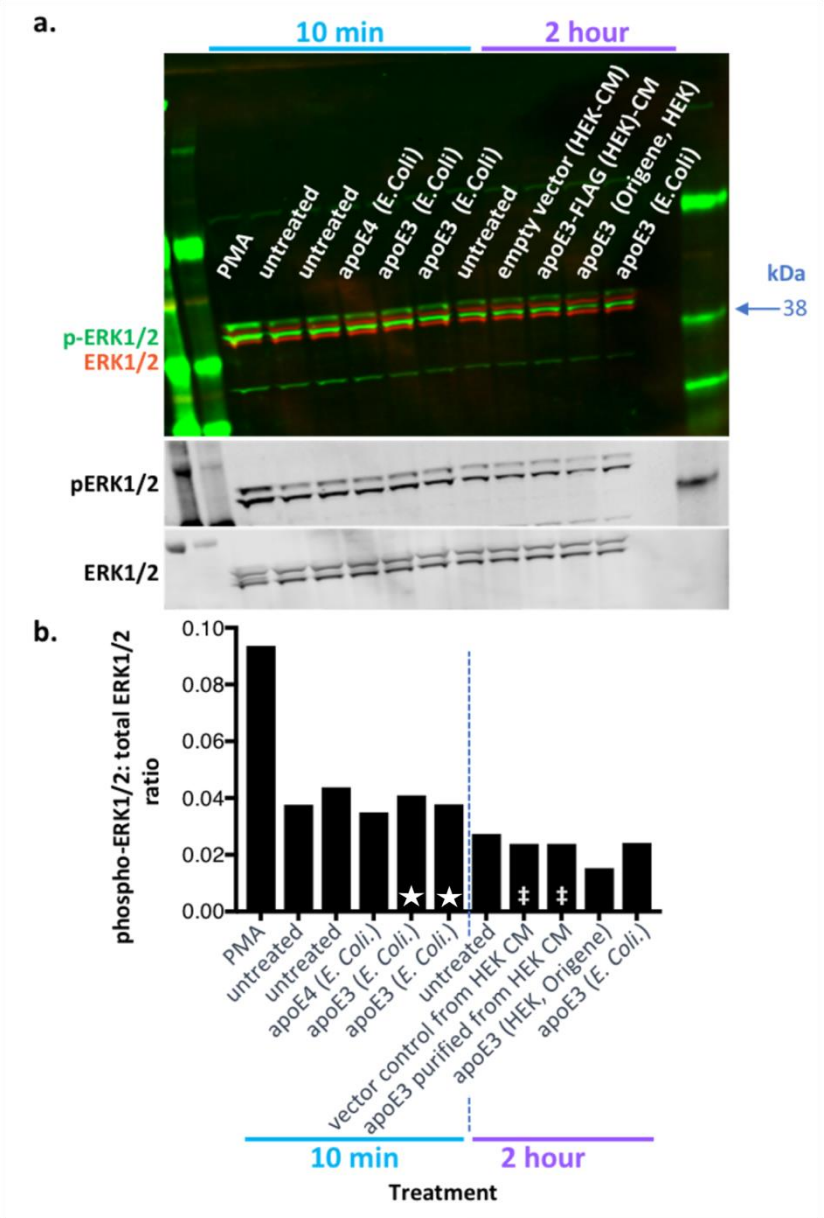

F.3.5 Appraisal of pERK1/2 levels in differentiated SH-SY5Y treated with ApoE

Immunoblots of protein extracts from ApoE-treated, day 15 differentiated SH-SY5Ys. Recombinant ApoE included bacterial- and mammalian-expressed proteins, as indicated. (a.) Phospho-ERK1/2 (green) and ERK1/2 (red) immunoreactivity bands at the 10-minute (left) and 2-hour (right) time points are shown. One lane represents 1 culture dish and stars show 2 independent replicates. (b.) Graphed ratio of pERK1/2 to total ERK. Daggers (‡) mark samples treated with secreted, lipidated ApoE (and cognate control vector) from transfected HEK cells.

F.3.6 Investigating components of non-canonical MAPK signaling

For both undifferentiated and differentiated SH-SY5Y cells, I evaluated whether LRP1 and MAP3K12 were expressed at the mRNA level. In the undifferentiated state, the RT-PCR amplification cycle threshold (CT) in the 40-cycle reaction were typically at 23 cycles (similar to that of the highly expressed GAPDH housekeeping gene) thus was a sign of readily detectable, robust expression of both genes at baseline. As Figure F.3.7 shows, upon differentiation for 15 days, LRP1 expression levels increased by 2-fold while that of MAP3K12 increased 3-fold compared to the undifferentiated state.

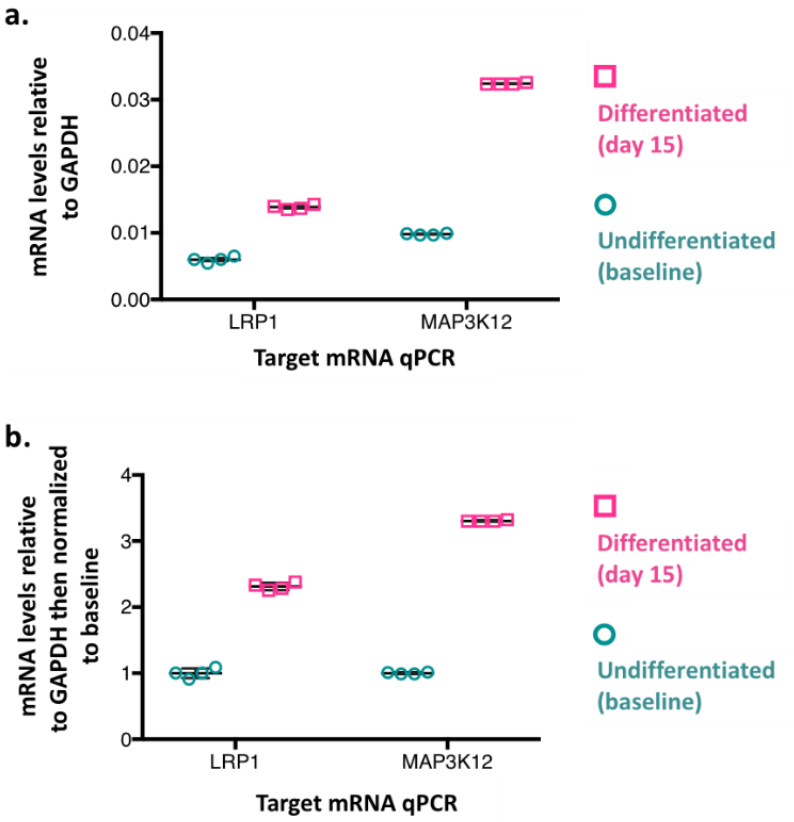

F.3.7 SH-SY5Y cells express LRP1 and MAP3K12

RT-PCR results for implicated signaling components, LRP1 and MAP3K12, in undifferentiated and 15 day differentiated SH-SY5Y cells. (a.) The mRNA levels are graphed relative to the reference gene, GAPDH. (b.) The same data from (a) plotted as relative expression fold-change over the undifferentiated state (set to 1) and shows, upon differentiation, LRP1 levels doubled while MAP3K12 expression tripled. Individual data points for 4 technical RT-PCR replicates from a single culture dish (60mm plate) are shown and error bars are SEM.

F.4 Discussion

I surmised that one way to establish the SH-SY5Y cell line's appropriateness as an ApoE study platform was to observe whether they recapitulate ApoE-induced biological changes that had

been reported for human ESC-derived neurons according to that discussed in Section 1.10.3. Huang *et al.* (2017) showed that, using *E. coli* produced recombinant ApoE variants, *APP* transcriptional modulation occurred in an ApoE isoform-dependent manner subsequent to stimulation of a signaling transduction cascade summarized in Figure 1.13 (132). Should the SH-SY5Y cell line demonstrate similar responsivity to ApoE, then these cells likely would provide a more tractable culture platform than the stem cell derived system because SH-SY5Y cells are comparatively easier and less costly to maintain.

In 2 independent experiments that each utilized *E. coli* produced ApoE recombinant protein from two independent commercial sources, I established that treatment of undifferentiated SH-SY5Y cells with 3 ApoE variants did not elicit a response in terms of modulating *APP* gene expression. One caveat in these experiments was the lack of a sufficiently robust *APP* inducing control with which to gauge modulation of *APP* transcription and this led me to monitor a different readout for which I had a well-characterized positive control.

Since Huang *et al.* (2017) implicated the upstream trigger for *APP* transcriptional induction was ApoE-induced activation of MAP kinase (Section 1.10.3), I measured MAP kinase ERK1/2 phosphorylation following ApoE treatment of undifferentiated SH-SY5Y cells. However, I again did not detect a response to ApoE. I then questioned the quality of the recombinant protein reagents which up to this point were all generated in *E. coli*. However, after repeating the ERK1/2 phosphorylation experiment using commercially sourced ApoE3 (ApoE2 and ApoE4 were not available) generated through a mammalian-recombinant expression system, I again failed to detect apoE responsivity.

Physiologically secreted ApoE is lipidated and the commercial ApoE3 generated through a mammalian-recombinant expression system was not a secreted product thus perhaps not fully biologically processed and lipidated. In the interest of increasing the chances of having a more physiologically representative ApoE preparation, as well as, having the full set of the 3 ApoE isoforms, I established an expression system that allowed for ApoE that was secreted from transfected HEK293 cells. When I treated undifferentiated SH-SY5Y cultures with conditioned media containing secreted ApoE, I still could not detect a response in ERK1/2 phosphorylation.

Because the PMA activation control consistently exhibited increased ERK1/2 phosphorylation, I was confident that the system was not saturated and that it was capable of responding. Because reduced signal strength tracked with reduced protein input (PMA lanes in the Western blots and the first 3 bars in the bar charts in F.2.7; a and b), this not only proved that my detection and quantification techniques for the Western blots were functioning appropriately, but it also confirmed that I was working within the linear range of the assay. Of note, once normalized, as

expected, the titrated PMA lysates showed phospho-ERK1/2:totalERK1/2 ratios that were similar to each other, irrespective of the amount of protein input (4-fold induction of phosphorylation) (Figure F.2.6, a).

My thinking was that undifferentiated SH-SY5Ys perhaps do not express the full complement of cellular machinery necessary for modeling ApoE-induced signal transduction. To investigate the possibility that differentiated SH-SY5Ys would respond to ApoE treatments, I first established and validated a differentiation procedure. The synaptic markers *SYP*, a ubiquitous component of synaptic vesicles, and *SV2B*, an isoform of SV2 which is a part of all synaptic vesicles, were both robustly induced in differentiating conditions. The MAP 2 gene transcript which doubled in differentiated versus undifferentiated conditions, encodes a protein known to stabilize neuronal shape by interacting with other components of the cytoskeleton and is a characteristic mature neuron marker (193). A well characterized marker of the developing neuronal crest (that is also upregulated in iPSC-derived neurons), NGFR, was also upregulated (242). Since, not only are *APP* and MAPT dysregulation associated with AD, but it has also been asserted that there is some interplay between ApoE4 and both Aβ and tau protein, I included them in the transcriptional profiling experiment. Both their transcript levels both increased further adding confidence to the neuronal nature of the differentiated cells. These transcriptional assessments, as well as the development of morphological characteristics consistent with neurons, denoted successful differentiation.

I subjected the differentiated SH-SY5Y cells to treatment with a selection of ApoE reagents that represented all of the various types that I had by now collected (Table E.1.7). Despite having shown elevated neuronal morphology and transcriptional markers, differentiated, there was no change in responsivity compared to the undifferentiated contexts, i.e., they failed to show ERK1/2 phosphorylation responsiveness after any of the ApoE treatments.

Most of the treatment concentrations I used were in the range of the physiological concentration in human CSF (6 to 9 µg/mL), as well as, the concentration used in the study that I was attempting to recapitulate (10 µg/mL) (95, 132). My ApoE secreted in HEK293 CM preparations were lower than the intended concentration (10 µg/mL). Of note, Wang *et al.* (2018) (introduced in Section 1.10.3) used ApoE3 from human astrocyte CM containing a concentration of 12 ng/mL for human iPSC-derived cell culture studies because this concentration approaches murine interstitial fluid (ISF) ApoE3 concentrations (133). The concentration of ApoE3 in human ISF is not known, to the best of my knowledge, so I do not know if this is concentration physiologically representative. However, its concentration in mouse ISF (18.7 ± 5.3 ng/mL) is 100-fold less than the concentration in mouse CSF (1.84 ± 0.08 µg/mL) (243, 244). Therefore, the possibility remains that the ApoE

concentration in the CM I prepared was indeed physiologically relevant and my observations reflect an insensitivity of SH-SY5Y cells to ApoE. In the absence of an orthogonal assay in which to validate ApoE functional activity, I was unable to determine the answer. However, I decided that since I had ApoE from several sources, it was more likely that the SH-SY5Y cells were not responsive.

One explanation for the absence of ApoE sensitivity could be that SH-SY5Y cells lack the relevant ApoE receptor, LRP1, or the kinase, DLK (encoded by the MAP3K12 gene), which are key components mediating the non-canonical MAP kinase signaling cascade implicated by Huang et al. 2017 (132). I, however, established that the SH-SY5Y cells exhibited robust expression of both the LRP1 and DLK at the transcriptional level. Furthermore, both transcripts were increased in the differentiated, more neuronal phenotype. I concluded therefore that SH-SY5Y cells are presumably deficient in some other component of the signaling pathway, but I do not yet know what that may be. One limitation of this conclusion is that I did not assess expression or function of LRP1 or DLK at the protein level.

Overall, weighted evidence from the various sources, concentrations, forms, and variants of ApoE that I used led me to conclude that SH-SY5Y cells, even if differentiated into a more mature neuronal nature, are not amenable to modelling ApoE signal transduction studies (Appendix F). My next step was to explore other systems. Using the scientific literature, it seemed a more robust and translational cellular system is human iPSC derived neurons. Therefore, I decided to move on to explore this possibility.

Appendix G

G.1 Additional assessment of candidate clones from Chapter 3

G.1.1 Treatment of puromycin resistant clones with doxycycline

To ascertain whether the NGN2 expression cassette was present but had integrated elsewhere in the genome, instead of at targeted AAVS1 locus, I evaluated whether candidate clones that came out of the screen would show a response to doxycycline treatment. I treated one clone each from the 3/3 (clone ID: 33AB10) and KO (clone ID: KOBC11) genotypes with doxycycline. However, neuronal morphology did not emerge upon 4 days exposure to doxycycline (Figure G.1.2). Meanwhile, as usual, at this timepoint the iNGN2-iPSC control line treated in parallel showed clear induction of neuronal morphology, indicating successful treatment procedures. One possibility for this observation is incomplete integration of the transgene such that the NGN2 portion of the expression cassette was not incorporated into the genome (245).

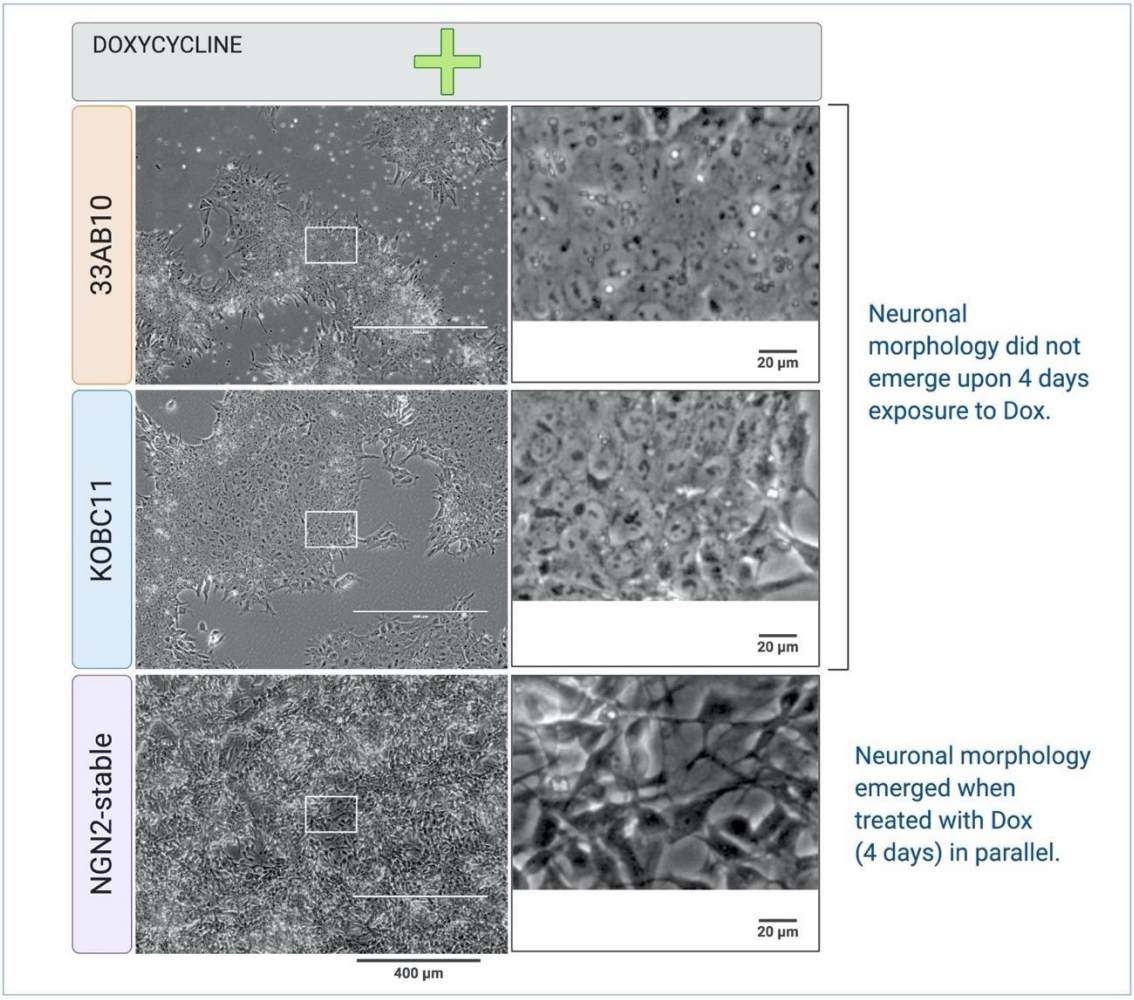

G.1.2 Doxycycline treatment of 1 candidate clone each from the 3/3 and KO genotypes.

The top two panels show representative phase contrast microscope images of two of the candidate integrant clones after four days of exposure to doxycycline. Panel 33AB10 shows the 3/3 derivative and panel KOBC11 shows the KO derivative. Neither clone expressed neuronal morphology upon doxycycline treatment as modeled in the bottom panel by the iNGN2-iPSC control line which was given the same treatment in parallel.

G.1.3 Evaluation of puromycin resistance despite lack of targeted genetic integration

I wanted to understand whether puromycin resistance was an artefact of some sort, therefore, performed a closer analysis of the puromycin resistance phenotype. I first confirmed that the parental lines were more sensitive to antibiotic because the minimal concentration required to kill them was lower than that for derived candidate clones. Then, I checked whether the protein encoded by the pac gene (Section Figure 2.8) was being expressed.

G.1.4 Concentration response curve to puromycin treatment (kill curve)

The 3/3 puromycin resistant iPSC clone from Section G.1 and its naïve parental counterpart were exposed to increasing concentrations of puromycin for 24 hours in a head-to-head comparison of their puromycin resistance phenotype. Figure G.1.5 documents representative cell morphologies when exposed to puromycin at 0, 0.2, 0.4, and 2.0 µg/mL. The naïve parental APOE 3/3-line of interest succumbed to 0.2 µg/mL puromycin as observed by lack of healthy morphology (Figure G.1.5, panel marked *), and all cells were dead when exposed to 0.4 µg/mL of puromycin treatment (Figure G.1.5, panel marked **). In contrast, its derivative candidate clone, 33AB10, remained healthy in 0.2 µg/mL puromycin (panel marked †) and some cells maintained healthy appearance at 0.4 µg/mL of puromycin (panel marked ††) and at 2.0 µg/mL of puromycin exposure (panel marked †††), all cells were still not completely destroyed. As expected, the iNGN2-iPSC control line was more resistant to puromycin induced cell death compared to unedited cells, remaining relatively healthy at 0.2 µg/mL puromycin (panel marked ‡). However, all cells in the iNGN2-iPSC control line died when the puromycin concentration was increased 10-fold to 2.0 µg/mL (panel marked ‡‡). A representative observation of complete culture death for candidate clone cells as a result of a control treatment of Staurosporine is shown in the bottom-most panels of **Error! Reference source not found.**. The differential resistance to puromycin induced cell death, from least to most resistant, for these lines was: naïve parental APOE 3/3-line < iNGN2-iPSC control line < 3/3 candidate clone derivative, 33AB10. This result suggests that the pac gene was functionally incorporated into the candidate clone genome upon electroporation.

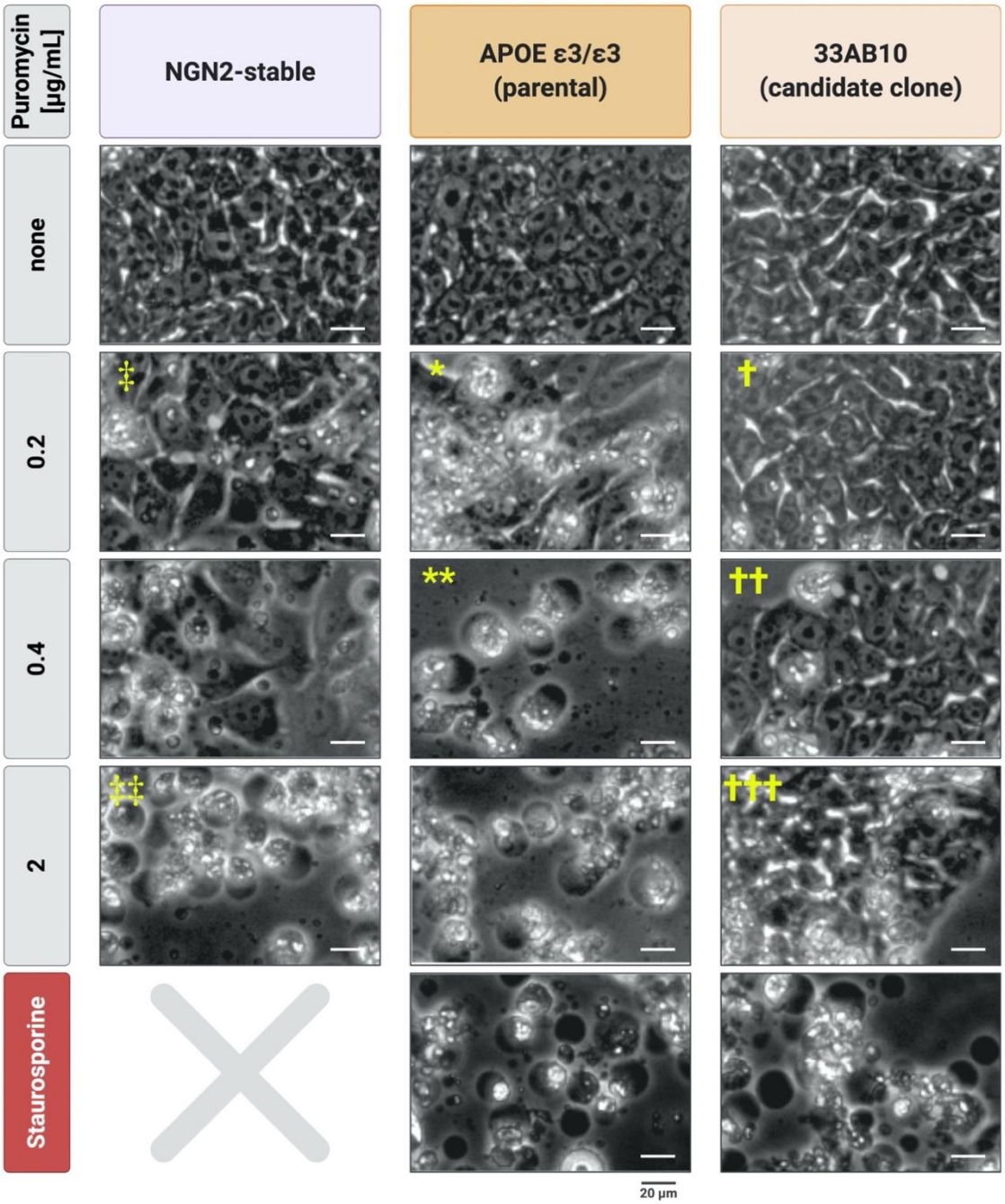

G.1.5 Puromycin kill curve comparison of a 3/3 candidate clone and its parental line.

Shown are representative cell morphologies when iPSCs were exposed to the following puromycin concentrations [µg/mL] for 24 hours starting at the top panel: 0, 0.2, 0.4, and 2.0. The panel marked with an asterisk (*) shows that for the naïve parental 3/3-line, healthy morphology was negatively impacted when exposed to 0.2 µg/mL puromycin and the cells did not survive 0.4 µg/mL of puromycin treatment (panel marked **). On the other hand, a 3/3-line derivative candidate clone, 33AB10, remained healthy in 0.2 µg/mL puromycin (panel marked †) and some cells maintained healthy appearance at 0.4 µg/mL of puromycin (panel marked ††) and at 2.0 µg/mL of puromycin (panel marked †††), not all cells died. The iNGN2-iPSC control line showed more resistance to puromycin induced cell death compared to unedited cells, remaining relatively healthy at 0.2 µg/mL puromycin (panel marked ‡) and dead when puromycin was increased to 2.0

µg/mL (panel marked ‡‡). The bottom-most panel is a view of complete culture death owing to a control treatment of Staurosporine.

G.1.6 Assessment of protein expression of the enzyme encoded by pac

Next, I further assessed the puromycin resistance phenotype by examining the protein expression levels of the enzyme encoded by pac, puromycin N-acetyltransferase, which functions to neutralize puromycin and is encoded in the HDR repair template. To do so, I subjected protein lysates from various lines to Western blot analysis using a puromycin N-acetyltransferase antibody. Two candidate clones, 1 each representing the 3/3 and KO backgrounds, were compared to their naïve parental counterparts. In both cases, a Western blot band consistent with the expected size (42 kDa pointed out by arrows in Figure G.1.7) of the puromycin N-acetyltransferase protein was evident in candidate clone samples and absent (as expected) in their respective parental lines. The iNGN2-iPSC control line did not yield as clear a puromycin N-acetyltransferase protein signal. The reason for this presumably was its overall protein expression level is lower than that of the clones, as reflected by its relatively lowered antibiotic resistance level compared to the candidate clones (illustrated in Figure G.1.5).

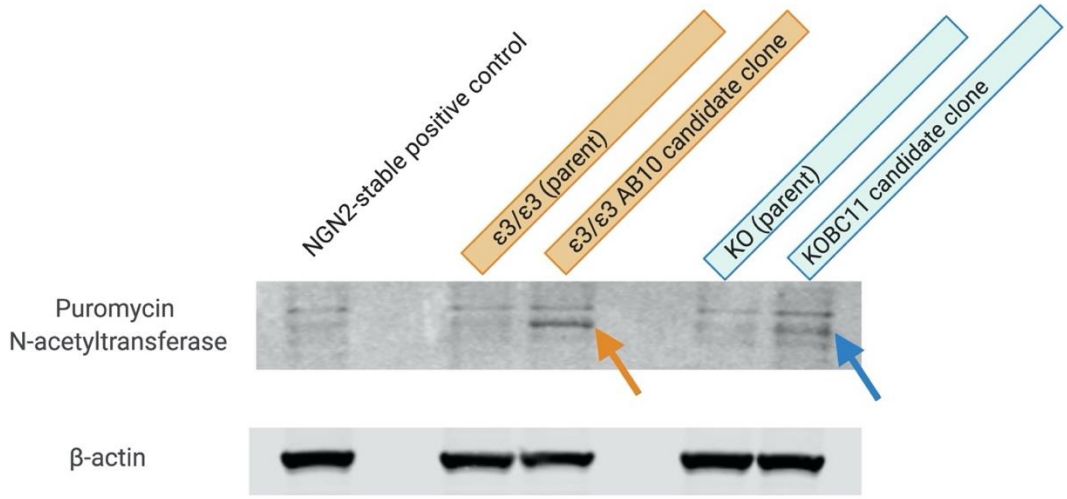

G.1.7 Western blot showing protein expression from the gene conferring puromycin resistance in select candidate clones.

Puromycin N-acetyltransferase protein expression was evident in 2 candidate clones compared to parental line; bands depicted by the arrows. The iNGN2-iPSC control line failed to show as robust a puromycin N-acetyltransferase protein band. The levels of the loading control, β-actin, indicated consistent and reliable amount of lysate was input onto the blot.